Validation of Satellite SAR Offshore Wind Speed Maps to In-Situ Data, Microscale and Mesoscale Model Results

Charlotte Bay Hasager, Poul Astrup, Rebecca Barthelmie, Ebba Dellwik, Bo Hoffmann Jørgensen, Niels Gylling Mortensen, Morten Nielsen, Sara Pryor and Ole Rathmann

Abstract A validation study has been performed in order to investigate the precision and accuracy of the satellite-derived ERS-2 SAR wind products in offshore regions. The overall project goal is to develop a method for utilizing the satellite wind speed maps for offshore wind resources, e.g. in future planning of offshore wind farms. The report describes the validation analysis for 16 cases in Denmark, 5 in Italy and 3 in Egypt. Wind speed maps and wind direction maps from the ERS-2 SAR satellite are derived at the Nansen Environmental and Remote Sensing Center. Wind speed and wind direction maps at 10 m above sea level have been compared to in-situ observations from a met-mast at Horns Rev in the North Sea located 14 km offshore. The SAR wind speeds have been area-averaged by simple and advanced footprint modelling. The comparison results are very promising with a standard error of ± 0.61 m s^{-1}, a bias ~ 2 m s^{-1} and $R^2 \sim 0.88$. Wind speeds predicted by the local scale model LINCOM and the mesoscale model KAMM2 have been sucessfully compared to the spatial variations in the SAR wind speed maps. Near the coast is an 800 m wide band in which the SAR wind speed observations have a strong negative bias. Shallow water and tidal currents bias in the SAR wind speed maps in some cases. At the Italian site the SAR wind speed maps compared very well to WAsP model results from the coast to 5 km offshore. Further offshore the KAMM2 model results seemed more reliable. This is likely due to mesoscale effects of high orography at Corsica. At least 60-70 randomly selected satellite images are required to characterize the mean wind speed and Weibull c parameter, while of the order of 150 images are required to obtain a variance estimate, and nearly 2000 are needed to obtain a robust estimate of energy density (or Weibull k). This is under the assumption of no error in the SAR wind speed maps and for an uncertainty of $\pm$ 10% at a confidence level of 90%. Around 100 satellite SAR scenes may be available for some sites on Earth but far few at other sites. The number of available satellite SAR scenes is increasing rapidly with ERS-2, RADARSAT-1 and ENVISAT in orbit. Hence the technique holds promise for future utilization in offshore wind resource assessment.

Contents

1 The WEMSAR project

Charlotte Bay Hasager

Funding to the WEMSAR project is given by the European Commission with the contract number ERK6-CT-1999-00017 within the EESD programme. WEMSAR is an acronym for Wind Energy Mapping using Synthetic Aperture Radar. The project period is March 1st, 2000 to February 28th, 2003. The WEMSAR project is co-ordinated at NERSC, Nansen Environmental and Remote Sensing Centre, in Bergen. WEMSAR homepages are available at NERSC http://www.nrsc.no/~wemsar/ and at Risø http://www.risoe.dk/vea-atu/remote/wemsar.htm. The partners are

- NERSC   Norway   Professor Ola Johannessen
- Risø National Lab.   Denmark   Dr. Charlotte Bay Hasager
- ENEA   Italy   Dr. Gaetano Gaudiosi
- NEG-Micon   Denmark   Dr. Lars Christensen
- Terra-Orbit   Norway   Mr. Geir Jevne

1.1 Deliverables

The deliverables reported on in the present report are highlighted in italic

D4(b): *Wind maps for three* [*] *test sites containing comparisons of SAR wind against in-situ wind and model results* (Re PU)

D5: *Maps of off- and near-shore atmospheric flow fields from a mesoscale model* (Da PU)

D6: *Local wind resource maps for micro-siting of wind turbines* (Da PU)

D7: *Wind climatology analysis of radar-derived wind speed for micro-siting use* (Re CO)

The planned way of distribution, either as report (Re) or data (Da) and either public (PU) or confidential (CO) is stated.

Risø is responsible for the work on deliverables D4(b), D5, D6 and D7. [*] Risø compares data at the test sites in Denmark, Italy and Egypt. NERSC compares data at the test site in Norway.

1.2 Method of reporting

A description of the work carried out on the deliverables D4(b), D5, D6 and partly D7 is contained in the present Risø-R-1298(EN) report.

It is regarded as equally important to disseminate the scientific results achieved through the WEMSAR project work, quickly and efficiently to potential users and other interested parties. Our on-going publications are listed in Appendix 1. The list contains publication of one refereed (peer-reviewed) paper, 8 proceed-

ings papers, 5 published abstracts from conferences and 5 other publications. Poster presentations are given on 8 occasions.

One of the posters was given the [Award for best poster](#) at the *Global Wind-power Conference, Paris, 2-5 April, 2002.* The choice of this as the best poster was explained by the committee to be:

"an innovative way of improving wind resource estimation by use of new technology and an eye-catching layout with good explanation of the method and results".

Please, refer to the Appendix 1 for the full reference of the poster with a link to the poster and proceedings paper.

1.3 Content and authors

The aim of the present report is to assess and document the accuracy and limitations of satellite SAR wind speed maps for offshore wind resource mapping. To achieve this a validation study of satellite SAR wind speed maps compared to in-situ wind speed observations, micro- and mesoscale model wind speed results is presented. The report is structured in 17 chapters.

Chapter 1 describes the project work in relation to the WEMSAR project deliverables and the main contributions of the many co-authors.

Charlotte Bay Hasager	Satellite SAR, comparison analysis, editing
Poul Astrup	LINCOM for Denmark
Rebecca Barthelmie	Meteorological analysis, offshore wind energy
Ebba Dellwik	Meteorological data analysis for Denmark
Bo Hoffmann Jørgensen	KAMM2 for Denmark, Italy and Norway
Niels Gylling Mortensen	Meteorological analysis & WAsP for Egypt
Morten Nielsen	Footprint theory and programming
Sara Pryor	Meteorological analysis, offshore wind energy
Ole Rathmann	WAsP for Italy and Norway

Chapters 2-10 contain general information and Chapters 11-14 are case descriptions of the sites in Denmark, Italy, Norway and Egypt, respectively. Chapters 15, 16 and 17 contain a summary, conclusion and recommendations for applied use. The content of each chapter is described briefly below.

Chapter 2 is an overview of the socio-economnic context on offshore wind energy resources and the specific need for remote sensing observations. In Chapter 3 is given an overview of satellite SAR with a special emphasis on possible errors on wind speed mapping. Chapter 4 and 5 briefly introduces the microscale models used, namely the WAsP model and the LINCOM model, respectively. The WAsP model is used for calculating offshore wind speeds from wind observations at coastal positions in order to avoid the bias of the influence of orography and land roughness on the in-situ data. The LINCOM model is used only for the Danish site at which in-situ observations from a tall meteorological mast 14 km from the coastline is available. At this site orography and land roughness is less important. The LINCOM model results provide maps of spatial wind speed variations in the region. Chapter 6 introduces the KAMM2 mesoscale model that is run with an independent data set, namely the NCAR/

NCEP reanalysis. The KAMM2 model is computationally more demanding than the spectral LINCOM model.

In Chapter 7 is described an analysis on how many SAR observations is needed to assess the wind resource parameters with a given accuracy. The study is based on multi-year 1-minute and 30-minute in-situ offshore wind speed observations. Chapter 8 is a brief analysis on the possible ways of extrapolating wind speeds from the 10 m level at which satellite SAR images are valid and up to hub-height of wind turbines. Chapter 9 describes in detail the footprint area-averaging, i.e. a method that is used for comparing spatial observations from satellite SAR to in-situ time-averaged wind speed observations from the Danish offshore site. In Chapter 10 the NOAA AVHRR satellite images used together with DWD weather charts to infer the synoptic weather is described.

Chapters 11-14 present each site. The available data are very different from site to site and so is the reporting.

Chapter 11 on the Horns Rev site in Denmark is the longest. It contains a description of the satellite ERS-2 SAR scenes from 16 days, the weather conditions during the overpass of the ERS satellite and also the meteorological observations from a tall meteorological mast 14 km offshore the coast. The data set is unique for comparing SAR and in-situ wind speeds for validation studies. At this site a large offshore wind farm is under construction by ELSAM/ ELTRA (Techwise). The tidal effects are included in the meteorological data analysis. Comparison to in-situ observations is done by footprint area-averaging. Microscale model results from LINCOM for all cases and KAMM2 mesoscale model results for five cases are compared to the SAR wind speed maps. The bathymetry is included in the analysis of the SAR wind speed maps.

Chapter 12 on the Maddalena site in Italy contains weather descriptions for nine cases. The meteorological observations are from a very tiny cliff in the Strait between Sardinia and Maddalena, i.e. the orography of the nearby coastlines is significant on the measured wind speeds. Therefore the WAsP model has been used to calculate the wind speeds further offshore. Also the KAMM2 model has been used and the orography of both Corsica and Sardinia had to be taken into account. A comparison analysis between SAR wind speed, in-situ observations, WAsP and KAMM2 model results is presented for five days.

Chapter 13 on Hellisöy in Norway only contains the WAsP and KAMM2 wind speed maps for seven days. The comparison analysis to SAR wind speeds is performed at NERSC. At Hellisöy the in-situ observations are from a mast on top of a stoker house near the lighthouse at the most westerly part of the Norwegian coastline. The coast is of cliffs with moderate orography. The WAsP model is used to calculate wind speeds offshore taken the local orography and roughness into account. The KAMM2 model is used to calculate the wind speed patterns in a larger region.

Chapter 14 on Gulf of Suez in Egypt contains a site description. Wind speed observations from a number of coastal meteorological masts are available along the Gulf of Suez. WAsP has been used to calculate the offshore wind speeds and compared to SAR wind speed maps on three days.

Chapter 15 is a summary on validation results on SAR wind speeds maps compared to in-situ observations micro- and mesoscale model results from the sites analyzed. Chapter 16 contains the conclusion and Chapter 17 is recommenda-

tions for applied use of SAR wind speed maps for offshore wind resource mapping.

1.4 Acknowledgements

2 Offshore wind energy

Rebecca J. Barthelmie and Sara C. Pryor

2.1 Socio-economic context

World energy demand increased by around 60 % between 1970 and 1995 (Milborrow, 1996). As the demand for energy increases and readily accessible fossil fuel reserves are depleted, new energy supplies are being sought. Renewable energy sources are an attractive alternative to fossil fuels because they can also help to meet environmental goals such as reducing emissions of greenhouse and other trace gases. In addition to reducing greenhouse gas emissions, use of renewable energy reduces emissions of nitrogen and sulphur oxides and volatile organic compounds which are implicated in acid rain, smog and aerosol production in the atmosphere. In addition to providing cleaner sustainable energy sources, renewable energy projects can also provide employment since they typically produce more jobs per energy unit installed than 'conventional' energy sources. A political motivation for the interest in renewable energy sources is to decrease the dependence of importing energy carriers. In several countries the oil crises in the 70's and 80's as well as the Gulf war form a good incentive for relying more on local resources.

According to agreements reached in Kyoto, the European Union (EU) must cut emissions of greenhouse gases by 8 %, the US by 7 % and Japan (and other industrialised countries) by 6 % by the year 2010. In 1999 a consortium of environment and industry groups warned that the EU will fail to meet these targets and is also losing a potentially valuable opportunity to create thousands of jobs by failing to implement a renewable energy directive. The directive suggested by the consortium has targets of 8 % of each country's energy coming from renewables by 2005 increasing to 16 % by 2010 and increasing by 2 % each year subsequently. In May 2000 the European Commission unveiled proposals to increase the proportion of energy supply from renewable sources to 12 % (22 % of electricity supply) by the year 2010 (Environment News Service, 2000). Offshore wind energy is expected to play a significant role in this expansion.

shore wind energy is expected to play a significant role in this expansion. Combining onshore developments with exploitation of large wind resources offshore, the target of 40 GW of installed wind capacity becomes feasible.

Offshore wind energy is currently about 15-20 % more expensive than onshore wind energy and nearly equivalent at good sites (sites with a good wind resource but where installation costs are excepted to be low) (Barthelmie and Pryor, 2001). Development of pilot projects in Denmark, Sweden and the Netherlands to assess turbine modification and optimisation and good monitoring and analysis programs to effectively assess wind resources have reduced costs considerably. Costs have been reduced from 0.086 ECU per kWH at Vindeby, Denmark to an estimated 0.048 ECU per kWh estimated for the large wind farms in the next Danish installations (Svenson and Olsen, 1999), (Kuhn and Bierbooms, 1999). Higher wind speeds and lower turbulence offshore are offset by increased installation and maintenance costs. Installation costs are increased by the requirement for seabed foundations, undersea cable connections and current relatively low unit production of offshore wind turbines. Maintenance and operation costs are increased by potential losses in grid connections over long distances and restricted times and modes of access for maintenance. The industry has been remarkably innovative in finding solutions to these difficulties (e.g. the use of monopile foundations) and more large wind farms offshore will, given economies of scale, continue to improve the economics of offshore wind farms.

Offshore wind energy developments are underway in many European countries with planned projects of several thousand megawatts to be installed in the first decade of the new millennium. By the end of the year 2000, approximately 80 MW of offshore wind energy were installed and operating in Denmark, Holland and Sweden and the UK. Some Northern European countries have relatively detailed plans for offshore wind farm development and these are described. If all plans are realised, more than 11,000 MW of offshore wind capacity will be installed by the year 2030.

2.2 Wind energy resources

Power output of a wind turbine is proportional to the cube of the wind speed and to the swept area of the rotor. Hence power output is increased significantly by increasing wind speed and by increasing the rotor diameter. Accurate determination of the wind resources at a prospective offshore wind farm site is a critical component of its economic feasibility, and therefore requires the entire probability distribution of wind speeds to be characterized.

A number of probability distribution functions have been fitted to, or used to represent, wind speed data (Justus *et al.*, 1976). However, the most commonly used is the two parameter Weibull distribution which has been shown to give a good fit to observed wind speed distributions particularly over water surfaces (Pavia and O'Brien, 1986), (Isemer and Hasse, 1991). The two parameters of the Weibull distribution are k, the dimensionless shape parameter, and c, the scale parameter. The shape parameter (k) is inversely related to the variance of wind speed (U) around the mean value, and the scale parameter (c) is related to the mean of the time series, both are a function of the data averaging period (Troen and Petersen, 1989). The Weibull cumulative probability distribution is:

Equation 1

$$P(U) = 1 - \exp\left\{-\left(\frac{U}{c}\right)^k\right\}$$

The available wind power density (which is proportional to the cube of the wind speed) may be calculated from the Weibull distribution parameters as follows:

Equation 2

$$E = \frac{1}{2}\rho c^3 \Gamma\left(1 + \frac{3}{k}\right)$$

Where, ρ is the air density, and Γ is the gamma function.

In the analysis presented in Chapter 7 we use the first to fourth moments of the distribution (described using the mean, standard deviation, skewness and kurtosis) (Rice, 1995) and the Weibull distribution (shape and scale parameters) to describe the probability density functions of wind speed data sets, and calculate the energy density as shown in (2) from each Weibull fit to the wind speed probability distributions. The Weibull parameters are calculated here from the mean and median of the data set and validated based on the variance according to the following taken from Troen and Petersen (1989):

Equation 3

$$Mean = A\Gamma\left(1 + \frac{1}{k}\right)$$

Equation 4

$$Median = A(\ln 2)^{1/k}$$

Equation 5

$$Variance = A^2\left[\Gamma\left(1 + \frac{2}{k}\right) - \Gamma^2\left(1 + \frac{1}{k}\right)\right]$$

2.3 Offshore wind resources

Wind speed values close to the ground, where we experience them, are a result of a balance between momentum transfer from higher wind speeds aloft and dissipation at the ground. The higher the roughness of the surface, the more momentum is lost at the ground. The result is a greater variation of wind speed with height and lower wind speeds near the ground. Surface roughness offshore is usually of the order 0.0002 m whereas for land surfaces roughness varies between 0.03 and 0.3 m for agricultural surfaces and much higher for areas like urban landscapes and forests. Not only are offshore wind speeds higher but their variation with height (wind shear) is lower. This suggests that vertical wind speed variations across blades will be lower than over land increasing power

output and reducing stress on blades offshore. Another way of viewing this is that the gain of wind speed with height is lower than over land, reducing the necessity for tall towers (Krohn, 1998). Hence, except where topographic forcing enhances flow, wind energy resources offshore are thought to exceed those of onshore regions due principally to (1) greater persistence of flow offshore and (2) higher wind speeds offshore due largely to lower surface roughness. An additional benefit to offshore location of wind farms is reduced turbulence intensity offshore leading to reduced stress on turbine components.

Previous research (Pryor and Barthelmie, 2001b) has shown that in maritime climates in the Northern Hemisphere mid-latitudes, the temporal autocorrelation of wind speeds measured at, or above, 40 m in the near-coastal zone is <u>not</u> significantly higher than that from land sites. However, the persistence of wind speeds above typical turbine cut-in speeds <u>is</u> higher at sites over water surfaces. This research indicates that both the magnitude and stability of wind resources are likely to be higher offshore.

The variation of power output from wind turbines with wind speed is commonly known as the power curve (Energy Centre Denmark, 1994). Power output is zero at low wind speeds, increases rapidly after the 'cut-in' wind speed, reaches the rated output of the wind turbine at about 12 m s^{-1} and drops to zero again after 'cut-out' to prevent damage to the wind turbine at high wind speeds. Using typical turbine specifications Pryor and Barthelmie (2002) quantified the enhancement of electricity production due to offshore location of turbines. They presented analyses of the potential power production from turbines located in the near-shore and offshore environment relative to an onshore location using half-hourly average wind speed data from four sites in the Danish wind monitoring network. These measurement sites are located in a relatively high wind speed environment and data from these sites indicate a high degree of spatial coherence. For these sites and representative turbine specifications (rated power = 1.3 – 2 MW) the fraction of time with power output in excess of 500 kW is twice as high for the offshore location as the land site. Also the fraction of time with negligible power production (defined as < 100 kW output from the turbines described herein) is less than 20 % for the offshore site and twice as high at the land based location. They also showed capacity factors are higher for coastal sites than for the land site and the annual capacity factor for the offshore location is twice that of the land site.

2.4 Wind energy resources in the coastal zone

The atmospheric flow in the coastal zone is highly complex leading to larger uncertainties in resource estimation. For example, analyses presented in Pryor and Barthelmie (2001b) indicate, under offshore flow, flow above 30 m height is not fully adjusted to reduced surface roughness even after over water distances of 20 km. This is in accord with analyses presented in Smith and MacPherson (1987) and indicates the maximum change in wind speed is not fully realised at this distance from the coastline. However, there is substantial acceleration of the flow even within 2 km of the coast-line. Observations presented in Pryor and Barthelmie (2001a) indicate that for offshore flow the mean wind speeds 2 km and 11 km offshore are approximately 30 % and 50 % higher than those from an onshore coastal site at 10 m, 6 % and 25 % higher at 30 m and 5 % and 24 % higher at approximately 50 m.

2.5 The need for remote sensing

At present wind resources offshore are estimated using data from meteorological masts. Although this is an accurate method it is expensive to install infrastructure offshore and the time lag for installation and collecting a suitable period of data (at least one year) is not optimal in a competitive market. Hence the opportunity of estimating wind resources from satellite images is very attractive - particularly since there is the additional advantage of obtaining spatial variations.

3 Satellite Synthetic Aperture Radar

Charlotte Bay Hasager

3.1 Introduction

Historical satellite Synthetic Aperture Radar (SAR) scenes from various microwave bands, X, S, C and L and different polarizations are available, see Table 3-1. Currently only the ERS-2 and RADARSAT-1 satellites are delivering new SAR scenes. Both satellites carry a C-band SAR instrument. The ERS-1 SAR is in hibernation ((Attema et al., 2000) but could potentially be used again. Last time was in mid 1998 for a short period of time. For further information on the SAR instruments, please refer to (Kramer, 1996).

Table 3-1 SAR scenes available from satellites and shuttle missions. [*] Optically processed. All other scenes are digitally processed. From (Hasager, 2000a).

Name	Period	Band	Polarization	$\forall$ (º)
SEASAT	July-Sep. 1978	L	HH	22
SIR 1 (A)[*]	Nov. 1981	L	HH	50
SIR 2 (B)	Oct. 1984	L	HH	20-50
ALMAZ 1	1987-	S	HH	25-50
ALMAZ 2	May 91-Oct. 92	S	HH	25-50
ERS-1	July 1991- June 96	C	VV	20-26
JERS-1	Feb. 1992- Oct. 98	L	HH	35
SIR 3(C)	Dec. 1993	L,C	HH VV HV VH	variable
		X	HH	variable
ERS-2	April 1995-	C	VV	20-26
RADARSAT-1	Nov. 1995-	C	HH	20-50

The European Space Agency (ESA) has successfully launched the ENVISAT satellite with the Advanced SAR (ASAR) instrument recently on March 1st, 2002 (http://envisat.esa.int/). The ASAR is a C-band VV and HH instrument with a 405 km swath with 150 m and 1 km resolution in wide-swath mode. In

image mode the swath in 100 km and a nominal 30 m resolution. With a 35-day repeat orbit the revisit frequency will give daily coverage near the poles and weekly at the equator. The ASAR has beam steering such that the same area can be mapped more frequently if desired ((Attema et al., 2000)). For research and application development ESA will fix the price at or near the cost of reproduction with special waivers for Announcements of Opportunity (AO). However also for operational and commercial use the price is expected to be comparable to that of research and application development. The AO's invitations are available at http://envisat.esa.int/faq/faq.html.

The Canadian RADARSAT-2 is planned for launch in year 2003. This satellite will carry a C-band VV and HH SAR instrument with a lifetime of 7 years (http://www.ccrs.nrcan.gc.ca/ccrs/tekrd/radarsat/rsat2/radnewse.html).

3.2 On ERS-2 SAR

In the current study only SAR scenes from the European satellite ERS-2 are investigated. Much information on ERS-2 is available on the web e.g. at ESA homepages http://earth.esa.int/ including technical specification. Among many others websites is http://www.deos.tudelft.nl/ers/ers2info.html with an MPEG movie of the ERS-2 SAR. The ERS-2 is in a sun-synchronous, near-polar orbit at an altitude of 785 km and an inclination of 98.5 degrees. This results in a repeat track of about 10 days as the swath is 100 km. In other words the same area of the Earth is viewed approximately three times per month at mid-latitudes. The local recording times are 10.30 AM in the descending node and 21.30 PM in the ascending node. The precise ERS orbit determinination is available at http://www.deos.tudelft.nl/ers/precorbs/. Quicklooks have recently become available through http://odisseo.esrin.esa.it .

The principle of the ERS SAR system is sketched in Figure 3-1. The SAR emits C-band microwave radiation in an angle to the side of the flight direction. The radar beam reaches the Earth with an incidence angle ($\forall$) between 20 and 26º in the cross track direction. The width of the cross track is the swath which is 100 km. The microwave signal is backscattered in all directions at the surface. Those signals that happen to travel back to the SAR are measured. As the satellite moves along track the Earth is imaged continuously. Through a calculation of the time delay between emitted and received radiation, the slant range, ground range and azimuth geometry a two-dimensional data set is obtained. The cell size of raw data is 12.5 m.
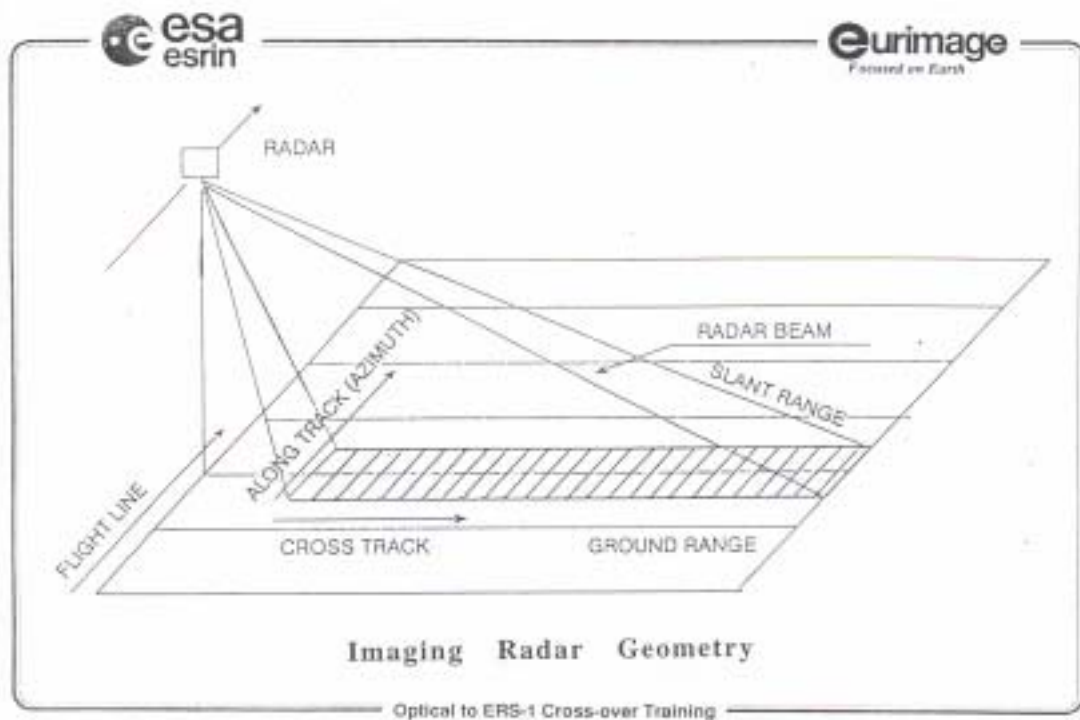
Figure 3-1 Principle of ERS SAR scanning system. From (ESA, 1993)

More precisely the spatial resolution in ERS SAR is 26 m in range (antenna look direction) and between 6 and 30 m in azimuth (in-flight direction) ((Horstmann et al., 2000b). An ERS SAR scene is 100 km by 100 km. The C-band frequency is 5.3 GHz and the wavelength 5.3 cm. As the radar signals are emitted from the SAR itself the recording is independent of daylight. Further does radar penetrate clouds so SAR scenes are obtained in all weather conditions.

3.3 SAR and ocean wind speed

The measured quantity in each resolution cell is the backscatter coefficient, Φ_0, the normalized radar cross section, which is dependent upon the relative wind direction, N, ($N = 0$ for a wind blowing against the radar), the local radar beam incidence angle, $\forall$, of the illuminated area and wind speed, U, expressed as

Equation 6

$$\sigma_0 = B_0(1 + B_1 \cos(\phi) + B_2 \cos(2\phi)).$$

The coefficients B_0, B_1, B_2 depend on $\forall$ and U and they are given in look-up tables (Offiler, 1994), (Quilfen et al., 1998). The accuracy of the model in Equation 6 solving for wind direction is $\forall$20E and solving for wind speed $\forall$2 m s^{-1} or 10 % in rms for wind speeds between 2 - 24 m s^{-1} (Stoffelen, 2002) or better 1.5 m s^{-1} in some cases (Offiler, 1994). (Mourad, 1999) cites the work of Vachon and Dobson and Katsaros et al. that in their studies find that in situ measurements and SAR wind speed are within $\forall$1.2 m s^{-1} for studies based on ship data and buoy data, respectively. The wind speed is for 10 m above sea level.

The ERS SAR data has a dB range of approximately 0 to -23 dB. Simply described does a wind speed of 5 m s^{-1} correspond to –19 dB, 10 m s^{-1} to -14 dB, 15 m s^{-1} to –12 dB, 20 m s^{-1} to –9 dB and 25 m s^{-1} to –7 dB for downwind conditions ($N = 0$).

The SAR wind speed retrieval method originates from C-band scatterometer models such as CMOD-4 (Stoffelen, 2002) and CMOD-IFR2 (Quilfen et al., 1998). These are built on correlation analysis between ECMWF ocean wind field results and/or global ocean buoy data and C-band scatterometer data.

Scatterometer data allows both wind speed and wind direction (with 180E ambiguity) to be retrieved simultaneously, whereas SAR data measures either wind speed or wind direction based on the model in Equation 6. However, in about 65 % of all SAR scenes the wind direction (with 180E ambiguity) can be determined by analysing the so-called wind streaks. These are linear features aligned with the wind direction and their dominant direction can be found e.g. with 2-dimensional Fast Fourier Transformation (Lehner, 1998).

3.4 Surface roughness and normalized radar cross section

The ERS SAR is operating at C-band with incidence angels between 20-26°. For these incidence angles, the radar backscatter, or more precisely, the radar cross section σ_0 is dominated by Bragg scattering from cm-scale ocean surface roughness, which is in resonance with the incidence radiation of the radar. The resonant wave number k_r is related to the electromagnetic wave number k_{el} and $\forall$ according to the Bragg condition

Equation 7

$$k_r = 2k_{el} \sin\alpha.$$

Hence for the ERS SAR the Bragg waves have length in the range of 6.5-8.3 cm ((Horstmann et al., 2000a),(Lehner and Schättler, 2000)). The shortest wavelength is found in the far range, the longest in the near range of the SAR scenes. This small-scale roughness is strongly influenced by the local wind field and therefore allows σ_0 to be a measure of wind parameters. In other words, the spectral density of small-scale surface waves is a strong function of the surface wind stress ((Thompson, 2000)).

Crosswind is wind blowing perpendicular to the range direction and this produces lower σ_0 values than an upwind or downwind (wind blowing along the range direction) owing to the different orientation of the wind wave facets in each case.

For the wind condition of a few meters per second the amplitude of gravity-capillary waves saturate. At increased wind speeds the momentum flux is continuously carried into the air-sea interface and causes underlying longer-wavelength surface waves to increase in amplitude on scale greater than or equal to tens of seconds. Such an increase induces tilting in the gravity-capillary wave field, which makes the ocean surface more visible (brighter) to radar. This accounts for the general increase in radar backscatter with mean wind speed ((Mourad, 2000)

Gravity-capillary waves are temporally and spatially periodic disturbances of the ocean surface on scale of 1-30 cm. Capillary waves with periods of less than 0.1 s and short gravity waves respond quickly to changes in wind speed ((Knauss, 1978), (Garratt, 1992)). The restoring force of these waves is a combination of gravity and surface tension. In addition to the wind induced gravity-capillary waves large-scale gravity waves and swell can modulate the gravity-capillary wave field, thereby producing variations in radar backscatter. Also small-scale features e.g. so-called "parasitic" and "microbore" cm scale waves can introduce variations in radar backscatter. These small-scale waves are dependent on the underlying wave properties rather than wind phenomena ((Mourad, 2000)).

The efficiency of Bragg wave generation is a function of wind speed and the air-sea temperature difference. For atmospheric stable stratification a lower wind shear stress will result in a decreased production of Bragg scattering waves and hence reduce σ_0 compared to neutral or unstable stratification. For stable stratification the cold sea surface will have an increased viscosity that further reduces Bragg wave generation(Clemente-Colón, 2000).(Mourad, 1999) explains the effect of unstable stratification on increased SAR backscatter to be cause largely by vigorous atmospheric turbulence (rather than the viscous forces in the water).

In atmospheric modelling, the ocean roughness is parameterised well by Charnock's relation ((Charnock, 1955)) :

Equation 8

$$z_0 = A_c \frac{u_*^2}{g}$$

where z_0 (m) is the roughness length, u_* (m s^{-1}) is the friction velocity and g (m s^{-2}) is the acceleration of gravity. A_c is approximately 0.011 for open ocean and the value was introduced as a constant by Charnock. The relationship between friction velocity and wind speed at a given level is given by the following profile for non-neutral conditions

Equation 9

$$\overline{u}(z) = \frac{u_*}{\kappa}\left(\ln \frac{z}{z_0} - \psi_m\left(\frac{z}{L}\right)\right),$$

where $\overline{u}$ (z) is the mean wind speed at height z (m), κ is the von Karmán constant, P_m (-) is the stability correction term and L (m) is the Monin-Obukhov length ((Stull, 1991)). L is dependent upon the surface sensible heat flux and the surface friction velocity. In case of a neutral atmosphere ψ_m is equal to zero.

3.5 Error estimation

Error estimation on wind speed retrieval from SAR is dependent on the input to the wind retrieval algorithm, i.e. σ_0, incidence angle and wind direction, and the wind retrieval algorithm itself. The errors associated with σ_0 include three independent sources of error. One is the calibration accuracy of the SAR. The second is the effect of speckle and the third is oceanographic and atmospheric noise. The different sources of error are described in the following.

- Radiometric accuracy

The radiometric accuracy of ERS-1 and –2 SAR's is within ±0.4 dB ((Attema et al., 2000), that translate to approximately ± 0.7 m s^{-1}. For very high wind speeds with around 0 dB, the error may be larger dependent on the calibration procedure ((Horstmann et al., 2000b)).

- Speckle noise

The speckle is due to scattering of coherent electromagnetic waves by rough surfaces. For the RADARSAT-1 ScanSAR with a 100 m resolution the backscatter variation caused by speckle can be up to ±3 dB on a single pixel and therefore should not be interpreted as wind variations. For ScanSAR the data must be averaged over at least 2 km * 2 km to reduce this effect of speckle according to ((Horstmann et al., 2000a)). For ERS SAR that has a 12.5 m resolution the same averaging results in a 250 m * 250 m grid size. Multi-looking reduces the speckle noise but also reduces the spatial resolution.

Based on an ERS SAR scene from the North Sea acquired under homogeneous wind conditions, (Horstmann et al., 2000b) estimated the effect of pixel resolution on wind speed accuracy. The figure 6, p 104 in their work shows the interesting finding that speckle noise is dominating for 100-400 m pixels. For very large grid cells (e.g. 10 km) in which speckle noise is reduced to an insignificant level, there still is some scatter in the SAR wind speed data. This is concluded to be a function of wind direction variations over the scene ((Horstmann et al., 2000b)).

- Oceanic and atmospheric noise

Rain may reduce σ_0 in C-band SAR by rain volume scattering from atmospheric attenuation. Raindrops may also impact on the sea surface by dampening the Bragg waves and thus reduce σ_0. The rain volume scattering is the most import of the two processes for C-band ((Clemente-Colón, 2000)).

Surfactants (e.g. oil slicks, algal blooms) at the ocean surface are very effective at damping the wind generation of Bragg waves. Hence under moderate winds surfactants can be delineated in SAR imagery. However for winds > 5 m s^{-1} the surface layer tends to mix down into the water column and become undetectable by SAR ((Clemente-Colón, 2000)).

Coastal waters may differ from the open sea in a number of ways. The CMOD algorithms are derived from open seas conditions. Hence in coastal seas additional parameters may influence the roughness of the sea as compared to that of the open sea. This may biased wind speed maps. The Charnock constant A_c (Equation 8) is 0.011 for open seas whereas 0.018 has proved appropriate in the coastal Danish seas ((Johnson, 1998)). The value of A_c is dependent on fetch, i.e. the distance from the shoreline. Fetch dependent roughness of the sea as measured by observed by coastal and offshore masts and modelled by atmos-

pheric flow modelling is described in (Hasager, 2000b). For offshore flow the roughness step change from land to sea influence the turbulence and hence the sea roughness ((Astrup et al., 1999). Further does the air temperature and sea surface temperatures have an impact on sea surface roughness as described in (Frank, 1997). In other words, atmospheric studies on the development of internal boundary layers at shorelines and the effect to the sea surface is important for coastal applications of interpreting SAR wind speed maps.

Sea currents such as tidal currents may modulate the surface roughness independent of atmospheric effects(Mastenbroek, 1998) and eextremely shallow regions such as mudflats at low tide can produce very smooth surface conditions that appear as dark features in SAR imagery ((Clemente-Colón, 2000)). The tidal currents may give artificial high wind speeds in SAR wind speed maps. The bottom topography may even be mapped through modelling of the variations in the backscattered signals from SAR as described by (Calkoen et al., 1998; Calkoen et al., 2001; Romeiser and Alpers, 1997). The basic principle is that the surface of the ocean may be more or less rough than the wind alone predicts due to marine features affecting the ocean surface. Figure 3-2 is a simple sketch of this phenomenon. Bathymetry mapping from SAR imagery is based on these variations.
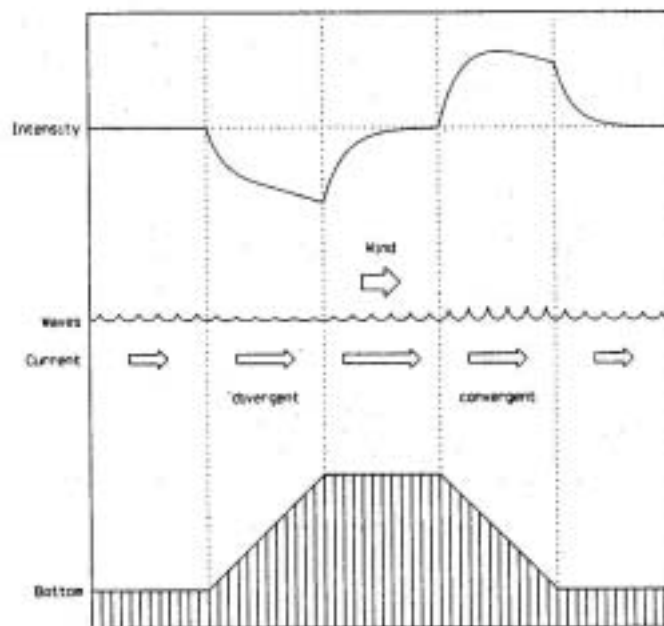
Figure 3-2 A schematic of ocean surface roughness variations due to bottom topography. From {Calkoen, Hesselmans, et al. 2001 85 /id}.

- Incidence angle

The error associated with incidence angle is negligible for ERS SAR as the incidence angle band is narrow (and well-known).

- Wind direction

Theoretical studies of the relation between σ_0 and wind direction as a function of downwind, crosswind and upwind for C-band VV (and HH) SAR are calculated by (Horstmann et al., 2000b). The results show a symmetrical response with minimum errors on crosswind, upwind and downwind cases and maximum

errors on winds at angles of ±45° from crosswind. For an incidence angle of 23° (in the middle of the ERS SAR incidence angle interval) and a ±10° uncertainty on wind direction, the results show an error less than 10 % for all wind speeds within 15° of upwind, downwind and crosswind angles. However for winds at angles of ±45° from crosswind the error is >20% for wind speeds > 7 m s^{-1}.

(Vachon, 2000) studied 56 ERS SAR scenes where the error on wind direction was estimated to be within 30° between in-situ wind direction and SAR wind direction and this uncertainty resulted in a R^2 error of 1.9 m s^{-1} on wind speed. The wind direction was most accurately determined in the SAR scenes under higher winds and unstable atmospheric conditions. In an earlier study {Vachon & Dobson 1996 125 /id} found SAR streaks to be within ±24º r.m.s. error in ERS-1 SAR in 16 scenes as compared to wind observations at a ship. They concluded the in-situ wind direction used in CMOD4 gave better SAR wind speeds compared to ship wind speed observations (±1.2 m s^{-1} r.m.s. error) than when using the wind direction from streaks (±3.0 m s^{-1} r.m.s. error).

- SAR wind speed retrieval algorithms

Within the WEMSAR project a report on SAR wind speed retrieval algorithms has been published (Johannessen, 2000). The CMOD-IFR2 algorithm (Quilfen et al., 1998) was concluded to be the best available for coastal area(Johannessen, 2001).

3.6 Collocation

- Collocation in space

The issue of collocation is that of precise geo-location and timing. Collocation is fundamental to wind speed retrieval from SAR. Problems related to collocation influence the CMOD algorithms themselves as well as the independent wind speed validation studies.

The CMOD4 and CMOD-IFR2 wind retrieval algorithms are derived from correlation analysis between C-band scatterometer data and atmospheric ocean wind field results and/or global ocean buoy data. The position of buoys and the accuracy of geometrical rectifications of the SAR scenes determine the absolute precision on geo-location.

The actual position of buoys may change significantly from their nominal position. (Gower, 2000) report the average changes in buoy position through GPS measurements on 16 buoys and found that the root-mean-square variation in latitude and longitude is about half of the water depths. For ocean the water depth was of the order of 2-3 km and in protected waters of the order of 100-300 m.

Geometrical rectification of satellite scenes from the open ocean only can be done from the nominal coordinates because no ground control points are available. For coastal images rectification to islands and shoreline is possible (preferable cliffs rather than sandy beaches due to coastal erosion that changes the actual position through time). The accuracy on geometrical rectification may be achieved at the sub-grid pixel scale provided adequate maps or GPS (global positioning system) control points are available ((Lillesand, 1987). For ERS SAR the error on geometrical rectification would be less than 12.5 m in most coastal

regions. In case the SAR scenes are regridded to a lower resolution prior to the geometrical rectification, the accuracy will decrease accordingly.

CMOD-IFRE2 is based upon wind speed data from 3433 collocated pairs of buoys and ECMWF model results. Buoy observations are too sparse to cover the global oceans, hence it is an advantage to use ECMWF model results in the correlations. Atmospheric model results may however not capture all atmospheric events equally well. The wind direction is not retrieved directly from the scatterometer data, but derived through a first guess approach on wind direction based on numerical weather prediction and combined with the scatterometer data (Quilfen et al., 1998).

Scatterometer data typically has a resolution of 25 by 25 km or 50 km by 50 km grid cells ((Atlas et al., 2001)). The correlation analysis between so large grid cells and e.g. buoy data can suffer from smaller scale gradients within the cells that are averaged out. Scatterometer subgrid scale variations can be investigated from SAR scenes. It has recently been demonstrated how near-real time SAR may be combined with scatterometer wind products to enhance the spatial resolution ((Beal, 2000; Thompson, 2001)) and (Monaldo, 2000).

In validation studies on SAR wind speed maps meteorological observations from buoys, ships, coastal or offshore masts (or platforms) may be used. Meteorological masts have the advantage of well-known positions, hence only the geometrical correction of satellite images can introduce error in collocation in space. The position of ships is probably better known than ocean buoys, yet less accurate than a mast.

- Collocation in time

Comparing spatial data to time samples poses different problems. SAR wind speed maps are spatial snap-shots within seconds. Meteorological observations are time-averaged data from single points. Taylor's hypothesis on frozen turbulence is used extensively to describe spatial atmospheric phenomena based on meteorological point observations. With a citation from (Stull, 1991) (p.5):

> *" Unfortunately, it is difficult to create a snapshot picture of the boundary layer. Instead of observing a large region of space at an instant in time, we find it easier to make measurements at one point in space over a long time period. For example, meteorological instruments mounted on a tower can give us a time record of the boundary layer as it blows past our sensors."*

Through the 1990'ties SAR wind speed maps provide us the snapshots. Taylor's hypothesis may now be used the other way round.

The marine boundary layer structure is investigated from SAR wind speed maps in a number of studies. Investigation on the marine boundary layer height ((Sikora et al., 1997; Sikora and Thompson, 2002; Young, 2000), organized large eddies (Brown, 2000b) and surface pressure fields ((Brown, 2000a)). From scatterometer data coastal sea-land breezes has been investigated ((Smith, 2002)).

Focusing on the buoy wind speed observations used for obtaining the CMOD algorithms a number of problems have been pointed out by(Brown, 2000a). The height of buoy sensors is between 2 and 10 m above sea surface and a height correction should include the thermal stratification, yet this may not be known

and as the deviation from a neutral profile generally amounts to $< \pm 1$ m s^{-1}, the correction may not be performed. Other problems related to buoy wind data is overestimation of low winds and overestimation of medium and high winds. Above 25 m s^{-1} the buoys fail to respond. The problems are due to tilting and displacement height in high seas ((Brown, 2000a)). According to (Atlas et al., 2001) available ship observations are of a poor quality compared to buoys, except for some research vessels when these meteorological data are properly processed.

The spatial and temporal scale have been considered in some SAR wind speed map validation studies e.g. (Sikora and Thompson, 2002) and (Thompson, 2001). Buoys typically average winds over an 8-10 minute period and record once per hour. (Sikora and Thompson, 2002) cropped a SAR wind speed map into square sub-scenes of the size order of 20-50 km^2 for comparing to 8-minute buoy observations. (Monaldo, 2001) chose a 3 km by 3 km area centered on the buoy location when comparing buoy data to SAR wind speeds. Katsaros et al cited in (Mourad, 1999) used a 64 km^2 area for comparison. {Vachon & Dobson 1996 125 /id} used a 4 km^2 area for ship comparison.

In the present study only observations from meteorological offshore and coastal masts are used for validation of SAR wind speed maps. Observations from meteorological masts do not suffer the same problems as the buoy data regarding tilting, displacement and ocean waves. At meteorological masts flow distortion due to the mast (or platform) or other instruments may occur. Yet the wind speed data typically is of a high quality. In some cases the temperature difference in the air or between air and sea is measured, hence it is possible to correct for atmospheric static stability.

For coastal masts the effect of the land surface orography (topography), even very modest orography, will influence the observations as compared to the wind speed over the ocean. A method for the correction of land surface orography is described in detail in (Hasager et al., 2002). For an optimal comparison between offshore mast observations and SAR wind speed maps a footprint method of area-averaging (please, see chapter 9 and section 11.9) has been applied.

3.7 Processing of ERS-2 SAR in the WEMSAR project

Satellite SAR wind speed maps were processed for four all test sites at NERSC. Please refer to (Johannessen, 2001)) on the full details on the processing of the scenes from the test sites

- Horns Rev   Denmark   20 scenes from 16 days
- Hellisöy   Norway   50 scenes from 44 days
- Maddalena   Italy   9 scenes from 9 days
- Gulf of Suez   Egypt   5 scenes from 3 days.

The ERS-2 SAR scenes from Denmark and Egypt are granted by the ESA AO3-153 project (PI Dr. C. Hasager).
The ERS-2 SAR scenes from Italy and Norway are granted by ESA AO3-281 project (PI Professor O. Johannessen).

Briefly described the processing of SAR satellite data into wind speed maps is performed from ERS-2 SAR PRI images. These are calibrated by use of the SAR Tool Box programme (http://earth.esa.int/stbx/documentation/manual/stbx_V-5_5.html) freely available from ESA User Services. For the detection of wind streaks in the SAR images a two-dimensional Fast (FFT) function is used. The calibrated SAR images are then calculated into wind speed by the CMOD_IFR2 algorithm from Quilfen.

4 WA^{S}P

Ole Rathmann

4.1 Introduction

The WASP program is described in detail in (MORTENSEN et al., 1993),(MORTENSEN et al., 2000) and used for the European Wind Atlas by (TROEN and Petersen, 1989), where the so-called wind atlas method was introduced WASP is an acronym for Wind Atlas and Analysis and Applications Program. It is a commercial software sold by Risø National Laboratory, Wind Energy Department. On basis of wind data measured at a reference location WASP applies the wind atlas method to predict the wind climate and wind resources at other locations in the same region, taking into account the difference in terrain between the reference site and the predicted site(s). Thus WASP is a suitable tool for making predictions of off-shore wind climates based on coastal met-stations.

The importance of taking the difference between wind climate at off-shore locations and relatively nearby coastal sites is documented in a paper by (Hasager et al., 2002). Here the difference of wind speeds measured at a small island in the Great Belt and those assumed to be effective offshore the island are analysed and the need to correct even for relatively small topographical effects is clearly seen.

In the following it is described how this procedure was applied to the sites in Norway and Italy.

4.2 Selection of wind scenarios for SAR comparison analysis

Unlike normal use of WASP, based on at least one year of wind measurements, the off-shore WASP predictions, to be compared to SAR-interpretations, must be based on a very short time range around the SAR-satellite passing. Therefore a procedure was established to select out short-time range wind scenarios over sea, for which the SAR-wind speeds can be compared to wind speeds estimated on basis of relevant coastal wind measurements.

Two off-shore areas were treated in to compare SAR-based wind speeds to WAsP predictions: The sea east of Northern Sardinia with the off-shore Mezzo

Passo meteorological station in the strait between Sardinia and the Maddelena Island as reference; and the sea west of West-Norway with the Hellisöy meteorological station as the reference.

For each of the sites those SAR-scenes were selected for comparison, where the measured time series showed sufficient stationary conditions over a two-hour period. The fingerprint plots and the other parts of the selection procedure, together with the prediction analysis are given for Maddalena in section 12.4 and for Hellisöy in section 13.1.

5 LINCOM

Poul Astrup

LINCOM (please refer to (Astrup et al., 1996), (Astrup and Larsen, 1999),(Astrup et al., 1999)) is a model for the wind flow over slightly complex terrain. LINCOM is an acronym for LINearized COMputational model. Based on the actual area orography and roughness pattern, it calculates the perturbations these surface parameters induce in a background flow that is otherwise in equilibrium with a flat area with uniform roughness. The sum of the perturbations and the background flow gives the final LINCOM flow field.

For the calculation of relatively small perturbations to a known background wind, the Navier-Stokes equation can with no great error be linearized, and a further simplification can be obtained by formulating the equations in a horizontally Fourier transformed space, the z-dimension remaining in real space. Analytical solutions are obtainable for the Fourier coefficients of the velocity components as functions of wave numbers and of z, but surface boundary conditions have also to be applied in Fourier space.

In the actual version of LINCOM two types of flow distortions are modelled, those due to hills, and those due to an uneven surface roughness over the calculational area. The corresponding boundary conditions can be formulated as: Near the ground the flow shall
   1) be parallel to the ground, and
   2) be in equilibrium with the local roughness.

With the Fourier coefficients found analytically at a given height, a Fast Fourier Transform quickly gives the corresponding real space velocity field.

The orography and the roughness pattern for the calculational area are normally input to LINCOM, but sea surface roughness is a function of the wind, and should therefore correspond to the LINCOM output. In order to obtain a realistic response for the wind over sea, LINCOM has been interfaced with a model for sea surface roughness (Astrup et al., 1999; Astrup and Larsen, 1999), and an iterative procedure leads to a wind field and a sea roughness field in mutual equilibrium.

LINCOM can fulfill a single wind speed/direction requirement, i.e. by iteration it can find the field that in a given point has a specified speed and direction. In order to allow specification of speed/direction pairs at more than one site, it is implemented so that a weighted sum of x- and y-components of the velocities

calculated by LINCOM for a number of specified positions match the weighted sum of the components of the velocities specified for these positions. This also works for offshore sites.

6 KAMM2

Bo Hoffmann Jørgensen

6.1 Model issues

The Karlsruhe Atmospheric Mesoscale Model 2 (KAMM2) is a three-dimensional, non-hydrostatic, and compressible meso-scale model (Adrian, 1998) related to KAMM (Adrian and Fiedler, 1991; Adrian, 1994). Spatial derivatives are calculated in the model by central differences on a terrain following grid. The turbulent fluxes are parameterized using a mixing-length model with stability dependent turbulent diffusion coefficients in stably stratified flow, and a non-local closure for the convective mixed layer. Lateral boundary conditions assume zero gradients normal to the inflow sides. On outflow boundaries, the horizontal equations of motion are replaced by a simple wave equation allowing signals to pass out of the domain without reflection. Gravity waves are absorbed in the upper part of the computational domain which acts as a damping layer. The model has been extended with a fetch-dependent sea roughness (Frank *et al.*, 2000). At initialization, the orography, roughness, and large scale forcing is loaded into the model as illustrated in Figure 6-1.

As when operating any finite difference model, it is necessary to run the model for different spatial grid resolutions in order to confirm that the model results are not sensitive to grid resolution. This must be done for each model domain corresponding to a new geographical location to be investigated. Normally three different resolutions are employed. If the computational results of the two finest resolutions are close to each other it is an indication of that the model results approach a distinct solution for increasing grid resolution. In this way an appropriate grid resolution can be chosen. When choosing very fine grid resolutions the computational resource requirements may increase significantly. It may then be appropriate to allow some difference between model results for different resolutions.
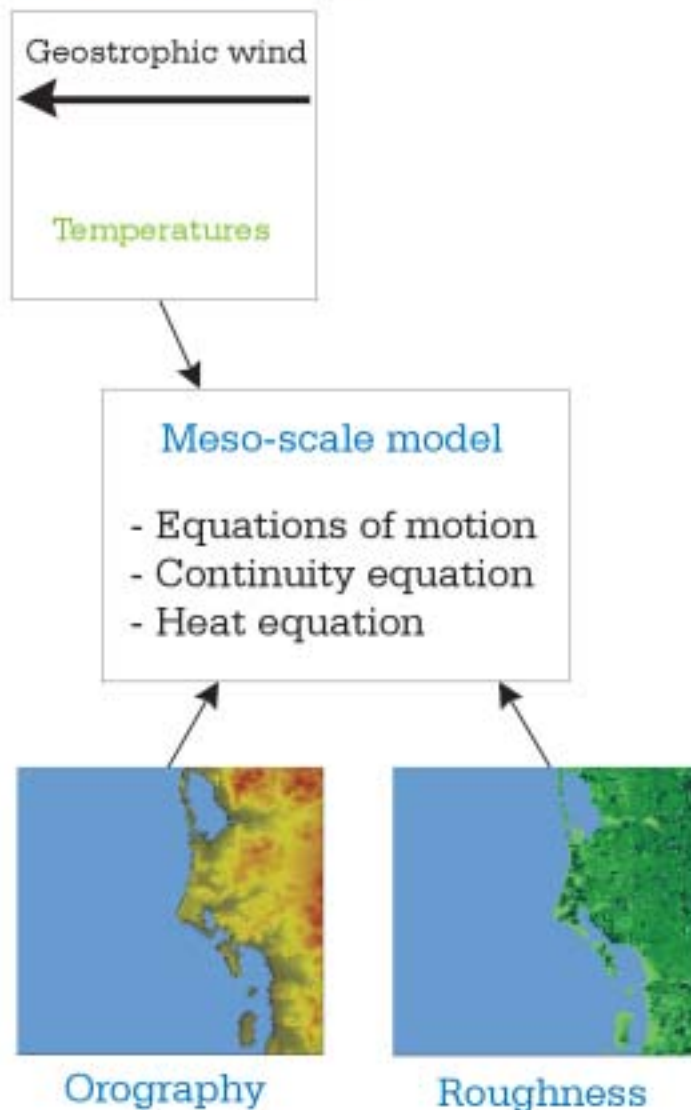
Figure 6-1 Illustration of the KAMM2 model and the input to the model.

A simulation time of several hours (physical model time - not computer CPU time) is necessary in order to approach a final state of the computational wind map. The mesoscale model variables are shown in Figure 6-2 for a station near Horns Rev for the case with large scale forcing of 12.00 (UTC), October 19. 1999. There is no specific correct way of deciding how many hours of simulation time is necessary to complete a mesoscale model run. Rather, this depends on the judgment of the model operator. However, for the present work, it was found appropriate to focus on the horizontal velocities, u and v, as they are the main variables of the computational results. In the figure, u and v are shown to the left in the plot in the middle.
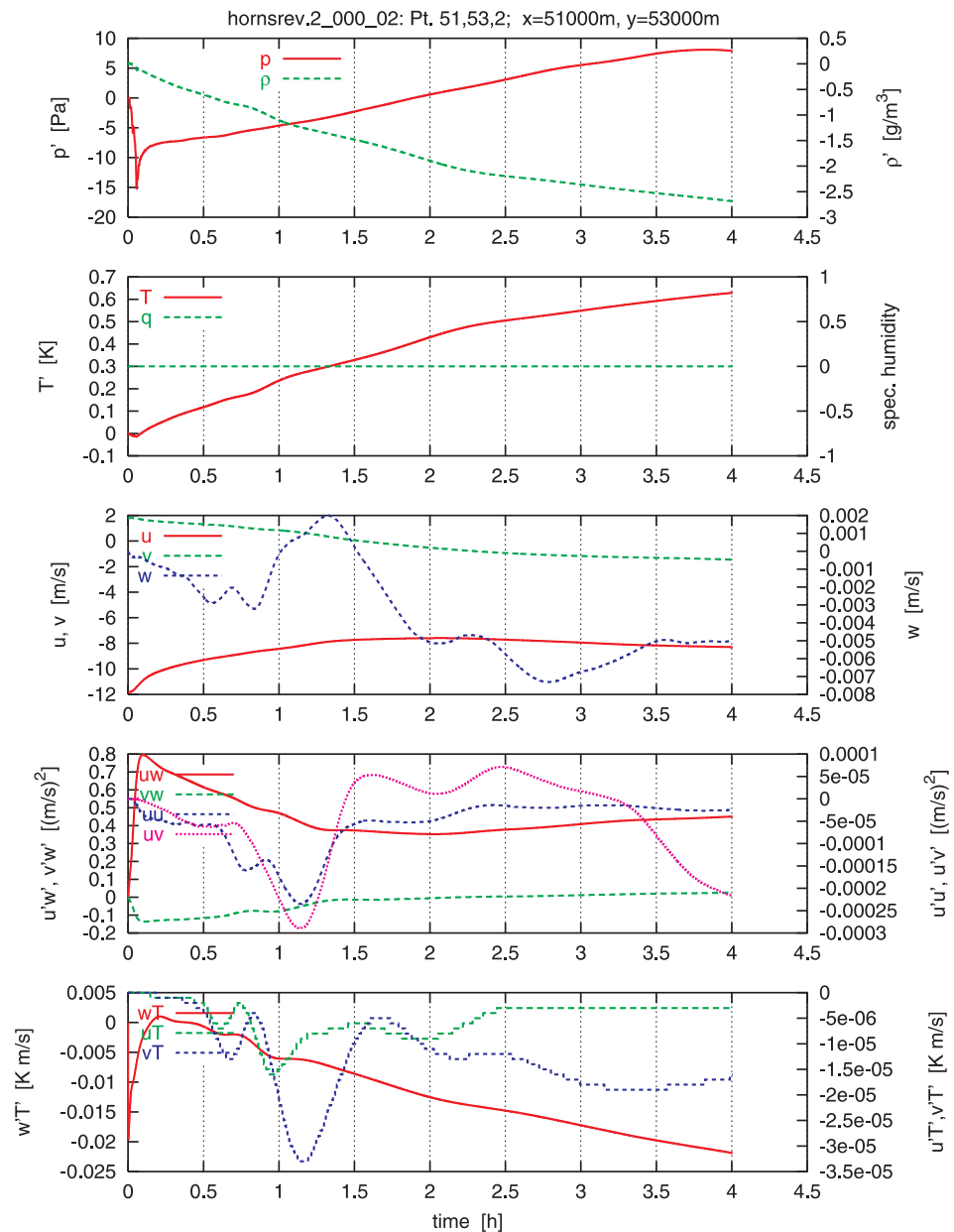
Figure 6-2 Mesoscale model variables shown at a station near Horns Rev starting at 12.00 (UTC), October 19. 1999. The horizontal velocities u and v are shown to the left in the plot in the middle. The other variables shown are the pressure perturbation, p', density perturbation, ρ', temperature perturbation T', specific humidity (no symbol), vertical velocity, w, Reynolds stresses, u'w', v'w', u'u', u'v' and the moments of the velocity perturbations and the temperature perturbation, w'T, u'T' and v'T'.

Like some finite difference models, KAMM2 is sensitive to non-smoothness of the computational grid. This means that, for complex terrain, the orography must be smoothed before the computational grid is generated. Otherwise, if the grid is not smooth, it may be very difficult to run the model. This is in particular a problem for high resolutions. For Horns Rev, which involves only simple orography, this is not an issue of importance. For Hellisøy, grid independent solutions have been obtained without any special filtering of the orography, although smaller time steps (selected by KAMM2) is required for the highest

resolutions. For Maddalena, which involves complex terrain, more filtering of the orography is required near the boundaries. Initial disturbances occur in the solution for the highest resolution due to non-smoothness of the grid at high resolution. It requires long simulation times for the model to transport the disturbances out of the computational domain as compared to the simulation time necessary to complete the runs for coarser resolutions. A different filtering scheme for complex orography may considerably shorten the simulation times, but this has not been pursued.

6.2 Re-analysis data from NCAR/NCEP

Data (4 times daily) from the global reanalysis of NCEP/NCAR at http://www.cdc.noaa.gov/ is used to obtain the geostrophic wind and other large scale forcing (vertical air temperature gradient, air temperature at 2 m height, and temperature at land and sea) which is suitable as input to the meso-scale model. The reanalysis grid is shown for an example for the North Sea in Denmark in Figure 6-3. Each grid cell is approximately 200 km by 200 km and data are freely available 4 times per day. The database contains more than 52 years of global data.
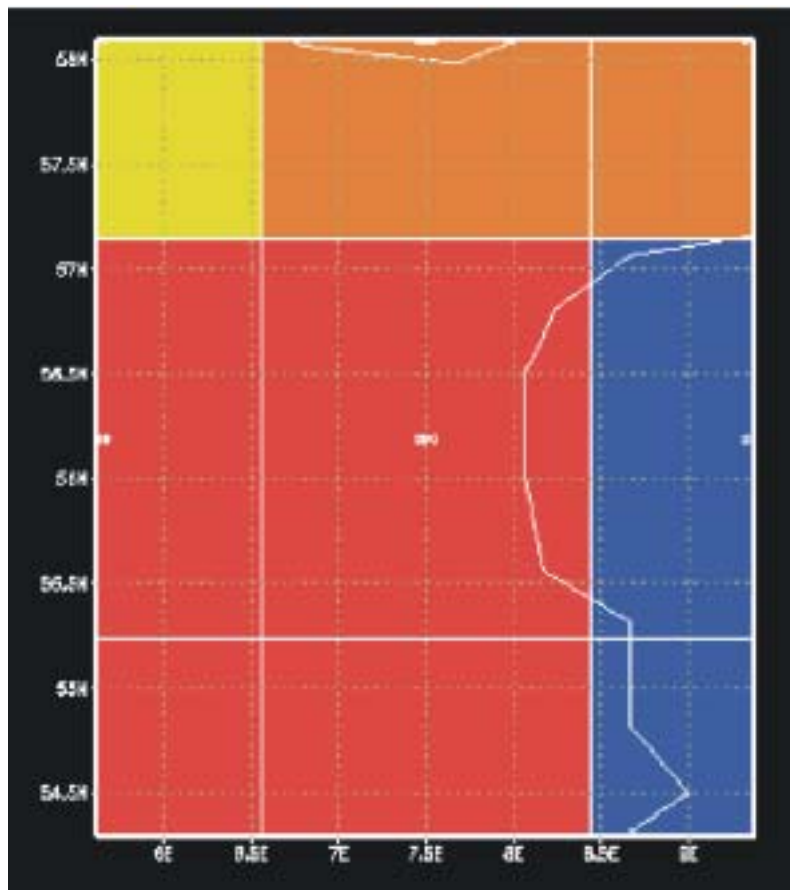

Figure 6-3 Example plot of the skin temperature of the North Sea in Denmark using the reanalysis grid.

KAMM2 is able to run as a "stand-alone" model, i.e. the model can be run by using only the large scale forcing from the reanalysis (see sketch in Figure 6-4). Hence, it is not necessary to nest the meso-scale model within a larger model supplying the boundary conditions. For each case, the time of the reanalysis data is chosen as close as possible to the time of the satellite overpassing. The input parameters are obtained from the reanalysis database for the cases at Horns Rev, Maddalena and Hellisöy.
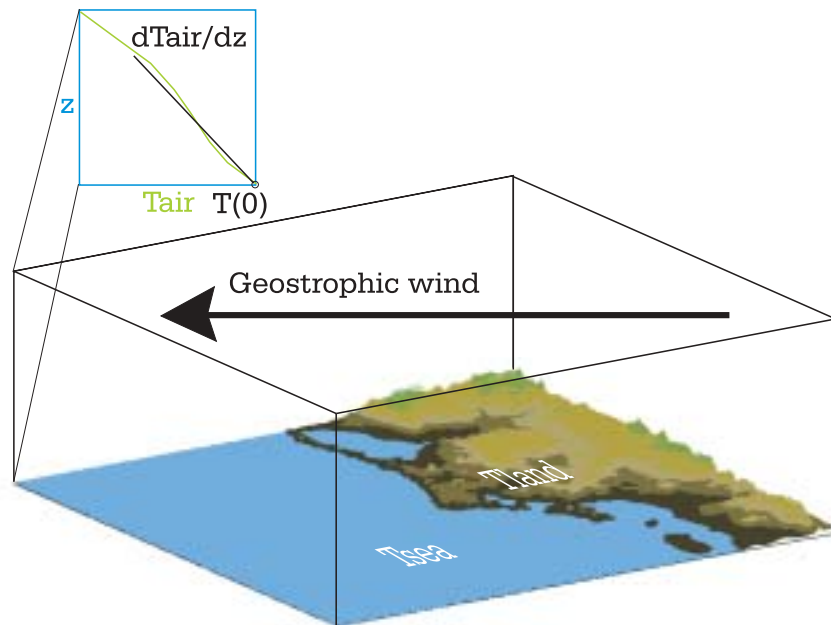
Figure 6-4 Sketch of the large scale forcing used for KAMM2 calculations.

Prior to running the KAMM2 model with the NCAR/NCEP input, a comparison to local meteorological observations is performed for each single case. This is reported in Section 11.6 for Horns Rev, Section 12.5 for Maddalena and Section 13.2 for Hellisöy. For the comparison, the reanalysis surface wind at 10 m height (agl.) is used. The surface wind of the reanalysis data does not represent the actual local wind of the mast. Rather it is a measure of the large scale wind for a reanalysis grid cell. However, it does give an impression of how realistic it is to apply the reanalysis data as large scale forcing to the mesoscale model. Of all available cases, a subset is selected. For each selected case the wind speed measured at the mast is constant for at least a few hours and compares well with the surface wind speed at 10m height from the reanalysis data. This is because the mesoscale model cannot be expected to perform very well if the applied large scale forcing is not realistic or if frontal activity appears.

Most of the experience with mesoscale modeling of wind resources is based on calculations for land regions rather than at sea. Thus, the accuracy of offshore mesoscale model results is not well known. This issue is complicated by the fact that the wind in offshore near shore areas may be affected by thermal stability effects. The reanalysis data set is rather coarsely defined whereas effects of more local temperature variations might influence the wind in coastal areas.

7 Representativeness of satellite data with regard to wind speed distributions

Sara C. Pryor and Rebecca J. Barthelmie

7.1 Introduction

Remote sensing offers the potential to develop more comprehensive and spatially resolved data sets over the oceans but the adequacy and robustness of these data remains uncertain. Wu (1995) presented an analysis of remotely sensed (altimeter) wind speeds relative to model output and coincident in situ observations and determined large, systematic deviations in the resolved mean flow fields. In the case of wind energy applications, available wind power density is related to the cube of the wind speed. Hence, to develop wind resource estimates for any location it is necessary not only to adequately characterise the mean wind speed but also the higher moments or other descriptive parameters of the wind speed probability distribution (Pryor and Barthelmie, 2002). This application, therefore, represents a stringent test of remotely sensed (and in situ) observations.

Aside from questions regarding the absolute accuracy of wind speeds derived from remote sensing, difficulties in reconciling remotely sensed wind speeds and in situ observations arise due to:

1. Differing averaging periods of the observations. For example, Synthetic Aperture Radar (SAR) responds most strongly to reflection at a wavelength of the wave spectra (capillary waves) which is almost instantaneously coupled to the atmospheric flow (equilibrium is reached in < 1 minute), whereas most in situ observations of wind speed are averaged over 10, 30 or 60 minute periods.
2. Data set density. In common with meteorological observations, satellite processing may occur over a short time period in climatological terms. In the case of in situ meteorological observations, assuming the data period is not less than one year and does not reflect seasonal bias, a measure of the inter-annual variability from nearby sites is typically used to provide an estimate of the error associated with disregarding longer time scale variability. However, in the case of remotely sensed observations, data set density is limited not only by sampling time (the time series length) but by the number of observations that can realistically be derived from remotely sensed images due to a limited number of satellite passes and limitations imposed due to image processing time.
3. Temporal biases. Remote sensing data may exhibit temporal selectivity introduced as the satellite orbits the globe. Despite the common belief that offshore areas do not exhibit diurnal wind patterns, these cycles have been shown to exist in coastal areas, although they may be inverted or shifted compared with typical onshore diurnal wind patterns (Barthelmie et al., 1996b).
4. Truncation of the actual wind speed distribution. The observations obtained by any technique may reflect only a portion of the actual data distribution due to limitations in the operational range of both in situ meteorological in-

strumentation (e.g. anemometers) and the algorithms used to derive wind speeds from the satellite borne instrumentation. In the case of the data presented here the cup anemometers have an operational range of 0.2 – 70 m s^{-1}. The operational range of the SAR calibration is assumed to be 2 – 24 m s^{-1}.

5. Selection criteria applied for image processing. A number of criteria may be used for image selection including exclusion of satellite passes where a front was observed to pass (to avoid highly complex wind fields) or preferential selection for high wind speeds (low wind speeds are associated with low radiation scatter and hence higher uncertainty in the SAR interpretation). Because image selection criteria are subjective and therefore are operator dependent we shall neglect biases associated with image selection in this analysis.

In this chapter we quantify the biases in derived wind speed distribution parameters (moments and parameters from the Weibull distribution) and forecast wind power potential resulting from points 1-4 given above. It is important to note that this analysis is not an evaluation of the _accuracy_ of SAR retrieval of wind speeds, rather it is an analysis focusing on the _biases_ relative to in situ measurements introduced by differing sampling protocols. These biases would remain even if the remotely sensed observations were perfectly accurate with respect to in situ measurements.

7.2 Data analysis

In this chapter we use the first to fourth moments of the distribution (described using the mean, standard deviation, skewness and kurtosis) (Rice, 1995) and the Weibull distribution (shape (k) and scale (c) parameters) to describe the probability density functions of wind speed data sets. We also present estimates of the energy density from the Weibull parameters using Equation 2.

The analysis presented is based on in situ data sets collected at two offshore sites in the waters around Denmark:

- An offshore mast in the Vindeby offshore wind farm located 2 km from the coast (Figure 7-1) (Barthelmie et al., 1996a).
- A meteorological mast at Horns Rev, the site of a prospective wind farm, located 16 km west of the coast of Denmark (Figure 7-1) (Neckelmann and Petersen, 2000). The data record from Horns Rev (June 1999 onwards) is considerably shorter that that from Vindeby (November 1993 onwards). These data are used here to evaluate whether the results of the analyses conducted using the Vindeby data set are significantly biased by near coastal effects.

To examine the impact of the sampling which characterizes SAR (and other remote sensing of wind speeds over oceans) has on the resulting observations relative to in situ observations we conditionally sample in situ data records to replicate data that might reasonably be obtained via remote sensing tools. We first present an analysis of the difference in wind speed distribution parameters derived using a data set containing 1 minute average observations compared to coincident observations recorded as 30 minute averages. Then we present an analysis of the 30 minute average wind speed data sets from Vindeby and Horns Rev where we degrade the observational data sets with respect to items 2-4 given above and repeatedly resample the data to determine the 'new' distribu-

tion parameters and to derive uncertainty bounds applicable for use with probability distribution parameters from a sparse wind speed data set. Finally, we present an assessment of the uncertainties in this analysis and document the implications for wind resource estimation.
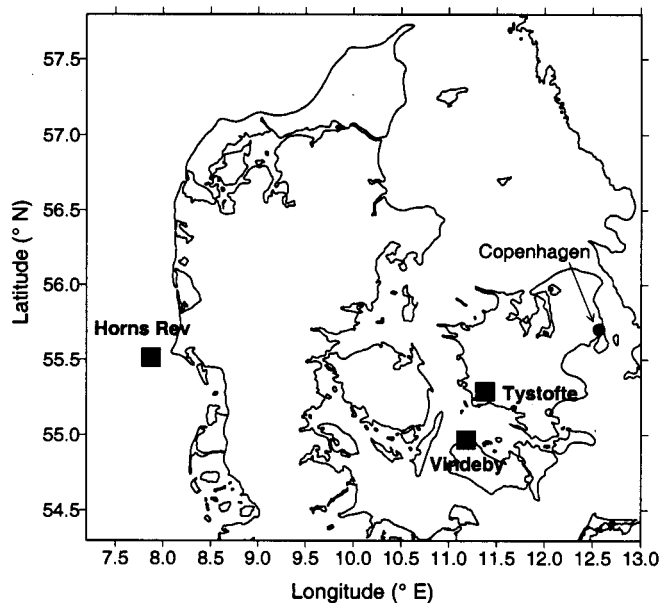
Figure 7-1 Location of the meteorological masts from which data are presented.

7.3 Sensitivity of the wind speed distribution parameters to averaging period

The influence of sampling period on resulting mean wind speed has long been an issue in meteorology and for marine wind sampling in particular (e.g. Borreson (1987), Petersen et al. (1981)). To examine the differences in wind speed probability distribution parameters derived from remotely sensed (SAR) pseudo-instantaneous realisations of the wind field versus 30 minute average data as would be derived from in situ measurements, probability distribution parameters from the Vindeby mast were computed for 1 minute and 30 minute average wind speeds measured at 48 m. The results are summarized in Table 7-1 and indicate that the 30 minute average data captures most of the variability present in the 1 minute data series and that the Weibull distribution parameters for the two data sets are equivalent. This result is not unexpected since the two data set blocking (or averaging) periods span part of what is commonly referred to as the 'spectral gap' {Stull 1991 80 /id} and as Petersen et al. (1981) note differences in statistics generated from 10 minute to one hour averages tend to be small due to the shape of the variance spectrum.

Table 7-1 Probability distribution descriptive parameters

Row #	Height (m)	Data averaging period (minute)	Moments				Weibull parameters		Energy density (W m^{-2})
			Mean (m s^{-1})	Standard deviation (m s^{-1})	Skewness	Kurtosis	Shape (k)	Scale (c) (m s^{-1})	
1	48	30	7.99	3.64	0.466	0.177	2.26	9.02	522
2	48	1	7.54	3.25	0.471	-0.244	2.32	8.52	431
3	48	30	7.54	3.20	0.434	-0.375	2.34	8.51	427
4	48	30	8.06	3.65	0.457	0.229	2.35	9.09	519
5	48	30	7.80	3.54	0.535	0.302	2.14	8.81	509
6	48	30	8.19	3.48	0.573	0.103	2.16	9.25	585
7	48	30	8.26	3.49	0.554	0.103	2.26	9.33	577
8	10	30	6.81	3.09	0.468	0.130	2.29	7.69	320
9	48	30	7.87	3.57	0.494	0.325	2.29	8.88	493

- *Row 1: The entire data set from 48 m height.*
- *Rows 2 and 3: 1 minute average data set (row 2) versus a 30 minute average data set (row 3) of measurements conducted at Vindeby SMW. The measurements were obtained at a height of 48 m using the same instrumentation. Data records were only included for measurement periods with coincident observations.*
- *Row 4: 30 minute data set from 48 m conditionally sampled for observations between 11:00-12:00 and 22:00-23:00 DST.*
- *Row 5: 30 minute data set from 48 m conditionally sampled for observations between 03:00 and 04:00 DST*
- *Row 6: 30 minute data set from 48 m conditionally sampled for observations between 2- 24 m s^{-1}.*
- *Row 7: Cumulative impact of selecting only data collected between 11:00-12:00 and 22:00-23:00 DST, for U= 2- 24 m s^{-1}*
- *Rows 8 and 9: Data sets from measurements conducted at 10 and 48 m a.s.l. at Vindeby SMW for the period (1996 to date) of coincident measurements.*

7.4 Dependence of the wind speed distribution parameters on data set density (number of observations)

To examine the dependence of the distribution parameters on data set density (i.e. number of observations in the time series) the data set from Vindeby SMW was randomly and multiply resampled for a range of number of observations from n = 21 (assumed to be the lower bound on the data set likely to be obtained using remote sensing) to n ~ one tenth of the actual number of observations available from Vindeby for the entire data collection period (i.e. n = 10,000). The results are presented in Figure 7-2 for the four moments of the distribution and the Weibull parameters for 1000 resampling iterations for each n. As expected the mean wind speed is the most robust characteristic of the data set, and both the random error associated with each resampled group and the systematic error (or bias) in estimation of the mean is low even for small n. The error is larger for the standard deviation (maximum difference in median standard deviation and the time series value is -0.12 m s^{-1} indicating the standard deviation is, on average, slightly underestimated for n = 21). Again, the error reduces rapidly with increasing n. The higher moments are, as expected, less robust with low sample numbers. As shown, the results further indicate very large range in the estimated distribution parameters for the resampling groups and hence high uncertainty at low n.
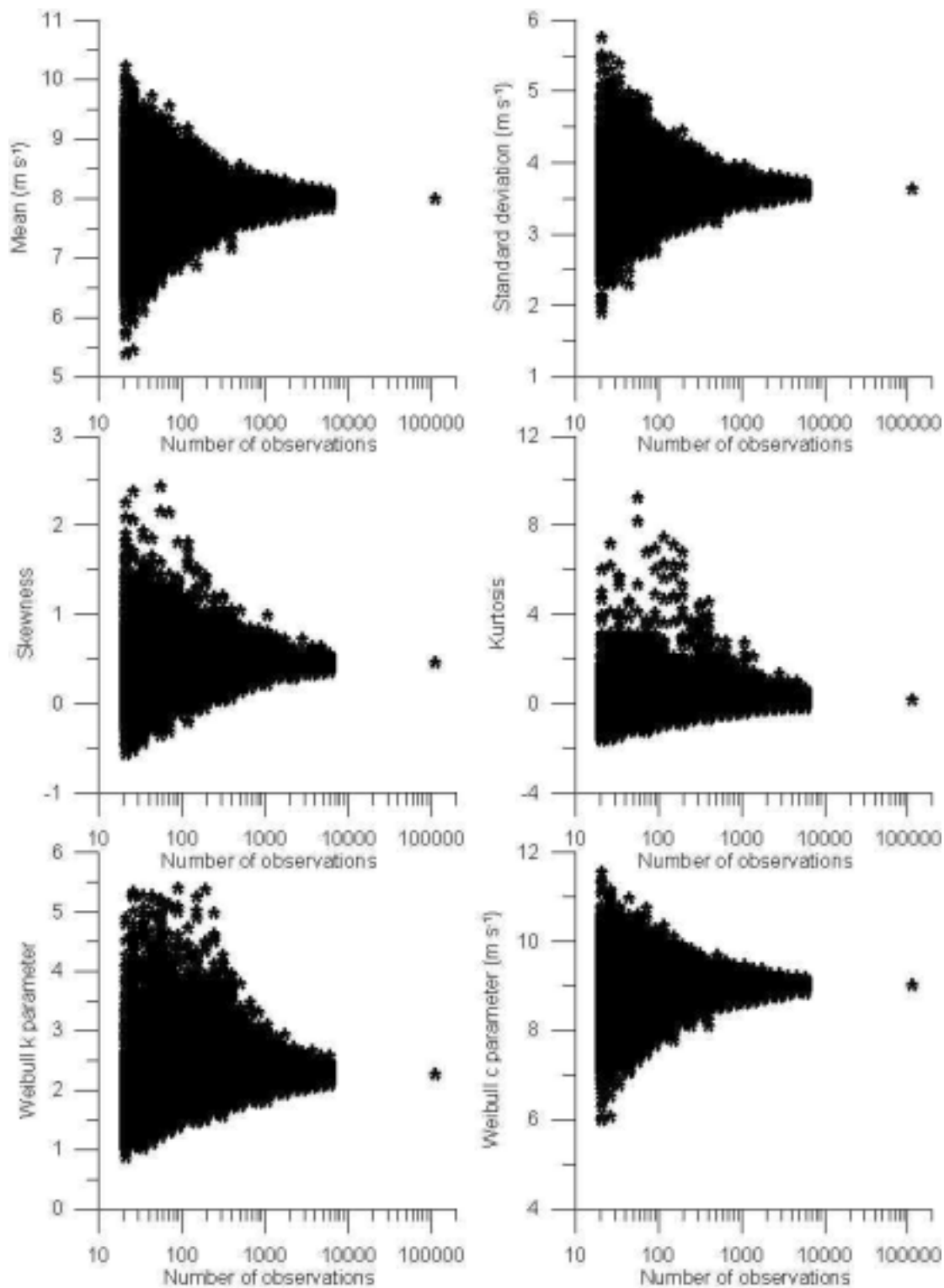
Figure 7-2 Six wind speed distribution parameters (mean, standard deviation, skewness, kurtosis and the Weibull k and c parameters) shown for each of the 1000 iterations for each number of observations (from n = 21 to n = 1/10*total number of observations in the data set), plus the value of each parameter calculated for the entire data set (i.e. for n = 111557).

Based on this analysis Table 7-2 summarizes the number of randomly distributed observations (i.e. observations taken without diurnal or seasonal bias) required to obtain an estimate of the distribution parameters within ± 10 % of the

actual time series value at a confidence level of 90 %. Figure 7-3 shows the upper and lower bounds on the 90 % confidence interval for the wind speed distribution parameters for varying numbers of observations (n). The confidence intervals exhibit a power form with increasing n (where $\ln(y) = \ln(n)+$constant, where y is the percent error and n is the number of observations) and are asymmetric for the higher moments reflecting the average bias in estimation of parameters at low sample numbers due to the non-Gaussian underlying probability distribution.

Table 7-2 The number of <u>randomly</u> distributed observations required to obtain an estimate of the distribution parameters within +/-10 % of the actual time series value for a confidence level of 90 % calculated based on the half hourly average wind speeds measured at 48 m at Vindeby SMW computed with statistics derived from the initial database of > 100,000 observations.

Mean	Standard deviation	Skewness	Kurtosis	Weibull k	Weibull c	Energy density
56	150	9712	>10,000	1744	71	1744
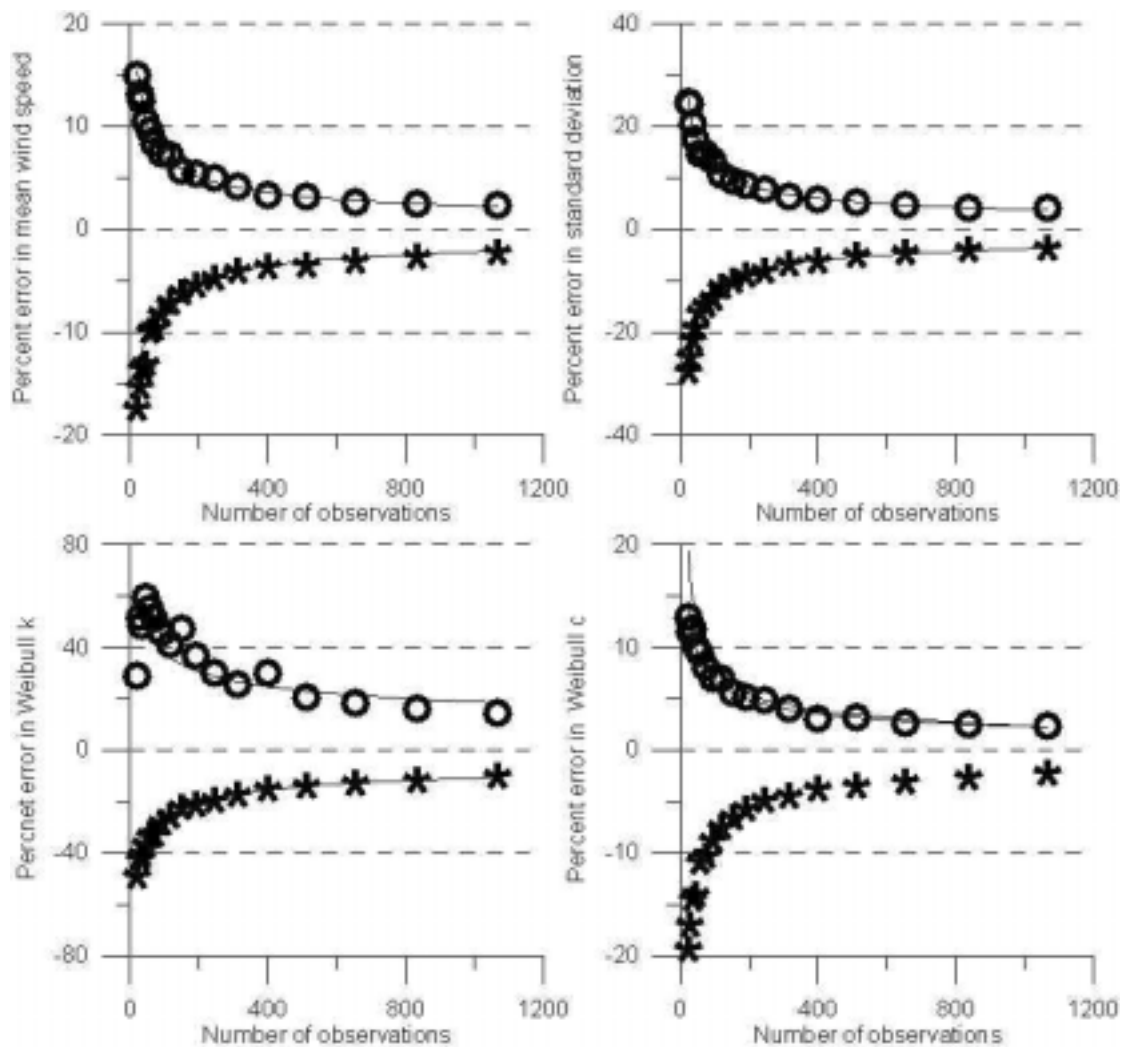
Figure 7-3 The 90% confidence interval for percent errors in the wind speed distribution parameters based on varying number of observations randomly selected from the Vindeby SMW data series. The open circles depict the upper bound, the asterisks the lower bound.

7.5 Dependence of the wind speed distribution parameters on diurnal bias

Because synoptic scale systems exhibit no significant diurnal cycle, on climatological time scales mid-latitude offshore locations experience homogenous forcing and hence exhibit no significant diurnal cycle. However, wind speed observations at both the Vindeby (2 km from the closest shoreline) and Horns Rev (16 km from the closest shoreline) masts exhibit significant diurnal cycles due largely to advective effects (see Barthelmie et al. (1996b)). Since the timing of the satellite overpasses are unlikely to be chosen specifically for wind resource analysis careful analysis of the diurnal cycle of wind speeds is appropriate for locations within the coastal zone particularly in complex areas such as archipelagos or where the thermal regime produces sea breezes or low level jets.

The European satellite carrying the SAR instrumentation passes over Denmark at 10.30 UTC or 21.30 UTC with a repeat track of approximately 10 days. To

determine the influence on the wind speed distributions resulting from this diurnal bias the observational data from Vindeby were conditionally sampled where records were only selected if the data record start time fell between 11:00 and 12:00 or 22:00 and 23:00 Danish Standard Time (DST). The resulting wind speed distribution parameters are shown in Table 7-1. As shown, selection of time periods associated with the ERS-2 passage over Denmark tends to lead to slightly higher mean wind speeds than those calculated using data set from Vindeby SMW but otherwise the distribution parameters are well characterized. However, if the satellite passed only at 3:00 – 4:00 DST then, as shown in Table 7-1, the wind speed distribution parameters would significantly deviate from those calculated for the data series as a whole.

7.6 Dependence of the wind speed distribution parameters on the operational range of the SAR algorithms

SAR has a reported operational range of $2 - 24$ m s^{-1}. To determine the influence on the wind speed distributions resulting from this truncation of the actual wind speed distribution, the data collected at a height of 48 m at Vindeby SMW were conditionally sampled for this wind speed range and the distribution parameters recomputed. As shown in Table 7-1, the bias introduced by exclusion primarily of low wind speeds (few half hour average observed wind speeds exceed 24 m s^{-1}) is manifest as an increase in the mean and positive skewness, and reduced variance and kurtosis. In terms of the Weibull parameters, the shape parameter is reduced and the scale is increased. The impact on the mean and skewness by truncation of the wind speed data set is more pronounced than any of the other sampling criteria and, as will be discussed below, has a profound impact upon the estimated wind resource.

7.7 Cumulative impact on wind speed distributions of sampling bias

The previous sections report the individual effects of sampling bias upon the wind speed distribution as manifest in the data collected at Vindeby. However, the bias resulting from these effects need not be additive, and so to assess the cumulative effect of biases associated with; non-random temporal allocation of data acquisition, low sampling number, and truncation of the wind speed distribution, the data set from Vindeby was conditionally sampled such that observations were selected only if they represented data collected between 11:00 and 12:00 or 22:00 and 23:00 (DST) and had values between 2 and 24 m s^{-1} (Table 7-1). These data were then multiply resampled (for n = 21 to 0.1* number of observations) to generate the wind speed distribution parameters and models of the 90 % confidence intervals (see Figure 7-4). As shown in Table 7-1 the cumulative impact of selecting data that most closely represents that which might be obtained from SAR for this region is to over-estimate wind speeds and hence energy density.

7.8 Model evaluation

To assess the generalizability of the 90 % confidence intervals derived for the mean, standard deviation and Weibull distribution parameters based on sparse

resampling of the Vindeby data set, the entire Horns Rev wind speed data set (measurement height = 62 m) was resampled for varying n and the 90 % confidence interval from the data compared to that predicted by the fits derived from the Vindeby data. The results, shown in Figure 7-4, indicate generally good agreement between the uncertainty bounds derived from the Vindeby data set and those determined from the Horns Rev data. The least well predicted parameter is the Weibull shape parameter due to its relationship with data variance. Nevertheless, based on this analysis it may be inferred that the uncertainty bounds derived from the Vindeby data have general applicability to other relatively high wind speed regimes.
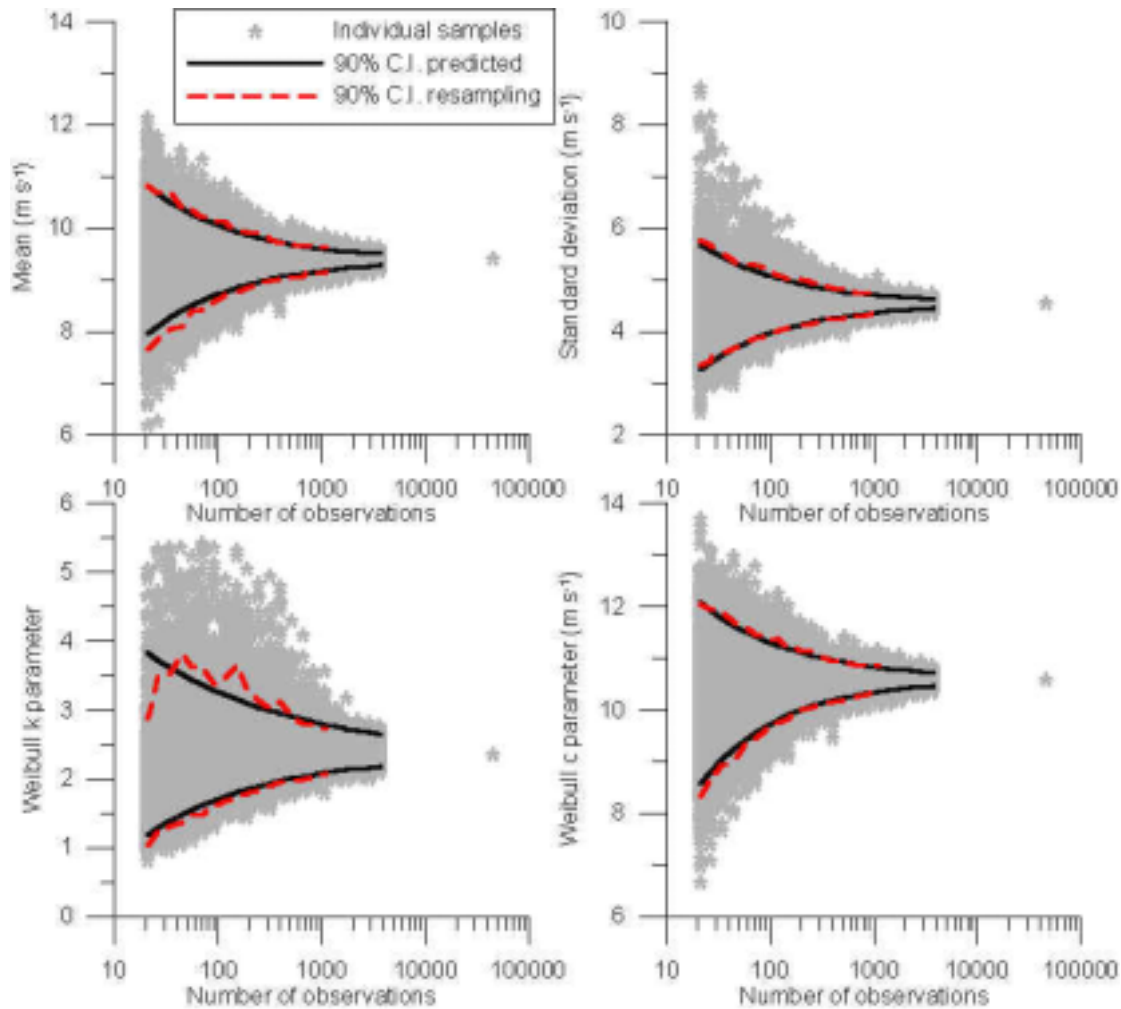
Figure 7-4. The mean, standard deviation and Weibull k and c parameters from the resampling of the Horns Rev data set and the 90 % confidence interval based on the data from Horns Rev (90 % C.I.Confidence Interval resampling) and the 90 % confidence interval predicted (90 % C.I. predicted) from the fits calculated from the Vindeby SMW data set.

Wind speeds derived from SAR equate to a nominal measurement height of 10 m a.s.l. while the data from Vindeby represent a measurement height of 48 m a.s.l.. To assess the magnitude of the difference in nominal measurement height on the wind speed distribution parameters, half hour average wind speed data

from Vindeby for the period when anemometers were operated at two measurement heights: 48 m and 10 m a.s.l. (1996 to date) were used to calculate the distribution parameters summarized in Table 7-1. As shown, the distribution parameters all exhibit height dependence except the Weibull shape parameter (k) which, in accord with the analysis of Dixon and Swift (1984), is equal at the two heights. However, the height dependencies of the other distribution parameters are large, with the lower measurement height indicating lower mean (and c parameter), variance, skewness and kurtosis. Hence, the uncertainty bounds calculated using the in situ observations from 48 m height are not directly applicable to remotely sensed data for a nominal height of 10 m. For this reason the analysis was repeated using a shorter data set available for a height of 10 m at Vindeby. The results are summarized in Figure 7-5 in terms of the 90 % confidence interval that can be applied to the wind speed distribution parameters and energy density estimates derived for sparse data sets as would be derived from SAR analysis. As shown, the asymmetries in the uncertainty bounds and the form of the power law fits to the uncertainty bounds are very similar to those derived for the data from 48 m.
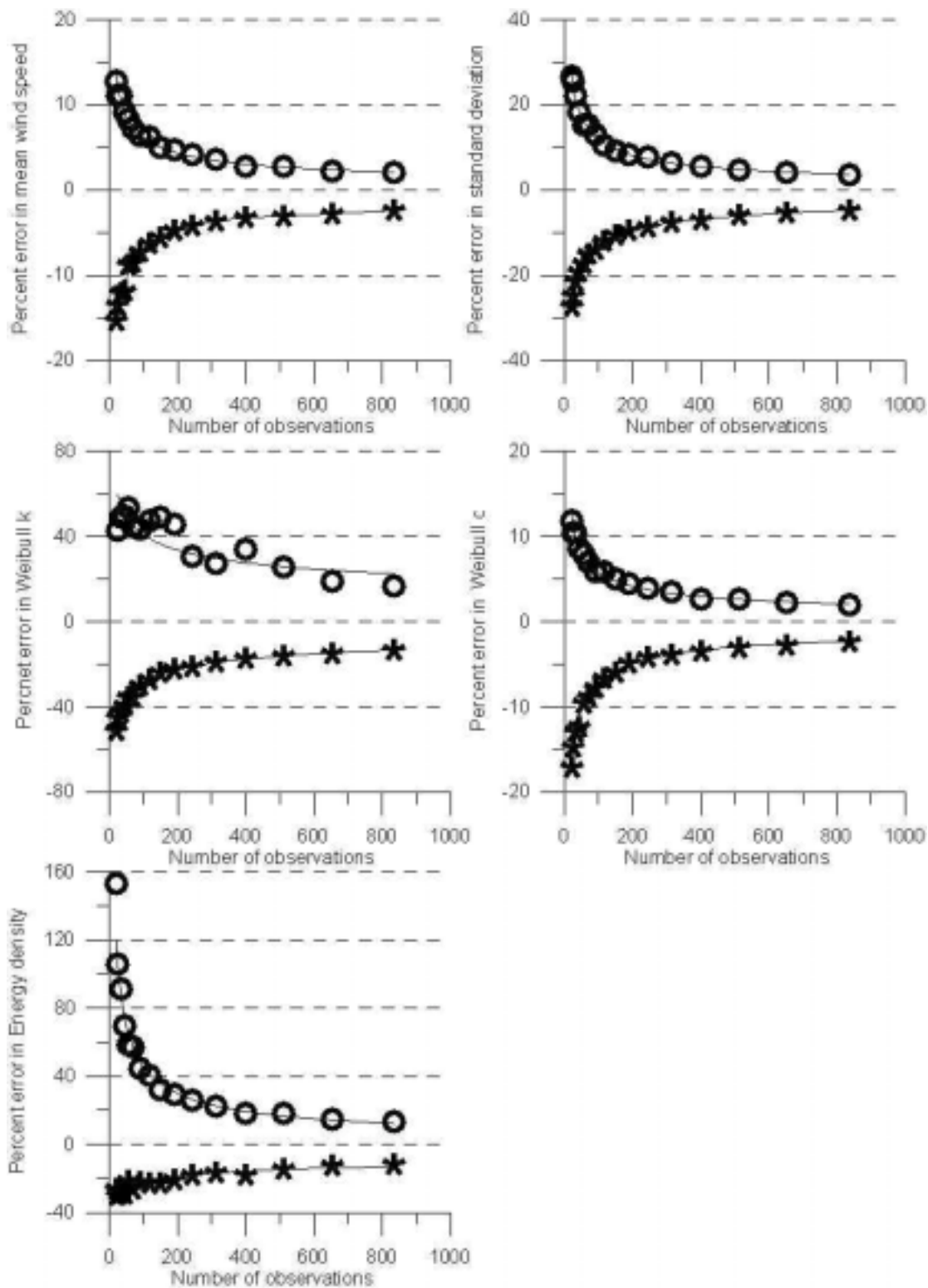
Figure 7-5 The 90 % confidence interval for percent errors in the wind speed probability distribution parameters and energy density for measurements from 10 m taken at Vindeby SMW.

It should be noted that a critical aspect of the analyses presented here is that the data sets are randomly drawn from the time series with respect to seasonality. It should further be noted that wind speeds vary on an inter-annual basis and that while this variability is small compared to the intra-annual variability, sampling

for one year does not provide a sufficient basis for a wind resource estimate (Barthelmie, 1999).

7.9 Concluding remarks and implications for wind energy resource estimation

Table 7-1 summarizes wind power (or energy) density calculated from the Weibull parameters for each of the selective sampling analyses. The results indicate that in terms of wind resource estimation for Vindeby, there is a small diurnal signal with slightly lower average energy density in the early morning (03:00 – 04:00 DST). Although the 1 v 30 minute data comparison differs from the long term average due to the dominance of summer data in the sub-sample, the higher temporal resolution data does not differ significantly from the 30 minute average in terms of estimated energy density. The largest effect, neglecting the sparse data series analysis, is the bias introduced by truncation of the data set to replicate the operational range of the SAR algorithms. The energy density calculated using the distribution parameters calculated for $2 < U < 24$ m s^{-1} is over 10 % higher than that calculated using the entire data series, as is the energy density computed for the data set conditionally sampled for all of the SAR data stratification parameters.

Assuming an uncertainty of ± 10 % at a confidence level of 90 % is acceptable for the end user, according to the results provided in Table 7-2, of the order of 60-70 randomly selected images are required to characterize the mean wind speed and Weibull c parameter, while of the order of 150 images are required to obtain a variance estimate, and nearly 2000 are needed to obtain a robust estimate of energy density (or Weibull k). As described herein, these estimates are conservative of actual needs since they assume perfect accuracy of the wind speed retrievals and that the remotely sensed data do not exhibit range or temporal biases such as those that characterize the current applications of SAR.

8 Vertical extrapolation of wind speeds derived from SAR to turbine hub-heights

Sara C. Pryor and Rebecca J. Barthelmie

8.1 Background

Use of Synthetic Aperture Radar (SAR) to develop wind resource estimates for wind energy development requires at a minimum

1. A high degree of accuracy in wind speed estimates derived from each remotely sensed scene (see Wu, 1995, Lehner et al., 1998).
2. Sufficient processed SAR images to derive a high degree of precision in the ensemble averaged wind speed probability distribution parameters –

which in turn relies upon sampling the wind climatology in an unbiased manner (see chapter 7).

3. An accurate method for vertically extrapolating from the SAR derived wind speeds which have a nominal height of 10 m to a turbine hub-height.

Issues 1 and 2 are described in detail in Chapter 7, item 3 is the focus of this analysis.

8.2 Wind profiles

Under the assumption of near-neutral stability vertical extrapolation of wind speed may be undertaken using the logarithmic wind profile:

Equation 10

$$ U_z = \frac{u_*}{\kappa} \ln\left(\frac{z}{z_0}\right) $$

U_z = wind speed at specified height z
z = height
u_* = friction velocity
z_0 = roughness length
κ = von Karman constant

Or the power law

Equation 11

$$ U_2 = U_1\left(\frac{z_2}{z_1}\right)^a $$

U_x = wind speed at specified height
z_x = height of measurement
a = power law exponent which is site dependent. As z_0 increases the power law exponent also exhibits an increase. Hsu (1988) suggested a power law exponent of 0.16 for flat coastal areas.

Under near-neutral stability, use of (1) requires; a measured wind speed and surface roughness or friction velocity or a highly accurate wind speed profile from which z_0 and u_* may be derived. Use of (2) requires a measured wind speed and knowledge of an appropriate power law exponent (or a method with which to derive one).

If the atmosphere is not near neutral but rather is unstable or is stably stratified the vertical wind profile is not logarithmic and the power law exponent is not constant[1]. Hence the vertical extrapolation of wind speeds must incorporate a

---

[1] The power law exponent is observed to increase under stable conditions and decrease under unstable conditions (Hsu, 1988)).

stability correction which is dependent on the dynamic stability. It should be noted that there are other confounding influences on the wind profile including development of internal boundary layers above which conditions are decoupled from the surface (Bergstrom et al., 1988, Pryor and Barthelmie, 2002) and development of low level jets (Smedman et al., 1996, Smedman et al., 1995). However, these effects will be neglected here.

8.3 The influence of stability on vertical wind profiles

Monin-Obukhov similarity theory is applicable to the surface layer (which to a first approximation is the constant flux layer). The Obukhov length scale (L) which defines stability in this layer is theoretically invariant with height in the surface layer and is given by

Equation 12

$$L = \frac{-\left[\overline{u'w'}^2 + \overline{v'w'}^2\right]^{3/4}}{\kappa \frac{g}{\theta_v} \overline{w'\theta_v'}}$$

g = gravity. The prime indicates deviations from the mean values of the wind components (u, v and w) and virtual potential temperature (θ_v) and the overbar represents a time average.

The Obukhov length and Richardson number (Ri) (a stability parameter used elsewhere in this report) are related in the following manner:
Unstable conditions:

Equation 13

$$Ri = \frac{z}{L}$$

Stable conditions:

Equation 14

$$\frac{Ri}{1 - 5Ri} = \frac{z}{L}$$

(Panofsky and Dutton, 1984).

Under unstable or stable conditions the diabatic wind profile is given by

Equation 15

$$U_z = \frac{u_*}{\kappa}\left[\ln\left(\frac{z}{z_0}\right) - \psi_m\left(\frac{z}{L}\right)\right]$$

Unstable conditions:

Equation 16

$$\psi_m\left(\frac{z}{L}\right) = 2\ln\left(\frac{(1+x^2)}{2}\right), x = \left(1 - \frac{15z}{L}\right)^{1/4}$$

Near-neutral conditions:

Equation 17

$$\psi_m\left(\frac{z}{L}\right) = 0$$

Stable conditions:

Equation 18

$$\psi_m\left(\frac{z}{L}\right) = \frac{-5z}{L}$$

Formulations taken from Hsu (1988).

The Obukhov length is valid only where $U \neq 0$ but has a theoretical range of $-\infty$ to $+\infty$ with $L \rightarrow 0$ indicating increasing stability when L is > 0, and increasing instability when $L < 0$. Here we shall use the following operational definitions:

$|L| > 200$ m = non-extreme stability (referred to in a qualitative sense as 'near-neutral' conditions)
-200 m $< L < 0$ m = unstable conditions
 200 m $> L > 0$ m = stable conditions.
Research objective

In this chapter we propose an operational methodology for deriving stability corrected vertical extrapolation of SAR derived 10 m wind speeds to turbine hub-heights and evaluate it based on data collected during the RASEX project (for references see section 8.5).

8.4 Methodology for computing stability corrected vertical wind profiles from remotely sensed data

Data and method assumptions

In the following we shall presume that the following data are available from remote sensing and that the data are both accurate and precise and are also at an appropriate horizontal and temporal resolution:
- A wind speed for a nominal height of 10 m.
- Air temperature at a nominal height of 10 m.
- Sea surface temperature.

We shall further assume that:
- The measurements are concurrent.
- The site of interest does not exhibit complex vertical wind speed profiles between the surface and hub-height, due for example to internal boundary layers (IBL), and hence that only atmospheric stability introduces deviations to the logarithmic wind profile.

Model tools

The purpose of the current analysis is to derive an operationally feasible method for deriving vertical wind profiles using only data that might reasonably be obtained from remote sensing and thus requires no in situ observations. Hence, in the following analyses validity of Monin-Obukhov similarity is assumed and stability is characterised using the Obukhov length (L) determined using parameterisations given in Beljaars et al. (1989) and applied in Pryor and Barthelmie (1998) and Pryor and Barthelmie (2002). The Obukhov length (L), z_0 and u_* are calculated using:
- Wind speed from 10 m height
- Air temperature measured at 10 m height
- Sea surface temperature

using the subroutine FLXSE1 from the KNMI libraries.

The results are then used in (6) to calculate the wind speed at the desired height applying the appropriate stability correction (7-9) according to the calculated value of L. In this analysis the height of prediction is 48 m because this was the highest measurement height during the RASEX project.

8.5 Method evaluation

The RASEX project (Risø Air-Sea Experiment) was conducted at the Vindeby wind farm (Barthelmie et al., 1994; Barthelmie et al., 1996; Barthelmie et al., 1995) (see Figure 8-1) during 1994 to examine the validity of Monin Obukhov similarity theory over sea using profile and eddy correlation data (Mahrt et al., 1998; Mahrt et al., 2001; Mahrt et al., 1996)[2]. Intensive campaigns were conducted during 28 April – 5 May and 3 October to 7 November during which time extensive instrumentation was deployed on the three measurement masts at Vindeby.

---

[2] The RASEX data were kindly supplied by Larry Mahrt and Dean Vickers of the Oregon State University.

Data from the RASEX project will be used here to evaluate the methodology described above. We focus here on stability, sea surface temperature and wind speed profiles collected on Vindeby sea mast west (SMW) which was the most heavily instrumented of the three meteorological masts. To reduce possible confounding of the model and measurement comparisons we have selected only data which were collected during periods of onshore flow to ensure we avoid cases where the 48 m measurement height may have been decoupled from the sea surface due to IBL effects (Pryor and Barthelmie, 2002).
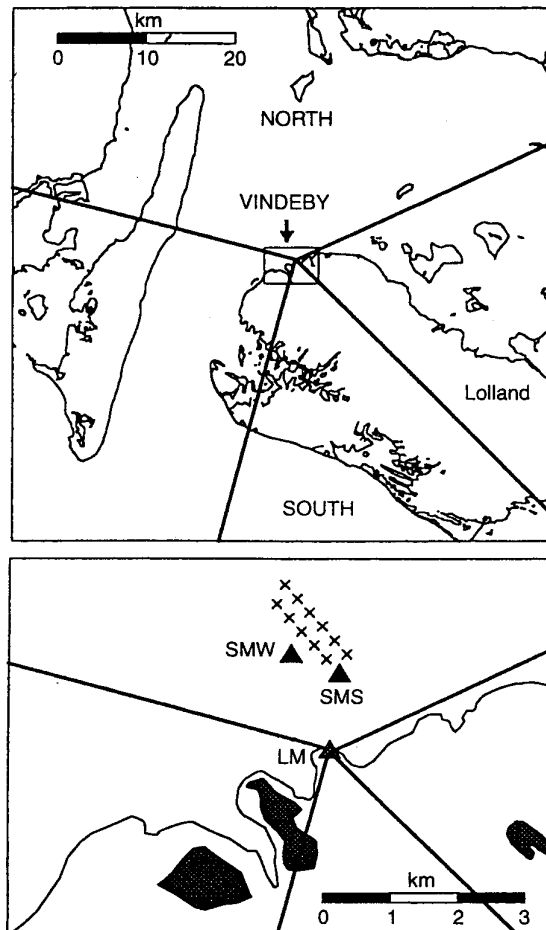
Figure 8-1 Map of the Vindeby wind farm. The crosses indicate the location of wind turbines. The measurement masts are indicated by the solid triangles and the identifiers: LM = land mast, SMS = sea mast south, SMW = sea mast west.

In the modelling presented only data were selected with wind directions 250 – 350 °. This selection criterion reduces the data set to 262 hourly averages but is undertaken to avoid effects associated with development of internal boundary layers during periods of offshore flow and to avoid possible wake effects associated with flow through the wind turbines.

8.6 Comparison of measured and modelled stability

It should be acknowledged that there is evidence that Monin Obukhov similarity theory is not fully applicable in the coastal zone (Mahrt et al., 1998). To examine the potential uncertainty due to this effect we present a summary analysis of the Obukhov length computed from different heights. During RASEX six sonic anemometers were operated on SMW at Vindeby. The five minute average values of z/L are shown in Figure 8-2 and clearly demonstrate that from a statistical perspective, as expected, L is nearly constant with height. However, the individual average L are inconsistent with height. Table 8-1 1 shows the Spearman correlations of the 5 minute and hourly average L from the sonic anemometers deployed at different heights between 3 and 48 m above mean sea level and demonstrates both a greater scatter when considering the individual measurements due to noise in the data and a decay of the association with height. For the heights used here, a value from 10 m will be used as representative of the near surface layer and will be computed over an hour period to generate more reliable estimates of L for comparison with the modelled values of L.

The comparison of measured L from the sonic located at 10 m and the modelled L derived as described above indicates a Spearman correlation of 0.61 for the 262 cases which is equivalent to the observed correlation between sonic anemometers displaced by 12 m. However, as shown in Table 8-2 the classed stability correspondences are rather low. For comparison in Table 8-3 are the classed occurrence of stability conditions (based on hourly data) from the sonic anemometers deployed at 10 and 32 m height.
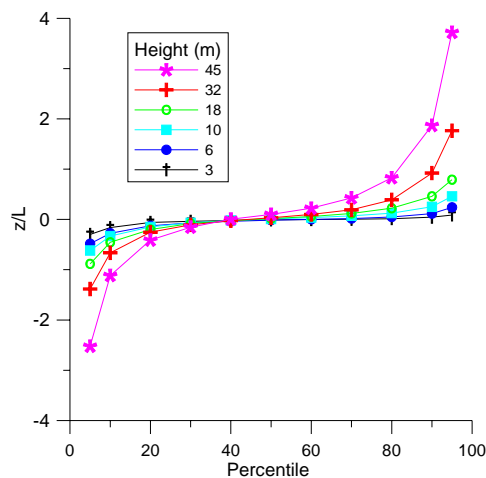

Figure 8-2 Probability distributions of the height normalized Obukhov lengths measured during RASEX. Note the data used to construct this plot are five-minute average and so may contain some measurement error.

Table 8-1 *Spearman correlations of the five minute mean height normalized Obukhov lengths (lower left hand corner) and the hourly average height normalized Obukhov lengths (upper right) measured during RASEX.*

Height (m)	Height (m)					
	3	6	10	18	32	45
3		0.89	0.83	0.68	0.43	0.40
6	0.84		0.81	0.70	0.39	0.39
10	0.78	0.76		0.78	0.44	0.49
18	0.63	0.63	0.72		0.53	0.57
32	0.38	0.36	0.41	0.54		0.56
45	0.35	0.35	0.42	0.52	0.52	

Table 8-2 *Associations of the class stability based on measured L and modelled L.*

Measured at 10 m	Modelled		
	0<L<200	|L|>200	-200<L<0
Stable	19	32	56
Near-neutral	0	0	0
Unstable	0	5	144

Table 8-3 *Associations of the class stability based on measured L at 10 m v. measured L at 32 m.*

Measured 10 m	Measured 32 m		
	0<L<200	|L|>200	-200<L<0
0<L<200	158	110	21
|L|>200	54	151	28
-200<L<0	54	53	147

8.7 Measured vertical wind profiles

Figure 8-3 shows one hour mean wind speeds from 48 and 7 m for all samples collected during RASEX (n = 764). As shown, the regression coefficient for a zero intercept model is 1.20 implying are average power law coefficient of 0.095.
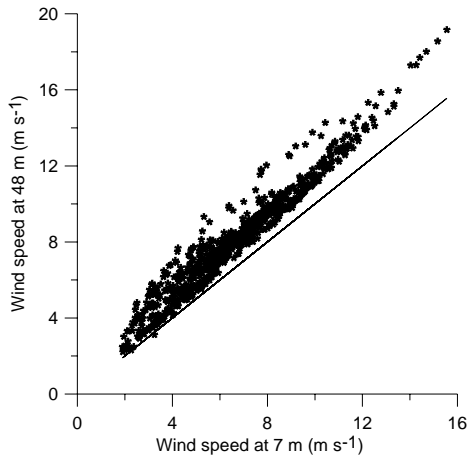
Figure 8-3   Hourly mean wind speeds as measured at 7 and 48 m during RASEX, also shown is the 1:1 line.

Figure 8-4 shows the mean vertical profiles for the stability classes defined above. The near-neutral profile implies a z_0 of 0.0009 m (which is appropriate to coastal offshore conditions {Stull 1991 80 /id} and a mean u_* of 0.35 m s^{-1}. As shown in Figure 8-4 there is some evidence of possible internal boundary layer effects associated with flow over speeding in the profile at 43 m.
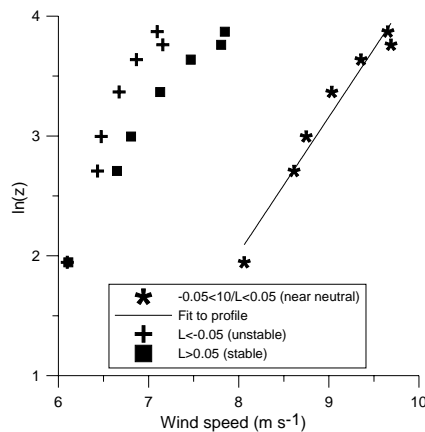
Figure 8-4   Mean vertical wind profiles calculated for the stability classes described above.

8.8 Comparison of modelled and measured wind profiles

A comparison of the modelled wind speed computed based on vertical extrapolation of the measured wind speed at 7 m, the observed SST and the observed air temperature at 10 m for wind directions 250 – 350 ° versus the observed wind speed at 48 m is shown in Figure 8-5. As shown the modelled wind speeds very closely approximate the observations. The statistics of the stability corrected extrapolation are given in Table 8-4 along with the vertical extrapolations based solely on the logarithmic wind profile. As shown, the stability corrected

profiles are more accurate than the extrapolation of the adiabatic profile. However, as also shown the stability correction for unstable conditions slightly over-predicts wind speeds on average, while the stable correction tends to underestimate the vertical wind shear. The mean absolute error (MAE) (measured wind speed at 48 m v. modelled wind speed at 48 m) in the vertically extrapolated wind speeds is 0.025 m s^{-1} indicating very low systematic bias, while the standard deviation of MAE is 0.60 m s^{-1}, indicating relatively low assystematic (or random) error. For comparative purposes the 48 m wind speed extrapolated from the 7 m data based on the logarithmic profile without the stability correction shows much higher bias (MAE = -0.25 m s^{-1}) and also higher random error (standard deviation of MAE is 0.76 m s^{-1}). The bias in the logarithmic profile extrapolation is probably the result of the high number of unstable conditions in the RASEX data set.
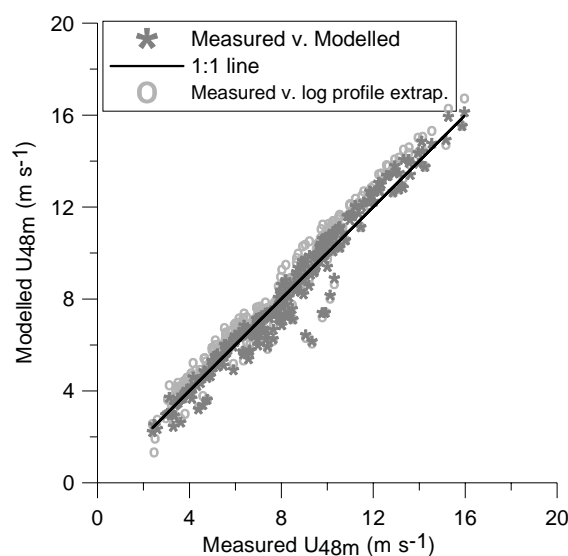
Figure 8-5 Modelled v. measured wind speeds at the Vindeby SMW. The modelled wind speeds are based on stability corrected vertical extrapolation from the measurements at 7 m. The data set has been conditionally sampled for wind direction (250 < dir < 350 °).

Table 8-4 The modelled v. measurement comparisons described by modelled stability class.

Parameter	0<L<200	-200<L<0	|L|>200
Number of cases	*25*	*200*	*37*
Stability corrected			
RMSE (m s^{-1})	1.21	0.46	0.69
Regression coefficient (ws48 = A*pred)	1.04	0.98	1.01
r^2	0.98	1.00	1.00
No stability correction			
RMSE (m s^{-1})	1.31	0.73	
Regression coefficient (ws48 = A*pred)	1.07	0.94	
r^2	0.98	1.00	

8.9 Summary

The analysis presented here is on a very temporally limited data set and so generalizations should be drawn with care. However, in accord with previous studies, the results here show the accuracy of vertical extrapolations of wind speeds is improved by the inclusion of stability corrections but that there are fundamental differences in modelled and observed values of the Obukhov length and indeed between Obukhov lengths calculated from sonic data collected simultaneously at different heights. Hence, while there is considerable benefit to the application of stability corrections on a statistical basis the individual profile extrapolations are highly uncertain. Further, again in accord with previous studies, there is evidence that the stability correction to the logarithmic wind profile may be underestimated in stable conditions by current correction formulations.

9 Scalar footprints

Morten Nielsen

The theory on scalar footprints originates from (Gash, 1986). Others have also modelled the footprints as described below in detail. The concept is that air is advected to a given sensor at a given height from the upwind source area graphed in Figure 9-1. In the area close to the sensor there is a large amount of influence whereas the area further away has less influence. The footprint area-averaging method has mainly been used for land surfaces but an example by (Smedman et al., 1999) shows the use of footprint theory in a marine study.
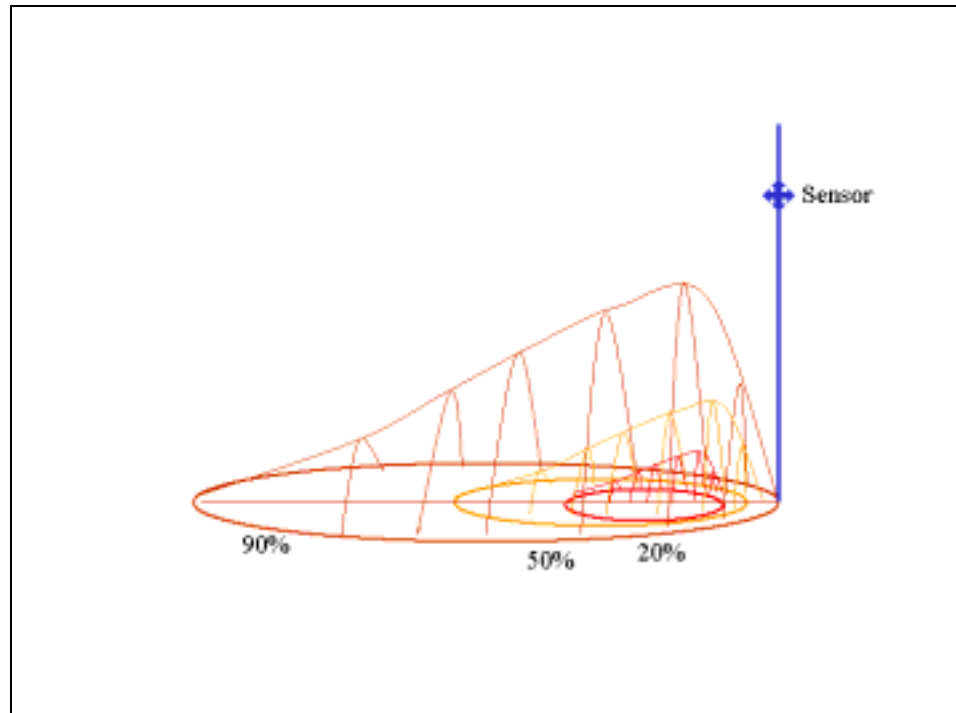

Figure 9-1 Schematic of the footprints for a given sensor. The area giving a certain percentage of influence to the signal is shown for 20 %, 50 % and 90 %.

9.1 The model of Gash (1986)

(Gash, 1986) proposed a crosswind-integrated footprint of the type

Equation 19

$$f^y(x) = \frac{A}{x^2} \exp\left(-\frac{A}{x}\right), \quad \text{for } x > 0$$

The length scale $A = uz_m / \kappa u_*$ depends on a uniform advection velocity, the flux measurement height, and the friction velocity. The footprint was derived under the assumption that the vertical profile of a plume from a ground source has an exponential shape and the advection speed is considered uniform. The x-axis is in the upwind direction and the integral from the mast position to infinity is unity. The maximum is found at the distance $x = A/2$ and the downwind footprint integral is:

Equation 20

$$F^y(x) = \exp\left(-\frac{A}{x}\right), \quad \text{for } x > 0$$

9.2 The model of Hsieh et al. (2000)

(Hsieh et al., 2000) proposed a semi-empirical enhancement of the model of (Gash, 1986) taking atmospheric stability into account. The footprint length scale is estimated by

Equation 21

$$A = \frac{Dz_u}{\kappa^2}\left(z_u/|L|\right)^{p-1} \quad \text{with} \quad \begin{cases} D = 0.28; p = 0.59 & z_u/L < -0.04 \text{ (unstable)} \\ D = 0.97; p = 1 & |z_u/L| \le 0.04 \text{ (neutral)} \\ D = 2.44; p = 1.33 & z_u/L > 0.04 \text{ (stable)} \end{cases}$$

Here, κ is von Karman's constant and L is the Monin-Obukhov length. The new length scale is

Equation 22

$$z_u = z_m \left(\ln(z_m/z_0) - 1 + z_0/z_m\right)$$

where z_m is the measurement height and z_0 is the surface roughness. The coefficients (D, p) were calibrated by numerical simulation with the particle model of Thompson run under various stability conditions. Unfortunately the range of height ratio z_0/z_m in these reference calculations seem too limited for offshore applications.

Power-law approximations

This paragraph is a brief review of classic diffusion theory, which the dispersion model of (van Ulden, 1978) and footprint model of (Horst and WEIL, 1994) relies upon, see below. The diffusion-advection equation

Equation 23

$$u \frac{\partial c}{\partial x} = \frac{\partial}{\partial z}\left[K \frac{\partial c}{\partial z}\right]$$

has analytic solutions when vertical profiles of velocity and eddy-diffusivity are approximated by power laws:

Equation 24

$$u = u_1 \left(z/z_1\right)^m \qquad\qquad K = K_1 \left(z/z_1\right)^n$$

With these approximations (Sutton, 1953) calculated the concentration field from of a surface line source of strength Q as

Equation 25

$$\frac{c(x,z)}{Q} = \frac{r}{u_1 z_1 \Gamma(s)}\left(\frac{z_1^2 u_1}{r^2 K_1 x}\right)^s \exp\left(-\frac{z_1^{2-r} u_1 z^r}{r^2 K_1 x}\right), \quad \text{with } r = 2 + m - n \text{ and}$$

Equation 26

$$s = \frac{1+m}{2+m-n}$$

With the local plume advection and average height defined as

Equation 27

$$\bar{u} \equiv \frac{\int_0^\infty uc\, dz}{\int_0^\infty c\, dz} \qquad\qquad \bar{z} \equiv \frac{\int_0^\infty zc\, dz}{\int_0^\infty c\, dz}$$

the local concentration profile is of the type

Equation 28

$$\frac{c(z)}{Q} = \frac{A}{\bar{u}\, \bar{z}} \exp\left[-\left(Bz/\bar{z}\right)^r\right]$$

where the new constants A and B are

Equation 29

$$A = \frac{r\,\Gamma(2/r)}{\Gamma^2(1/r)} \qquad\qquad B = \frac{\Gamma(2/r)}{\Gamma(1/r)}$$

The growth of the plume height and the plume advection velocity obey two convenient relations

Equation 30

$$\frac{d\bar{z}}{dx} = \frac{K(p\bar{z})}{u(p\bar{z})\,p\bar{z}} \qquad\qquad \bar{u} = u(q\bar{z})$$

i.e. we may evaluate integral plume properties by the profile values at the heights $p\bar{z}$ and $q\bar{z}$, using the factors:

Equation 31

$$p = \left[r^{1/r}\,\Gamma(2/r)/\Gamma(1/r)\right]^{r/(1-r)} \qquad q = \frac{\Gamma(s)^{1/m}\,\Gamma(1/r)^{1-1/m}}{\Gamma(2/r)}$$

The optimal power-law fit to the profiles known from surface-layer theory, at a reference height z_1 has the exponent

Equation 32

$$m = \frac{\varphi_m(z_1/L)}{\ln(z_1/z_0) - \psi_m(z_1/L)}$$

and it may be argued that the eddy-diffusivity exponent should be

Equation 33

$$n = 1 - m \qquad r = 1 + 2m \qquad s = \frac{1+m}{1+2m}$$

since this provides a constant momentum flux.

9.3 The model of Horst & Weill (1994)

(van Ulden, 1978) substituted power-law expressions in the convenient relations for plume advection and growth rate by more appropriate surface-layer profiles.

Equation 34

$$\bar{u} = \frac{u_*}{\kappa}\left[\ln(q\bar{z}/z_0) - \psi_m(q\bar{z}/L)\right]$$

Equation 35

$$\frac{d\bar{z}}{dx} = \frac{\kappa^2}{\left[\ln\left(p\,\bar{z}/z_0\right) - \psi_m\left(p\,\bar{z}/L\right)\right]\varphi_h\left(p\,\bar{z}/L\right)}$$

The conclusions were that the plume advection relation is mathematically correct in stable conditions and accurate within 10% for unstable conditions. The plume growth-rate relation is accurate within 20%. From the growth-rate (van Ulden, 1978) deduced the distance necessary for the plume to reach a given height as

Equation 36

$$\frac{x}{z_0} = \kappa^{-2}\int_{z_0}^{\bar{z}}\left[\ln\left(p\,z'/z_0\right) - \psi_m\left(p\,z'/L\right)\right]\varphi_h\left(p\,z'/L\right)dz' \equiv \Psi\left(\bar{z}\right) - \Psi\left(z_0\right)$$

(Horst and WEIL, 1994) calculated this $\Psi\left(z\right)$ function for Businger-Dyer expressions of the non-dimensional profiles.

Equation 37

$$\Psi\left(\bar{z}\right) = \begin{cases} \dfrac{1}{\kappa^2}\dfrac{\bar{z}}{z_0}\left\{\ln\dfrac{p\bar{z}}{z_0} - 1 + \dfrac{\beta p\bar{z}}{L}\left[\dfrac{1}{4} + \dfrac{\beta p\bar{z}}{3L} + \dfrac{1}{2}\ln\dfrac{p\bar{z}}{z_0}\right]\right\}, & \dfrac{\bar{z}}{L} \geq 0 \\[4mm] \dfrac{1}{\kappa^2}\dfrac{2|L|}{\gamma p z_0}\left\{y_p\left[\ln\dfrac{p\bar{z}}{z_0} - \psi_m\left(y_p\right)\right] + 2\tan^{-1}y_p + \ln\dfrac{y_p+1}{y_p-1} - 4y_p\right\}, & \dfrac{\bar{z}}{L} < 0 \end{cases}$$

Here $y_p = \left(1 - \gamma\,p\bar{z}/L\right)^{1/4}$ and the coefficients $\left(\beta = 5, \gamma = 16\right)$ originates from the thermal gradient formula

Equation 38

$$\varphi_h\left(z/L\right) = \begin{cases} \left(1 + \beta z/L\right), & z/L \geq 0 \\ \left(1 + \gamma z/L\right)^{-1/2}, & z/L < 0 \end{cases}$$

and corresponding velocity gradient and profiles.
(Horst and WEIL, 1994) expressed the fundamental foot-print relation as the upward flux from a surface point source

Equation 39

$$\bar{f}^y\left(x, z_m\right) = -\frac{\partial}{\partial x}\int_0^{\bar{z}}u\left(z\right)\frac{c^y\left(x, z\right)}{Q}dz$$

An approximation is provided by insertion of van Ulden's (1978) plume model

Equation 40

$$\bar{f}^y \rvert x, z_m \lvert \approx -\frac{d\bar{z}}{dx} \frac{\partial}{\partial \bar{z}} \int_0^{z_m/\bar{z}} \frac{u \rvert \xi \bar{z} \lvert}{\bar{u} \rvert \bar{z} \lvert} A \exp\left[-\rvert B\xi \lvert^r \right] d\xi$$

$$= \frac{d\bar{z}}{dx} \frac{z_m}{\bar{z}^2} \frac{u \rvert z_m \lvert}{\bar{u} \rvert \bar{z} \lvert} A \exp\left[-\rvert Bz_m/\bar{z} \lvert^r \right]$$

This is evaluated for a given plume heights $\bar{z}$ and the corresponding distances is calculated by

Equation 41

$$x/z_0 = \Psi \rvert \bar{z} \lvert - \Psi \rvert z_0 \lvert .$$

(Horst and WEIL, 1994) fixed the profile shape parameter to $r = 1$ for unstable conditions, $r = 1.5$ for neutral conditions and $r = 2$ for stable conditions, and adopted a fixed growth-rate height factor $p = 1.55$ from (van Ulden, 1978), who found that this had insignificant variation. (Horst and WEIL, 1994) did however suggest a new variable advection height factor

Equation 42

$$q = \frac{\Gamma \rvert 1/r \lvert}{\Gamma \rvert 2/r \lvert} \exp\left[\rvert 1/r \, \psi \rvert 1/r \lvert \right]$$

which was calculated by insertion of a logarithmic velocity profile in the $\bar{u}$ integral instead of the power-law approximation. The argument of the exponential function involves the digamma function, which relates to the gamma function by

Equation 43

$$\psi \rvert x \lvert = \Gamma' \rvert x \lvert / \Gamma \rvert x \lvert$$

As an optional modification, we may revert to the power-law estimates of *r* and *p* - with limits on the shape parameter $r \in [1, 2]$. We introduce optional limits on the stability parameter in accordance with the definition range f the Businger-Dyer expressions.

9.4 Crosswind variation

(Horst and WEIL, 1994) state that the crosswind footprint variation is equivalent to the concentration field in a surface plume from a point source, usually modelled as a Gaussian distribution with a crosswind spreading growing in the downwind direction. We can express this as

Equation 44

$$f(x,y) = \frac{f^y(x)}{\sqrt{2\pi}\,\sigma_y(x)}\exp\left\{-\frac{y^2}{2\sigma_y^2(x)}\right\}, \quad \text{for } x > 0$$

Crosswind integration of this two-dimensional footprint formula will reproduce the one-dimensional footprint. (Gryning et al., 1987) modelled plume spreading up to distances of 5 km as

Equation 45

$$\sigma_y = \sigma_v\,t\big/\left(1 - \sqrt{t/2T_y}\right)$$

where σ_v is the standard deviation of the crosswind velocity perturbations, $t \approx x/u(z_m)$ is the travel time and T_y is the Lagrangian time scale, which in the lack of accurate information is estimated to 600 s. The authors recommend the use of measured crosswind velocity perturbations. If unavailable, they could be modelled by

Equation 46

$$\frac{\sigma_v^2}{u_*^2} = \begin{cases} 0.35(-h/\kappa L)^{2/3} + 2 - z_m/h & \text{for } h/L < 0 \\ 2(1 - z_m/h) & \text{for } h/L > 0 \end{cases}$$

where h is the mixing height, which we estimate to 500 m - also in the lack of accurate information.

9.5 Pixel-area integral

The satellite image is described in the UTM system, with X (East) and Y (North) in meters and the mast position is (X_m, Y_m). The wind direction θ is measured anticlockwise from North, see Figure 9-2, and the transformation to footprint coordinates is:

Equation 47

$$\begin{bmatrix} x \\ y \end{bmatrix} = \begin{bmatrix} \sin\theta & \cos\theta \\ -\cos\theta & \sin\theta \end{bmatrix} \cdot \begin{bmatrix} X - X_m \\ Y - Y_m \end{bmatrix} \Leftrightarrow \begin{bmatrix} X \\ Y \end{bmatrix} = \begin{bmatrix} X_m \\ Y_m \end{bmatrix} + \begin{bmatrix} \sin\theta & -\cos\theta \\ \cos\theta & \sin\theta \end{bmatrix} \cdot \begin{bmatrix} x \\ y \end{bmatrix}$$

The footprint in image resolution is estimated by a set of observation point distributed evenly over the footprint area. This is done by the reverse functions of the accumulated downwind and lateral distributions and the observation point is translated to image coordinates. With a large number of observation points, e.g. 1000×1000, the particle count becomes a reliable estimate of the relative weight of individual pixels.

Equation 48

for $i = 1 \ldots N_x$ do

begin

$\qquad x = F^{-1}\left[\left(i - \tfrac{1}{2}\right)/N_x\right]$

$\qquad$ for $j = 1 \ldots N_y$ do

$\qquad$ begin

$\qquad\qquad y = \sigma\left(x_i\right)\cdot\Phi^{-1}\left[\left(j - \tfrac{1}{2}\right)/N_y\right]$

$\qquad\qquad \left(x, y\right) \to \left(X, Y\right)$

$\qquad$ end

end
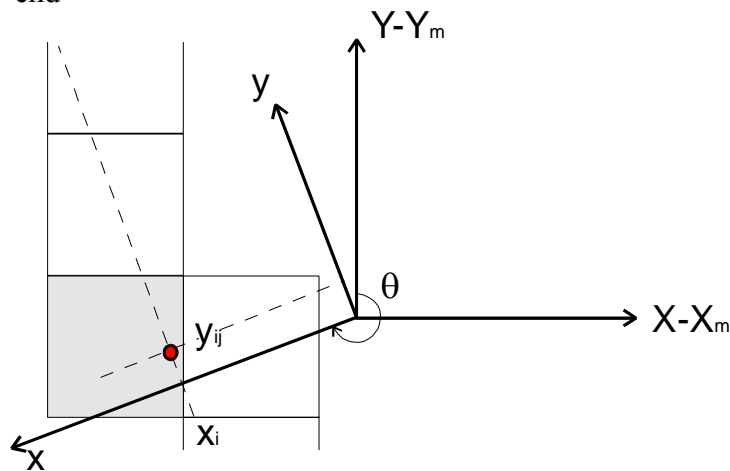
Figure 9-2: Sketch of the geometry of pixel-area integration.

10 Weather from NOAA AVHRR and DWD weather maps

Charlotte Bay Hasager

10.1 NOAA AVHRR satellite image description

NOAA AVHRR satellite data are received from a series of meteorological observation satellites. It is NOAA (National Oceanic and Atmospheric Administration (USA)) platforms that carry the instrument type AVHRR (Advanced Very High Resolution Radiometer). Data are available since 1978 as listed in Table 10-1 with the satellite numbers indicated.

Table 10-1 List of available NOAA AVHRR satellite images. From
http://www.sat.dundee.ac.uk/avhrr.html

AVHRR	Operational
(5)	1978-06-11 to 1980-11-01
6	1979-07-17 to 1986-07-09
7	1981-06-24 to 1985-01-08
8	1982-06-20 to 1985-10-17
9	1984-12-17 to 1995-01-19
10	1986-10-08 to 1994-10-06
11	1988-10-21 to 1994-09-15
12	1991-07-16
14	1995-01-19
15	1998-05-13 to 2000-07-10)
16	2000-09-21 (launch)

The AVHRR instruments are scanning radiometers with 1.1 km spatial resolution at nadir and a >2600 km swath width. The radiometers have either five or six channels. NOAA-5 to NOAA–14 have 5 channels (1-5 in Table 10-2). NOAA-15 onwards carries an enhanced version of the AVHRR scanner. It has six channels (three visible and three infra-red) but, for compatibility at receiving stations, only five are transmitted. Channel 3 is the visible channel during the daytime and the infra-red channel at nighttime. The primary use of the channels is listed in Table 10-2.

Table 10-2 Channels, bands widths and primary use of NOAA AVHRR satellite images. From http://www.sat.dundee.ac.uk/avhrr.html

Channel	Wavelength (microns)	Primary Use
1	0.58 - 0.68	Daytime cloud/surface mapping
2	0.725 - 1.10	Surface water delineation, ice and snow melt
3A	1.58 - 1.64	Snow / ice discrimination (NOAA K,L,M)
3 (or 3B)	3.55 - 3.93	Sea surface temperature, nighttime cloud mapping
4	10.30 - 11.30	Sea surface temperature, day and night cloud mapping
5	11.50 - 12.50	Sea surface temperature, day and night cloud mapping

Channel 1 and 2 measure the reflected sunlight in the visible bands. Channel 4 and 5 measure the emitted thermal radiation in the "window" region of the electromagnetic spectrum. By use of a split-window algorithm the surface temperatures of land and sea can be calculated from channel 4 and 5.

All the NOAA AVHRR satellites are in polar sun-synchronous orbits around the Earth, i.e. they are traveling roughly pole-to-pole and map the same area of the Earth at a certain local hour. The images are taken either at northbound (ascending) or southbound (descending) tracks.

10.2 Quicklooks for weather description

NOAA AVHRR satellite data are available from several receiving stations. One is the Dundee Satellite Receiving Station, Dundee University in Scotland. Archived data are freely available at http://www.sat.dundee.ac.uk/ in quicklook format since November 6th, 1978. A quicklook image is a reduced-resolution image.

The copyrights of the quicklook images are the following. The image is credited to us "Dundee Satellite Receiving Station, Dundee University, Scotland" (or "Image courtesy of the University of Dundee" as a minimum) with a link to our home page http://www.sat.dundee.ac.uk/. We are notified of the full details of the publication (author, title, journal etc. as appropriate). If the publication is for education or research we would appreciate more details of the topic, and a copy of the publication if possible.

The local sites studied in the WEMSAR projects are located in Denmark, Norway and Italy. These sites are all viewed by NOAA AVHRR images from the Dundee receiving station. The Gulf of Suez site in Egypt is not covered. Figure 10-1 shows the area viewed from Dundee.
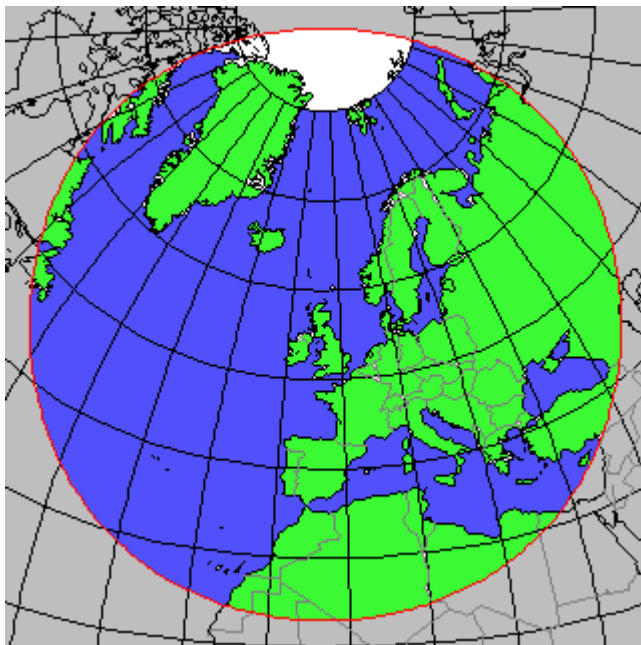

Figure 10-1 The area viewed by the Dundee Satellite Receiving Station concerning NOAA AVHRR imagery. Information from http://www.sat.dundee.ac.uk/avhrr.html.

The information of interest from NOAA AVHRR images in the WEMSAR project is to map the general weather situations for local areas. As both day and night conditions have to be investigated, the thermal channels are best suited for this as the visible channels only useful in daylight. Further does the thermal channels generally give a very clear mapping of clouds compared to land and sea surfaces because the clouds are very much colder. When a grid of latitude and longitude as well as a coastline in contrasting colour (black/white) depending of the content of the image is overlaid, it is easy to see large- and fine-scale weather conditions.

Complementary information on the in-situ meteorological time series are DWD weather maps(1999) and two AVHRR scenes for each case. One AVHRR scene is prior to the ERS-SAR overpass; the other is after. From this material the development in weather is assessed.

10.3 DWD weather maps

For the analysis of synoptic weather conditions maps from DWD (1999) for 1997-2000 have been used for the Horns Rev and Maddalena sites.

11 Horns Rev in Denmark

Charlotte Bay Hasager, Ebba Dellwik, Bo Hoffmann Jørgensen and Poul Astrup

11.1 Site description

Horns Rev is located west of the Jutlandia North Sea coast in Denmark. At distance of 14 km from the Jutlandic shoreline, a tall meteorological tower is erected, see the map in Figure 11-1. From the tower a long-term data series of atmospheric observation of wind speed, wind direction and air temperatures has been collected by ELSAM/ELTRA(Neckelmann, 2000). The data series from 16-5-1999 to 31-5-2000 is studied in the WEMSAR project.

Figure 11-1 Map of the Horns Rev site in the North Sea, Denmark. From *https://www.elsam.com/default_ie.htm.*
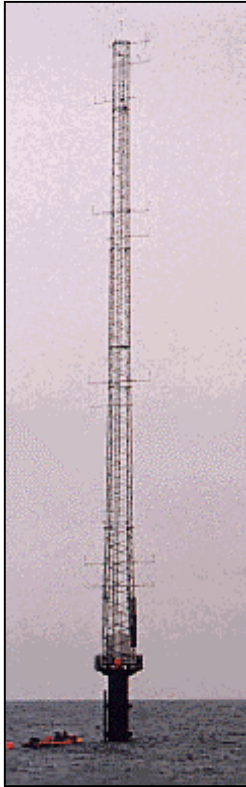
The geographic coordinates of the meteorological tower is 55E30'27.82'' N, 7E52'30.05'' E (in UTM32/WGS84 Easting 428.946, Northing 6.152.003). The data are collected for the planning of a large offshore wind turbine farm (https://www.elsam.com/default_ie.htm). A photo in Figure 11-2 shows the mast.

The wind data from the Horns Rev meteorological tower is measured at four levels. For the three lower levels identical cup anemometers are placed at booms in two directions. One boom is pointing to the southwest at 225 degrees and the other boom to the northeast at 45 degrees. So for the sector 135-315 degrees the southwest data are analysed, and for the 315-135 sector the northeast data are analysed. The reason for two booms in opposite directions is to avoid flow distortion from the tower itself in the dataset. The wind speeds are measured at 15 m, 30 m, 45 m and 62 m above DNN (Dansk Normal Nul), the temperatures are measured at 13 m and 55 m, and the wind direction is measured at 60 m.

Figure 11-2 Meteorological mast at Horns Rev. From https://www.elsam.com/default_ie.htm.

11.2 Satellite scenes from ERS-2 SAR

ERS-2 SAR scenes in the PRI format has been calibrated by the SAR Tool Box software and processed into maps of offshore wind speed by the CMOD-IFR2 algorithm at the Nansen Environmental and Remote Sensing Centre (NERSC) by Dr. Birgitte Furevik ((Johannessen, 2001)). The wind speed maps each cover an area of 100 km * 100 km with a cell size of 400 m * 400 m.

There are 32 available ERS-2 SAR scenes in the study period from the Horns Rev site, i.e. the ERS-2 SAR sensor observed the site approximately three times per month. From the ESA archives a subset of these satellite scenes have been selected and ordered. The scenes are granted free of cost through the ESA AO3-153 project.

In order to study the physical relations between SAR backscatter signals and the wind speed a special series of satellite scenes are retrieved. The ERS SAR satellite scenes series are selected from a set of ideal criteria:

- ❖ 1. Wind speed regimes (low 5-9 m/s, medium 9-13 m/s, high > 13m/s)
- ❖ 2. Wind direction (on-shore 270°, along-shore 0°/180°, off-shore 90°)
- ❖ 3. Stability (stable typical spring, unstable typical autumn).

The SAR scenes are selected from the in situ wind speed observations at 62 m level. Wind speeds lower than 5 m s^{-1} adds only little to the wind power potential. The 16 days from which scenes are ordered are listed in Table 11-1. In four cases two scenes (frames) have been ordered to cover the area of interest.

Table 11-1 Selected ERS-2 SAR scenes from Horns Rev, Denmark

Date	Time (UTC)	Orbit	Track	Frames
20-5-1999	21:30	21340	444	1107
21-6-1999	21:24	21798	401	1107
10-7-1999	20:57	22070	172	1107
29-7-1999	21:30	22342	444	1107
10-8-1999	10:30	22507	108	2493
30-8-1999	21:24	22800	401	1107
3-10-1999	10:30	23280	380	2475+2493
7-10-1999	21:30	23344	444	1107
19-10-1999	10:30	23509	108	2493
23-11-1999	10:30	24010	108	2493
16-12-1999	21:30	24346	444	1107
16-1-2000	10:30	24783	380	2475+2493
1-2-2000	10:30	25012	108	2493
7-3-2000	10:28	25513	108	2475+2493
26-3-2000	10:31	25785	380	2475
16-5-2000	10:28	26515	108	2475+2493

The meteorological observations for the 16 cases are listed in Table 11-2.

Table 11-2 Meteorological observations at the Horns Rev site: wind speed (U), wind direction and standard deviation, air temperature (T_a) and sea temperature (T_{sea}) averaged to one hour mean values. Measured by ELSAM/ELTRA.[*] estimated value.

Case	Date	Hour (UTC)	U at 62 m (m/s)	Dir. at 60 m (°)	Std.dev. at 60 m (°)	T_a at 55 m (ºC)	T_a at 13 m (ºC)	T_{sea} at – 4 m (ºC)
1	20051999	21:30	8,2	122,3	1,6	15.2	13.4	10.9
2	21061999	21:24	11,2	313,9	3,9	11.4	12.3	14.6
3	10071999	20:57	7,3	71,8	2,0	21.3	20.3	17.1
4	29071999	21:30	7,6	34,9	10,6	17.8	18.3	17.7
5	10081999	10:30	12,2	328,8	2,6	16.3	17.8	19.5
6	30081999	21:24	8,1	291,8	4,3	14.8	15.7	17.3
7	03101999	10:30	13,8	240,8	4,8	13.7	14.6	16.2
8	07101999	21:30	12,3	274,4	3,2	13.8	14.7	15.4
9	19101999	10:30	9.4*	88,8	4,8	7.8	8.8	12.5
10	23111999	10:30	3,0	233,3	4,3	8.9	9.4	-
11	16121999	21:30	13,5	244,3	2,9	7.0	-	-
12	16012000	10:30	11,5	305,6	3,4	6.0	6.6	-
13	01022000	10:30	15,6	235,1	2,6	6.6	6.8	-
14	07032000	10.28	17,6	256,3	2,8	6.3	6.7	-
15	26032000	10.31	4.8	125.6	3.8	16.3	17.1	-
16	16052000	10.28	8,3	182,3	1,3	11.2	11.9	-

The criteria on different wind speed regimes are covered well by the chosen scenes. The scenes are graphed as a function of wind direction and wind speed in Figure 11-3. However, only for low wind speeds are all wind directions rep-

resented. For wind speeds > 10 m s^{-1} the wind direction was always between southwest and northwest.

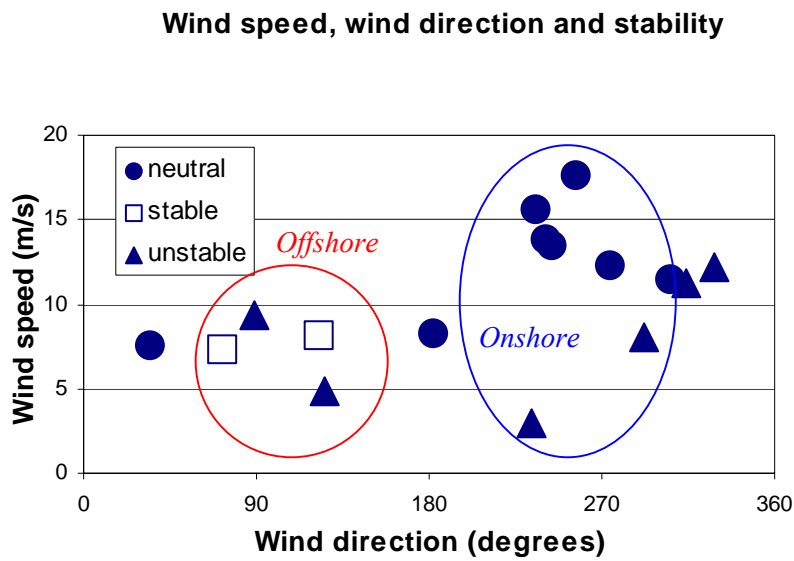**Wind speed, wind direction and stability**

Figure 11-3 Wind speed, wind direction and stability for the cases at Horns Rev. Offshore and onshore cases are indicated

The atmospheric static stability is assumed to be mainly stable in spring and unstable in autumn. In spring cold air from land may be advected over the relatively warm ocean. In autumn warm air from land may be advected over the relatively cool ocean. In Figure 11-4 the stability is graphed as a function of time of year. See section 11.3 for the calculation of stability. The two cases of stable conditions occur in spring and summer. The unstable conditions occur during all times of the year. For the cases of strong winds the atmospheric stability is near- neutral from autumn to early spring.
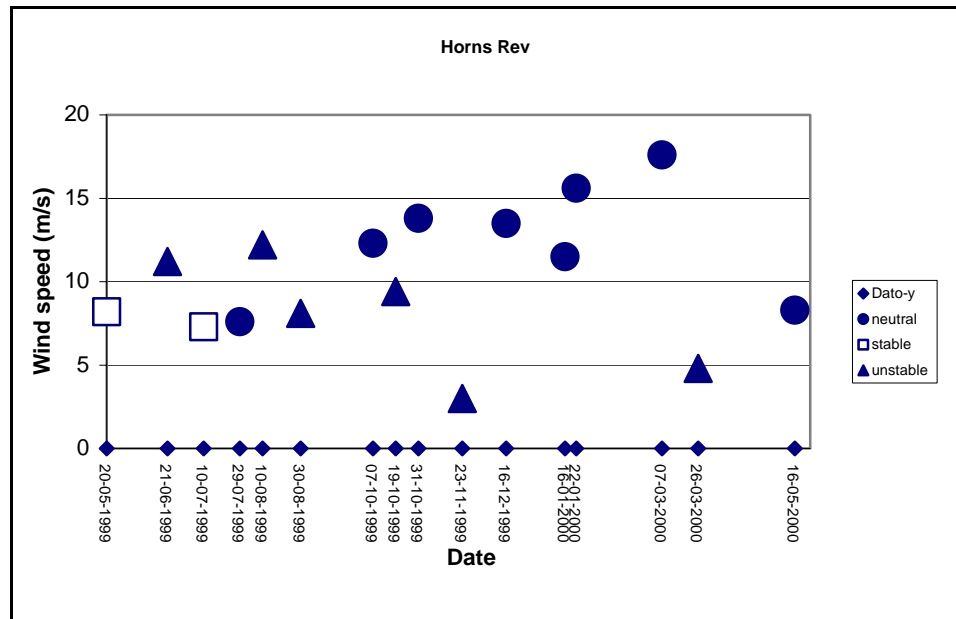
Figure 11-4 Horns Rev wind speed and atmospheric stability through time.

Four scenes map offshore flow. These are cases of weak to medium winds and only two cases are stable. These took place in spring and summer. Alongshore flow is mapped 4 times in low and medium wind speeds. Onshore flow is mapped 8 times covering low, medium and high wind speeds.

11.3 Analysis of micrometeorological data

In order to evaluate and calibrate SAR wind speed maps careful comparison with micro-meteorological in-situ measurements is necessary. Wind profile data from a 62 m tall mast at Horns Rev (see Figure 11-1 and Figure 11-2) has been compiled and analysed with the intention of providing a good comparison material for the satellite image analysis. The Horns Rev mast is operated by ELSAM/ELTRA (Neckelmann, 2000). The micro-meteorological time series were selected to match with 16 satellite-passes between May 1999 and May 2000.

The analysis has two objectives

(1) to derive estimates of the 10m wind speed u_{10m}, the friction velocity u_* and the roughness length z_0
(2) to estimate the atmospheric stability in order to facilitate footprint calculations.

General method for the derivation of $\bar{u}_{10m}$, u_* and z_0

The wind speed is measured at 15 m, 30 m, 45 m and 62 m height above DNN, the Danish Normal zero. The measurement levels are corrected for local sea level changes due to tidal effects, see section 11.4. For each time series, mean values are calculated for consecutive 60-minute intervals from the original 10-minute mean values. The wind profile is theoretically described as in Equation 9. There are three unknowns in Equation 9: u_*, z_0 and L. By using temperature measurements at 13 and 55 m in the mast, L can be estimated from the Richard-

son bulk number (see Equation 49) and a least square log-linear fit can be applied to Equation 9 to calculate u_* and z_0. The inclination of the fitted line gives u_* and the extrapolated intercept at $\bar{u}=0$ gives z_0. The wind speed at 10 m height can then easily be calculated from Equation 9. The least square fit has been applied both with the assumption of a neutral atmosphere ($\psi_m=0$) and with the stability correction included.

The calculation of z_0, which normally is in the order of 10^{-4} m from Equation 9, is very sensitive to errors. A small error either in the model or in one of the cup anemometer measurements could easily lead to an error of an order of magnitude in the roughness length estimate. Charnock's relation in Equation 8 ((Charnock, 1955)) gives a more robust estimate. Here we choose $A_c = 0.018$ as recommended for Danish waters by (Johnson, 1998).

Estimates of the atmospheric stability

The bulk Richardson number Ri_B has been calculated according to

Equation 49

$$Ri_B \frac{g}{T} \frac{[\theta(z_1)-\theta(z_2)]/(z_1-z_2)}{([u(z_3)-u(z_4)]/(z_3-z_4))^2} \equiv B \frac{(z_3-z_4)^2}{z_1-z_2},$$

with $g = 9.81$ m s^{-2} and T and θ signify absolute and potential temperature, respectively. In order to estimate the Monin-Obukhov length L from the accessible data, the logarithmic expressions for wind profiles Equation 9 and temperature have been applied in Equation 49. By comparing the resulting equation with the definition of L, the following relation can be deduced:

Equation 50

$$L = B^{-1} \frac{\ln(z_1/z_2)-\Psi_h(z_1/L)+\Psi_h(z_2/L)}{[\ln(z_3/z_4)-\Psi_m(z_4/L)]^2}.$$

Equation 50 describes a non-linear equation, which can be solved iteratively for L.

For the Ψ functions we have used

Equation 51

$$\Psi_m = \ln \frac{(1+x)^2(1+x^2)}{8} + 2\tan^{-1}\left(\frac{1-x}{1+x}\right), x = \left(1-16\frac{z}{L}\right)^{1/4}$$

Equation 52

$$\Psi_h = \ln \frac{(1+y)^2}{4}, y = \left(1-8\frac{z}{L}\right)^{1/2}$$

for unstable conditions ($L < 0$) and

Equation 53

$$\Psi_m = \Psi_h = -5\frac{z}{L}$$

for stable conditions ($L > 0$).

Once the Monin-Obukhov length is estimated, the wind profiles can be corrected for deviation from neutral atmospheric stability. However, this method is very uncertain. One problem is that the Ψ functions over sea are very poorly known. Another problem, which is more specific for this application, is that we are interested in the wind profiles on an hourly time scale, in which case a lot of scatter from an ideal profile is to be expected (Barthelmie 2001, personal communication). In order to check whether a correction for atmospheric stability actually leads to an improvement for the wind profile modelling, the following error estimate was introduced

Equation 54

$$s = \sqrt{\frac{\sum_i (\bar{u}_{meas} - \bar{u}_{mod})^2}{n}},$$

where n is the total number of observations during the satellite passing and *meas* and *mod* signify measured and modelled wind speeds respectively.

Results of $\bar{u}_{10m}$, u_* and z_0

The results of the analysis described above for the exact satellite passing times are summarized in Table 11-3.The are obtained by taking mean values for the measurement period half an hour before and half an hour after the passing of the satellite

Estimates of $\bar{u}_{10m}$, u_* and z_0 were calculated both with the assumption of neutral atmosphere and with stability corrections included. Only in 5 out of the 16 cases did the error estimate according to Equation 54 decrease when the atmospheric stability was included in the model. In these 5 cases the absolute level of improvement was so slight, that it was considered being beyond the accuracy of the instruments. The assumption of neutral profiles, although incorrect, yields in general better results, which is why no results for atmospheric stability corrected $\bar{u}_{10m}$, u_* and z_0 are shown.

The measurement levels at Horns Rev were corrected for tidal effects following Equation 55. The deviations from DNN were small for all the cases with a maximum of 0.69 m.

The method was able to determine $\bar{u}_{10m}$, u_* and z_0 in all cases, but the results for October 19, November 23 and December 16 in 1999 should be regarded as rough estimates, since not all cup anemometers functioned properly when the satellite passed.

Results on atmospheric stability

The bulk Richardson number was calculated according to Equation 49 with $z_1=$ 55 m, $z_2 = 13$ m, $z_3 = 62$ m and $z_4 = 15$ m. The results are shown in figures in Appendix II and summarized for the satellite passing time in Table 11-4. Equations (6-9) were solved for the Monin-Obukhov length L with an equation solver in Matlab3. The method uses a combination of bisection, secant, and inverse quadratic interpolation methods.

Table 11-3 Horns Rev summary of results on $\bar{u}_{10m}$, u_* and z_0. These have been corrected for tidal effects, but not for atmospheric stability. The second column shows the calculated sea level deviation from DNN due to tidal effects.

Date and time (UTC)		DNN dev. (m)	z_0 (10^{-4}m)	u_* (m s^{-1})	$\bar{u}_{10m}$ (m s^{-1})
1999-05-20	21:30	-0.34	0.11	0.077	7.8
1999-06-21	21:54	0.37	0.93	0.22	10.1
1999-07-10	20:57	0.39	8.8	0.69	4.2
1999-07-29	21:30	-0.39	3.5	0.43	5.6
1999-08-10	10:30	0.65	0.63	0.18	11.2
1999-08-30	21:24	-0.41	0.46	0.16	7.0
1999-10-03	10:30	0.37	3.5	0.44	11.9
1999-10-07	21:30	0.56	2.8	0.39	10.4
1999-10-19	10:30[a]	-0.33	0.98	0.23	8.9
1999-11-23	10:30[b]	0.57	2.3	0.32	1.6
1999-12-16	21:30[c]	0.30	13	0.83	9.9
2000-01-16	10:30	0.03	11	0.81	7.7
2000-02-01	10:30	0.69	19	1.1	10.5
2000-03-07	10:30	0.47	23	1.1	12.2
2000-03-26	10:30	-0.47	0.16	0.089	4.3
2000-05-16	10:30	0.37	12	0.81	4.8

[a] The cup anemometer at 62 m did not work during this period.

[b] The parameters are very poorly decided, since only the cup anemometers at 30 and 45m worked during the passing of the satellite.

[c] The cup anemometer at 15 m did not work during this period.

---

3 Copyright The Math Works Inc.

Table 11-4 Atmospheric stability for Horns Rev. The bulk Richardson number Ri_B has been calculated from measurements and the corresponding Monin-Obukhov length L has been estimated in an iterative equation

Date, time (UTC)		Ri_B (m)	L (m)	Classification[a]
1999-05-20	21:30	45	0+	very stable
1999-06-21	21:54	-1.3	-41	unstable
1999-07-10	20:57	0.24	17	stable
1999-07-29	21:30	0.11	-410	neutral
1999-08-10	10:30	-2.48	-22	unstable
1999-08-30	21:24	-2.39	-24	unstable
1999-10-03	10:30	-0.32	-154	neutral
1999-10-07	21:30	-0.39	-133	neutral
1999-10-19	10:30[b]	-1.1	-21	unstable
1999-11-23	10:30[c]	-0.8	-26	unstable
1999-12-16	21:30[d]	-	-	-
2000-01-16	10:30	-0.01	8170	neutral
2000-02-01	10:30	-0.02	1730	neutral
2000-03-07	10:30	-0.03	-1530	neutral
2000-03-26	10:30	3.0	-23	unstable
2000-05-16	10:30	-0.08	-536	neutral

[a] Atmospheric conditions are considered to be unstable if $-130 \leq L \leq 0$,
   neutral if $130 < L$ or $L < -130$ and stable if $0 \leq L \leq 130$
[b] The cup anemometer at 62m did not work during this period
[c] The parameters are very poorly decided since only the cup anemometers
   at 30 and 45 m worked during the passing of the satellite
[d] The thermometer at 13 m did not work during this period

11.4 Marine observations

The coast from Horns Rev and towards the south is named the Wadden Sea. It stretches all the way from Denmark to the Netherlands and is well-known for its marshes and large tidal flats. Much of the coast and the islands are threatened by flooding when high tide and strong winds appear. The coast north of Horns Rev and all the way to the northern tip of Denmark, Skagens Odde, is a broad white sandy beach, except for a few locations with clay cliffs. At Horns Rev a stony underwater reef stretches out towards the west. A bathymetry map is shown in Figure 11-5. The bathymetry map was generated by Danish Hydraulic Institute (DHI) /50395/2.ed.Nov.2001/PH/KAE. The large shallow areas in the Wadden Sea are seen as well as the reef to the west of Horns Rev.The mast is located at 6.0 m depth.
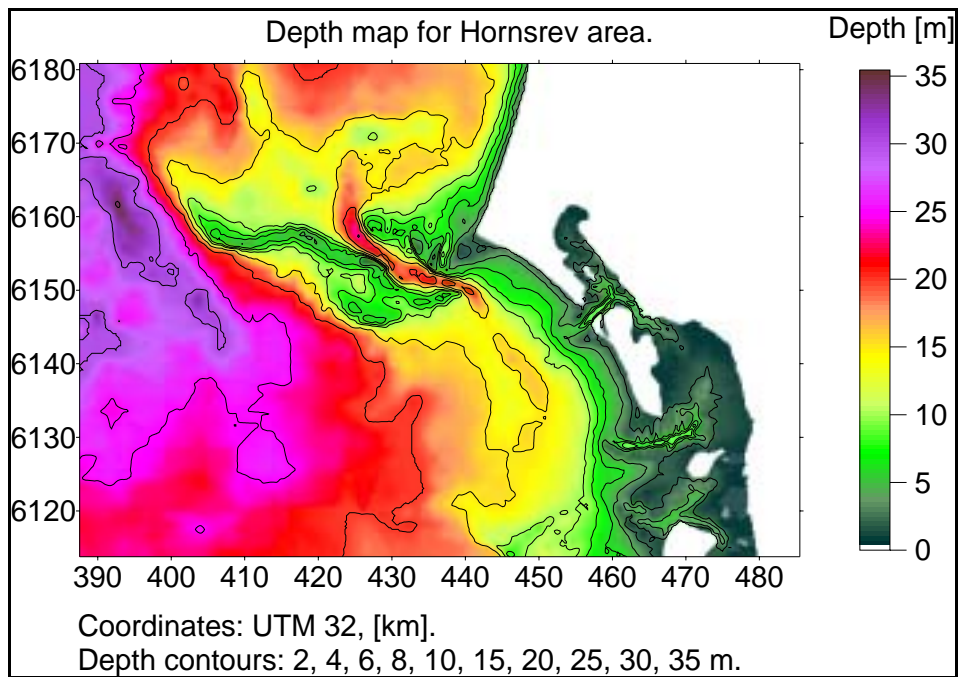
Figure 11-5 Bathymetry of Horns Rev. From DHI/50395/2.ed.Nov. 2001/PH/KAE.

Tide

The tidal range is more than 4 m in Esbjerg near the Horns Rev site. The sea level is measured in Esbjerg Harbour every 15 minutes and the values are listed in Table 11-5 at the time of the satellite scenes.

Table 11-5 Esbjerg Harbour sea level deviation from DNN. * indicate towards low (L) and high (H) tide .Observations from Danish Meteorological Institute/Farvandsvæsenet.

Date	(UTC)	Sea level (cm)	*
0051999	21:30	-50	H
21061999	21:24	54	L
10071999	20:57	45	H
29071999	21:30	-57	H
10081999	10:30	95	H
30081999	21:24	55	L
03101999	10:30	82	H
07101999	21:30	-48	L
19101999	10:30	44	H
23111999	10:30	84	H
16121999	21:30	44	L
16012000	10:30	5	L
01022000	10:30	102	L
07032000	10:28	69	H
26032000	10.31	-70	L
16052000	10:28	54	H

On a buoy near the Horns Rev mast, the mean sea level was measured. Unfortunately this data series deteriorated from its initial calibration (July 1999) and was considered unreliable. In order to estimate the mean sea level at Horns Rev, the buoy data series was compared and correlated for the first 10 days of July 1999 to the Esbjerg Harbour data. During this time the deviation from the original calibration of the instrument on the buoy is considered negligible. The correlation function was estimated from

Equation 55

$$\delta_{HR} \approx 0.68\delta_{Esb},$$

where δ is the sea level deviation from the Danish normal zero (DNN), and suffix *HR* and *Esb* signify Horns Rev and Esbjerg Harbour, respectively. The results are shown in Figure 11-6 and Figure 11-7. The mean sea levels at the Horns Rev site are summarized in Table 11-3.
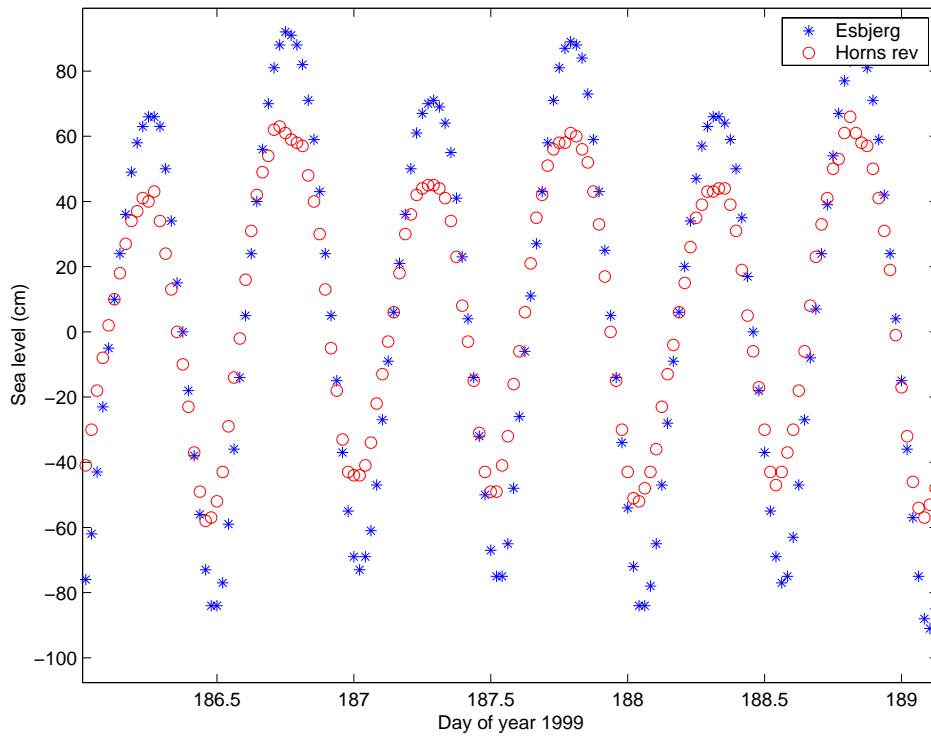
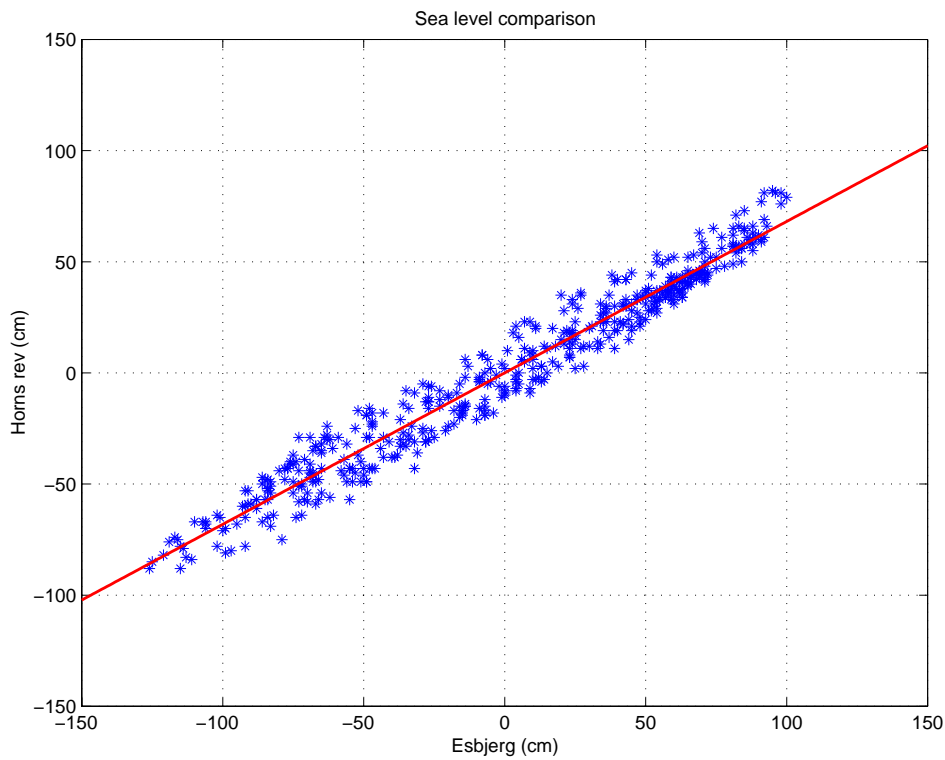*Figure 11-6 Horns Rev mean sea level compared to Esbjerg Harbour*

Figure 11-7 Horns Rev and Esbjerg Harbour sea level correlation

Ocean currents and waves

Ocean currents are measured at two buoys at the Horns Rev site by ELSAM/ELTRA (Neckelmann, 2000). Data from the southern buoy near the mast is extracted for the half hour before, at and after the satellite overpass. Table 11-6 lists the *direction in which the current flows* and speed of the current. Ocean current data are not available from the following dates: 20-5-99, 21-6-99, 16-1-00, 1-2-00 and 26-3-00. The current typically is either north or south and with speeds of 0.1 to 0.8 m s^{-1}.

On the 3 and 7 October 1999 the current turned much within the 1.5 hours centered at the satellite observation time. In all other cases the current was steady in direction but often changing in speed.

Table 11-6 Ocean current direction and speed measured at Horns Rev at a depth of -2.33 m. Wave height and wave periods measured at Horns Rev. Hs is significant wave height, Hmax is maximum wave height, TO2 is significant wave period, and Tp maximum wave period Local time (DST) is one hour ahead of UTC.Data from Techwise.

Date, time (DST)		Ocean current		Ocean waves			
		Dir. (°)	Speed (m s^{-1})	Hs (m)	Hmax (m)	TO2 (s)	Tp (s)
10-07-1999	21:30	346	0,24				
10-07-1999	22:00	349	0,19	0,43		3,10	3,33
10-07-1999	22:30	352	0,13				
29-07-1999	22:00	196	0,28				
29-07-1999	22:30	198	0,31	0,50		2,73	3,57
29-07-1999	23:00	198	0,31				
10-08-1999	11:00	351	0,15				
10-08-1999	11:30	358	0,04				
10-08-1999	12:00	6	0,10	1,29		4,30	5,00
30-08-1999	22:00	186	0,10				
30-08-1999	22:30	185	0,08				
30-08-1999	23:00	184	0,07	0,99		3,47	5,00
03-10-1999	11:00	14	0,25				
03-10-1999	11:30	23	0,40				
03-10-1999	12:00	133	0,74	1,86		5,26	7,14
07-10-1999	22:00	239	0,85				
07-10-1999	22:30	352	0,14				
07-10-1999	23:00	1	0,02	1,76		4,57	7,14
19-10-1999	11:00	358	0,03				
19-10-1999	11:30	303	0,84				
19-10-1999	12:00	235	0,82	0,92		3,22	3,57
23-11-1999	11:00	309	0,78				
23-11-1999	11:30	347	0,23				
23-11-1999	12:00	352	0,14	0,92	1,41	4,51	6,25
16-12-1999	22:00	34	0,55				
16-12-1999	22:30	38	0,62				
16-12-1999	23:00	67	0,92	1,59	2,35	4,59	6,25
16-01-2000	12:00			0,89	1,36	3,65	4,17
01-02-2000	12:00			2,00	2,68	4,86	7,14
07-03-2000	11:00	163	0,28				
07-03-2000	11:30	137	0,68				
07-03-2000	12:00	121	0,86	2,40	3,31	5,48	8,33
16-05-2000	11:00	335	0,42				
16-05-2000	11:30	352	0,15				
16-05-2000	12:00	351	0,16				

Wave height and periods are measured at buoys at Horns Rev. During some periods also the maximum wave height is measured. Wave data are not available from the following dates: 25-5-1999, 21-6-1999, 26-3-2000 and 16-5-2000. The relation between wave height and wave period are

graphed in Figure 11-8. According to (Neckelmann, 2000) some cases are dominated by swell. Usually however the wave pattern is dominated by the regional atmospheric situation. On the 23-11-1999 swell waves are expected according to the data.
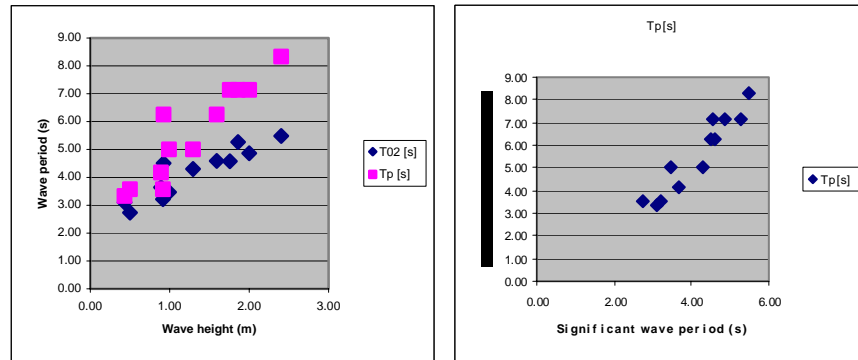

Figure 11-8 Left figure) Wave height and wave periods of the significant (TO2) and maximum waves (T_p). Right figure) Significant and maximum wave periods at Horns Rev

11.5 Weather conditions

For each of the 16 ERS SAR scenes an analysis of the weather systems are performed. The analysis is based on the European Meteorological Bulletin surface charts from Deutscher Wetterdienst in resolutions 1:30.000.000 and 1:60.000.000 ((1999; 2000)). For each of the 16 cases two NOAA AVHRR satellite scenes one prior to and one after the ERS SAR scenes are downloaded. The NOAA AVHRR scenes are quicklooks from Dundee (please refer to Chapter 10). The recording time and NOAA AVHRR satellite numbers are listed in Table 11-7. The meteorological and marine in-situ observations as reported in section 11.3 are also included for the description of the atmospheric flow. From the in-situ observations it is especially import to note whether or not the atmosphere was stationary prior to the satellite overpass.

*Table 11-7 ERS-2 SAR and NOAA AVHRR satellite numbers and recording times for Horns Rev. ⇑ ascending, ⇓ descending mode.*from the day after.*

Date	ERS SAR	At Time (UTC)	NOAA AVHRR	Prior Time (UTC)	NOAA AVHRR	After Time (UTC)
20-5-1999	2⇑	21:30	12⇑	16.16	14⇓	02.19*
21-6-1999	2⇑	21:24	12⇑	17.45	14⇓	03.02*
10-7-1999	2⇑	20:57	12⇑	17.22	14⇓	02.49*
29-7-1999	2⇑	21:30	12⇑	16.59	14⇓	02.35*
10-8-1999	2⇓	10:30	12⇓	06.03	14⇑	12.08
30-8-1999	2⇑	21:24	15⇑	18.04	14⇓	03.17*
3-10-1999	2⇓	10:30	15⇓	09.01	14⇑	13.41
7-10-1999	2⇑	21:30	15⇑	19.01	14⇓	02.49*
19-10-1999	2⇓	10:30	15⇓	08.06	14⇑	14.00
23-11-1999	2⇓	10:30	12⇓	07.00	14⇑	14.05
16-12-1999	2⇑	21:30	15⇑	18.06	14⇓	02.58*
16-1-2000	2⇓	10:30	15⇓	08.27	14⇑	13.53
1-2-2000	2⇓	10:30	15⇓	09.10	14⇑	14.11
7-3-2000	2⇓	10.28	15⇓	07.50	14⇑	14.12
26-3-2000	2⇓	10.31	15⇓	09.06	14⇑	13.55
16-5-2000	2⇓	10.28	12⇓	06.23	14⇑	14.09

11.6 KAMM2 mesoscale model considerations

The present calculations for Horns Rev have mainly been performed with a grid containing 121*121*51 cells for an area which is 120 km*120 km, i.e. 1 km horizontal resolution. A few runs with 500 m and 2 km resolution have been performed to ensure grid independence. The orography (EMD, 2001a) used for the mesoscale model calculations with 1 km horizontal resolution and the corresponding aerodynamic roughness length (EMD, 2001b) is shown in Figure 11-9.
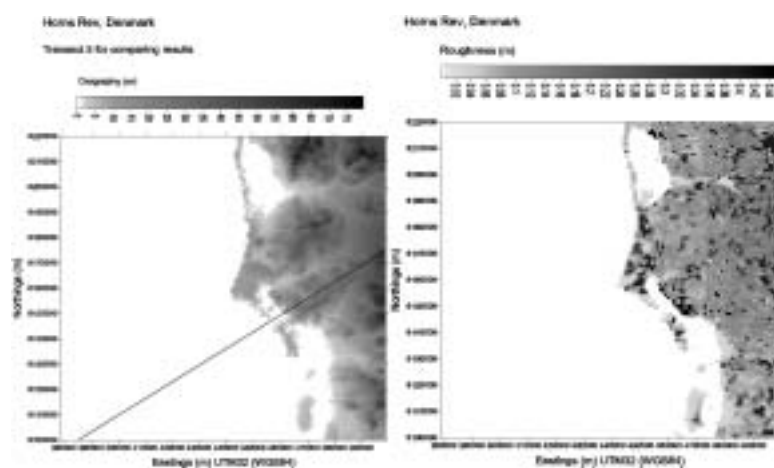

Figure 11-9 Horns Rev with 1 km horizontal resolution used for the mesoscale model calculations: a) orography; b) aerodynamic roughness length map. A horizontal transect proceeding from the sea towards land is depicted in the orography map.

NCAR/NCEP reanalysis data has been compared to in-situ data for all 16 cases at Horns Rev. The times of available SAR wind speed maps and NCAR/NCEP data are listed in Table 11-8. As described in Chapter 6, it is necessary to select a subset of the cases for which the wind speed measured at the mast is stationary for at least a few hours and compares well with the surface wind speed at 10 m height from the reanalysis data. This is because the mesoscale model cannot be expected to perform well if the applied large scale forcing is not realistic. For Horns Rev cases for which the wind speed difference between in-situ observations from the mast and reanalysis surface wind speed exceeds 3 m s^{-1} are excluded. For the five selected cases, the wind speed from in-situ observations, the reanalysis grid data, the KAMM2 results at the mast position and the SAR wind speeds all assumed valid for 10 m height are listed in Table 11-9. The wind direction and atmospheric stability are also shown.

Table 11-8 Horns Rev cases. One time per case is selected from the 4 times daily reanalysis data set to match the time of the satellite overpassing for each SAR scene. This defines the possible cases of reanalysis data to be used as large scale forcing for the mesoscale model. Five cases 5 are selected for further study, i.e. the (boldface) cases 4, 7, 8, 9 and 13.

Case	SAR scene date, time (UTC)		Reanalysis date, time (UTC)	
1	20.5.1999	21:30	21.5.1999	00:00
2	21.6.1999	21:24	22.6.1999	00:00
3	10.7.1999	20:57	10.7.1999	18:00
4	**29.7.1999**	21:30	**29.7.1999**	**18:00**
5	10.8.1999	10:30	10.8.1999	12:00
6	30.8.1999	21:24	31.8.1999	00:00
7	**3.10.1999**	10:30	**3.10.1999**	**12:00**
8	**7.10.1999**	21:30	**8.10.1999**	**00:00**
9	**19.10.1999**	10:30	**19.10.1999**	**12:00**
10	23.11.1999	10:30	23.11.1999	12:00
11	16.12.1999	21:30	17.12.1999	00:00
12	16.1.2000	10:30	16.1.2000	12:00
13	**1.2.2000**	10:30	**1.2.2000**	**12:00**
14	7.3.2000	10:28	7.3.2000	12:00
15	26.3.2000	10:31	26.3.2000	12:00
16	16.5.2000	10:28	16.5.2000	12:00

A typical example illustrating the selection procedure is depicted in Figure 11-10. It seen in the figure that the wind speed and direction measured at the mast is relatively close to the surface wind at 10 m height from the reanalysis data. Also, temperature data from the mast is utilized to select scenes with reasonably constant Monin-Obukhov length to ensure stationary atmospheric stability. Furthermore, fronts cannot be simulated, so frontal activity found from DWD weather charts and NOAA AVHRR scenes are disregarded. The resulting selection consists of the five scenes 4, 7, 8, 9 and 13 (boldface in Table 11-8) which have been analyzed in the present work.

Table 11-9 Comparison of the wind speed at 10 m height at the position of the mast at Horns Rev. Meteorological in-situ observations, reanalysis grid data, KAMM2 results at the mast position and the SAR wind at the mast position. The wind direction and stability is from the in-situ data.

Case	In-situ			Reanalysis	KAMM2	SAR
	Speed m s^{-1}	Dir deg.	Stability	Speed m s^{-1}	Speed m s^{-1}	Speed m s^{-1}
4	5.6	35	neutral	3.2	3.1	5.5
7	11.9	241	neutral	11.5	10.5	8.6
8	10.4	274	neutral	8.0	7.4	9.4
9	8.9	89	unstable	9.5	8.7	8.4
13	10.5	235	neutral	11.5	11.0	9.7

The five cases include one offshore (9), one alongshore (4) and three onshore (7, 8 and 13). The time lag between the KAMM2 model results and the SAR wind speed maps vary from 1.5 hours (cases 7, 9 and 13), 2.5 hours (8) up to 3.5 hours (4). The time lags necessity rather stationary conditions for comparisons to be useful.

As explained in Chapter 6, grid independence of the mesoscale model solution was tested by plotting the wind speed for three different horizontal resolutions along different horizontal transects, one of which is located in the computational domain as illustrated in Figure 11-9a. The transect proceeds from the sea towards land.

Since the SAR derived wind speeds and the LINCOM results were already available, it was found useful to investigate these other data sources in order to evaluate the performance of the mesoscale model. The satellite SAR derived wind speeds and the mesoscale model results have been plotted together with the LINCOM results along a number of differently oriented transects. An example for case 9, which has offshore wind and unstable atmospheric conditions, is shown in Figure 11-11 for the transect depicted in Figure 11-9a. In the bottom of Figure 11-11 the corresponding sea depth (DHI, 2001) is shown (zero depth corresponding to the coast). The transect position is shown at the x-axis. The shore is located at 92 km. However, for this particular transect, the SAR data at positions greater than 80 km are unreliable because the transect goes through tidal flats and surges (the Esbjerg Harbour area with a deep manmade shipping route). The first part of the SAR data show increasing wind speeds as the distance to the coast decreases. This is not as found in the KAMM2 and LINCOM results.

The mesoscale model results are very similar for the two different horizontal resolutions of 1 km and 500 m, proving that grid independence is achieved for a resolution of 1 km. It is found that in general a resolution of 1 km is sufficient for the mesoscale calculations at Horns Rev.

As can be seen from Table 11-9 the wind speed calculated by the mesoscale model at the position of the mast is lower than the surface wind speed of the reanalysis data for the large grid cell located over the North Sea (see Figure 6-3). The difference is less than 1 m s^{-1}. The deviation between the KAMM2 wind speed results and in-situ data largely follows the deviation between the surface wind speed of the reanalysis data and the in-situ wind speed.

As an example of the mesoscale model results the wind speed at 10 m (agl.) is shown for Horns Rev at 12.00 (UTC), October 19, 1999 in Figures in Appendix II. It is clear why the land orography and roughness length must be taken into account in this case because the predominant wind direction from the east causes a significant influence of the land topography in the offshore part of the computational domain. Four hours of simulation time (physical model time - not computer CPU time) was found to be necessary in order to approach a final state of the computational wind map. The amount of simulation time is discussed in Chapter 6.
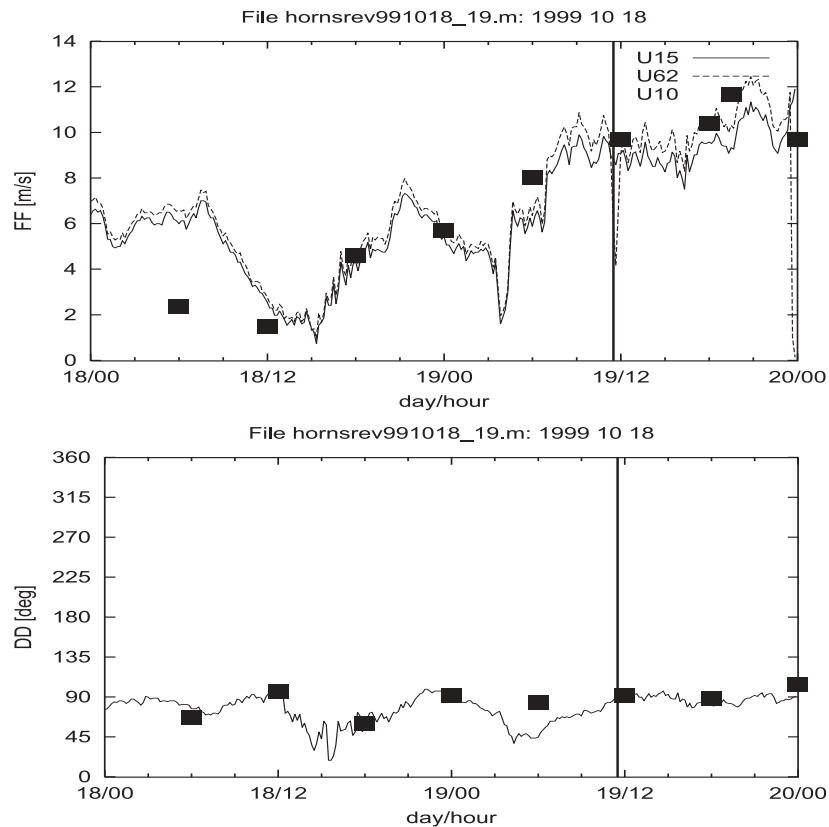
Figure 11-10. Wind speed (above) and wind direction (below) measured at the mast at Horns Rev compared to the surface wind at 10m height from the re-analysis data (filled boxes). The satellite overpassing time corresponding to case 9 is indicated with a vertical line
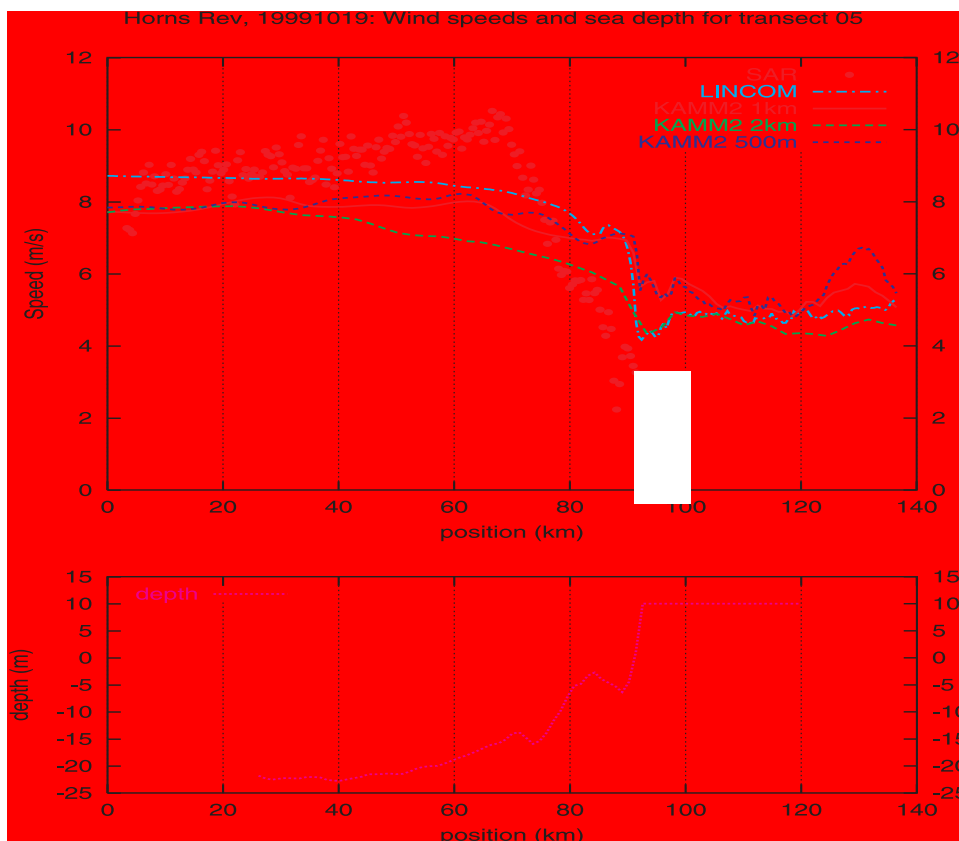
Figure 11-11. Wind speeds (above) derived from SAR compared to the corresponding mesoscale model results for three different horizontal resolutions and compared to the LINCOM results along an example transect. Depths (below) extracted from a bathymetry from the Danish Hydraulic Institute. The SAR data are not valid on land, i.e. for positions greater than 92 km.

11.7 LINCOM

LINCOM has been run with input of the same maps on orography and roughness as the KAMM2 model. The meteorological input to LINCOM is the observations at the meteorological mast at Horns Rev, hence the LINCOM model result at this point is per definition equal to the mast observations. The spatial pattern of wind speed and wind direction in the domain can be compared to the KAMM2 model results and the SAR wind speed maps.

11.8 Horns Rev case descriptions

The Horns Rev site in Denmark is analysed case by case. The conditions for each of the 16 cases are described case by case based on the information on weather and sea status in sections 11.3, 11.4 and 11.5. Due to a significant tide and strong sea currents near the shallow water areas of Horns Rev, some marine effects are noted in several SAR cases.

The graphs in Appendix II show the micrometeorological conditions near the time of the satelllite overpass measured from in-situ observations, the cloud patterns from NOAA AVHRR quicklooks, a weather description based on DWD maps, LINCOM model results on wind speed, SAR wind speed maps and for five cases also a comparison of re-analysis data to in-situ data and KAMM model results on wind speed.

11.9 Comparison of SAR scenes to in-situ data

The comparison analysis between in-situ meteorological wind observations and SAR wind speed maps are done by area-averaging through footprint theory. It is assumed that the atmospheric flow is stationary (frozen turbulence). According to theory the mast observation is under influence of the conditions of a certain area upwind of the sensor dependent on sensor height, wind speed and stability. The SAR data are spatial snap-shots recorded in a few seconds. The spatial and temporal time scales are related. At Horns Rev the in-situ observations of 10-minute means are averaged into hourly values (section 11.3) and corrected for atmospheric stability effects as well as variations in tidal height. Then the values are extrapolated down to the 10 m height comparable to the SAR wind speed maps.

The SAR wind speed maps are retrieved under two different assumptions. The first is that the wind direction is known from the in-situ data, i.e. from anemometers at the meteorological tower in the ocean. The second assumption is that wind streaks in the SAR imagery reveal the wind direction through linear features parallel to the dominant wind direction. The direction is determined from two-dimensional Fast Fourier Transform (FFT) analysis with a cut-off wavelength in order to only map a certain scale of features.

The wind direction has to be known a priori before applying the scatterometer-based ocean wind speed algorithm CMOD-IFR2 to the calibrated raw SAR scenes. The accuracy of wind direction is evaluated in relation to the wind speeds.

Footprint area-averaging has been performed with a very simple approach and with a more advanced approach (see chapter 9). In the simple approach neutral wind profiles were assumed and the contribution from an elliptic area positioned in the upwind area was calculated to have a certain length and width from the equations in (Gash, 1986) in which the footprint model predicts the area from which a certain percentage of the surface flux pertains to.

The footprint formula for neutral conditions derived from (Gash, 1986) gives

Equation 56

$$X_P = \frac{z}{\kappa^2}\ln(\frac{z}{z_0}) \Big/ \ln(\frac{100}{P})$$

which expresses that a percent fraction, P (%), of the measured flux derives from within an upwind distance X_P (m). In Equation 56 z_0 (m) is the local aerodynamic roughness, z (m) is the observation height and κ is the von Karman constant (0.4). The maximum contribution to the flux stems from a distance, X_{max} given by

Equation 57

$$X_{max} = \frac{z}{2\kappa^2}\ln(\frac{z}{z_0}).$$

Because of turbulence in the lateral direction the footprint area is ellipse-shaped. The footprints vary as a function of measurement height and local roughness. For a roughness of 0.0002 m and heights of 10 and 62 m, the maximum response comes from a distance of 338 m and 2450 m, respectively.

The area-average was not weighted in regard to local position within the footprint but average linearly, similar to a land-based flux study on satellite data by (Bastiaanssen et al., 1998). Result from this simple type of footprint area-averaging on SAR wind speed maps based on wind direction information from the in-situ data is presented in Hasager et al. (2001). More detail on the study is given below.

Footprint ellipses for 90% contributions for 10 and 62 m heights were calculated. For 10 m observations the footprint ellipse has a semi-major axis of 2732 m and a semi-minor axis of 482 m, i.e. a total area of $4.1*10^6$ m^2 and 26 resolution cells (as the SAR wind speed maps were gridded at 400 m by 400 m). For the 62 m observations the footprint ellipse has a semi-major axis of 20.292m and a semi-minor axis of 3.578 m with an area of $228*10^6$ m^2 and 1425 resolution cells.

One case is graphed in Figure 11-12 to show an examples of how the footprints look.

North Sea, Denmark 7 Mars 2000   ERS SAR wind speed map
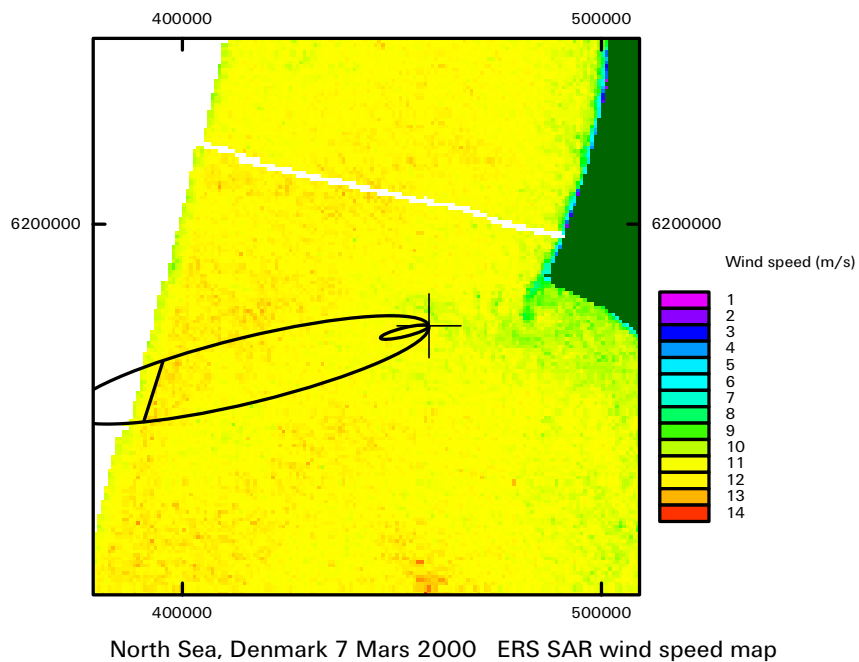
Figure 11-12 Mast position and the small and large footprints for10 m and 62 m heights, respectively. The large footprint is truncated due to lack of SAR data.

Results for simple footprints at 10 m

It was possible to area-average over the ellipse-shaped upwind area for 14 out of the16 cases for the 10 m level. In the last two cases the ellipses stretched into areas of no data. Therefore a box-area was drawn in the vicinity and used as a proxy. For the 62 m level ellipses could only be extracted in 5 cases and truncated ellipses or boxes had to be made for 11 cases. The wind speed data from the pixel that gives a maximum contribution according to Equation 57 and the mean, minimum, maximum and standard deviations of wind speed over the footprint areas for the SAR wind speed maps based on in-situ wind direction is listed in Table 11-10 and for SAR wind speed maps based on wind streaks in Table 11-11.

Table 11-10 SAR wind speed values at Horns Rev for the pixel with maximum contribution and mean, minimum, maximum and standard deviation of simple footprints for 10 and 62 m height. Values from ellipses are in bold font. Values from boxes are in normal font.

SAR wind speeds are derived from in-situ wind direction.

	Date	Height	Max.pixel	Footprint values (m/s) from in-situ data (no streak)			
		(m)	(m/s)	Mean	Min.	Max.	Std. dev.
1	19990520	10	**2.9**	**1.7**	**1.2**	**2.4**	**0.41**
		62	**1.9**	1.9	0.5	3.1	0.52
2	19990621	10	**9.7**	**9.0**	**6.8**	**11.2**	**0.85**
		62	**9.3**	8.6	6.7	10.6	0.57
3	19990710	10	**1.8**	**1.8**	**1.2**	**3.0**	**0.43**
		62	**2.0**	1.6	0.0	6.6	1.1
4	19990729	10	**5.1**	**5.2**	**4.0**	**6.6**	**0.56**
		62	**5.3**	5.2	4.0	6.6	0.56
5	19990810	10	**8.3**	**8.8**	**8.0**	**9.5**	**0.41**
		62	**9.1**	8.9	7.4	10.4	0.49
6	19990830	10	**6.8**	**6.3**	**4.3**	**8.0**	**1.1**
		62	**7.4**	6.3	4.8	7.9	0.63
7	19991003	10	None	**11.5**	**8.9**	**13.4**	**0.95**
		62	**8.5**	12.0	9.9	15.0	0.73
8	19991007	10	**9.0**	**9.4**	**8.9**	**10.2**	**0.34**
		62	**8.9**	10.3	8.5	12.3	0.58
9	19991019	10	**8.4**	**8.4**	**7.1**	**9.5**	**0.53**
		62	**8.5**	7.9	6.2	9.5	0.60
10	19991123	10	**0.2**	**0.5**	**0.1**	**0.9**	**0.21**
		62	**0.5**	1.5	0.0	3.9	1.34
11	19991216	10	**8.6**	**9.5**	**8.6**	**10.0**	**0.30**
		62	**9.4**	**10.8**	**8.3**	**12.7**	**0.71**
12	20000116	10	None	6.8	5.5	8.5	0.54
		62	None	7.0	5.2	9.4	0.67
13	20000201	10	**9.2**	**9.7**	**8.8**	**10.7**	**0.46**
		62	**9.8**	**10.3**	**8.7**	**11.8**	**0.46**
14	20000307	10	**10.6**	**11.4**	**10.5**	**11.9**	**0.35**
		62	**11.2**	11.6	10.0	13.1	0.45
15	20000326	10	None	2.0	0.7	4.6	0.82
		62	None	2.0	0.7	4.6	0.82
16	20000516	10	**0.3**	**0.4**	**0.0**	**1.0**	**0.27**
		62	**0.2**	**3.1**	**0.0**	**4.5**	**0.97**

Table 11-11 SAR wind speed values at Horns Rev for the pixel with maximum contribution and mean, minimum, maximum and standard deviation of simple footprints for 10 and 62 m height. Values from ellipses are in bold font. Values from boxes are in normal font.

<u>SAR wind speeds are derived from SAR streak wind direction.</u>

	Date	Height	Max. pixel	Footprint values (m/s) from SAR streak direction			
		m	(m/s)	Mean	Min.	Max.	Std.dev.
1	19990520	10	**3.1**	**1.8**	**1.3**	**2.5**	**0.33**
		62	**1.4**	2.0	0.5	3.3	0.54
2	19990621	10	**10.4**	**9.6**	**7.2**	**12.3**	**0.98**
		62	**9.3**	9.2	7.8	11.4	0.62
3	19990710	10	**1.9**	**1.8**	**1.3**	**3.0**	**0.40**
		62	**2.0**	2.3	0.8	4.6	0.80
4	19990729	10	**6.4**	**5.8**	**4.6**	**9.3**	**1.2**
		62	**5.0**	4.7	3.0	6.6	1.03
5	19990810	10	**8.3**	**8.8**	**7.6**	**9.5**	**0.45**
		62	**8.9**	8.8	7.5	10.4	0.52
6	19990830	10	**7.3**	**6.9**	**4.8**	**8.6**	**1.2**
		62	**8.0**	6.9	5.3	8.5	0.65
7	19991003	10	None	**9.2**	**7.6**	**10.8**	**0.83**
		62	**8.8**	12.3	6.8	16.4	1.44
8	19991007	10	**10.0**	**10.4**	**9.9**	**11.4**	**0.38**
		62	**8.9**	**12.1**	**9.5**	**14.8**	**0.91**
9	19991019	10	**10.6**	**9.9**	**8.4**	**11.2**	**0.67**
		62	**8.6**	9.3	7.4	11.2	0.72
10	19991123	10	**0.5**	**0.8**	**0.2**	**1.2**	**0.27**
		62	**0.5**	**1.9**	**0.0**	**4.8**	**1.64**
11	19991216	10	**8.6**	**9.5**	**8.6**	**10.0**	**0.30**
		62	**9.4**	**10.8**	**8.3**	**12.7**	**0.72**
12	20000116	10	None	8.5	7.0	10.6	0.62
		62	None	8.5	6.5	11.1	0.65
13	20000201	10	**9.2**	**9.8**	**8.9**	**10.8**	**0.48**
		62	**9.8**	**10.6**	**8.9**	**12.3**	**0.56**
14	20000307	10	**10.8**	**11.9**	**10.8**	**12.6**	**0.43**
		62	**11.7**	12.7	10.6	14.7	0.64
15	20000326	10	None	2.8	1.4	5.6	0.87
		62	None	2.8	1.4	5.6	0.87
16	20000516	10	**0.04**	**0.1**	**0.0**	**0.4**	**0.11**
		62	**0.2**	**2.0**	**0.0**	**3.2**	**0.73**

Graphical presentations of comparisons of in-situ wind speed and footprint mean values as well as the wind speed from the pixel that contribute the maximum to the total is given in Figure 11-16. It is clear that the in-situ observations in all cases are larger than SAR wind speeds. A linear regression quantifies the negative bias. The result is given in Figure 11-17. Some correspondence between in-situ and SAR wind speed is seen. Linear regression results show a correlation of R^2 of 0.81 for the footprint with a bias of -2.3 m s^{-1}. For the maximum contribution pixel R^2 is 0.83 and the bias is -2.4 m s^{-1}.

SAR wind speed maps are only assumed to be reliable for wind speeds >2 m s^{-1}. In two cases the SAR wind speeds are much below this value and on three occasions close to 2 m s^{-1}. The data has however not been omitted of the above analysis.

The SAR wind speed maps seem to show a mixture of atmospherically induced surface stress and ocean features probably related to tidal currents or bathymetry. For three cases ocean features are very distinct within the footprint. Therefore it was investigated to what extent box-average wind speeds in the vicinity of the ellipses differ from those within the ellipses. Based on box-averages from the three days (19990729 with a current (?), 19991003 with a rain cell (?) and 20000516 with current (?)) a new comparison was undertaken. The result of linear correlation gives y=1.0379x-1.7851 and R^2 of 0.88 and a standard error on the wind speed of 0.61 m s^{-1}. The bias is -1.78 m s^{-1}. The linear regression does not show any special tendencies for low, medium or high wind speeds ({Hasager, Furevik, et al. 2001 116 /id}.

The wind direction derived from SAR streaks was different from the in-situ observations in all 16 cases. This means that wind speed maps calculated from in-situ data and from SAR streaks differ. This is clear from a simple comparison of the values in Table 11-10 and Table 11-11. The wind speeds calculated based on SAR streak wind direction generally are higher and so are the standard deviations.

Based on the SAR wind speed maps where the wind direction input is from SAR wind streak analysis (instead of in-situ wind direction observations), a similar set of results based on simple footprint ellipses are obtained and compared to in-situ data. In Figure 11-16 SAR wind speed from footprints and maximum contribution pixels are shown. Again the data seem to correspond well, however with the difference that for a few cases the SAR wind speeds are larger than the in-situ data. This was never the case in Figure 11-13.
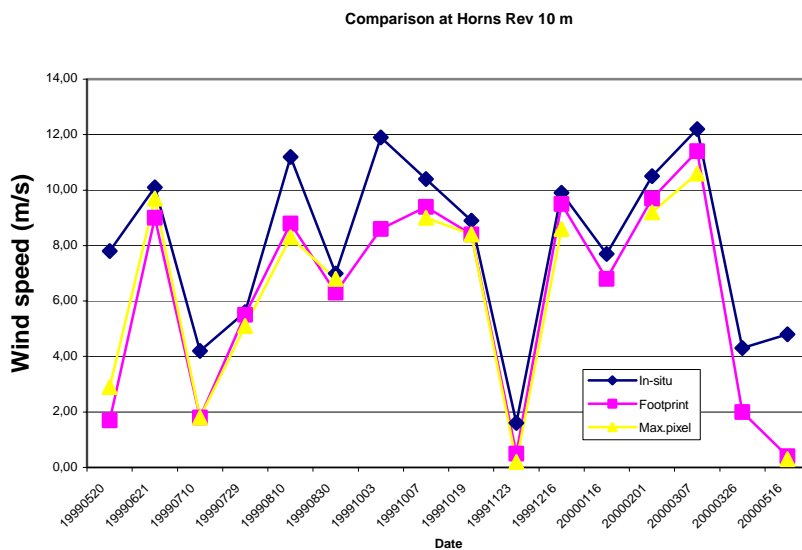
Figure 11-13 Comparison of wind speed from SAR (in-situ wind dir.) footprint, maximum contribution pixel and in-situ data for Horns Rev.

Horns Rev linear regression 10 m
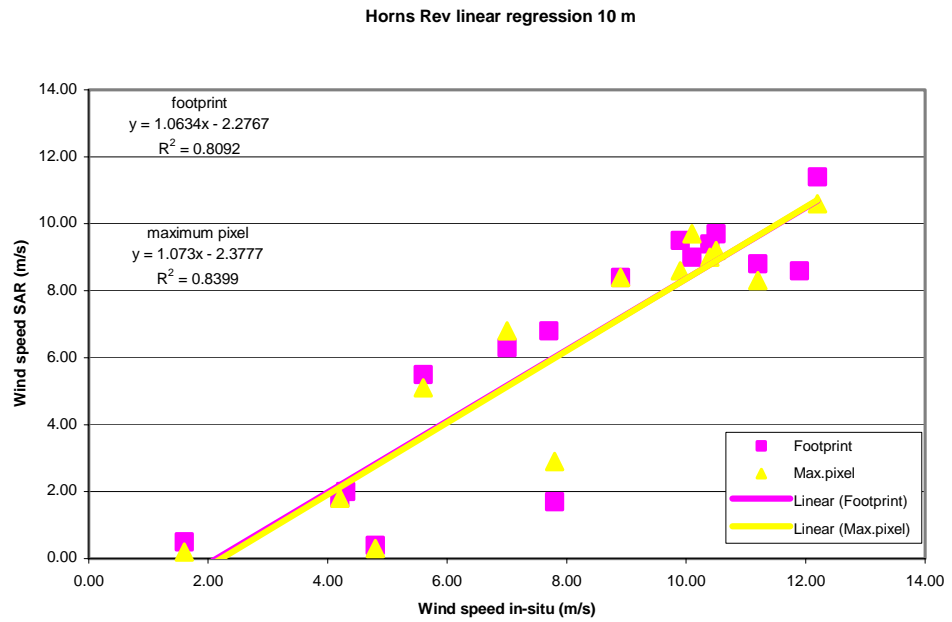
Figure 11-14 Linear correlation between in-situ wind speed and SAR wind speed simple footprints and maximum contribution pixel for Horns Rev.
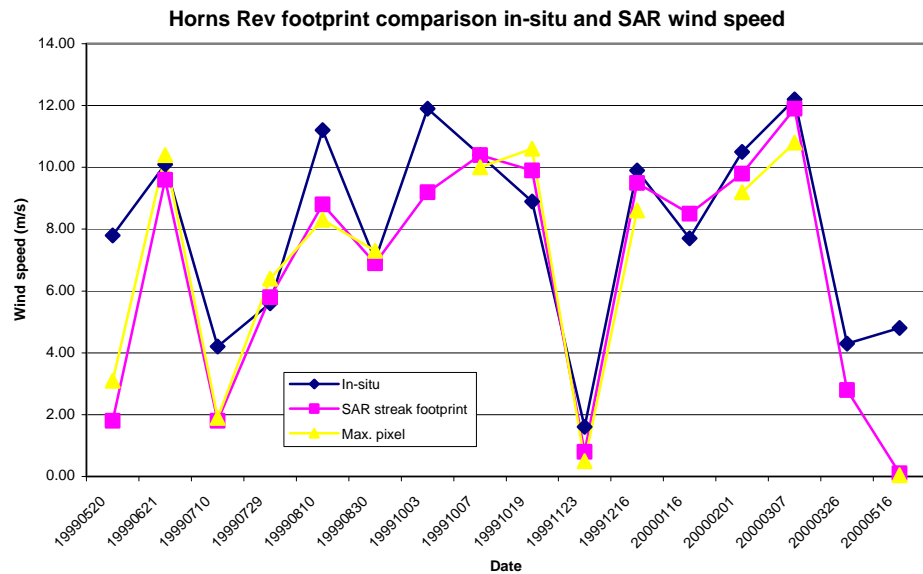
Figure 11-15 Comparison of wind speed from SAR (wind dir. from streak) footprint, maximum contribution pixel and in-situ data for Horns Rev.

The linear correlation between in-situ and SAR wind footprints data is $y = 1.1016 \text{ x} -2.1263$ with $R^2 = 0.7678$. For the in-situ and maximum pixel contribution the linear correlation is $y = 1.0851 \text{ x} -1.9947$ with $R^2 = 0.7578$. As mentioned above three cases have strong currents/rain cells that may give noise to the footprint. So substituting these with box-averages as before, the linear correlation results in $y = 1.092 \text{ x} -1.7879$ with $R^2 = 0.8121$. Hence the bias is the

same for the SAR wind speed maps based on in-situ and streak wind direction, however the root mean square error is unexpectedly lower for the latter.

It seems important to consider local ocean current/rain cell phenomena. In both cases the bias was reduced slightly and the R^2 was increased. The wind speed in the pixel with a maximum contribution is correlated reasonably well to the in-situ data. It is however less accurate than taking a mean value of the footprint.

Further it has been tested how the cases of wind speeds <2 m s^{-1} affect the correlations. These data were left out and new correlations were calculated. For footprints on SAR with "no streak" R^2 decreased to 0.8146 (from 0.8824), with "streak" R^2 increased to 0.7965 (from 0.7678) and for maximum contribution pixel with "streak" R^2 decreased to 0.4194 (from 0.7578).

The SAR wind speed maps based on in-situ wind direction have a higher correlation to in-situ wind speeds than does the SAR wind speed maps based on streaks. This may indicate that the wind direction from the mast better describes the true winds than does the wind streaks (in the vicinity of the mast). This was also found in an early study of {Vachon & Dobson 1996 125 /id} where the in-situ wind speed and wind directions were measured at a ship and compared to ERS-1 SAR wind speeds derived both from in-situ wind direction and from SAR streak directions inserted into the CMOD-4 model.

In-situ wind directions and SAR streak directions is very similar, see Figure 11-16. The differences in direction and the retrieved wind speed differences are shown in Figure 11-17. No clear pattern is seen which is supported also by a scatter plot of the differences between wind directions and wind speeds in Figure 11-18. From the linear correlation in the scatter plot it is found that the wind speeds are calculated to be 0.27 m s^{-1} higher on average by CMODIFR2 with wind streak direction instead of in-situ wind direction.

This positive bias is a step forward in eliminating the systematic error of around 2 m s^{-1} according to the previous results. The influence of errors in wind direction related to the retrieval of wind speed is described in section 3.5. It is a function of crosswind, upwind and downwind direction compared to the wind speed level. So in principle the SAR wind speed maps could be evaluated case by case with a direct estimate of the associated uncertainty due to wind direction variations but this has not been done (yet).

The linear correlation between in-situ wind direction and SAR streaks was found to be $y = 1.1113x - 31.576$ with $R^2 = 0.9487$ so the correlation is high, yet with a bias of 31º {Hasager, Jensen, et al. 2002 128 /id}.

Horns Rev wind direction
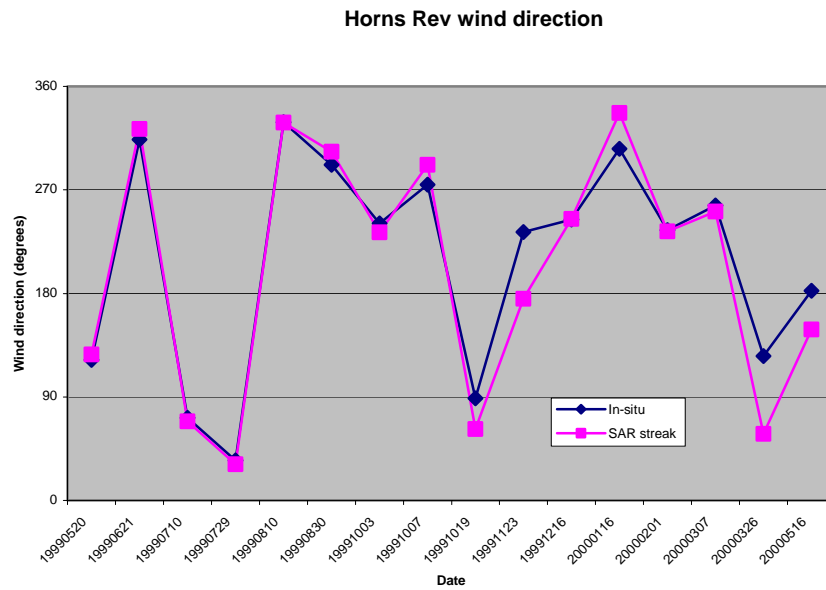
Figure 11-16 Wind direction comparison between in-situ and SAR streak for Horns Rev.

Horns Rev wind speed and direction
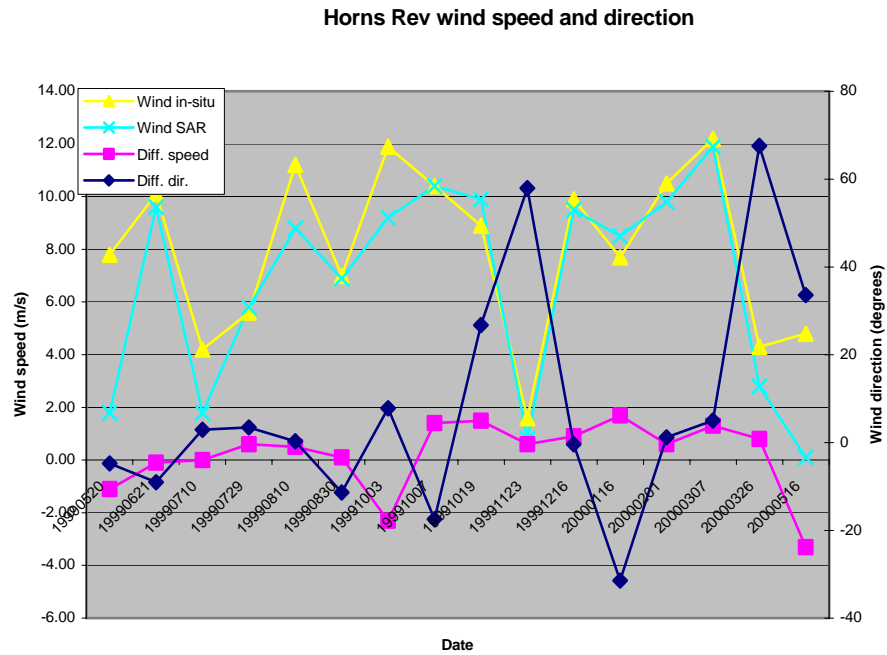
Figure 11-17 Comparison wind speed and wind direction for Horns Rev
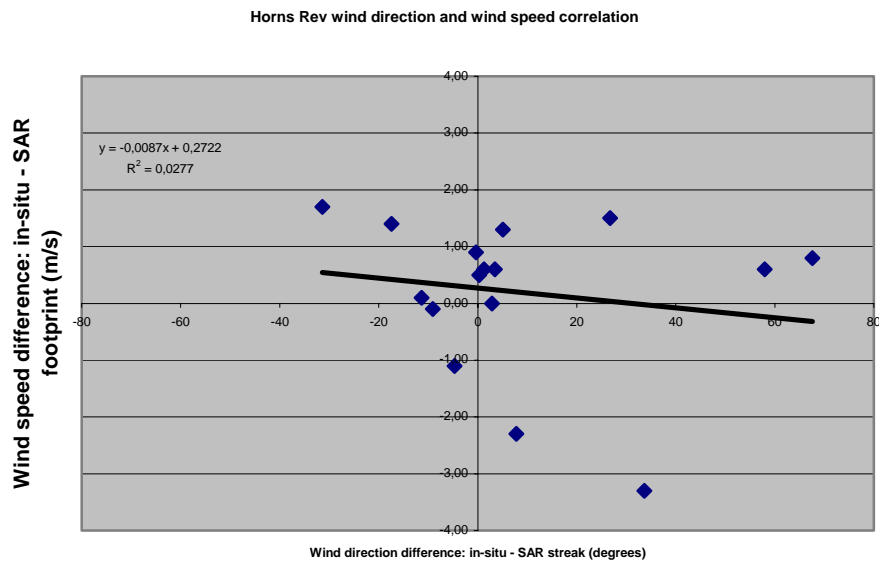
Figure 11-18 Comparison wind speed difference and SAR wind speed difference at Horns Rev.

Results for advanced footprints at 10 m

A more detailed approach than the simple footprints described above has also been investigated. The footprints of {Gash 1986 39 /id}, {Hsieh, Katul, et al. 2000 107 /id} and {Horst & Weil 1994 106 /id} were programmed by Dr. Morten Nielsen with the inclusion of static stability effects to the footprints. Please refer to Chapter 9. The different methods were tested and in the following the results found from the footprint based on {Gash 1986 39 /id} is described in detail. In Table 11-12 is listed the number of pixels that are within the footprint and the percentage area this includes of the total footprint and the wind speed herein. Further is the percent of the maximum pixel and the wind speed listed. The SAR wind speeds are calculated based on SAR wind streak directions.

Table 11-12 SAR wind speed values at Horns Rev for the footprint according to Gash corrected for stability with the % of influence within the SAR scene and the number of pixels contributing. For the maximum influence pixel the percentage and wind speed is listed.

Case	Date	pixels (number)	footprint (%)	footprint U (m s^{-1})	max. pixel (%)	max. pixel U (m s^{-1})
1	20051999	85	63	1.8	10	2.2
2	21061999	123	68	9.8	19	9.3
3	10071999	243	85	1.9	66	1.6
4	29071999	76	78	5.0	46	6.2
5	10081999	194	73	9.3	14	8.1
6	30081999	40	56	7.8	20	8.0
7	03101999	1391	95	4.6	24	8.9
8	07101999	1319	89	10.2	25	9.9
9	19101999	326	80	10.4	14	9.7
10	23111999				75	0.1
11	16121999	1181	91	7.5	46	8.6
12	16012000				57	
13	01022000	934	86	9.4	57	9.2
14	07032000	640	91	10.2	46	11.3
15	26032000				14	
16	16052000	925	83	0.1	69	0.0

First of all the wind speed from the footprints are compared to in-situ data. This is shown in Figure 11-19 and the linear correlation between the footprints and in-situ data is shown in Figure 11-20. The R^2 is only 0.50 and there is a bias of 1.76 m s^{-1}. Omitting one data point where SAR in near zero gives the following linear correlation $y = 0.7913x + 0.0888$ with $R^2 = 0.3859$. The results are not as good as for the simple footprints. Regarding the pixel with the maximal contribution to the flux, the linear correlation between SAR and in-situ is $y = 1.0486x - 2.0423$ with $R^2 = 0.7439$ but again if we omit one data point (with SAR wind speed near zero) the correlation is $y = 0.9168x - 0.6308$ with $R^2 = 0.5919$ is lees good
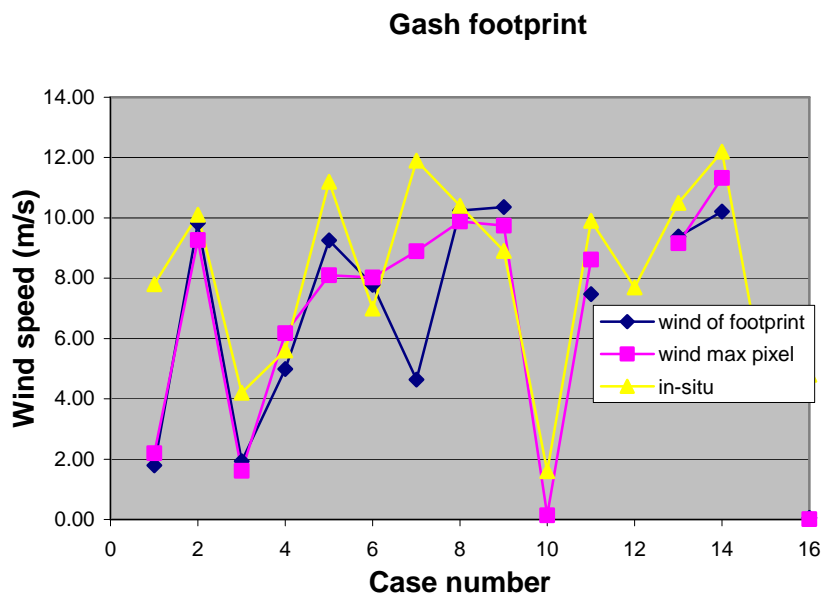
Gash footprint

Figure 11-19 Gash footprint wind speed from SAR (wind dir. streak), the maximum contribution pixel wind speed and in-situ data.

Linear correlation

$$y = 0.9681x - 1.7626$$
$$R^2 = 0.5041$$
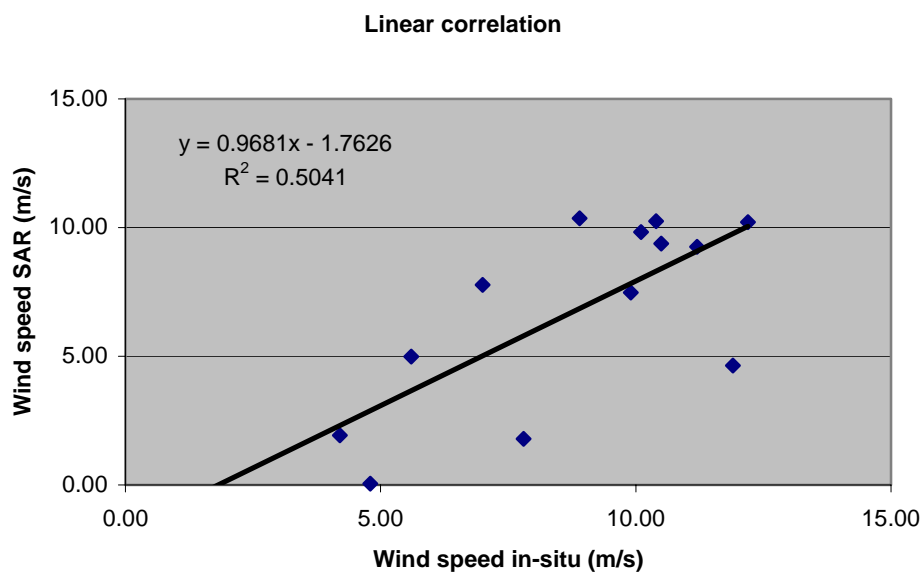
Figure 11-20 Linear correlation between SAR wind speed from Gash footprints and in-situ data. SAR wind based on SAR wind direction. from streaks.

On average 80% of the footprint was within the SAR scenes. The maximum pixel contribution on average was 38% but with very large variations, see Figure 11-21. The large differences are due to especially variable static stability.

Footprint percentage
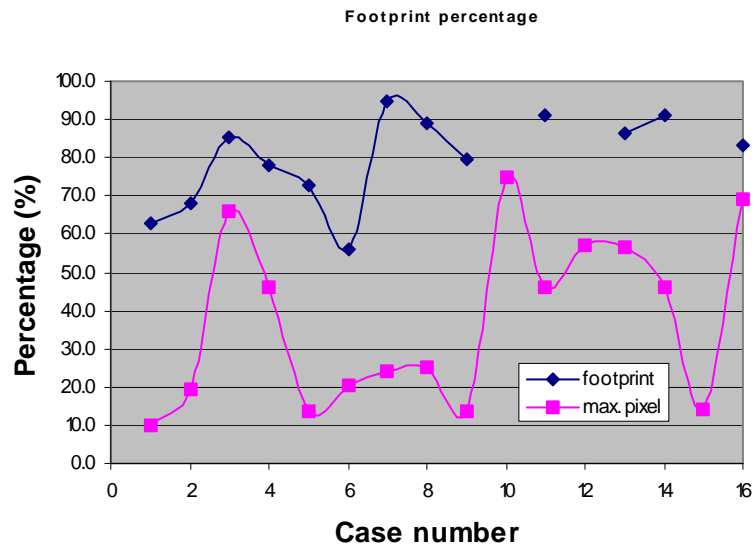
Figure 11-21 Percentage explanation by the footprint within the SAR scenes and the pixel contributing the most to the observed wind.

From a physical point of view the more advanced footprints are more exact than the simple footprints (simple ellipses), hence the linear correlation between SAR wind speeds and in-situ observations was expected to be better than with the simple footprint method. This is however not the case.

The explanation is believed to origin from the SAR data rather than from the method of comparison. In SAR data there may be noise from speckle, ocean currents and atmospheric damping. For reducing the speckle noise the chosen resolution of the SAR grid cells may not be adequate. It is remarkable that in the cases of simple footprints where all pixels get equal weight the linear correlations are much improved compared to the advanced footprints. In the latter one single pixel gets a very heavy weight (of up to 75% in the cases investigated). Therefore even minor errors in SAR wind speeds may introduce a significant error to the footprint averages. Please see Table 11-12 on how many pixels were in each of the advanced footprints and how much weight one pixel was given maximum.

Speckle noise and the ideal resolution of SAR wind speed maps have not been investigated further. In section 3.5 an estimate of error in SAR wind speed maps is given. An idea may be to filter high-resolution wind speed maps prior to calculating the footprint averages.

Noise from ocean currents, shallow water and atmospheric damping is briefly described the section 3.6.

Results for simple footprints at 62 m

Footprint results for larger ellipses relevant for comparing to the 62 m level in-situ wind speed data are listed in Table 11-11 and Table 11-12 and graphed in Figure 11-22. It is clear from the results that the SAR wind speeds are always lower than the in-situ data. The linear correlation between in-situ data and SAR

94   Risø-R-1298(EN)

wind speeds is shown in Figure 11-24. The R^2 values are around 0.8 with a bias of -2.2 m s^{-1}. It is however only in 5 of the 16 cases that a large footprint could really be extracted (see Table 11-11 and Table 11-12). In most of the cases a box-area or a smaller (truncated) part of the ellipse was used. The reason for the relatively high correlation could be that when many pixels are averaged, the noise in the SAR data is reduced. The negative bias is similar to the comparisons at 10 m. The classic method of extrapolation of wind speeds from 10 m to hub-height is analysed and discussed in Chapter 8. That method may still be superior to footprint area-averaging for levels above 10 m because the SAR wind speed maps are valid for the 10 m.

The pixel in the footprint that theoretically is contributing the most to the footprint is placed on average at a downwind distance of 2450 m. The wind speed in these pixels are listed in Table 11-11 and Table 11-12 and graphed in Figure 11-24. Again the SAR wind speeds are always lower than the in-situ observations. The linear correlations for SAR wind speeds based on in-situ wind direction is $y = 0.8744x - 2.5599$ with $R^2 = 0.6545$ and for SAR wind speed based on SAR streak wind direction $y = 0.8823x - 2.6394$ with $R^2 = 0.6365$. The results are practically identical. The bias is larger and the R^2 is lower than for the footprints. Again it is concluded that a footprint average is a better estimate of the in-situ wind than a single (maximum) pixel SAR wind speed value.

All the linear correlation results are listed in Table 11-13. All results show a negative bias on the SAR wind speed maps.

Table 11-13 Summary of linear correlation results between in-situ observations and SAR wind speed maps for 10 m and 62 m, and linear correlation on wind directions from in-situ and SAR streaks.

m	Condition	Equation	R^2
10	In-situ dir., simple footprint	y=1.06x-2.28	0.81
	In-situ dir., simple footprint, avoid ocean feature 3 times	y=1.04x-1.79	0.88
	In-situ dir., maximum pixel	y=1.07s-2.38	0.84
	Streak, simple footprint	y=1.10x-2.13	0.77
	Streak, simple footprint, avoid ocean feature 3 times	y=1.09x-1.79	0.81
	Streak, maximum pixel	y=1.09-2.00	0.76
62	In-situ dir., simple footprint	y=0.88x-2.22	0.81
	In-situ dir., maximum pixel	y=0.87x-2.56	0.65
	Streak, simple footprint	y=0.93x-2.29	0.77
	Streak, maximum pixel	y=0.88x-2.64	0.64
	Streak, advanced footprint	y=0.97x-1.76	0.50
	Streak, advanced footprint, maximum pixel	y=1.05x-2.04	0,74
Dir.	Wind dir. & SAR streak dir.	y=1.11x-31.57	0.95

Comparing in-situ and SAR wind speed for 62 m level
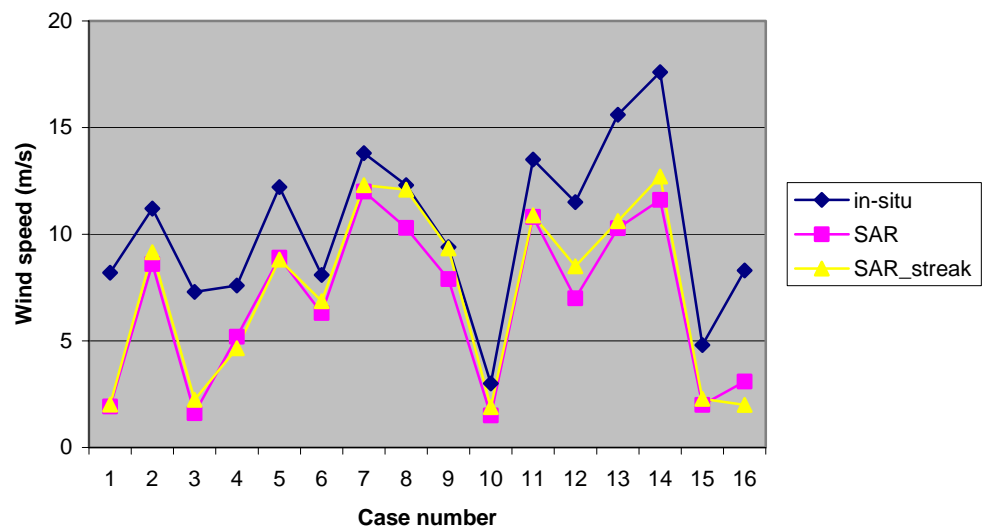
Figure 11-22 Comparing in-situ wind speed at 62 m to footprint averages from SAR wind speed calculated from in-situ wind direction and from SAR streak wind direction at Horns Rev, Denmark.

Linear correlation
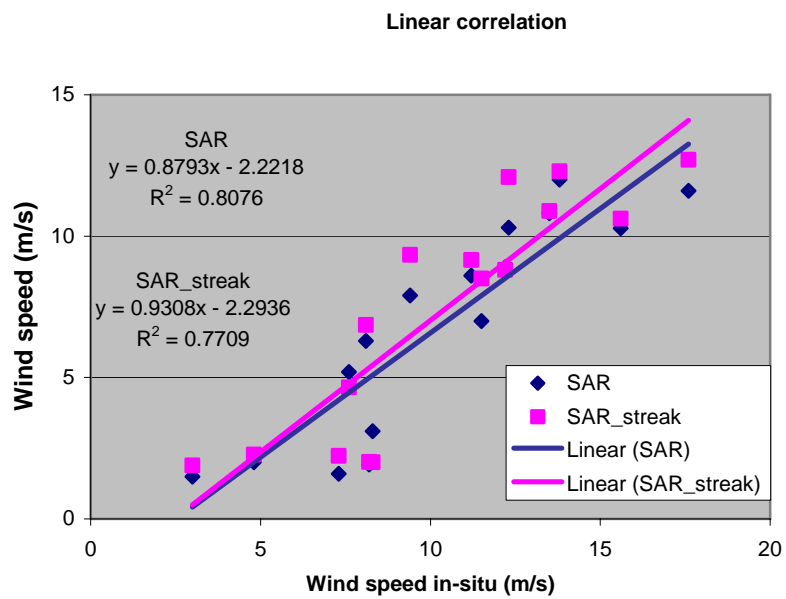
Figure 11-23 Linear correlation between in-situ data at 62 m level and SAR wind speed from large simple footprints.

Maximum pixel for 62 m heigth
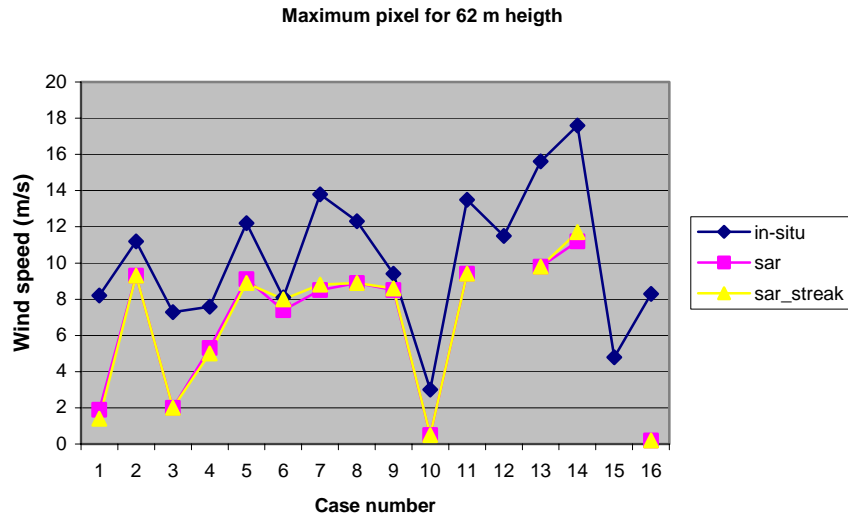
Figure 11-24 Wind speed from in-situ mast observations and simple footprints from SAR wind speed maps based on in-situ wind direction and SAR wind streak direction.

11.10 Comparison of SAR scenes to LINCOM and KAMM2 results

The LINCOM model has been run for all 16 cases for Horns Rev based on the in-situ wind speed observations from the mast. Therefore the wind speed at the mast position per definition is identical to the in-situ observation.

The KAMM2 mesoscale model has been run for five cases out of 16. The five cases are carefully selected such that the NCAR/NCEP reanalysis data compares well to the in-situ observations and avoid unstationary (frontal) flow.

The LINCOM and KAMM2 wind speed model results and SAR wind speed maps are graphed in figures in Appendix II. The SAR wind speed observations and the model results are compared from horizontal transects upwind of the mast. The mast is position at distance zero (0) and the upwind distance vary from 4 to 20 km dependent upon the availability of SAR observations in each case.

The description of results is grouped into offshore, alongshore and onshore flow.

For offshore flow under highly stable conditions (20-5-1999) and stable conditions (10-7-1999) the LINCOM model results are significantly larger than the SAR wind speed observations, see Figure 11-25. This may be a result of an internal marine boundary layer that is decoupled from the near-surface layer, hence the capillary waves do not reflect the wind speed at higher levels.

For offshore flow under unstable conditions (19-10-1999) there is a very good correlation between SAR observations and LINCOM and KAMM2 model results, Figure 11-25. The wind speed increases offshore. SAR wind speeds are calculated both from in-situ wind direction and from SAR streaks. For the unstable case the latter gives the highest wind speeds.

For alongshore flow from the North under neutral (29-7-1999) and unstable (10-8-1999) conditions the LINCOM model results are slightly larger than the SAR observations, see Figure 11-26. In the unstable case the SAR wind speed is constant. For the neutral case a significant variation exists. That may be related to the sea bottom topography or ocean currents. For alongshore flow from the South (16-5-2000) it also appears that the bottom topography influence the SAR wind speed under neutral conditions, see Figure 11-26, and again the LINCOM model results are larger than the SAR wind speed. The KAMM2 results (29-7-99) seems too low compared to the SAR wind speeds.

Onshore flow under near-neutral conditions is mapped by SAR in five cases, i.e. for one of these cases the stability is unknown (16-12-1999) but the data has much similarity to a neutral case (3-10-1999). Figure 11-27 and Figure 11-28 show that the LINCOM wind speed is close to the SAR wind speeds far offshore but significantly larger near the mast for three cases. The relatively low SAR wind speeds may be due either to decreased winds or an influence from the sea bottom topography. For two cases the LINCOM results are larger than SAR wind speeds. The KAMM2 model captures the SAR winds speeds well for two cases (1-2-00 and 3-10-99) but seems too low on the 7-10-99.
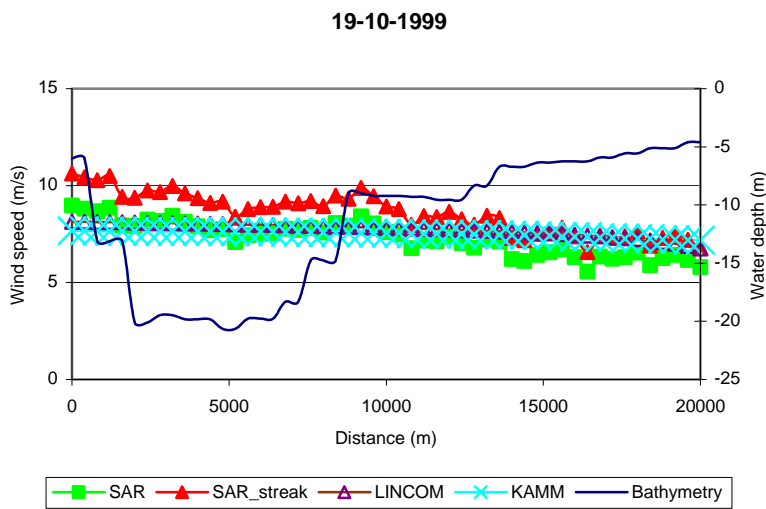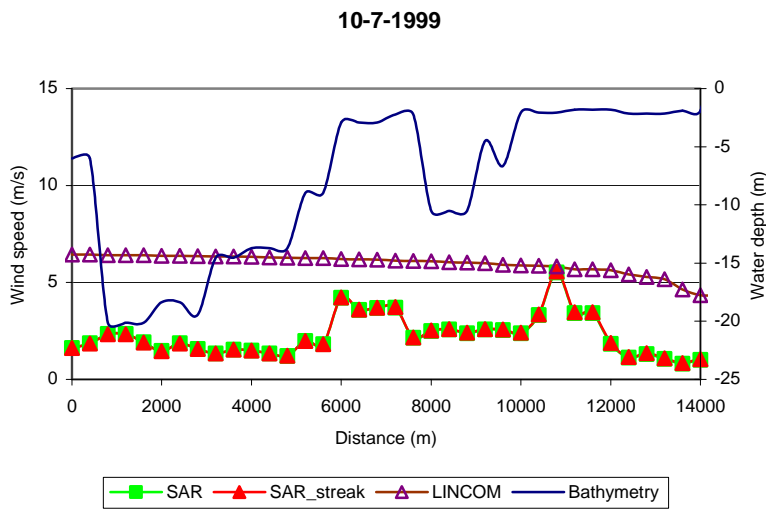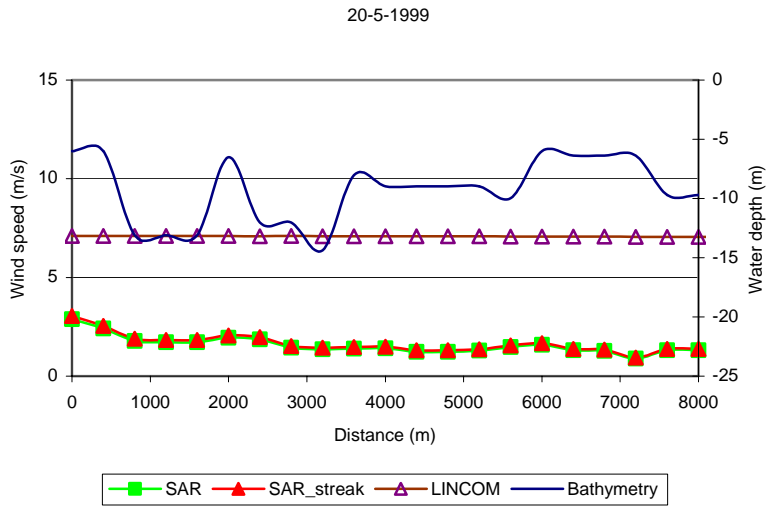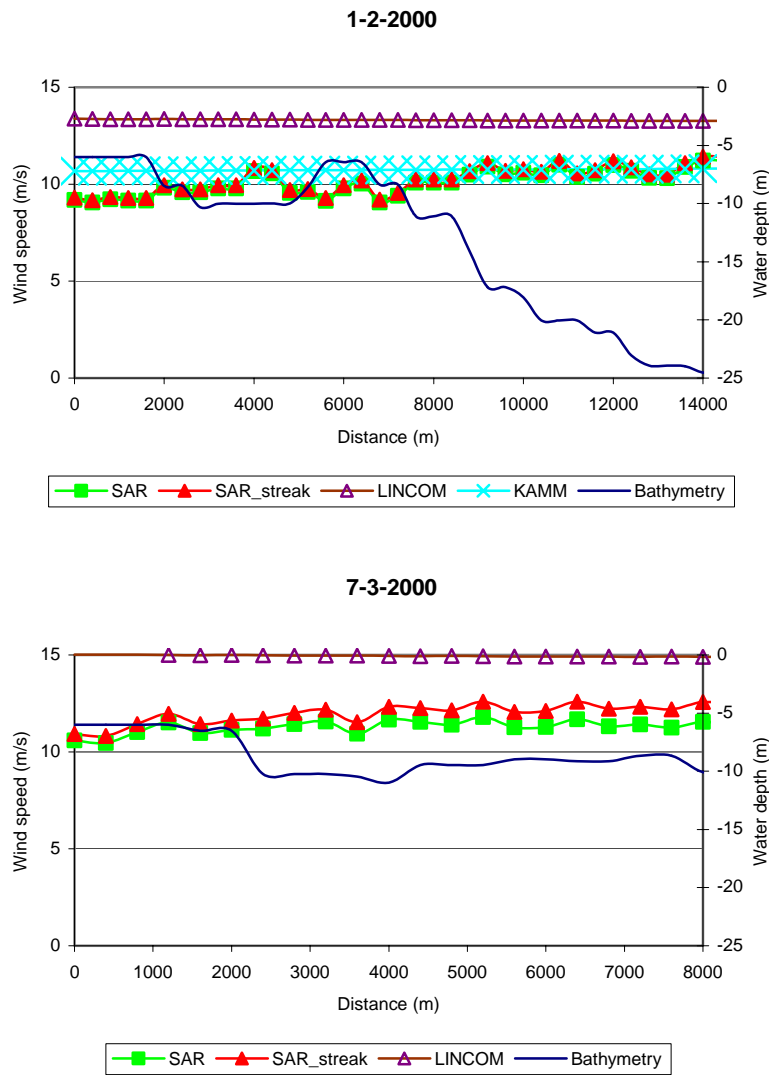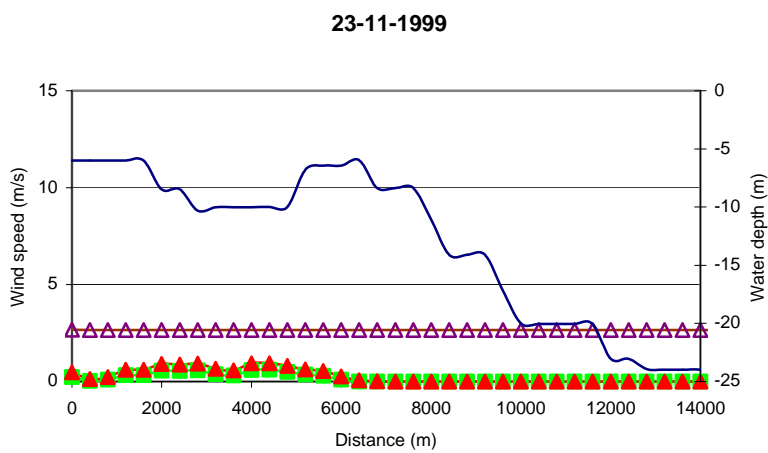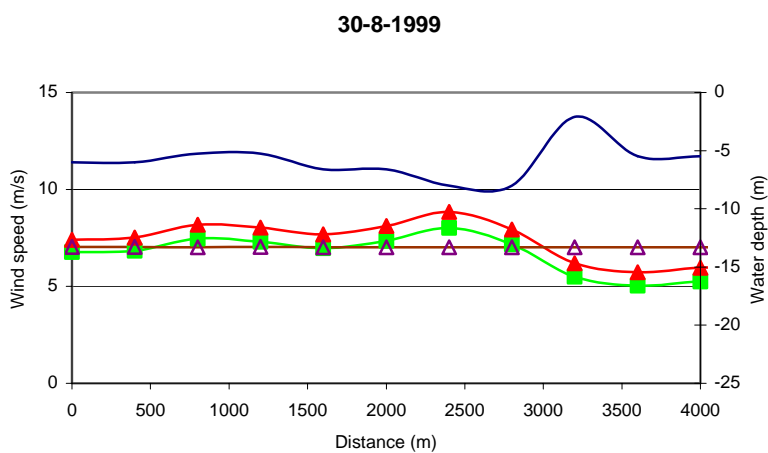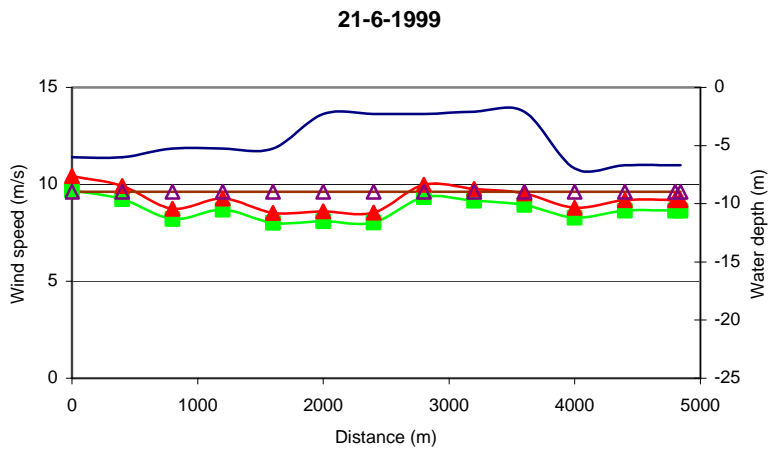
*Figure 11-25 Comparison of SAR, LINCOM and KAMM2 wind speeds upwind of the mast positioned at distance 0. **Offshore** flow under a) very stable conditions 20-5-1999, b) stable conditions 10-7-1999 and c) unstable conditions 19-10-1999.*

29-7-1999
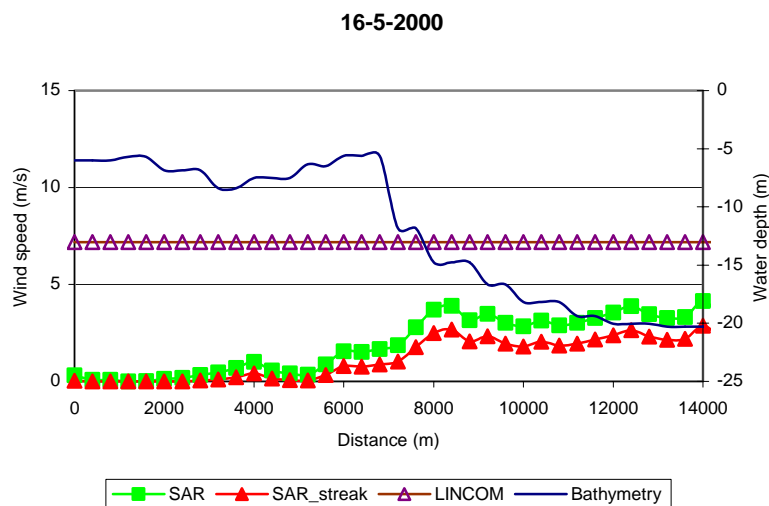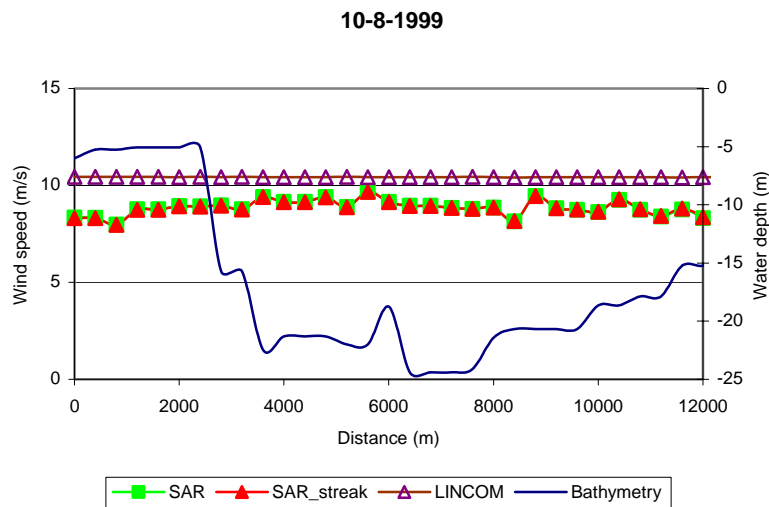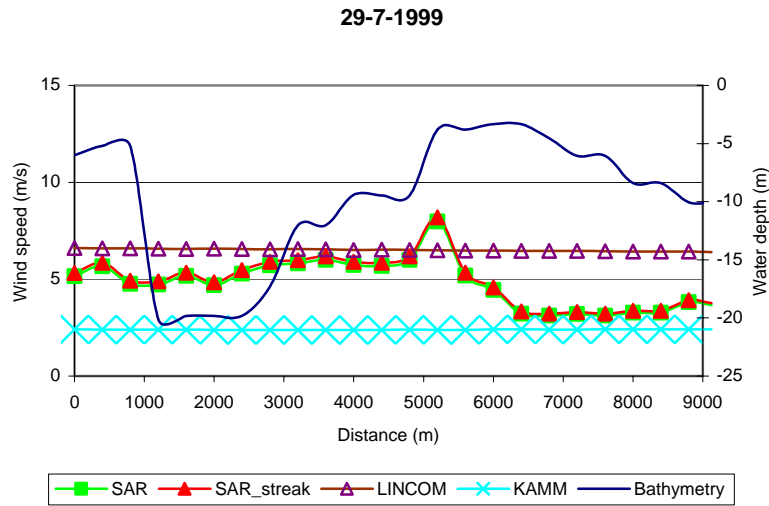
10-8-1999

16-5-2000

*Figure 11-26 Comparison of SAR and LINCOM wind speeds upwind of the mast positioned at distance 0. **Alongshore** flow from North under a) neutral conditions 29-7-1999, b) unstable conditions 10-8-1999 and from South under c) neutral conditions 16-5-2000.*

3-10-1999
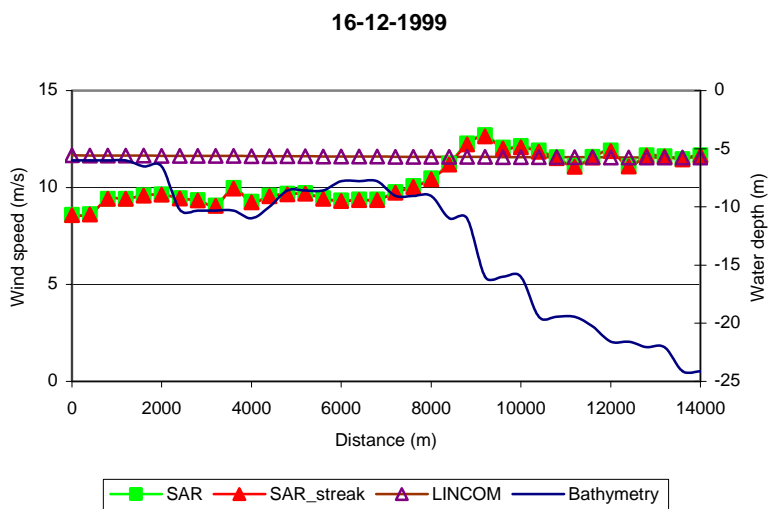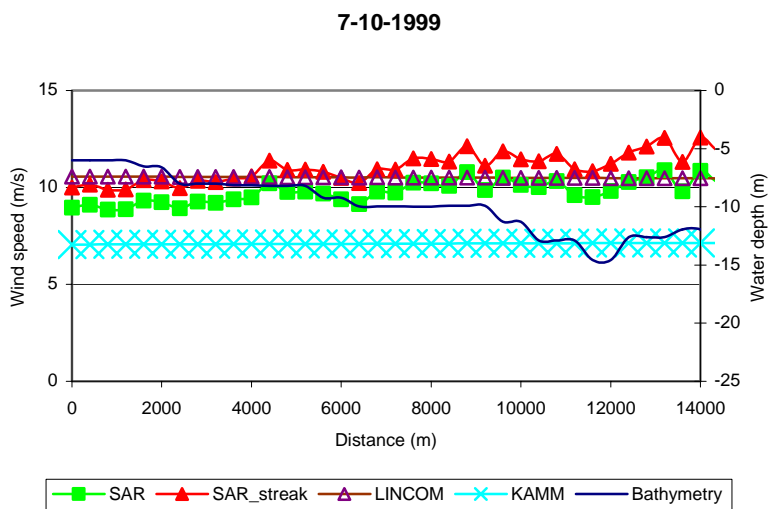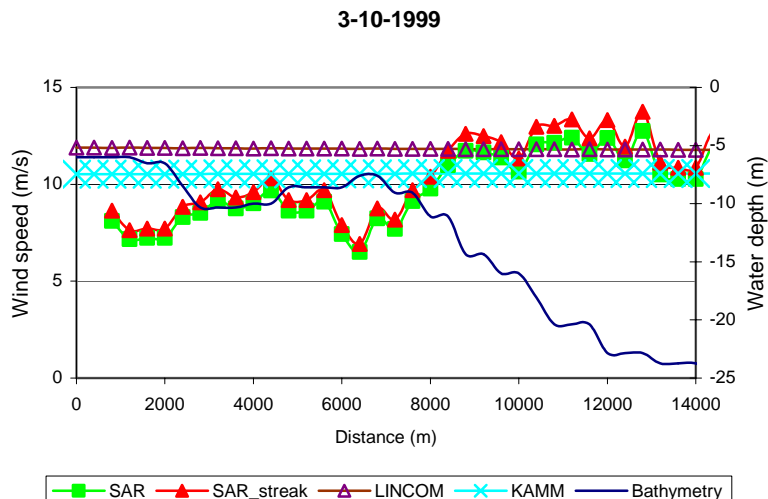
7-10-1999

16-12-1999

Figure 11-27 Comparison of SAR, LINCOM and KAMM2 wind speeds upwind of the mast positioned at distance 0. **Onshore** *flow under neutral conditions a) 3-10-1999, b) 7-10-1999 and c) 16-12-1999.*

1-2-2000

7-3-2000

*Figure 11-28 Comparison of SAR, LINCOM and KAMM2 wind speeds upwind of the mast positioned at distance 0. **Onshore** flow under neutral conditions a) 1-2-2000 and b) 7-3-2000.*

The horizontal transects showing onshore flow under unstable conditions are shown in Figure 11-29. The SAR and LINCOM wind speeds agree very well on the 21-6-1999 and 30-8-1999 For one case (23-11-1999) the SAR wind speed is very low, actually below the 2 m s^{-1} for which SAR is useful.

21-6-1999

30-8-1999

23-11-1999

*Figure 11-29 Comparison of SAR, LINCOM and KAMM2 wind speeds upwind of the mast positioned at distance 0. **Onshore** flow under unstable conditions a) 21-6-1999, b) 30-8-1999 and c) 23-11-1999.*

The best agreement between SAR and KAMM2 wind speeds is found for an offshore, neutral case (19-10-1999). The wind speed increases from the shore towards the mast. For the alongshore cases (29-7-1999 and 7-10-1999) the KAMM2 results are lower than SAR and LINCOM, especially so for the neutral case (29-7-1999). In the onshore cases (3-10-1999 and 1-2-2000) the KAMM2 results agree very well to the SAR observations far offshore but at the mast the SAR wind speed is lower than the KAMM2 (and LINCOM) results. The SAR wind speed drops gradually from the open sea to the coastal area. This effect may be related to the sea bottom topography or to the deceleration of the air mass prior to landfall.

Investigation in more detail on the possible effect of the sea bottom bathymetry on wind speeds is undertaken. The position of the mast is on a shallow reef, see Figure 11-30. The mast is located at a depth of –6.1 m at DNN (Danish Normal Zero). A significant tide may change the actual depth. Two horizontal transects 60 km long, one from North to South (Figure 11-31) and one from West to East (Figure 11-32 and Figure 11-35), are graphed with bathymetry and SAR wind speeds.
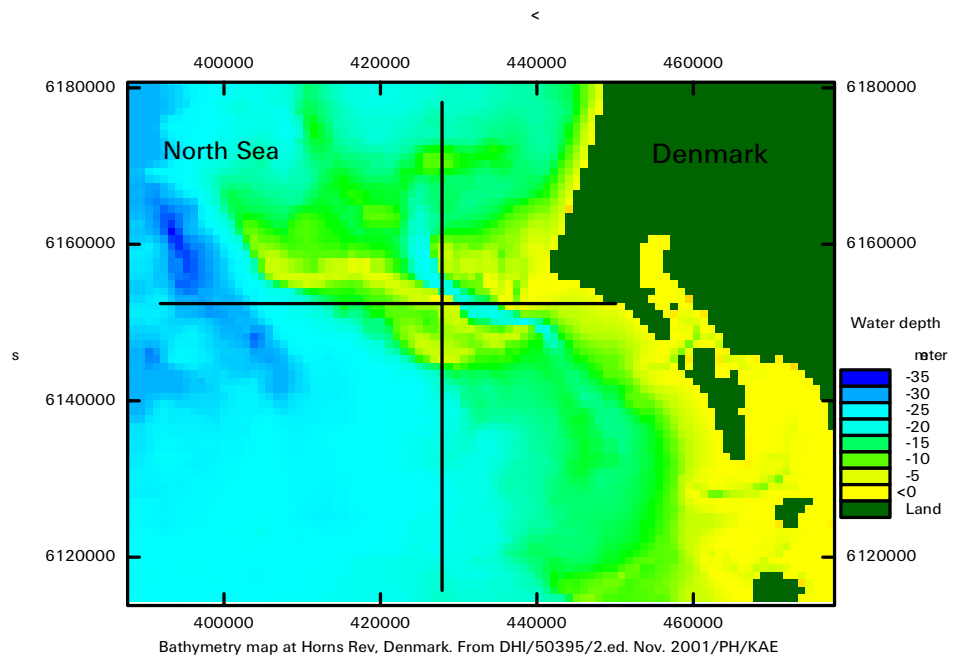
Figure 11-30 Bathymetry at Horns Rev. The lines indicate two horizontal transects and their crossing is at the position of the meteorological mast.
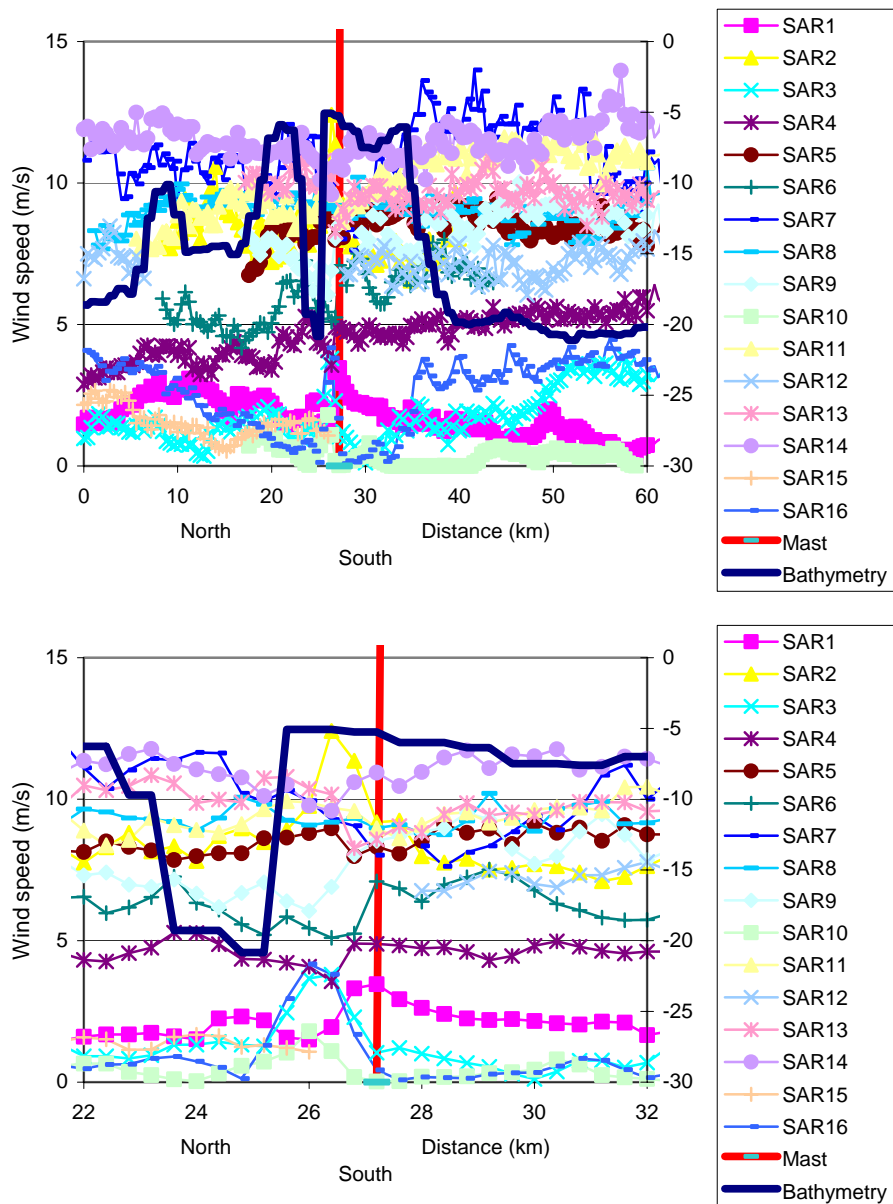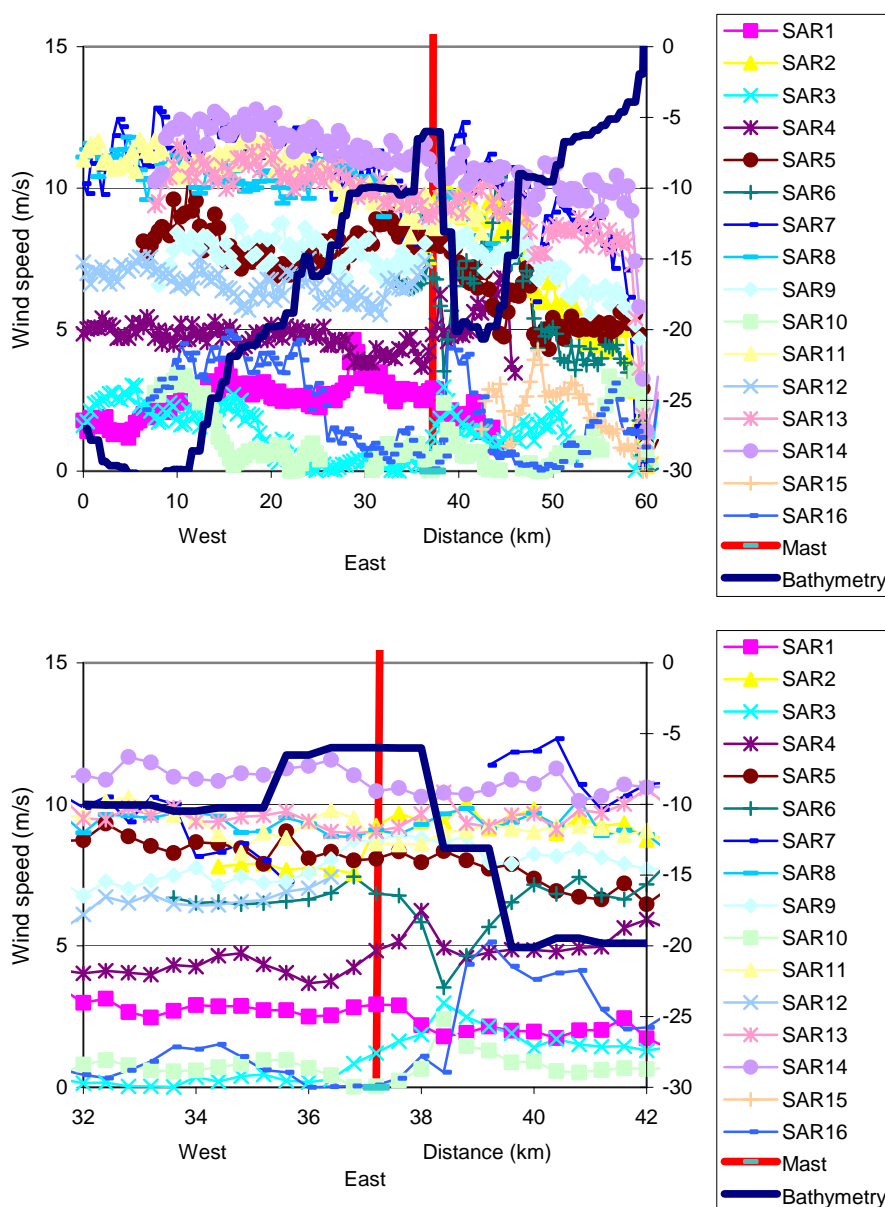
Figure 11-31 Longitudinal horizontal transect of the SAR wind speeds and the water depth at Horns Rev. The location of the mast is indicated.a) is the full 60 km transect and b) a 10 km subset of the transect centered at the mast. For SAR case numbers please refer to Table 11-2.

It is seen in the North-South transect (Figure 11-31) that a –20 m deep trough is right in front of the mast. There are too many SAR wind speed curves that a clear picture is visible. However from the subset 10 km transect near the mast it stands out that the SAR wind speeds are increased 2 km upstream for three cases of low winds (cases 10, 16, 12) and one of high wind (case 2). For medium wind speeds the increase is seen right at the location of the mast (cases 1, 4, 6, 9).

The latitudinal transect from West-East (Figure 11-32) shows the sea bottom to increase gradually from –30 m to –6 m. The mast is position right at the top. Behind the reef a –20 m deep trough is seen. The overall picture of the many SAR wind speed curves is a gradual decrease in wind speed from the coast to

the shore. In the 10 km subset it is seen that a sudden increase in wind speed east of reef appears for case 16, 10, 12 and 4, all cases with relatively low wind speeds. On contrary, for case 6 a sudden drop in wind speed is seen.

Figure 11-32 Latitudinal horizontal transect of the SAR wind speeds and the water depth at Horns Rev. The location of the mast is indicated.a) is the full 60 km transect and b) a 10 km subset of the transect. For SAR case numbers please refer to Table 11-2.

The sea current flows in the longitudinal direction mainly, see Table 11-6. The classic situation of SAR intensity response to a reef is shown in Figure 3-2. An in-depth analysis on bottom topography and SAR wind speed is not carried out within the project. It may however be concluded that especially at low wind speeds the effect of bottom topography is apparent. Hence in an area such as Horns Rev with a complex sea bottom topography and with a significant tide, it may be useful to investigate the relations between wind, waves, sea current, tide and stability in more detail. It is beyond the scope of the current project.

One example of sea bottom variations compared to SAR wind speed is given for case 8 (3-10-99). This is a case of onshore flow with strong wind under neutral conditions. Four long profiles have been selected for display. The location of the horizontal transects is given in Figure 11-33. Three of these transects are parallel to the wind direction and one is a North-South transect. The results are that the SAR wind speed drops significantly at the coast in all profiles and that the Horns Rev reef seems to influence the SAR wind speed significantly (see profile 1 and 4), whereas profile 2 and 3 are very similar. Profiles 2 and 3 may map only the influence of the wind and not that of the sea bottom topography. Profile 2 cuts over a shallow region (near the 15 km location) but this does not seem to affect the SAR wind speed. The tide was high (+82 cm).

SAR wind speed map from ERS-2. 3-10-1999 Horns Rev, Denmark
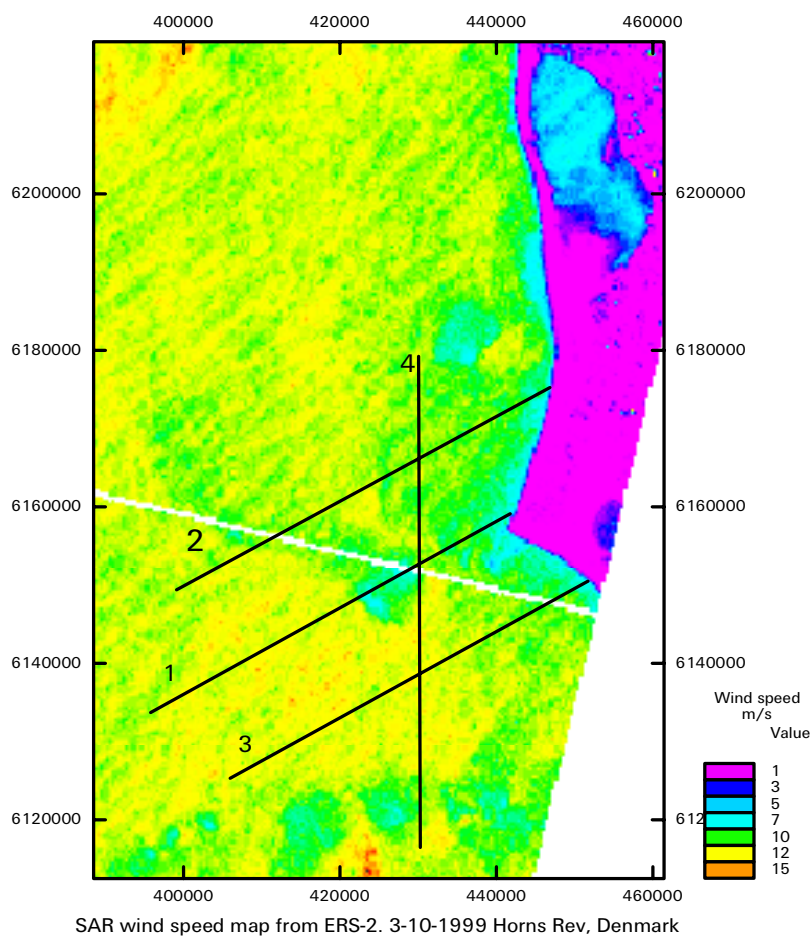
Figure 11-33 Position of four horizontal transects. The mast is position where profile 1 and 4 intersects.
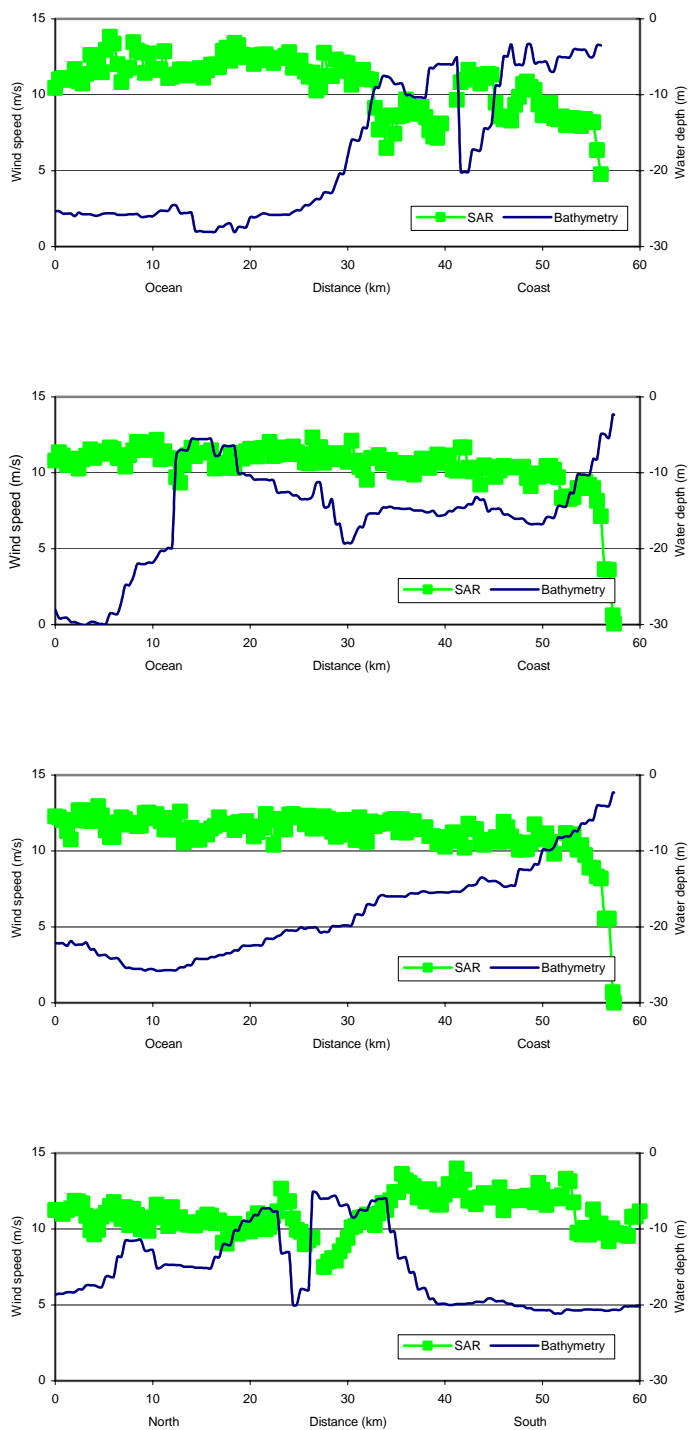
Figure 11-34 Horizontal transects for 3-10-1999 for bathymetry and SAR wind speed aligned with the wind direction for a) profile 1, b) profile 2, c) profile 3 and d) North-South profile.

The influence of the coastal zone to the SAR wind speed observations has been investigated in more detail and is described in the following. The latitudinal transect (Figure 11-32) goes all the way in to the coast. A 5 km long coastal

subset is shown in Figure 11-35 and from this it is clear that SAR wind speeds decreases dramatically near the coast. It is true for all wind speeds. The coast is positioned at 59.5 km, i.e. the data further east are over land for which the SAR algorithm is not applicable. Near the coast sub-pixel contamination for mixed pixels containing land and sea are most likely to prevail. The geometrical recti-fication is only accurate to around one pixel. It means that wind speeds from distances closer than 400 m to the coastline are unreliable.

The SAR wind speeds start decreasing 1.0 to 1.5 km offshore. It is most clear for the high wind speeds.
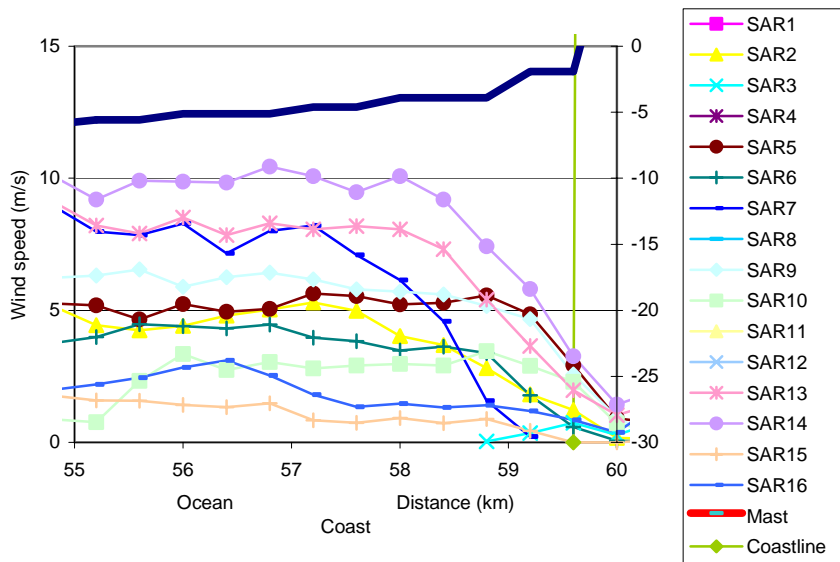
Figure 11-35 Latitudinal horizontal transect of the SAR wind speeds and the water depth at Horns Rev 5 km offshore and to the coast. For SAR case num-bers please refer to Table 11-2.

The coastal zone of interest for the Horns Rev site is about 15 km wide. There-fore coastal transects of this length are analysed, please see Figure 11-36 for the geo-positions. For profile 1, SAR wind speeds and LINCOM model results are shown for all available cases, see Figure 11-37. The SAR wind speeds drop abruptly near the coast. The LINCOM model results also drop near the coast but in a more moderate way. For profile 2 that stretches from the position of the met-mast to the nearest coastline, the SAR wind speeds also drop abruptly near the coast, see Figure 11-38. Many more SAR scenes are available in this tran-sect (than in profile 1) and the overall pattern is more complex. This is most likely caused by the complex sea bottom topography. The third coastal profile shows a pattern very similar to that of profile 1. The sea bottom decreases very gradually at this position, see Figure 11-38.

From the coastal transects it is concluded that the wind speeds consistently are lower near the coast than further offshore. This trend is also anticipated from the LINCOM model results. However, it appears that the SAR wind speeds are too low at a distance of roughly 2 pixels offshore (not counting the pixel right at the shoreline because this always is a mixed pixel mapping both sea and land). In other words, for the nearest 800 m of the coastal zone the SAR wind speed maps have a negative bias. Further it may be noted (again) that the complex sea bottom topography may influence SAR wind speed maps considerably.
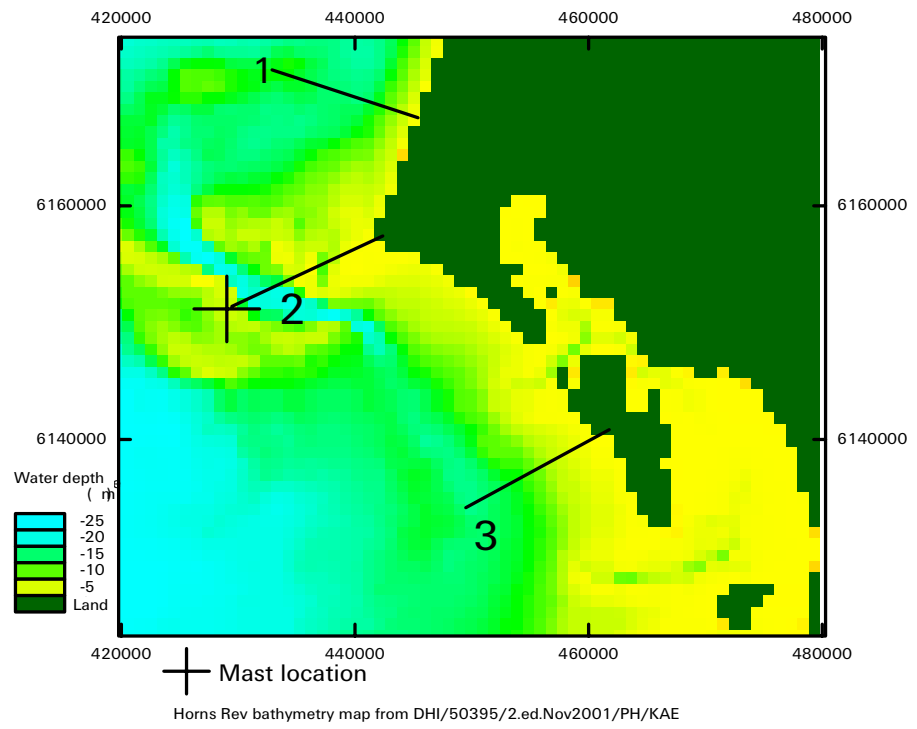
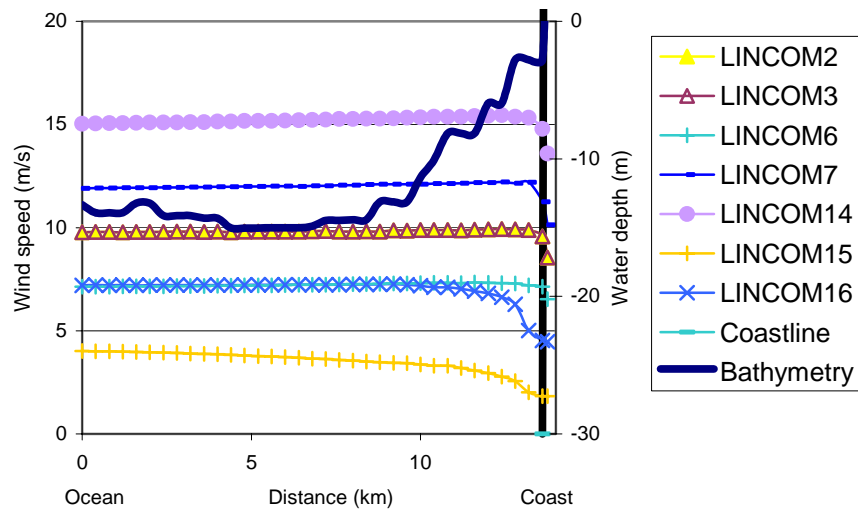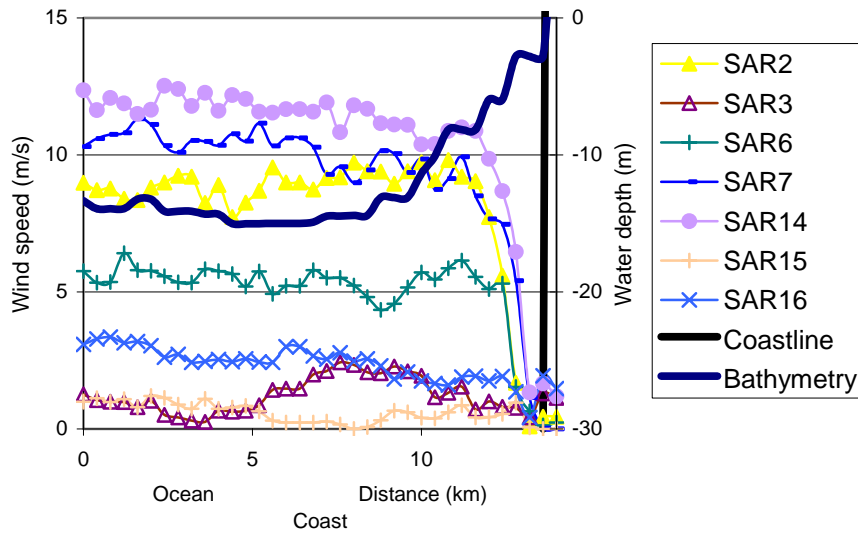*Figure 11-36 Position of three horizontal transects.*

Figure 11-37 Horizontal transects a) of SAR wind speeds and b) LINCOM model results and bathymetry for the coastal zone, profile 1.
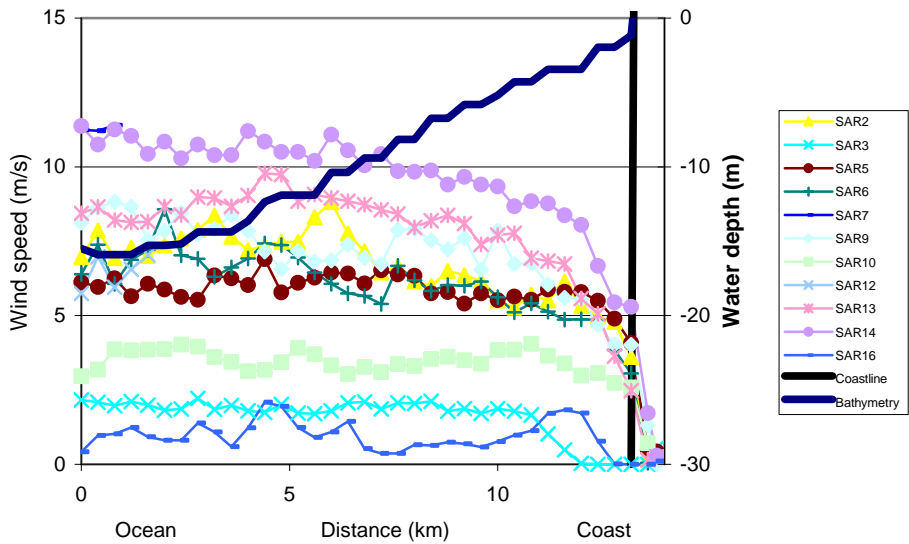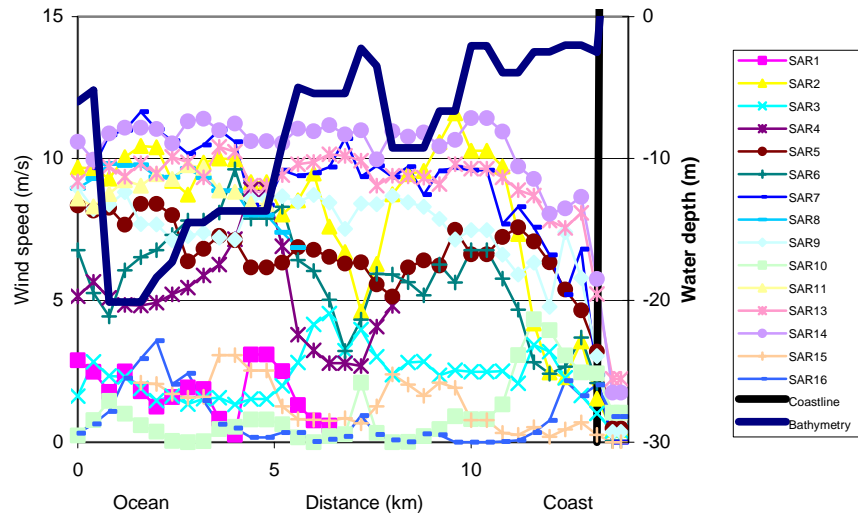
Figure 11-38 Horizontal transects of SAR wind speeds and bathymetry for the coastal zone a) profile 2, b) profile 3.

11.11 Summary on Horns Rev

Horns Rev is located in the North Sea on the West coast of Jutland in Denmark. It is an area where ELSAM/ELTRA, a Danish electrical utility, is constructing the worlds largest offshore wind farm. Prior to the construction a time-serie of meteorological in-situ observations have been collected offshore by the company since May 1999.

SAR wind speed maps from the Horns Rev site has been retrieved from ERS-2 SAR scenes by the CMOD-IFR2 for 16 different days in the period 21 May 1999 to 16 May 2000. To calculate the wind speeds from SAR imagery, the wind direction has to be known a priori. Wind speed maps have been calculated both from in-situ wind direction and from wind direction inferred from wind

streaks in the SAR images. The processing of SAR scenes has been done at NERSC.

The 16 cases cover atmospheric flow from onshore (9 cases), alongshore (4) and offshore (3). For the onshore flow atmospheric stability was either neutral or unstable. Stable conditions were found only for offshore wind in the spring and summer. The cases encompass low (5-9 m s^{-1}), medium (9-13 m s^{-1}) and high (> 13 m s^{-1}) wind speed regimes. High wind speeds occur only during on-shore flow.

The SAR wind speed maps have been validated against offshore in-situ wind observations by applying footprint theory to the SAR wind speed maps. The footprint theory describes the upwind contribution to the atmospheric response by at given sensor on the meteorological mast to the unwind conditions. The footprint is an ellipse-shaped area located in the upwind direction of the mast and each sub-area contributes a certain percentage to the total flux. The shape of the footprints varies as a function of sensor height and atmospheric stability.

Comparing SAR wind speed maps valid for 10 m height, the neutral footprints are around 5 km long and 1 km wide, i.e. 26 pixels as the SAR wind speed maps are multi-looked to a 400 m by 400 m resolution. These footprints explain 90% of the contribution and the footprints do not reach any coast as the mast is positioned 14 km offshore from the nearest land point. The footprints are shorter under unstable and longer under stable conditions.

The stability is calculated from air temperatures at the mast and the wind speed at 10 m is extrapolated by the logarithmic wind profile law from wind speed measurements at 15, 30, 45 and 62 m above Danish Normal Zero (DNN). Booms are extended towards the Southwest and the Northeast at the three lower levels and wind data from each are used dependent on the wind direction to avoid flow distortion from the mast itself. The wind profile is corrected for tidal deviations based on local water level measurements as the tide can reach ± 2 m. This meteorological data set is quite unique for the comparison analysis.

SAR wind speed maps are snapshots in time recorded within seconds whereas the time-series from the mast is averaged into hourly values centered at the time of the satellite overpass. The SAR wind speed footprints have been calculated in two different ways, one is a very simple approach where all pixels within the 90% footprint area are weighted equally (arithmetic average) under the assump-tion of neutral stability, the other is an advanced approach where each pixel is contributing with a certain percentage to the total flux and the footprint varies with stability.

The most promising result is achieved from simple footprints applied to the SAR wind speed maps derived based on in-situ wind direction. The linear corre-lation between in-situ and SAR wind speeds gives y = 1.04x-1.79 with R^2 of 0.88 and standard error of 0.61 m^{-1}. In this case three ellipses were truncated to avoid errors caused by tidal current effects visual in the SAR maps.

Linear correlation results were produced for a large number of comparisons. In all cases a negative bias of the order of -2 m s-1 was found. The comparison result of in-situ wind direction and SAR wind streaks was good with R^2 0.95 and a bias of –31°. However, using the SAR wind streak directions as input to the CMOD-IFR2 gave a larger scatter in the SAR wind speed maps. This was evident both in the overall linear regression results and in the standard devia-

tions within each of the footprints evaluated case by case. It was noted that for SAR wind speed maps based on in-situ wind direction, the wind speed was always lower than the in-situ wind speed, whereas for SAR wind speed maps based on SAR streak directions the footprint values happened to be also larger than the in-situ observations.

The advanced footprint area-averaging technique is more correct from a physically point of view. Therefore it was expected that the linear correlations between spatial SAR wind speed averages and in-situ wind observations would be improved. This was however not the case. R^2 was only 0.50 (based on SAR wind streak direction, the input that will be used in future studies where no in-situ data are available). The linear correlation equation was $y = 0.97x-1.76$, hence the result of the advanced footprint does not change the overall finding of a bias of around -2 m s^{-1}.

The explanation for the low R^2 value is most likely due to noise in the SAR wind speed maps. When a very few pixels are given a large weight, noise will be a larger problem than when a number of pixels are average by equal weights. In the advanced footprints the pixel of main contribution is weighted from 10 to 75%. Linear correlation results on SAR wind speed from the single pixel that contributes a maximum to the total footprint, both as estimated in the simple footprint and from the advanced footprint, have R^2 around 0.75. This is lower than for the simple footprints.

The wind speed at hub-height is of higher relevance for wind turbines rather than at the 10 m level. Footprints valid for the 62 m level (identical to the height of the highest wind speed in-situ observation) were also analysed. But as these simple footprints are very large (40 km long, 7 km wide) most often the footprints stretched into areas outside the 100 km by 100 km scenes or over land areas (where the wind speeds cannot be extracted from SAR observations). Only in five out of 16 cases were the full footprints available, otherwise truncated footprints had to be used as a proxy. The linear correlation between these large SAR footprints and in-situ observations had a greater scatter than for the 10 m level also gave a slightly larger negative bias.

It is concluded from the validation analysis, that the most robust method of comparing SAR wind speeds to offshore in-situ observations is for area-averaging simple footprints for the 10 m level. In order for the advanced footprint to give results better than those from the simple footprint, it would be necessary to reduce the level of noise in the SAR wind speed maps. This could be achieved through spatial filtering or multi-looking to lower resolutions but it has not been investigated. The advanced footprints can only be calculated when the atmospheric stability is known which may not be available in many studies.

For the Horns Rev site the LINCOM model has been used to calculate the wind speed for the whole region. The model is computationally fast (it is a spectral model) and the atmospheric model input was the observations from the offshore met-mast. The LINCOM model is a microscale model in which the local details in the terrain, orography and land use roughness changes, and also variations in the sea roughness dependent on wind speed and fetch is modelled.

The results of LINCOM model are compared to the SAR wind speed maps along horizontal transects stretching from the met-mast and a few kilometers upwind for all cases. From this comparison analysis it is clear that the SAR-derived wind speed maps are strongly underestimating the wind speed at the 10

m level for stable conditions. There are two such examples where the wind is offshore and stable. Apparently the lowest part of the marine surface layer is decoupled from the upper part. It is explained by the development of a marine internal boundary layer. In an offshore case with unstable flow LINCOM compares very well to the SAR wind speed map.

The mesoscale model KAMM-2 has been run for five cases for the Horns Rev site. Based on information from the in-situ observations, NOAA AVHRR images of cloud formations and weather charts, all cases have been excluded which show fronts or other unstationary conditions. Further has the in-situ observations been compared to an independent data set, the NCAR/NCEP reanalysis data of the nearest 200 km by 200 km grid cell. Only for those cases where the reanalysis data compares well to the in-situ observations has the KAMM2 model been run with input of the reanalysis data at the geostrophic level as well as surface temperatures. KAMM2 is a non-hydrostatic model and it has been run in several resolutions to check for grid independence for the given orography and land use roughness map.

The wind speed results of the KAMM2 model compare well to the LINCOM results and SAR wind speed maps.

Finally has the LINCOM and KAMM2 model results been used in an investigation of the effect of sea bottom topography to the SAR wind speed maps. The meteorological tower is sited at -6.01 m depth (DNN) and the variations between low and high tide reached at the extreme, -0.47 and +0.65 m, respectively, at the overpass time of the 16 SAR scenes. The tidal current strength and direction as well as waves are known from a buoy and the bathymetry from a digital map from Danish Hydraulic Institute (DHI). Significant variations in the SAR wind speed maps were noticed close to regions of complex sea bottom near the Horns Rev reef. In certain wind directions the SAR wind speeds were much higher or lower than over the open sea. For the very shallow areas between the Wadden Sea islands tidal currents and other features not related to the wind speed only, are clearly visible in the SAR wind speed maps.

In the coastal zone the wind speed is reduced as compared to that over the open sea both for onshore and offshore flow. This is seen in the LINCOM and KAMM2 model results as well as in the SAR wind speed maps. From horizontal transects located orthogonal to the open ocean coastline, it is clear that the SAR wind speed in the first two pixels offshore shows considerably lower values than the models. This implies that the SAR wind speed maps are strongly negatively biased near the shoreline for a distance of around 800 m at the Horns Rev site.

12 Maddalena in Italy

Charlotte Bay Hasager, Ole Rathmann and Bo Hoffmann Jørgensen

12.1 Site description

The Maddalena site in Italy is located north of the island Sardinia (Figure 12-1). A meteorological mast was established on a concrete block in the sea in the narrow strait between the islands Sardinia and Maddalena (Figure 12-2). The station is named Mezzo Passo. The geographical coordinates are 41°12'19"N, 9°22'30"E (UTM32, E531440, N4561701). The wind measurements are available as 10-min. mean values for the period January 1997 – June 1999.
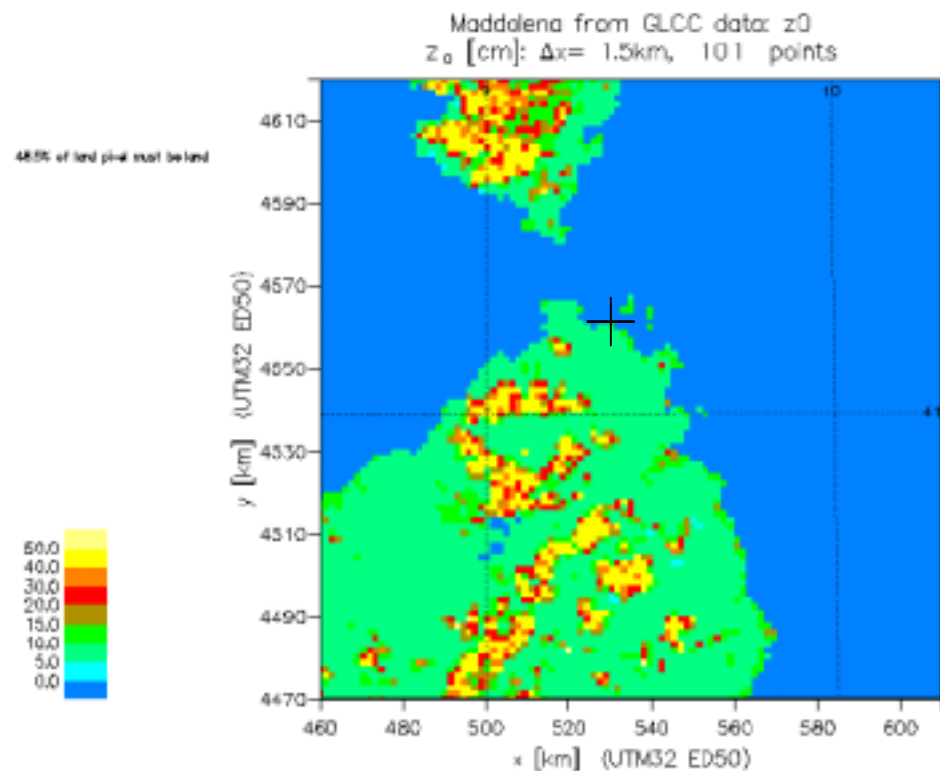
Figure 12-1 Map of Maddalena site. The cross indicate the position of the meteorological mast.

12.2 Satellite scenes from ERS-2 SAR

The ERS SAR scenes were selected for Maddalena based on in-situ wind speed and wind direction observations from a 10 m high sea mast. The scenes are listed in Table 12-1. Please note the Maddalena observations are in local times in the meteorological file but here given in UTC (in(Johannessen, 2001) the one hour time difference was not corrected for).

Figure 12-2 The meteorological mast at La Maddalena.

Table 12-1 Maddalena ERS SAR scene overpass times and in-situ wind speed and direction in 10 minute mean values.

Date	Time (UTC)	Dir. (º)	U (m s^{-1})
97-05-21	21:37	237.7	8.78
97-05-31	10:06	91.7	9.26
97-10-18	10:06	77.2	8.31
97-11-22	10:06	17.5	8.96
97-12-27	10:06	285.1	15.47
98-04-11	10:06	212.6	7.47
98-05-06	21:37	249.6	6.40
98-07-25	10:06	255.9	11.22
98-12-12	10:06	18.7	7.92

Seven scenes are from the descending morning pass and two from the ascending evening pass. The ERS SAR scenes are processed at NERSC (Johannessen, 2001) by the CMOD-IFR2 algorithm. In all cases where wind streaks are found

from two-dimensional FFT, this wind direction is input to the algorithm. Otherwise the in-situ wind direction is used as input. (one hour corrected?)

12.3 Weather conditions

The NOAA AVHRR quicklook satellite data from the Dundee Satellite Receiving station in Scotland is listed below in Table 12-2 together with the ERS SAR scenes. Weather charts from (1999) are also used for the description of the weather at all the dates.

Table 12-2 Time and satellite number for the ERS SAR and NOAA AVHRR scenes from the Maddalena site. The arrows ⇑ ⇓ indicate ascending and descending tracks, respectively.* is from the following day.

Date	NOAA AVHRR	UTC	ERS SAR	UTC	NOAA AVHRR	UTC
97-05-21	12⇑	17.16	2⇑	21:37	14⇓	00.59*
97-05-31	12⇓	07.07	2⇓	10:06	14⇑	12.30
97-10-18	14⇓	02.17	2⇓	10:06	14⇑	12.12
97-11-22	14⇓	02.35	2⇓	10:06	14⇑	12.29
97-12-27	12⇓	06.59	2⇓	10:06	14⇑	12.47
98-04-11	12⇓	06.51	2⇓	10:06	14⇑	13.36
98-05-06	12⇑	17.30	2⇑	21:37	14⇓	02.15*
98-07-25	12⇓	06.39	2⇓	10:06	14⇑	12.42
98-12-12	14⇓	03.42	2⇓	10:06	14⇑	13.36

12.4 WASP

Five wind speed scenarios were selected on the basis of the fingerprint plot Figure 12-3.
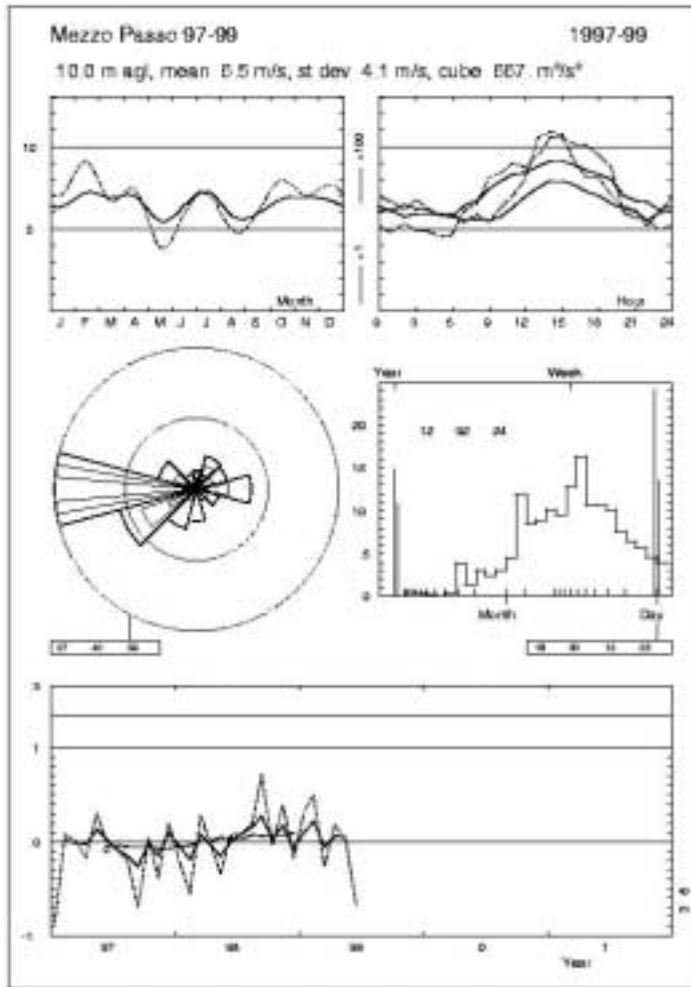
Figure 12-3 Mezzo Passo fingerprint plot

WAsP has been run for five of these nine cases, namely those for which the wind speed was stationary and the modelling could take place. The results are shown in Appendix III. The WasP predicted wind speed distributions (grids) from the selected scenes apply also to 10 m above sea level. In the colour maps the position of the Mezzo Passo mast is indicated. For each scene, a 24-hour plot of the measured wind data is shown; the time of the SAR-scene is in the middle of the plot, marked with a circle. A frame indicates the selected part of the time series, on basis of which the predictions are made: 2½ hour before and ½ hour after the SAR-time. The cases are listed in Table 12-3 where the category of wind speed (low, medium, high) is indicated.

Table 12-3 Scenes from the Mezzo Passo met-mast time series. Measurements at 10 m above sea level. Selected scenes are printed in bold. The category (Cat) indicates low, medium or high wind case

No	SAR date	UTC	Time	Frac. Day	Index	Dir	Speed	Cat
1	**97-05-21**	**21:37**	**22:40**	**35571.9444**	**16338**	**237.7**	**8.78**	**M**
2	97-05-31	10:06	11:10	35581.4653	17709	91.7	9.26	M
3	97-10-18	10:06	11:10	35721.4653	37869	77.2	8.31	L
4	97-11-22	10:06	11:10	35756.4653	42909	17.5	8.96	L
5	**97-12-27**	**10:06**	**11:10**	**35791.4653**	**47949**	**285.1**	**15.47**	**H**
6	**98-04-11**	**10:06**	**11:10**	**35896.4653**	**14468**	**212.6**	**7.47**	**L**
7	98-05-06	21:37	22:40	35921.9444	18137	249.6	6.40	L
8	**98-07-25**	**10:06**	**11:10**	**36001.4653**	**29588**	**255.9**	**11.22**	**M**
9	**98-12-12**	**10:06**	**11:10**	**36141.4653**	**49748**	**18.7**	**7.92**	**L**

12.5 KAMM2 mesoscale model considerations

The present calculations for Maddalena have mainly been performed with a grid containing 101*101*61 cells for an area which is 150 km*150 km, i.e. 1.5 km horizontal resolution. A few runs with 1 km and 2 km resolution have been performed to test grid independence. The aerodynamic roughness length (GLCC, 2001) used for the mesoscale model is shown in Figure 12-4. The orography used for the mesoscale model calculations with 1.5 km horizontal resolution is shown in Figure 12-5a. The orographic data originates from the Global 30 Arc-Second Elevation Data Set (GTOPO30, 2001). However, because KAMM2 is sensitive to non-smoothness of the computational grid (See Chapter 6), the orography is filtered with a Gaussian filter. More filtering is applied near the boundary than near the middle of the domain. Figure 12-5a depicts the filtered orography. For comparison, the unfiltered orography is shown in Figure 12-5b.
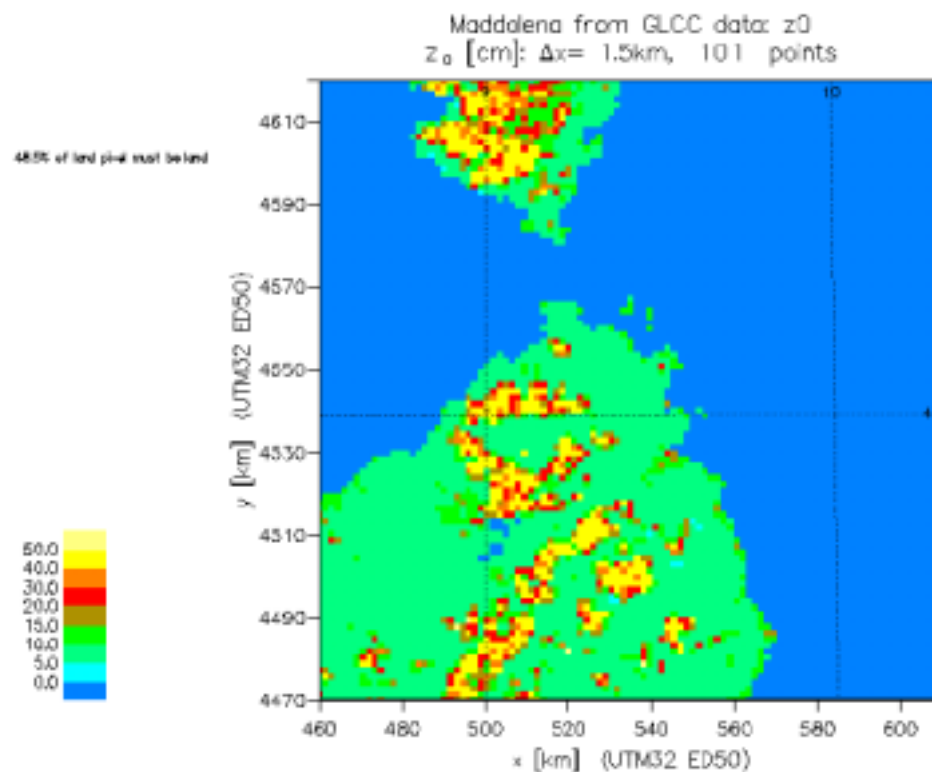
Figure 12-4 Aerodynamic roughness length map of Maddalena with 1.5 km horizontal resolution used for the mesoscale model calculations

h [m]: Mezzo Passo from GTOP030 data
Δx= 1.5km, α= C°, 101× 101 points

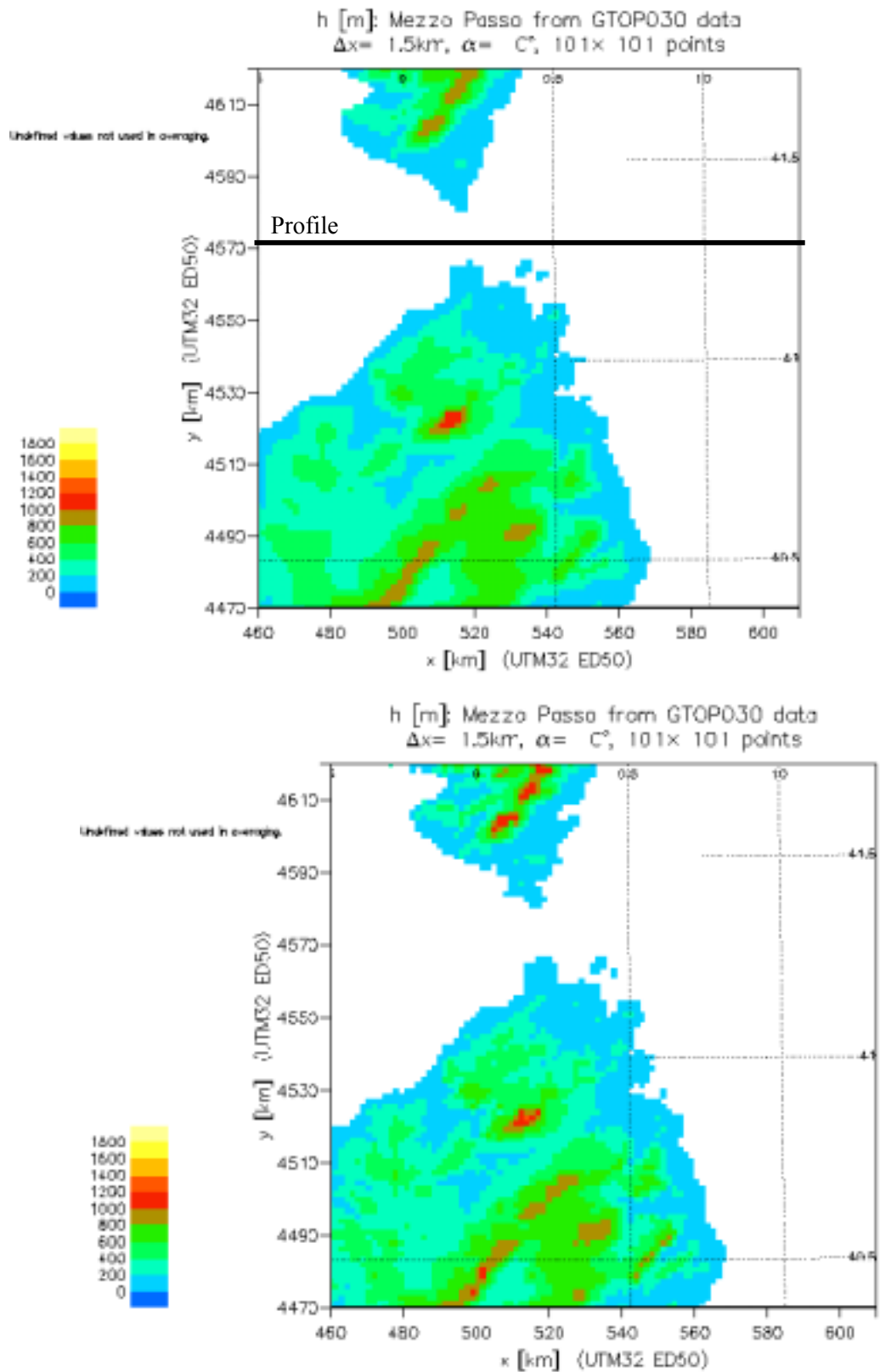h [m]: Mezzo Passo from GTOP030 data
Δx= 1.5km, α= C°, 101× 101 points

Figure 12-5 Filtered orography (a) of Maddalena with 1.5 km horizontal resolution used for the mesoscale model calculations. The unfiltered orography (b) is shown for comparison. A horizontal profile is indicated in the upper graph.

The five cases treated in the study of Maddalena are listed in Table 12-1. These cases have been selected from a larger set of nine cases. The reason is that it is necessary for the wind speed measured at the mast to be stationary for at least a few hours and that the reanalysis data surface wind speed at 10 m height compares well to the in-situ data. Otherwise the mesoscale model cannot be expected to perform well if the applied large scale forcing is not realistic (see Chapter 6). Weather charts and NOAA AVHRR satellite images have also been studied to infer possible fronts and avoid modelling those cases.

Table 12-4 Cases of the Maddalena study.

Case	SAR scene date, time (UTC)		Reanalysis date, time (UTC)	
1	05.21.1997	21:37	05.22.1997	00:00
2	12.27.1997	10:06	12.27.1997	12:00
3	04.11.1998	10:06	04.11.1998	12:00
4	07.25.1998	10:06	07.25.1998	12:00
5	12.12.1998	10:06	12.12.1998	12:00

An example illustrating the selection procedure is depicted in Figure 12-6. It seen in the figure that the wind speed and direction measured at the mast is relatively constant, although there is a difference of 2 m s^{-1} to the surface wind at 10 m height from the reanalysis data. Furthermore there is a wind direction difference of approximately 50 degrees.
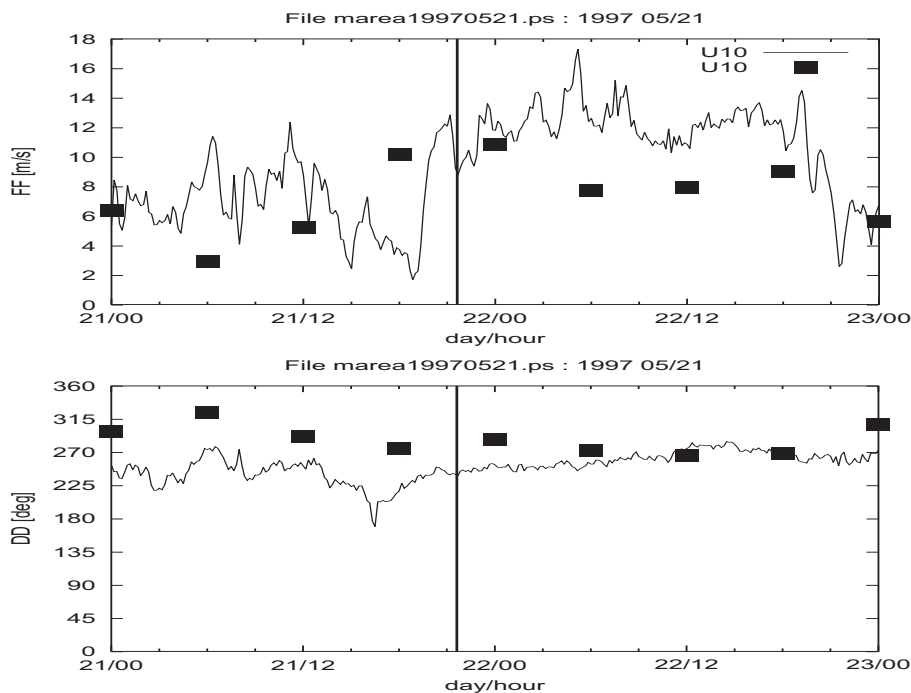

Figure 12-6 Wind speed (above) and wind direction (below) measured at the mast at Maddalena compared to the surface wind at 10m height from the reanalysis data (filled boxes). The satellite overpassing corresponding to case 1 is indicated with a vertical line.

Since the SAR derived wind speed maps and the WAsP model results were already available, it was found useful to investigate these other data sources in order to evaluate the performance of the mesoscale model. The satellite SAR

derived wind speeds and the mesoscale model results have been plotted together with the WAsP results along transects (see Figure 12-7).
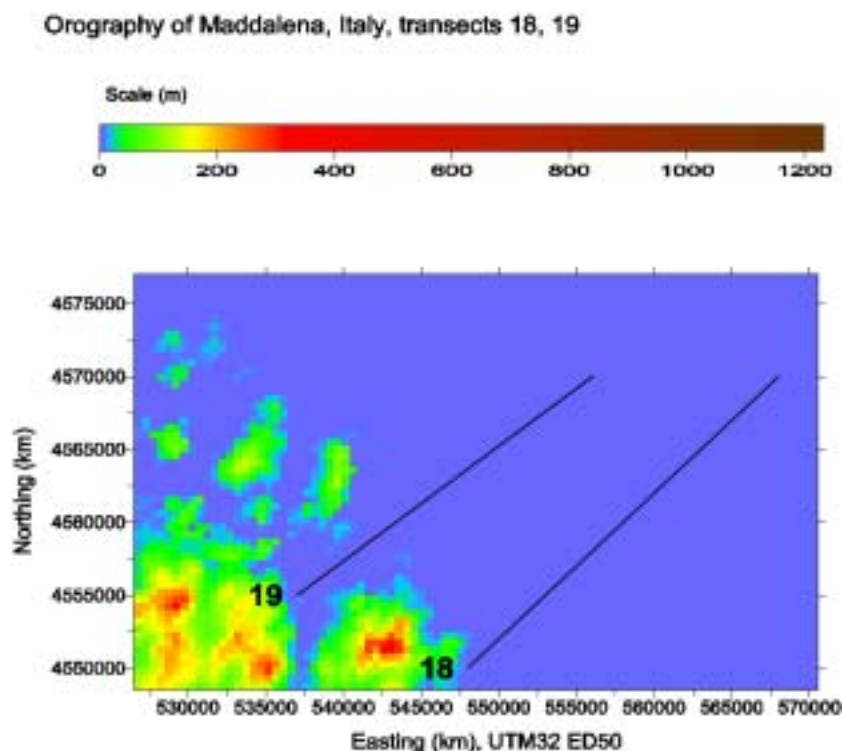

Figure 12-7. Two of the transects used for comparing different model resolutions for Maddalena near the Sardinia close to the Mezzo Passo where the WAsP calculations were performed. The transect starts near land.

The wind speeds from SAR, KAMM2 and WAsP in the horizontal transect number 19 is shown in Figure 12-8a. The in-situ wind direction is from the Southwest whereas the reanalysis wind direction is from the West-northwest (Table 12-3). This offset between wind directions is also clear from Figure 12-8b. For the modelling of wind speeds the offset in wind direction means that the KAMM2 model does not model an offshore flow but an alongshore flow. Therefore the KAMM2 model does not capture the roughness change from land to sea in the start of the horizontal transect. The WAsP model captures the land–sea roughness change. The SAR wind speed map shows increasing wind offshore as expected for an offshore flow. The increase appears along the first 5 km of the horizontal transect and also at the 10-15 km offshore distance. Further out at sea, the general levels of the wind speed of SAR and the mesoscale model have a correspondence within the expected margin of error of 2 m s^{-1} of the KAMM2 model.

The SAR wind speed maps capture features not present in the model results. In other investigated cases, a similar oscillating behavior of the SAR derived wind speeds with transect position is observed. These features may be caused by atmospheric mechanisms similar to land-sea breezes driven by horizontal temperature gradients in the sea temperature or deviations in the SAR derived wind speeds due to physical phenomena related to the fetch limitations. The mesoscale model results are similar for the two different horizontal resolutions

of 1.5 km and 2 km. We assume in general that a resolution of 1.5 km is sufficient for mesoscale calculations at Maddalena.
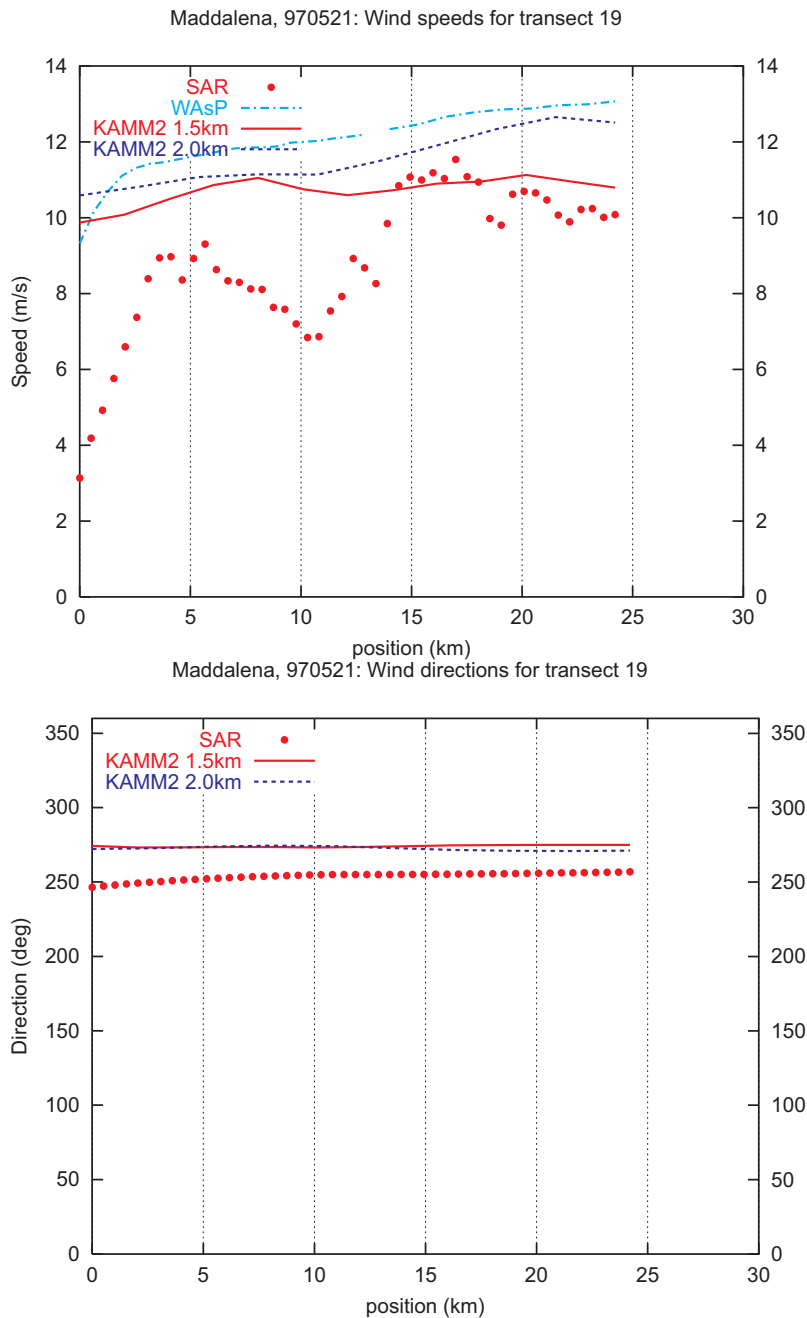

Figure 12-8 Comparison of SAR, WAsP and KAMM2 model results for two horizontal resolution along the transect 19 for case 1. a) wind speed, b) wind direction.

Comparison of SAR wind speeds and KAMM2 model result for a long horizontal transect entirely over sea is shown in Figure 12-9, the geo-location of the profile is indicated in Figure 12-5a. The KAMM2 model results are similar for the horizontal resolutions of 1.5 km and 2.0 km and also appear to be close to the SAR data. At position 60-80 km fetch limitations in the vicinity of the Mezzo Passo may affect the wind speeds derived from the SAR data. As stated previously the KAMM2 model was run with an offset in wind direction com-

pared to in-situ observations and therefore do not model the land effect well in that local area.

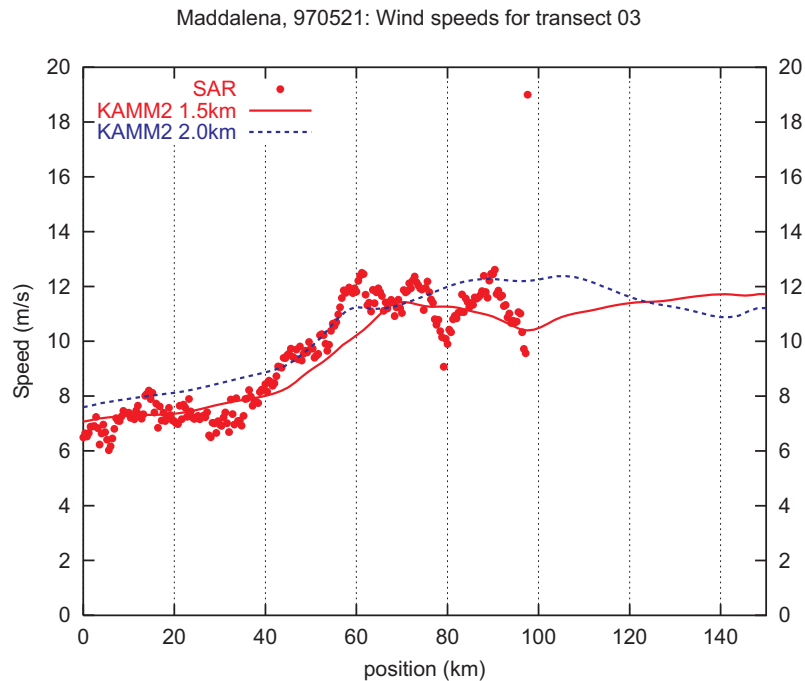Maddalena, 970521: Wind speeds for transect 03

Figure 12-9 Wind speeds derived from SAR compared to KAMM2 model results for two horizontal resolutions for the case 1 Position zero is to the west, position 140 to the east..

From the five cases studied it is evident that the land topography has a significant influence on the offshore wind field. Only wind from the West is modelled. Relatively high wind speeds are found in the strait in between Sardinia and Corsica both in KAMM2 model results and in the satellite SAR derived wind speed map.

A summary of wind speed and wind direction results from one grid point located at longitude 9.375 deg. E, latitude 40.9517 deg. N is given in Table 12-5. The wind speeds modelled by KAMM2 are lower than the reanalysis data for all but one case. Concerning wind direction the KAMM2 results are very close to the reanalysis data. A deviation in wind direction between in-situ data and reanalysis data is clear. This may explain why the wind direction results of the KAMM2 model (initialized from reanalysis data) deviate significantly from the SAR derived wind direction whereas the SAR wind directions compares well to the in-situ data for case 1 and 2.

Table 12-5. Summary for the cases of the Maddalena study of wind speed and direction. The KAMM2 and SAR values are taken from the coordinate UTM32: E532782.9, N4562053 and the reanalysis data from longitude 9.375 deg. E, latitude 40.9517 deg. N.

Case	In-situ		Reanalysis		KAMM2		SAR
	Speed (m/s)	Dir (deg)	Speed (m/s)	Dir (deg)	Speed (m/s)	Dir (deg)	Dir (deg)
1	8.8	237.7	10.82	287.0	10.4	273	240.3
2	15.5	285.1	11.19	312.0	9.5	322	282.0
3	7.5	212.6	10.20	232.0	7.4	259	139.3
4	11.2	255.9	4.44	255.0	8.0	262	247.0
5	7.9	18.7	9.58	18.0	5.8	354	337.3
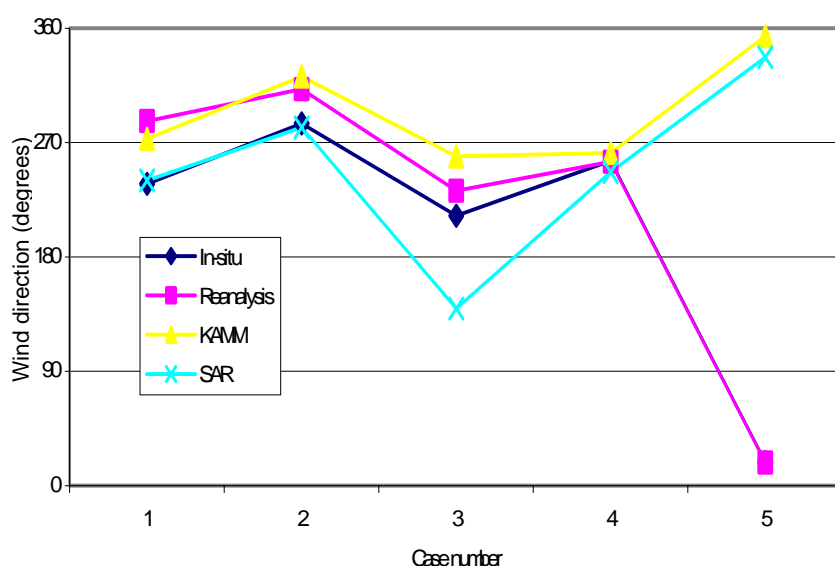
Figure 12-10 Comparison of wind direction from in-situ, reanalysis, SAR data and KAMM2 model results.

Eight hours of simulation time (physical model time - not computer CPU time) was found necessary in order to approach a final state of the computational wind map for case 1 (see Chapter 6). For the four other cases 4 hours of simulation time was applied. For case 4 and 5, it would be an advantage if more simulation time could be applied, but this has not been carried out.

A further check for grid independence at 1 km resolution has been pursued. However, the solution is computationally intensive because of the current setup of the model. In addition to having a large number of grid cells (150x150x60) for 1 km resolution, it has also been found that the model is sensitive to non-smoothness of the grid near the surface. At present, initial disturbances occur in the solution due to non-smoothness of the grid at high resolution. It requires long integration times for the model to transport the disturbances out of the computational domain as compared to the integration time necessary to complete the runs for coarser resolutions. A different filtering scheme for complex

orography may considerably shorten the integration times. However, this has not been attempted.

12.6 Maddalena case descriptions

The conditions for each of the 9 cases are described case by case based on the information on weather from information in section 12.3, i.e. NOAA AVHRR quicklooks of the temperatures (see chapter 10) and (1999) weather charts. ERS SAR wind speed maps from NERSC, WASP and KAMM2 model results and a comparison of NCAR/NCEP reanalysis data to in-situ observations are also shown. All figures are in Appendix III.

12.7 Comparison of SAR scenes to in-situ data

A simple comparison of the in-situ wind observations and the SAR wind speed and direction at the location of the Mezzo Passo station at UTM32 E531440, N4561701 is given in Table 12-6. Please note that the SAR wind speed and direction are taken from the pixel UTM32 E532782.9, N4562053.7. It is slightly displaced from the above coordinates. The new coordinate is chosen from visual interpretation of the SAR wind speed maps with a guess of land-sea borders (no coastline information used so rather uncertain procedure). The in-situ observations are different from those in (Johannessen, 2001) due to the time zones of Italy and UTC are offset one hour.

Table 12-6 Comparison in-situ and SAR wind speed and direction for Maddalena. SAR values taken from the pixel at UTM32 E532782.9, N4562053.7

Date	UTC	U (m s^{-1})		Dir. (º)	
		In-situ	SAR	In-situ	SAR
97-05-21	21:37	8.8	5.7	237.7	240.3
97-12-27	10:06	15.5	13.2	285.1	282.0
98-04-11	10:06	7.5	3.6	212.6	139.3
98-07-25	10:06	11.2	9.5	255.9	247.0
98-12-12	10:06	7.9	4.1	18.7	337.3

The observations in Table 12-6 are graphed in Figure 12-11, Figure 12-12 and Figure 12-13. The graphs show a good correlation between wind speed in-situ and SAR data. The correlation R^2 is 0.977. However there is a large bias of -5.2 m s^{-1}. The wind directions are in good accordance for three cases but around 70º offset in one case.
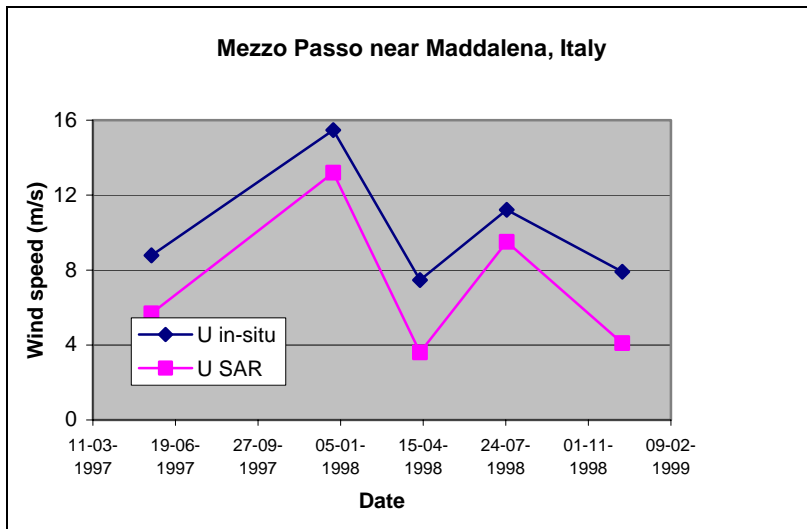
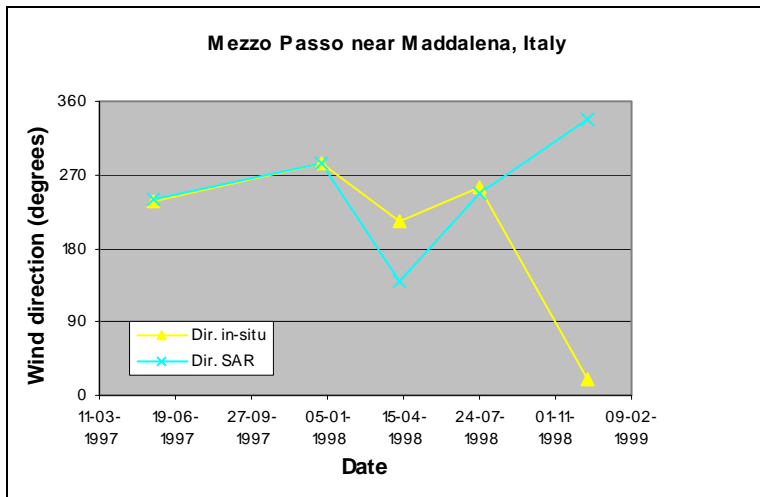*Figure 12-11 Maddalena wind speed in-situ and SAR comparison*

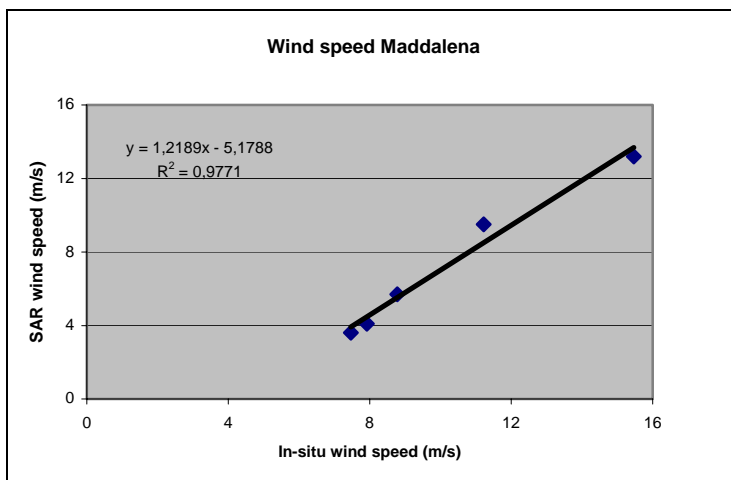*Figure 12-12 Maddalena wind direction in-situ and SAR comparison*

Figure 12-13 Maddalena wind speed linear correlation in-situ and SAR

The method of comparing SAR wind speed from a single pixel to in-situ obser-
vations in the near-coastal zone cannot be recommended. This is due to three
facts:

- The in-situ data are under influence from local orography and land use
  roughness
- The SAR wind speed maps in the near-coastal zone may have a nega-
  tive bias (please refer to section 11.11).
- The SAR wind speed maps with a resolution of 400 m may have errors
  due to speckle noise.

To remedy on the above issues in the comparison. Three actions are taken

- The WAsP model has been used to calculate the wind speed further off-
  shore and hence avoid the local effects of orography and roughness.
- The local winds further offshore are compared instead of near the coast.
- Area-average over an area of appropriate size for comparison and hence
  avoid the (speckle) error of single pixels in the SAR wind speed maps.

12.8 Comparison of SAR scenes to WAsP and KAMM2 model results

The coast of Maddalena is characterized by a rugged coastline and numerous
small islands. For comparison of SAR wind speed maps and WAsP and
KAMM2 model results, a large area offshore was chosen, please see Figure
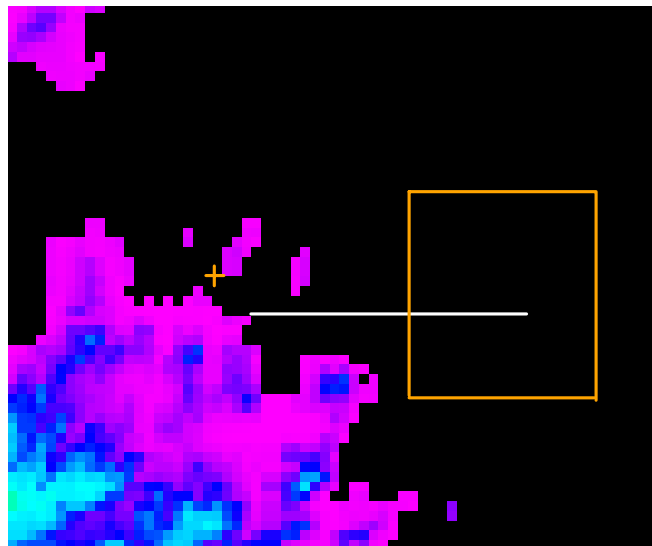12-14 for the location.

Figure 12-14 Map of box area and horizontal profile locations.

The box covers an area of 48*48 pixels = 2304 pixels, or 19.2 km *19.2 km = 369 km^2, and is placed at a distance of minimum 4 pixel (1600 m) from the coast. The statistics on wind speed for the five cases are listed in Table 12-7.

Table 12-7 Wind speed from SAR, WAsP and KAMM2 for a box area offshore Maddalena. Mean, minimum, maximum values and standard deviations are listed for five cases.The in-situ wind speed and direction is also listed.

Case		1	2	3	4	5
Date		221-5-97	27-12-97	11-4-98	25-7-98	12-12-98
In-situ	wind speed (m s^{-1})	8.8	15.5	7.5	11.2	7.9
	wind direction (degr.)	237.7	285.1	212.6	255.9	18.7
SAR	mean (m s^{-1})	7.9	14.7	4.0	7.2	6.9
	min.(m s^{-1})	0.6	9.5	2.4	3.1	5.4
	max. (m s^{-1})	12.4	17.4	5.5	11.8	10.2
	std.dev. (m s^{-1})	1.9	0.9	0.6	1.5	0.6
WAsP	mean (m s^{-1})	12.7	16.0	9.1	11.9	10.7
	min. (m s^{-1})	7.6	9.3	6.7	6.7	10.4
	max. (m s^{-1})	13.2	16.4	9.4	12.3	10.8
	std.dev. (m s^{-1})	0.6	0.6	0.3	0.5	0.0
KAMM2	mean (m s^{-1})	10.7	12.9	7.0	7.6	7.2
	min. (m s^{-1})	9.9	11.7	5.4	4.8	6.9
	max. (m s^{-1})	11.7	14.2	8.1	9.1	7.5
	std.dev. (m s^{-1})	0.3	0.6	0.6	1.0	0.1

The mean values are also shown in Figure 12-15 in which figure it is obvious that there are significant differences. The linear correlation results between WAsP and SAR and between KAMM2 and SAR are shown in Figure 12-16. For WAsP the correlation has a R^2 of 0.95 but a very large bias - 9.9 m s^{-1}. For KAMM2 the correlation R^2 is 0.80 and the bias of - 4.1 m s^{-1}. Five data points seems far too few for the linear correlation analysis.

On average the difference between WAsP and SAR wind speeds for the box area is 4.0 m s^{-1} and between KAMM2 and SAR is 1.0 m s^{-1}. The standard deviations on wind speed in SAR wind speed maps within the box area are moderate. For the model results the standard deviations are smaller. It is surprising that the WAsP results are significantly larger than the SAR wind speeds. The KAMM2 results, on the other hand, compare well to the SAR wind speeds in the box area.
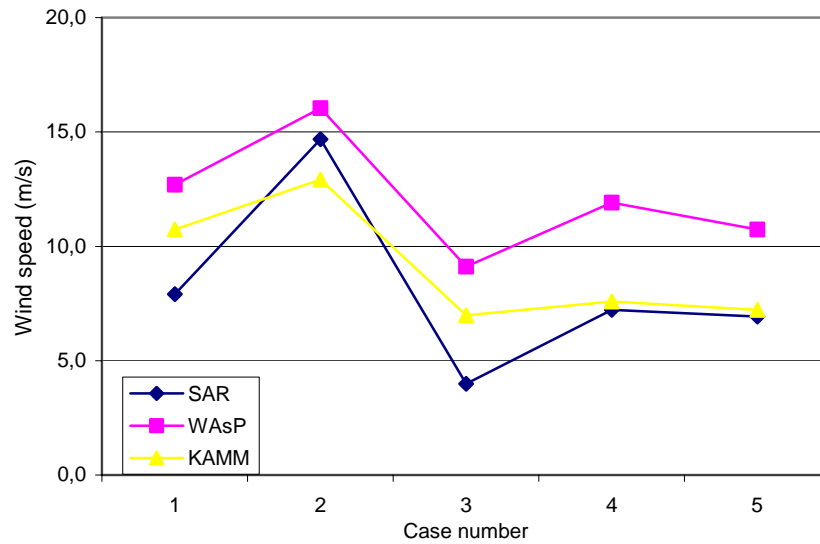
Figure 12-15 Wind speeds from SAR, WAsP and KAMM2 for five cases at Maddalena from a box–average offshore.
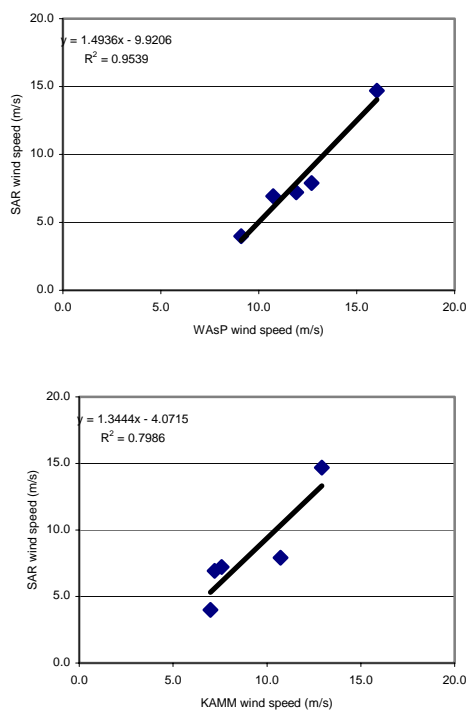

Figure 12-16 Linear correlations on wind speeds from a) WAsP and SAR, b) KAMM2 and SAR.

Horizontal profiles of wind speed from SAR, WAsP and KAMM2 from the coast and stretching 18 km towards the East are shown for the five cases in Figure 12-17a-e. The position of the horizontal transect is indicated in Figure 12-14.

The wind direction was from the West for three cases, so in those an offshore wind pattern is expected. The cases are the 21-5-97, 27-12-97 and 25-7-98. It is clear that the SAR wind speed increases gradually in all three cases for the first 5 km. At this distance they all show a local minimum probably caused by the effect of a small (sub-pixel scale) island. The KAMM2 model results compare well for two of the cases but over predicts the wind pattern on the 21-5-97 case. The KAMM2 model does not model the abrupt decrease in wind speed very close to the shoreline. The abrupt near-shore decrease in wind speed the WAsP model predicts successfully however overestimates the wind speed in general.

The 11-4-98 and 12-12-98 cases have alongshore wind from the South and North, respectively. In these cases the SAR wind speeds do not increase abruptly offshore. Again the WAsP model overestimates the wind speed. So does the KAMM2 model for the 11-4-98 but KAMM2 result agrees well with the SAR observations on the 12-12-98.

The stability and water depth are not know at Maddalena. It is believed that the atmospheric stability in the Mediterranean is unstable or neutral during the day and possibly stable at night (21-5-97). Further is it believed that the water depth is somewhat greater than in the Wadden Sea, Denmark. Based on the above assumption it is likely that the SAR wind speed in the near-coastal pixels may be less negatively biased than at the Horns Rev site in Denmark.
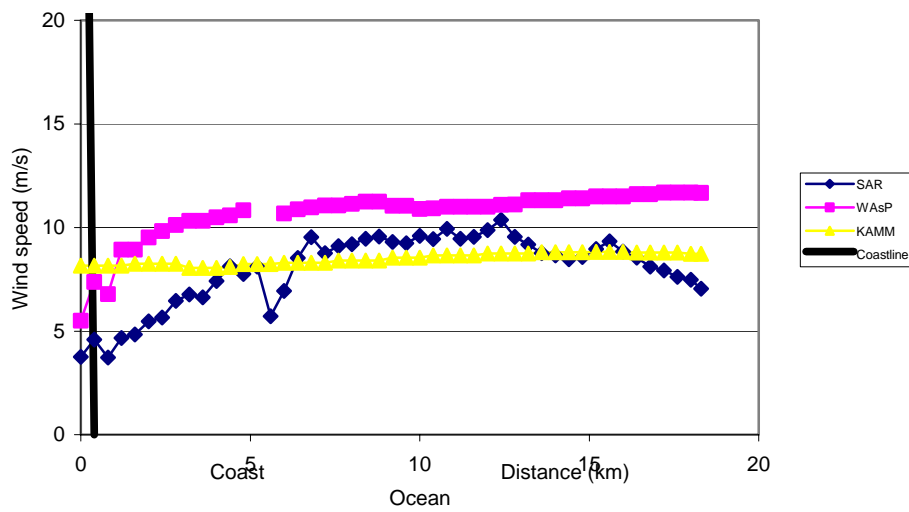
27-12-1997

11-4-1998

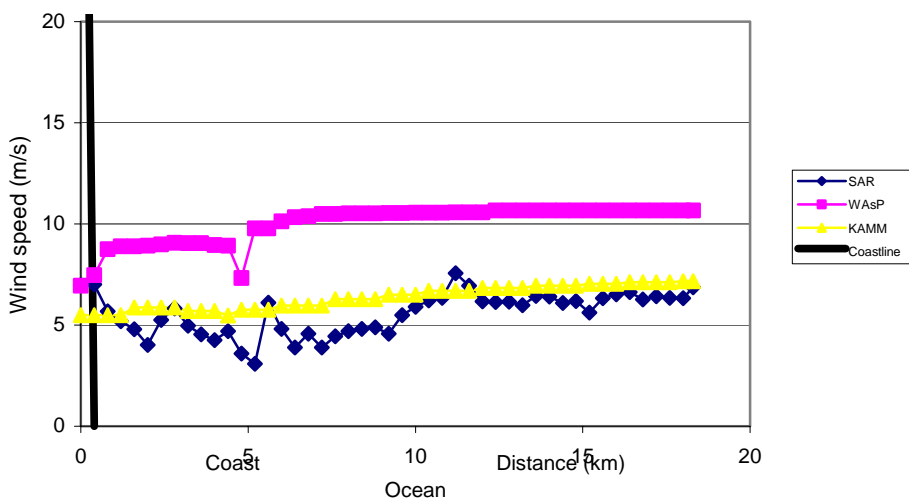Risø-R-1298(EN)
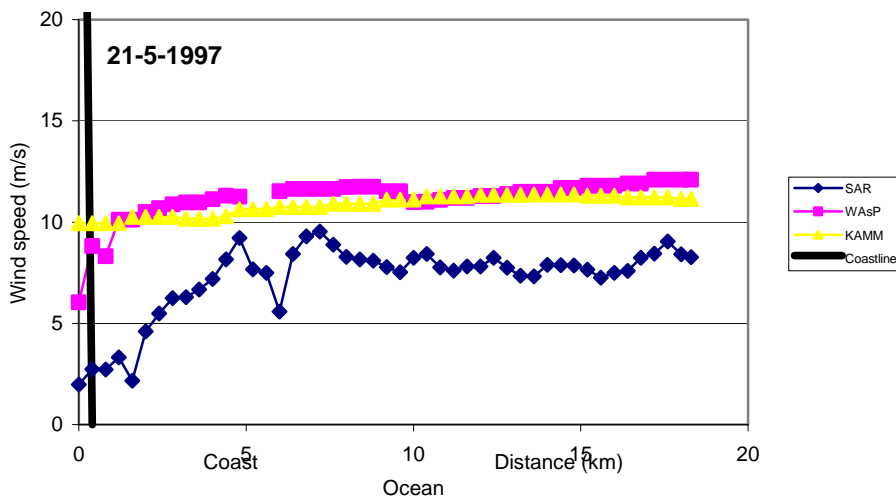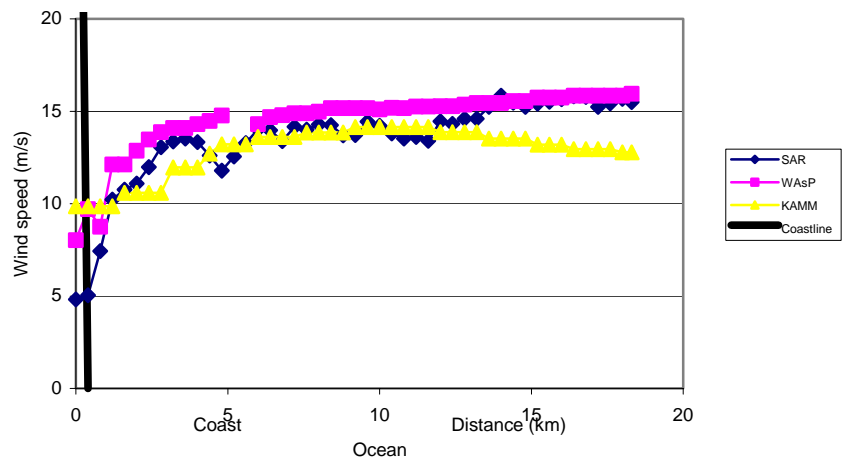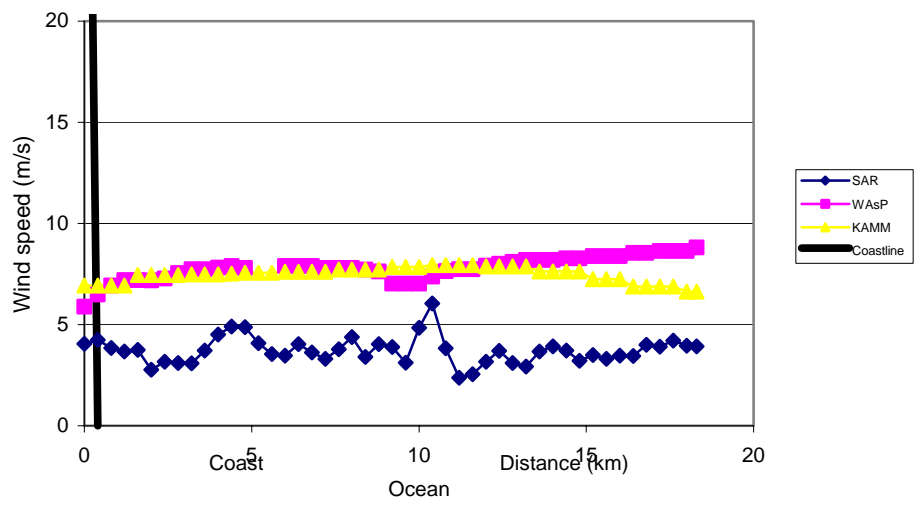
25-7-1998

12-12-1998

Figure 12-17 Wind speed from SAR, WAsP and KAMM2 for horizontal profiles from Maddalena, Italy for five day in five panels.

12.9 Summary on Maddalena

The Maddalena site in Italy is located between the island Sardinia and La Maddalena near the strait Bonifacio between Corsica and Sardinia in the Mediterranean sea. Meteorological in-situ observations from a tiny offshore cliff are used for the validation study.

Five SAR wind speed maps derived from SAR streaks wind direction with the CMOD-IFR2 are available for comparison to the in-situ observations. Linear correlation results between the met-observations and the SAR wind speed from

a nearby pixel gives R^2 of 0.98 but a bias of -5.2 m s^{-1}. It is however far from ideal to use only 5 data pairs in a correlation analysis. A simpler estimate is the mean difference between WAsP and SAR that gives a value of 3.0 m s^{-1}, i.e. the SAR wind speeds are biased too low. The pixel is located close to the shore and therefore may have a negative bias due to this geoposition. As stated in chapter 11 the noise in SAR wind speed maps is so pronounced in the 400 m by 400 m resolution, that it is not reliable to compare single pixels to in-situ observations.

The met-observations observations are under significant influence of the orography and land cover roughness of the nearby islands. Therefore the WAsP model has been used to calculate the winds further offshore. The WAsP model is a microscale model developed for predicting the wind resources from climatological wind speed time-series.

The mesoscale model KAMM2 has been used to calculate the wind fields in the region. The KAMM2 model was run in different spatial grid resolutions to check grid independence. It proved very important to include the orography of Corsica in an adequate manner. The KAMM2 model was initialized with NCAR/NCEP reanalysis data from a 200 km by 200 km grid cell with the geostrophic wind speed and surface temperatures. The reanalysis data were compared to the in-situ data and only cases where the two data set had a reasonably similarity was the KAMM2 model run. Fronts and instationarity was excluded based on the in-situ observations, NOAA AVHRR satellite cloud images and synoptic weather maps.

A box-area average of roughly 20 km by 20 km in the ocean East of the Maddalena site was used for the comparison study. The SAR wind speed observations, the WAsP and KAMM2 model results were then compared. On average the difference in the mean wind speed for the area between WAsP and SAR was 4.0 m s^{-1} and between KAMM2 and SAR 1.0 m s^{-1}. This indicates that the WAsP results are not very accurate far offshore for this site. That could be due to the fact that not only the local effects in a small domain as used by WAsP are significant for the far offshore wind field. It complies to the findings of the KAMM2 analysis where the Northern parts of (tall) mountains of Corsica have a profound impact on the calculated wind field far offshore.

Horizontal transects extending from the East coast of Sardinia and 20 km offshore for comparing the SAR wind speeds, WAsP and KAMM2 model results are made. The on- and offshore cases show a distinct pattern of increasing wind speeds offshore both in the SAR observations as well as in the model results. Especially the WAsP model captures these changes well. For alongshore flow no variation in wind speed along the transects is seen.

The WAsP model over predicts the far offshore winds whereas the KAMM2 model results have a good correspondence to the SAR observations in three cases but over predicts the winds similar to WAsP for two cases.

The small number of cases and the rather complex topography at the Maddalena site makes the validation study partly inconclusive. It may be that the SAR wind speed maps have a bias (around -3 m s^{-1}).

13 Hellisöy in Norway

Bo Hoffmann Jørgensen and Ole Rathmann

13.1 WAsP

Table 13-1 Position of the Hellisöy meteorological station in West Norway

Hellisöy	60°45'10"N, 4°42'40"E	E266342 N6742900 m (UTM Z32)

The Meteorological station Hellisöy is a met-mast with the wind sensors approximately 12 m above terrain; the mast is situated in connection with an approximately 5 m high light house on the island of Hellisöy in the West Norwegian archipelago. The position is given in Table 13-1. A fingerprint plot of the wind data (hourly mean speeds and direction 1996-1997) is shown in Figure 13-1. The scenes selected are given in Table 13-2.

Table 13-2 Selected wind speed scenarios from the Hellisöy met-station.

Scene #	Date - time	Speed range	Direction
1	1996-02-14 21:31	M (9-13 m/s)	211°
2	1996-06-22 10:49	L (5-9 m/s)	331°
3	1996-06-23 10:49	L	331°
4	1996-11-29 10:52	L	114°
5	1997-02-07 10:52	Rejected	----
6	1997-02-23 10:49	M	181°
7	1997-03-30 10:49	L	241°
8	1997-06-08 10:49	Rejected	----
9	1997-10-21 21:34	L	270°

Scenes 5 and 8 were rejected due to instationarity as illustrated in Figure 13-2.

Similarly to the North Sardinian case, at a suitable distance from the coast line the Hellisöy scenarios are used to make estimates of the wind speed over a neighboring candidate sea area, where comparisons with wind interpretations of SAR images can be made.
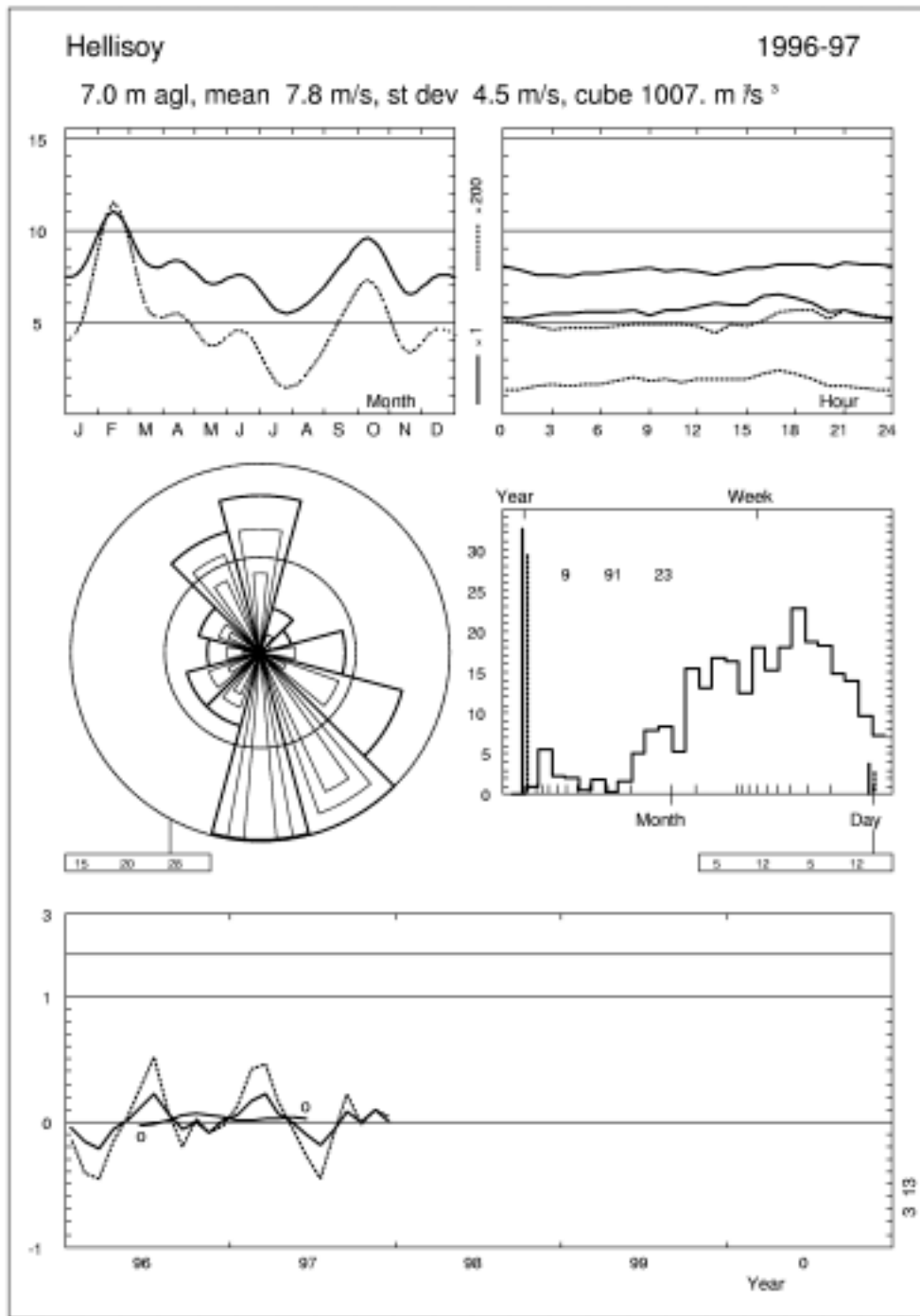
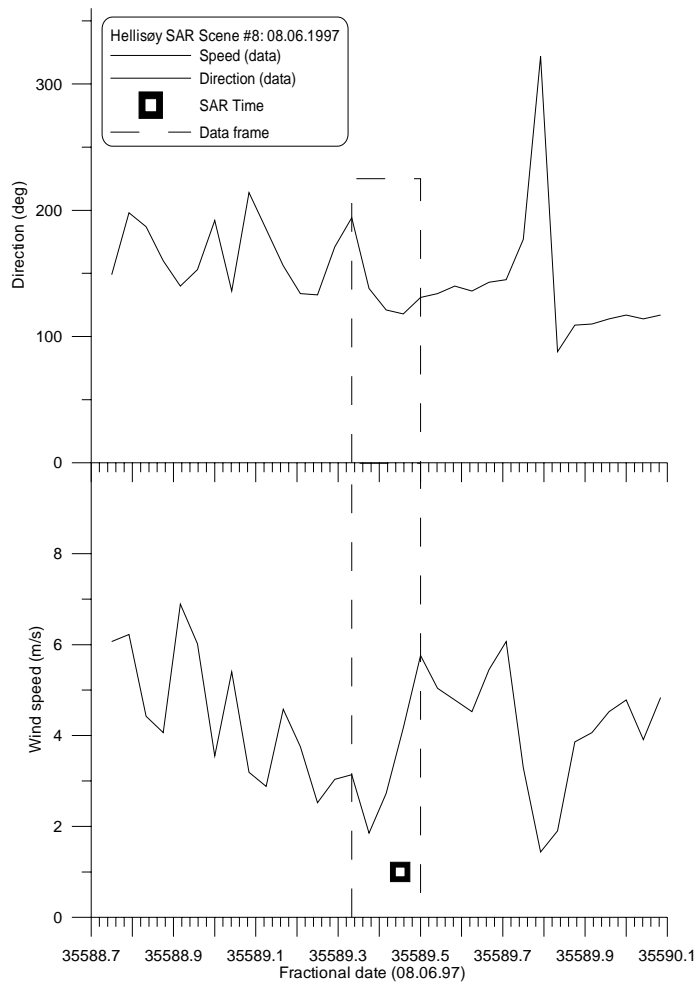*Figure 13-1 Fingerprint-plot of Hellisöy met-data.*

Figure 13-2 Example of rejected scene.

13.2 KAMM2 Mesoscale model considerations for Hellisøy

The present calculations for Hellisøy have mainly been performed with a grid containing 80*80*60 cells for an area which is 120 km*120 km, i.e. 1.5 km horizontal resolution. A few runs with 2 km and 3 km resolutions have been performed to test grid independence. The orography (GTOPO30, 2001) used for the mesoscale model calculations with 1.5 km horizontal resolution is shown in Figure 13-1. The corresponding aerodynamic roughness length (GLCC, 2001) is shown in Figure 13-2.
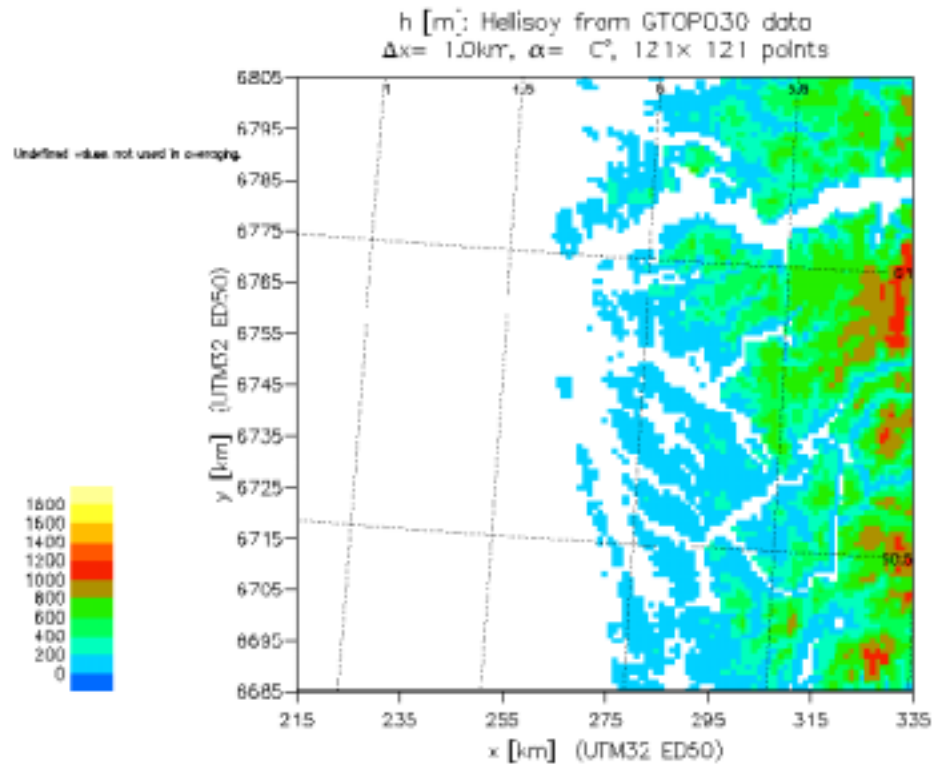
Figure 13-3 Orography of Hellisøy with 1.0 km horizontal resolution used for the mesoscale model calculations.
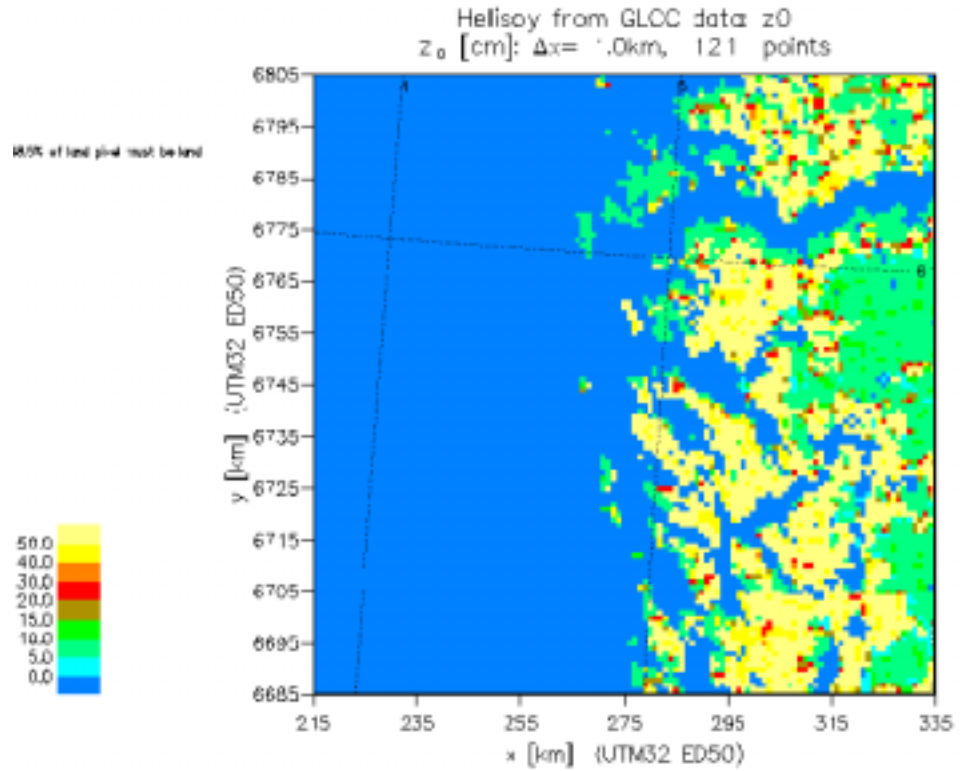

Figure 13-4 Aerodynamic roughness length map of Hellisøy with 1.0 km horizontal resolution used for the mesoscale model calculations.

The cases treated in the Hellisøy study are listed in Table 13-3. As described in Chapter 6, it is necessary to select a subset of the cases for which the wind speed measured at the mast is stationary for at least a few hours and compares well with the surface wind speed at 10 m height from the reanalysis data. This is because the mesoscale model cannot be expected to perform well if the applied large scale forcing is not realistic.

Table 13-3 Cases of the Hellisøy study.

Case	SAR scene date, time (UTC)		Reanalysis date, time (UTC)	
1	02.14.1996	21:31	02.14.1996	18:00
2	06.22.1996	10:49	06.22.1996	12:00
3	06.23.1996	10:49	06.23.1996	12:00
4	11.29.1996	10:52	11.29.1996	12:00
5	02.07.1997	10:52		
6	02.23.1997	10:49	02.23.1997	06:00
7	03.30.1997	10:49	03.30.1997	06:00
8	06.08.1997	10:49		
9	10.21.1997	21:34	10.22.1997	00:00

A typical example illustrating the selection procedure is depicted in Figure 13-3. It seen in the figure that the wind speed and direction measured at the mast is relatively close to the surface wind at 10 m height from the reanalysis data. As we do not want to simulate fronts in the mesoscale model, we have analyzed weather charts (DWD) to exclude SAR scenes containing abrupt spatial changes in wind speed caused by fronts. The resulting selection consists of the scenes 1,2,3,4,6,7 and 9 (see Table 13-1) which have been analyzed in the present work.
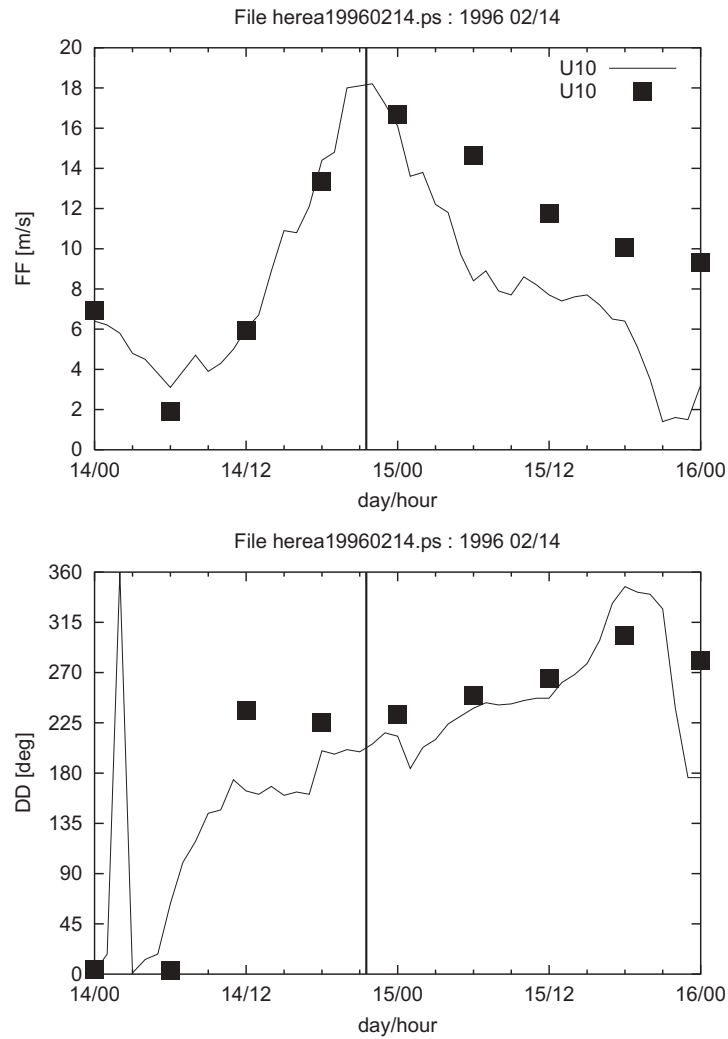
Figure 13-5 Wind speed (above) and wind direction (below) measured at the mast at Hellisøy compared to the surface wind at 10m height from the reanalysis data (filled boxes). The satellite overpassing corresponding to case 1 is indicated with a vertical line.

A horizontal grid resolution of 1.5 km for KAMM22 has was decided. In order to test grid independence, for one case the mesoscale model results for three different horizontal resolutions (see Chapter 6) was plotted along three differently oriented transects located as indicated on Figure 13-4. Each transect starts at the label and proceeds towards the other end.

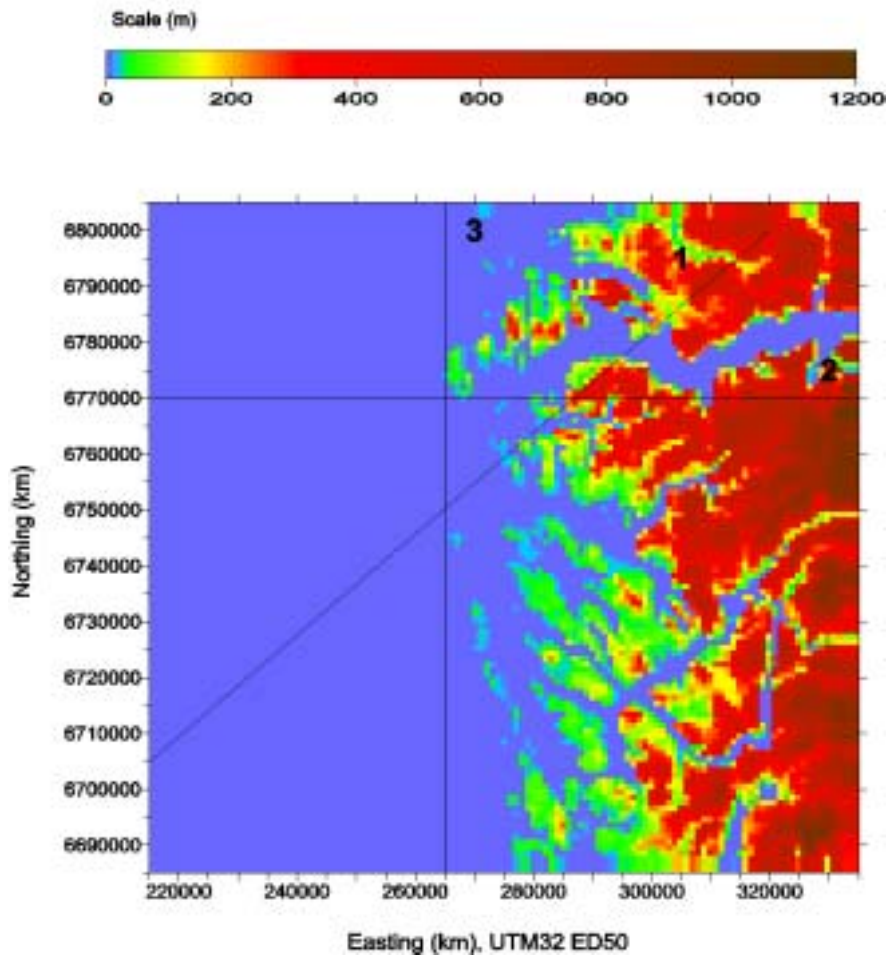Orography of Hellisoy, Norway, transects 01, 02, 03

Figure 13-6 Transects used for comparing mesoscale model wind speeds for different spatial resolutions. Each transect starts by the label number and proceeds towards the other end.

An example for case number 1, which has onshore-alongshore wind, is shown in Figure 13-5 for the transect 01 which is depicted in Figure 13-4. The transect position is shown at the x-axis. The mesoscale model results are similar for the two different horizontal resolutions of 1.5 km and 2.0 km, indicating that grid independence is achieved for a resolution of 1.5 km. The results for 3 km resolution are quite different from the results for 2.0 km and 1.5 km resolutions. We have assumed in general that a resolution of 1.5 km is sufficient for mesoscale calculations at Hellisøy.
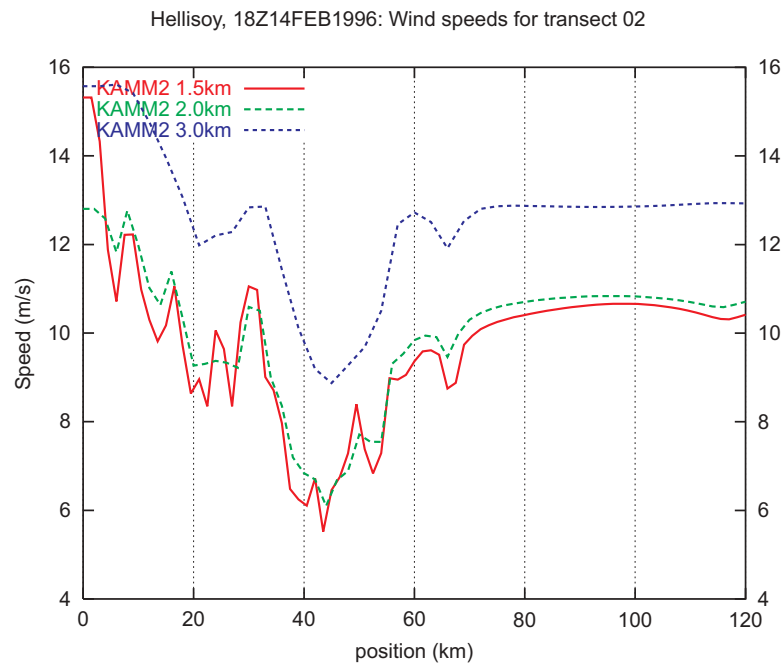
Hellisoy, 18Z14FEB1996: Wind speeds for transect 02

Figure 13-7 Wind speeds from mesoscale model results of Hellisøy for case 1 for three different horizontal resolutions along transect 02.

As an example of the mesoscale model results the wind speed at 10 m (agl.) is shown for Hellisøy at 18.00 (UTC), February 14. 1996 in Figure 13-6. It is can be seen that the land orography and roughness length must be taken into account in this case because the influence of the land topography causes changes in the wind speed and direction in the coastal zone.

Three hours of simulation time (physical model time - not computer CPU time) was found to be necessary in order to approach a final state of the computational wind map (see Chapter 6).
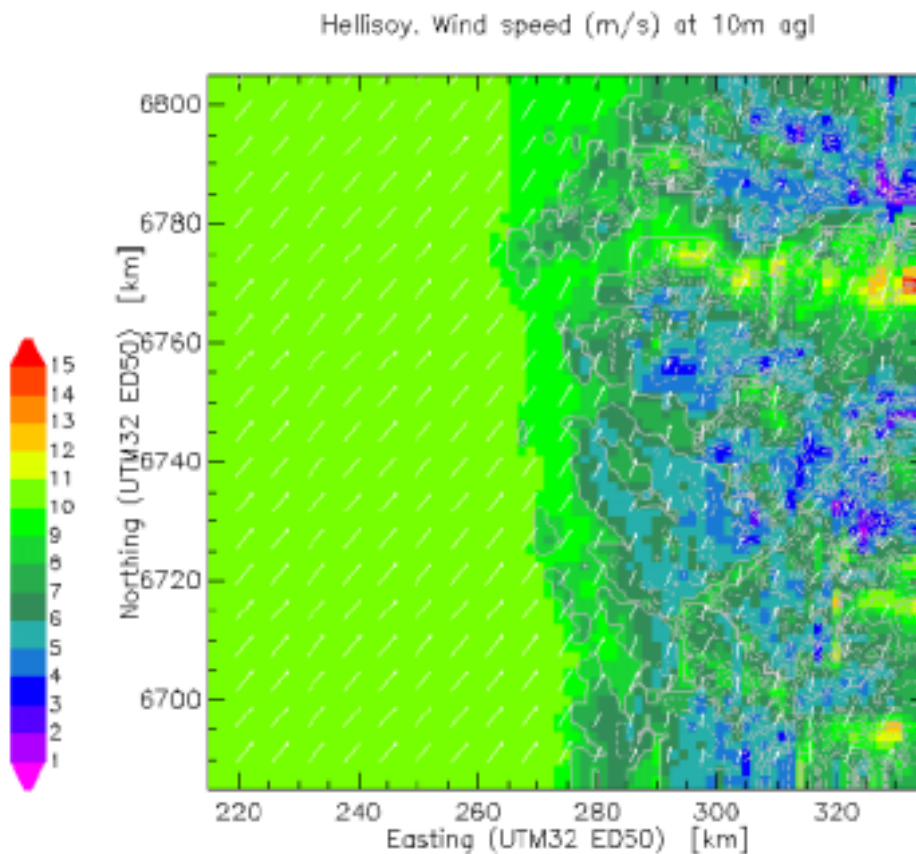
Figure 13-8 Wind speed at 10 m (agl.) resulting from the mesoscale model calculations with 1.5 km horizontal resolution shown for Hellisøy for case 1 (18.00 UTC, February 14. 1996).

For the selected cases 1, 2, 3, 4, 6, 7 and 9 (see Table 13-1) the wind speed and wind direction measured at the mast at Hellisøy is compared to the surface wind at 10m height from the reanalysis data in Appendix IV. The corresponding wind speeds of the mesoscale model are plotted also in Appendix IV.

14 Gulf of Suez in Egypt

Charlotte Bay Hasager and Niels Gylling Mortensen

14.1 Site description

The Gulf of Suez in Egypt has for many years been investigated in regard to the wind resources (Mortensen and Said, 2002). The wind resources are very good due to the regional weather systems given generally high wind power potentials. So far a wind farm at Zafarana has been installed on land and more are being planned. A number of meteorological masts have been operated for several years. Currently 12 are in operations. Comparison to these data may offer a unique opportunity. Below is given the results of three cases where SAR wind speed maps are compared to meteorological observations.

14.2 Comparison of SAR scenes and WAsP results

To assess spatial features of the wind climate in the Gulf of Suez, three cases are studied from satellite images. The ERS SAR satellite data from ESA (European Space Agency; AO3-153) are analysed for wind speeds over the ocean. The C-band radar signals are processed with the CMOD-IFRE2 by NERSC (Nansen Environmental Remote Sensing Centre) in Bergen, Norway.

Case I: 5 April 1996

The first case is from 5 April 1996 at 20.10 UTC. Three satellite scenes, each 100 km * 100 km large covers the Gulf of Suez. The original cell resolution in the images is 25 m * 25 m. However, to avoid so-called speckle noise, the image data has been regridded into a 400 m * 400 m cell size. The wind speed is calculated for 10 m above the ocean assuming the wind direction to be constant at 20º as measured in Zafarana (see Table 14-1). The processed data are shown in Figure 14-2. It is possible to see two thin lines across the Gulf (the upper line is near Zafarana). It is a technical artifact of the mosaic of three satellite scenes.

Meteorological observations are available from three masts near the coast: in the north Abu Darag and Zafarana and in the south Gulf of El-Zayt. The observations are graphed in Figure 14-1 and listed in Table 14-1. At the 25 m level the wind speeds in Abu Darag is 15.7 m s^{-1}, in Zafarana 18.8 m s^{-1} and in Gulf of El-Zayt only 5.3 m s^{-1}. This indicates a north-south gradient decreasing from the north towards south. In the satellite image a similar trend is observed. In the northern part of the Gulf strong winds occur and lower winds in the southern part.

For comparing the mast observations over land to the 10 m wind over sea, the WAsP model has been used. The results of the of WAsP calculated wind speeds at 10 m level above the sea is listed in Table 14-1 together with the SAR wind speed observations. The comparison shows that the SAR wind speeds are very much lower than the observations. Near Gulf of El-Zayt the SAR wind speed map shows values below 2 m s^{-1} which is below the validity range of SAR for wind speed mapping. For the Abu Darag and Zafarana sites it is not clear why the differences of up to 10 m s-1 can appear between observations and the SAR wind speed map. The atmospheric flow was stationary prior to the satellite overpass as shown in Figure 14-1 so it cannot be due to e.g. frontal activity. Uncertainty on wind direction in the SAR algorithms could not lead to errors of this magnitude. No conclusion is found and further analysis is needed.
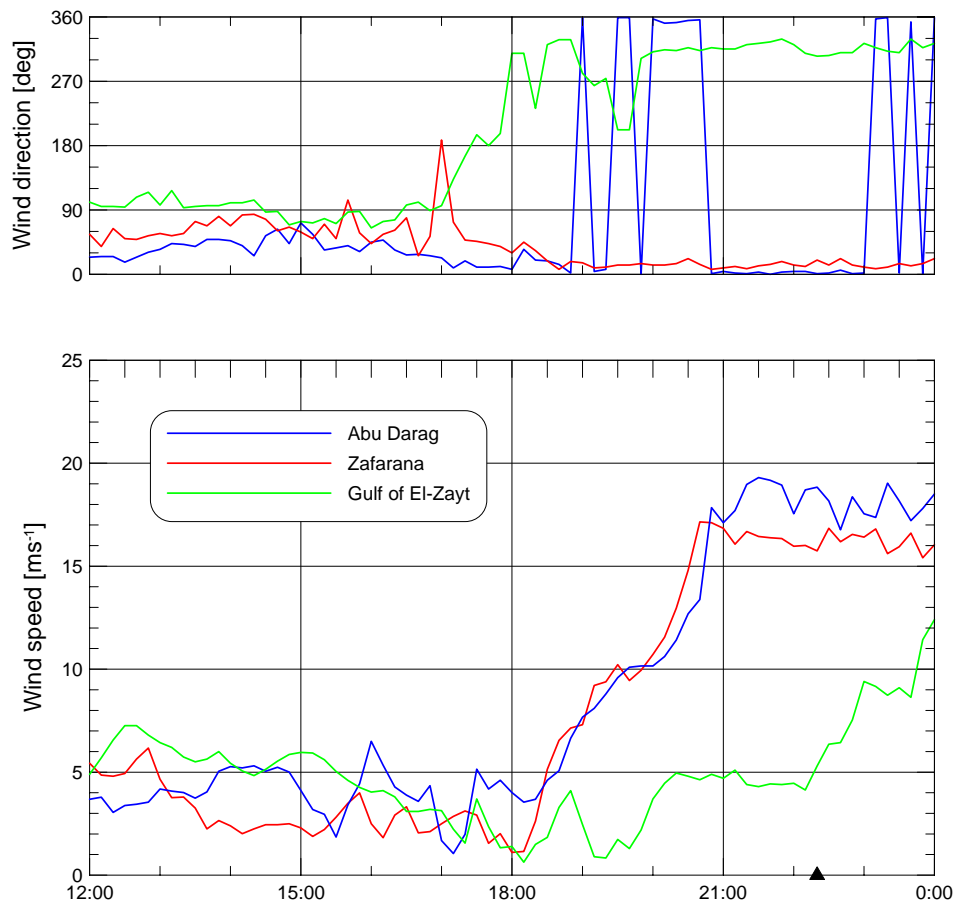
Figure 14-1 Meteorological data fromAbu Darag, Zafarana and Gulf of El-Zyat on the5 April 1999. The ERS SAR overpass time is indicated with a '▲'

Table 14-1 Observations and predictions for 5 April 1996: site name, measured mean wind speed U at 24.5 m a.g.l., wind direction D and temperature T. Estimated wind speed U_e and direction D_e at 10 m a.s.l., about 5 km offshore. U_{SAR} is from the SAR wind speed map.

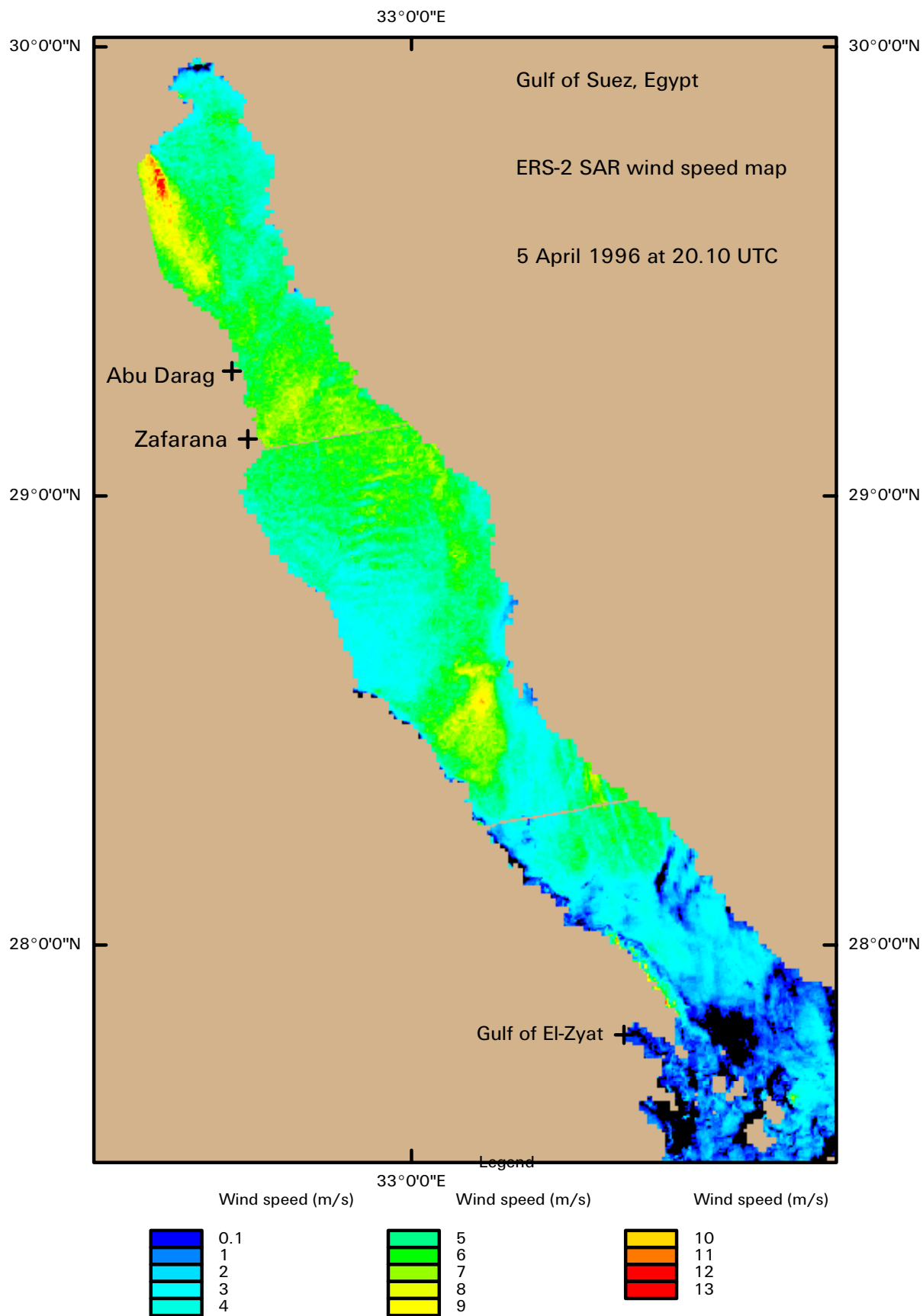| Met. station	U	D	T	U_e	D_e	U_{SAR}
	[m s^{-1}]	[°]	[°C]	[m s^{-1}]	[°]	[m s^{-1}]
Abu Darag	15.74	001	19.6	15.66	001	6.3
Zafarana	18.83	020	19.8	18.45	020	7.5
Gulf of El-Zayt	5.30	305	22.9	6.25	305	1.5

Figure 14-2 ERS SAR wind speed map of Gulf of Suez, Egypt. 5 April 1996 at 20.10 UTC. Courtesy of Birgitte Furevik, NERSC.

Case II: 2 October 1999

The second case is from 2 October 1999 at 20.07 UTC. It covers only the southern part of the Gulf of Suez and part of the Red Sea. The ERS SAR wind speed map is shown in Figure 14-4 calculated for a wind direction of 246°. Meteorological observations from Hurghada at the time of the satellite overpass are shown in Figure 14-3 and Table 14-2. Streaks in the image data shows the wind direction is from the North. A local maximum in wind speed around 10 m s^{-1} is found North of the Gulf of El-Zayt. Hurghada is located 10 km south of the image. WAsP has been used to calculate the local wind speed at 10 m above sea level 5 offshore from Hurghada. This result and SAR wind speed observations in the southern part of the image are compared in Table 14-2. It is seen that the SAR wind speed of 3.8 m s^{-1} is lower than the estimated wind speed of 5.0 m s^{-1}. But as may be noted in the image (Figure 14-4) winds up to 6.4 m s^{-1} are also found in the southern part of the image. Local wind gradients within few kilometer could also be found further south.
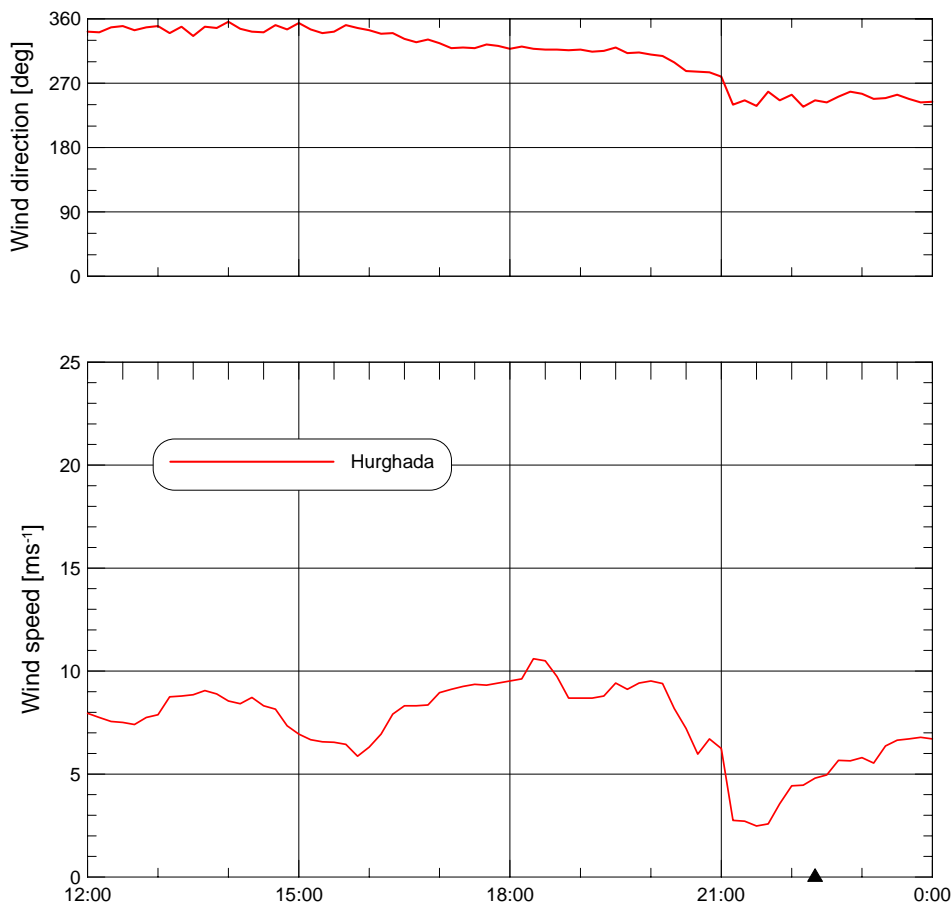

Figure 14-3 Meteorological data from Hurghada on the 2 October 1999. The ERS SAR overpass time is indicated with a '▲'

Table 14-2 Observations and predictions for 2 October 1999: site name, measured mean wind speed U *at 24.5 m a.g.l., wind direction* D *and temperature* T. *Estimated wind speed* U$_e$ *and direction* D$_e$ *at 10 m a.s.l., about 5 km offshore* U$_{SAR}$ *is from the SAR wind speed map.*

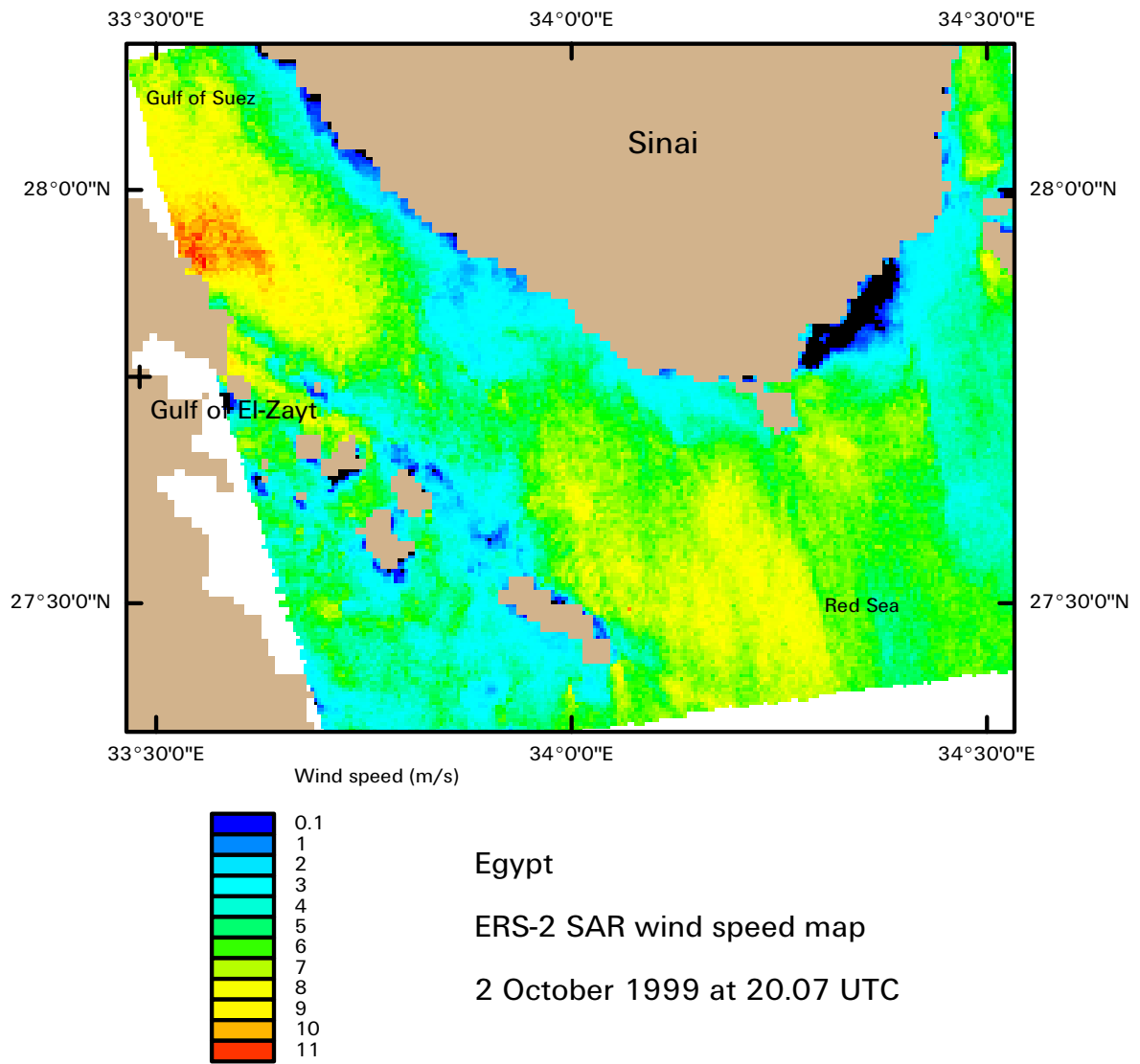| Met. station	U	D	T	U_e	D_e	U_{SAR}
	[m s^{-1}]	[°]	[°C]	[m s^{-1}]	[°]	[m s^{-1}]
Hurghada	4.80	246	27.8	5.08	246	3.8

*Figure 14-4 ERS SAR wind speed map of Gulf of Suez, Egypt. 2 October 1999
at 20.07 UTC. Courtesy of Birgitte Furevik, NERSC.*

Case III: 10 November 1999

The third case is from 10 November 1999 at 20.13 UTC. It is a scene from the middle part of the Gulf of Suez Figure 14-6. The meteorological observation at Zafarana at 24.5 m is a wind speed of 4.57 m s^{-1}. The daily observations are given in Figure 14-5. The wind direction is from the west. This wind direction was used in the SAR wind speed algorithm. WAsP has been used to calculate the 10 m sea level wind speed and the result is shown in Table 14-3 and compared to the observations in the SAR wind speed map. There is a strong wind gradient from 5.3 m s^{-1} to 2.5 m s^{-1} i.e. average 3.9 m s^{-1} at a distance of 5 km offshore from Zafarana. The result compares reasonably.
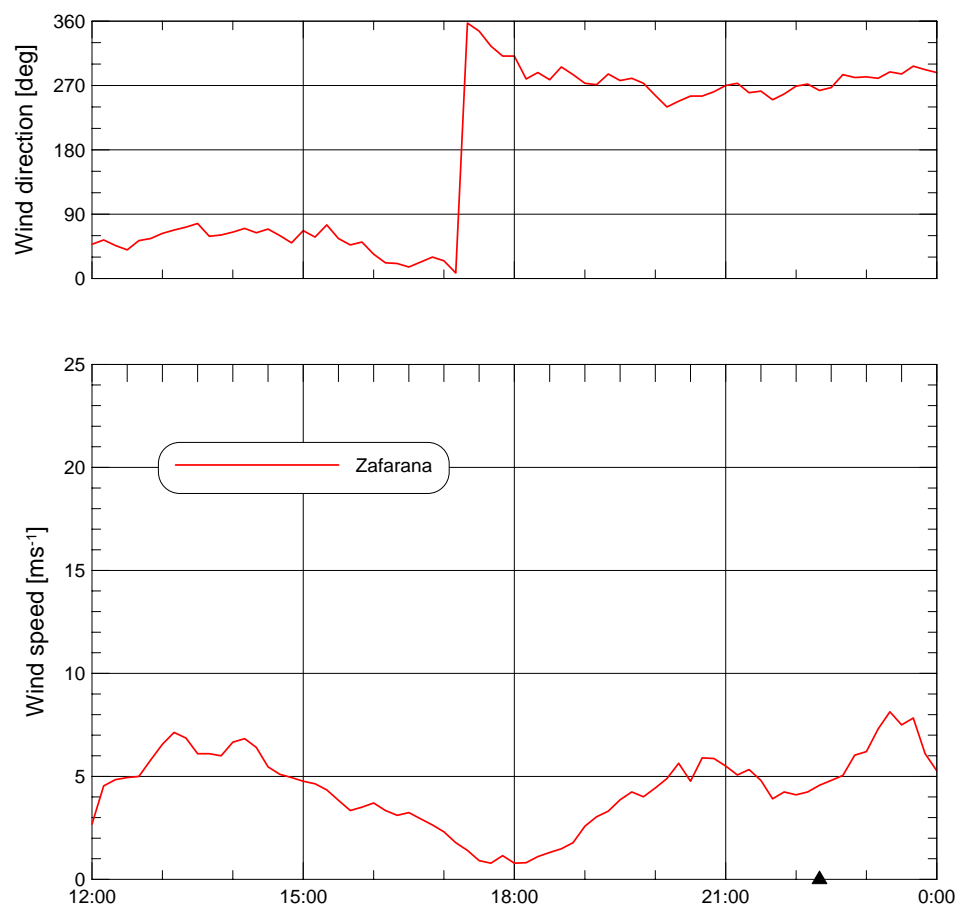
Figure 14-5 Meteorological data from Zafarana on the 10 November 1999. The ERS SAR overpass time is indicated with a '▲'

Table 14-3 Observations and predictions for 10 November 1999: site name, measured mean wind speed U *at 24.5 m a.g.l., wind direction* D *and temperature* T. *Estimated wind speed* U$_e$ *and direction* D$_e$ *at 10 m a.s.l., about 5 km offshore.* U$_{SAR}$ *is from the SAR wind speed map.*

Met. station	U	D	T	U_e	D_e	U_{SAR}
	[m s^{-1}]	[°]	[°C]	[m s^{-1}]	[°]	[m s^{-1}]
Zafarana	4.57	263	18.1	5.03	263	3.9

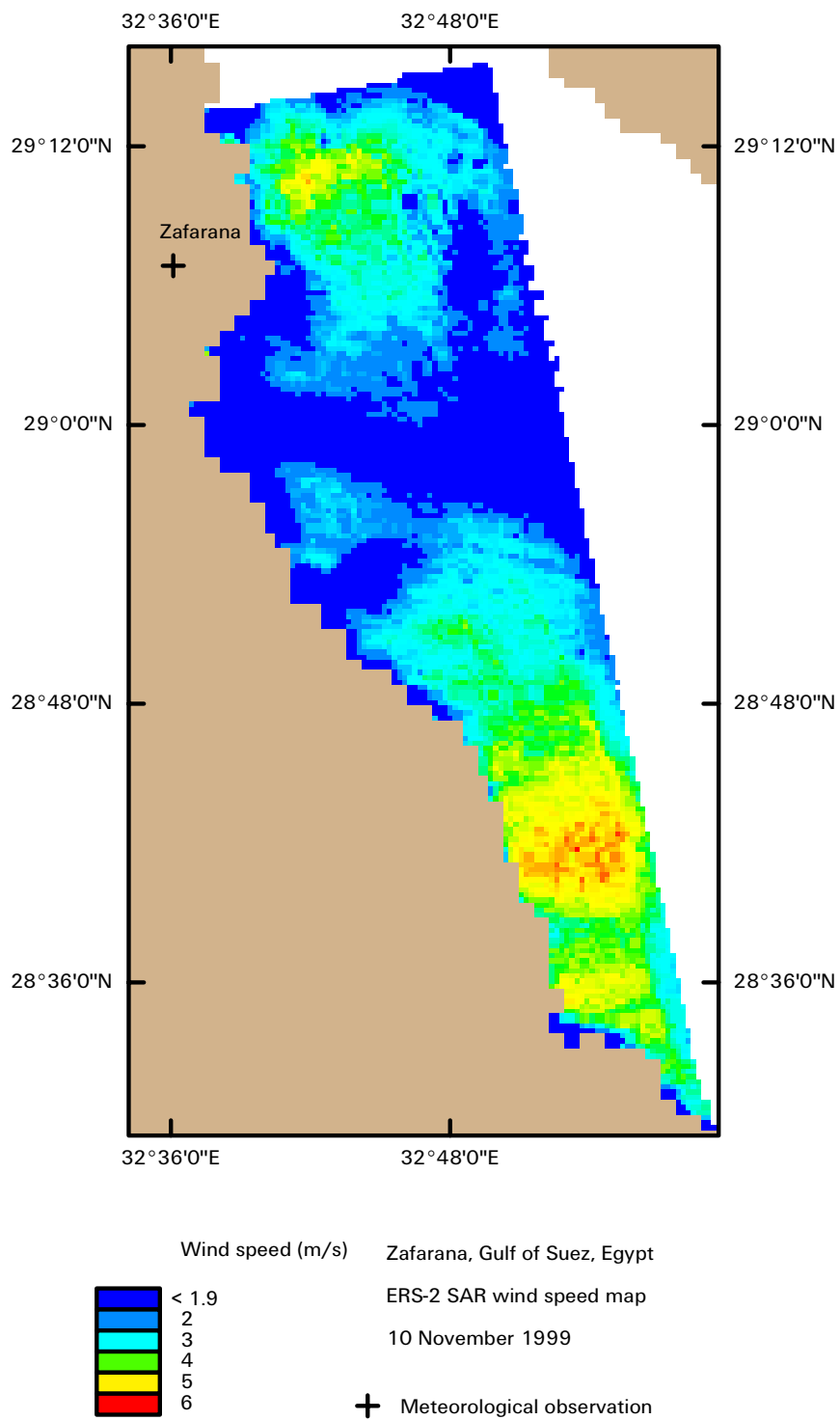*Figure 14-6 ERS SAR wind speed map of Gulf of Suez, Egypt. 10 November 1999 at 20.13 UTC. Courtesy of Birgitte Furevik, NERSC.*

Linear correlation analysis between the WAsP wind speed results at 5 km off-shore distance and the SAR wind speed maps is shown in Figure 14-7. All SAR wind speeds are systematically lower than the WAsP wind speed. For two observations the differences are as much a 10 m s^{-1}, for one observation 5 m s^{-1} and for two observations only 1.3 m s^{-1}. The data set is rather small and no clear conclusions can be made. The positive bias of 1.3 m s^{-1} is opposite to the values found for Horns Rev (section 11.11) and Maddalena (section 12.9). It may be that the two data points for wind speeds larger than 15 m s^{-1} are outliers. The average difference between in-situ wind speed and SAR wind speed is 2.5 m s^{-1}. That is in better agreement with the previous findings. Validation studies are challenging in the Gulf of Suez due to the pronounced spatial wind speed gradients in all the SAR scenes. Meteorological observations at coastal stations may be difficult to extrapolate far offshore.
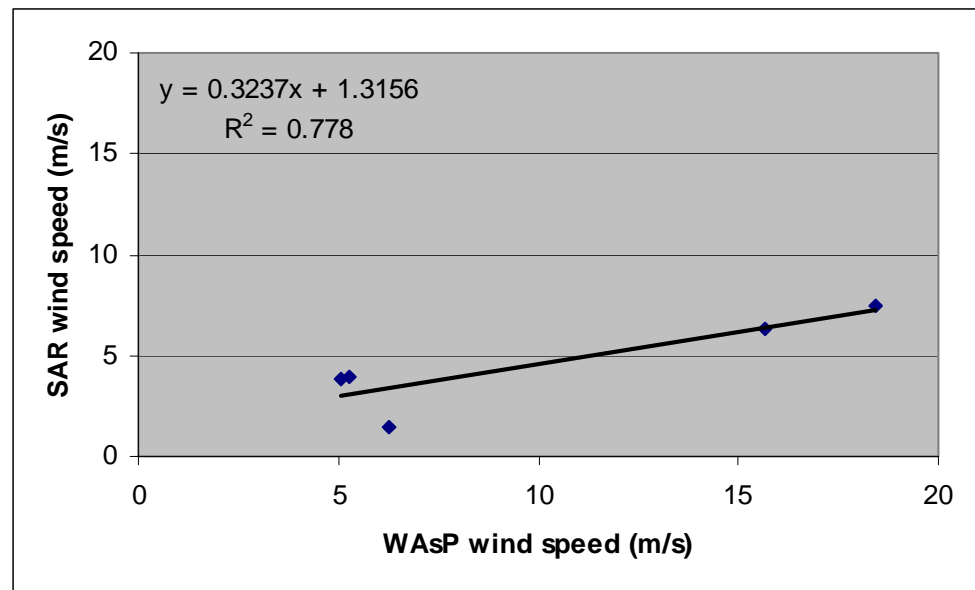

The chart displays: y = 0.3237x + 1.3156, R^2 = 0.778, with SAR wind speed (m/s) on the y-axis and WAsP wind speed (m/s) on the x-axis.

Figure 14-7 Linear correlation between wind speed from WAsP 5 km offshore and SAR wind speed observations.

14.3 Summary on Gulf of Suez

The SAR wind speed maps for the Gulf of Suez area in Egypt have been retrieved from the CMOD-IFR2 model with input of wind direction from local in-situ observations collected at the coast. The SAR scenes map only three cases, hence no clear statistically-based conclusions can be made. The finding though, seems to be a negative bias in the SAR wind speed maps as compared to the wind speeds offshore as calculated by WAsP model. Validation studies are challenging in the Gulf of Suez due to the pronounced spatial wind speed gradients that are obvious in all three cases.

15 Summary on comparison analysis

SAR wind speed maps are calculated from ERS-2 SAR satellite scenes by use of the CMOD-IFR2 with wind directions taken either from in-situ observation and/or wind streaks in the SAR scenes themselves. The SAR streaks are found from Fourier analysis in the scenes. The processing of SAR scenes is done at NERSC.

The SAR wind speed maps have been compared to in-situ observations and model results for three very different sites. A general finding from all the sites is that the SAR wind speed maps are negatively biased. At the Danish site in the North Sea the bias is around -2 m s^{-1}; at the Italian site in the Mediterranean Sea the bias is around -3 m s^{-1} and at the Egyptian site in the Gulf of Suez the bias is maybe even larger. The uncertainty on the bias is due to the very limited data set from the sites.

The most comprehensive set of observations is available from the Horns Rev site in Denmark. The SAR wind speed validation analysis for this site is performed by comparing footprint area-averages of SAR wind speeds to in-situ observations from a 62 m tall meteorological mast positioned 14 km offshore. There is a total of 16 cases encompassing different wind speed regimes, wind directions and stabilities. The local scale model LINCOM and the mesoscale model KAMM2 have been used for calculating the offshore wind field. The data set has been used to investigate several more specific issues such as

- different methods of footprint area-averaging,
- the effect of sea bottom topography and tide,
- the influence of the near-coastal zone on the SAR-derived wind speeds,
- the development of marine internal boundary layers,
- the errors associated with speckle noise,
- the uncertainty on wind direction between in-situ and SAR wind streaks

For a description on the results on these specific issues, please refer to section 11.11.

The Maddalena site in Italy has been investigated only for 5 cases and this makes the data set too small for linear correlation analysis. The comparison results between SAR wind speeds, WAsP local scale and KAMM2 mesoscale model for an offshore box-area located East of the Maddalena site shows a negative bias on the SAR wind speed maps. The KAMM2 model results are much closer to the SAR wind speeds and this may be due to the rather large horizontal domain used include mountainous areas at the island Corsica. The WAsP model did only include a smaller local area for the model calculations. The finding indicates that large-scale features have a significant influence to the winds at in the investigated area.

The site in Egypt is characterized by very strong wind speed gradients in the Gulf of Suez. This is what makes the area an excellent area for wind farming, yet a challenging area for SAR wind speed validation studies. Only three cases have been investigated and several issues remain to be looked into e.g. the dependence on the input of wind direction in the CMOD-IFR2 model. The number of meteorological masts with in-situ observations is very large in the area but not fully included in the present study. The result from the site in Egypt con-

firms the likelihood of a general negative bias in the SAR wind speed maps. Otherwise this small part of the study is inconclusive.

The validation results for the sites in Denmark, Italy and Egypt are graphed in Figure 15-1. Most data points lie below the 1:1 line. A linear regression (excluding the two outliers from Egypt) gives $y = 1.1158x - 2.3961$ with R^2 0.84.
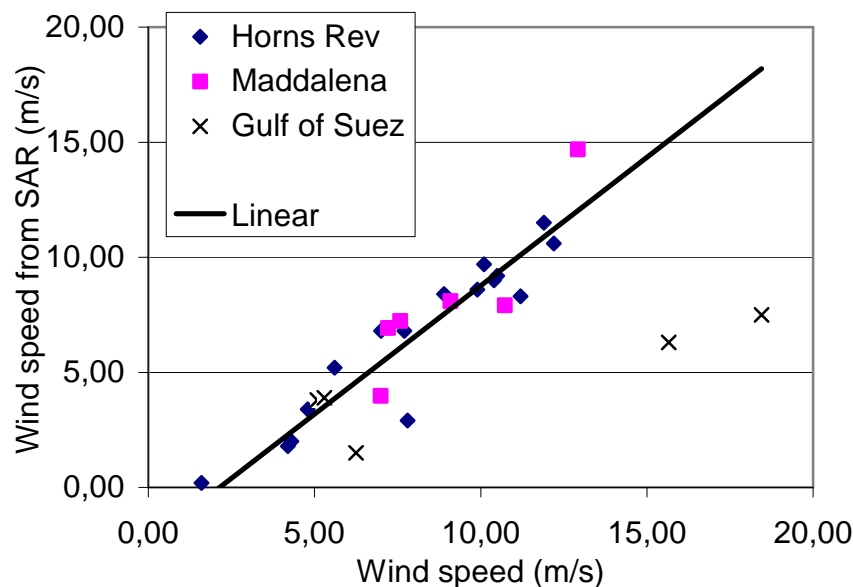

Figure 15-1 Validation of SAR wind speed to offshore in-situ observations at Horns Rev, Denmark; KAMM2 mesoscale results at Maddalena in Italy and WAsP results for Gulf of Suez in Egypt.

The wind speeds for Horns Rev are from an in-situ mast and the SAR wind speeds the area-average of a footprint upwind of this mast. For Maddalena the wind speeds are the results of the KAMM2 mesoscale model and the results from KAMM2 and SAR are from a box-area in the ocean. The WAsP model results in the Gulf of Suez are compared to a box-average of SAR wind speeds in the area. For Horns Rev and Gulf of Suez the in-situ wind directions were used in the CMOD-IFR2 whereas the SAR wind streaks were used at the Maddalena site.

16 Conclusion

The goal of the validation study is to assess the accuracy of offshore wind speed maps from satellite SAR. The accuracy is a very important factor for the possible use of a satellite SAR wind speed maps for offshore wind resource prediction. The validation study deals with ERS-2 SAR satellite scenes.

The comparison analysis at the Horns Rev site shows the promising result of a standard error of only 0.61 m s-1 on the linear correlation between footprint area-averaged SAR wind speed maps and in-situ observations. The unique data set at Horns Rev allows for the first time a footprint comparison. This method of comparison is from a physical point of view superior to box-averages. It ap-

pears however that simple footprint averaging is necessary instead of the advanced stability corrected and weighted pixel-by-pixel footprint. This is due to speckle noise in the 400 m by 400 m SAR wind map resolution.

In addition to the excellent meteorological observation time series at Horns Rev, the site is simple, hence atmospheric flow models can capture the local wind fields well. The site is situated in the North Sea 15 km west of the coast of Jutlandia. The terrain in Jutland is flat. Model results from the microscale LINCOM and the mesoscale KAMM2 model show good agreement to the SAR wind speed maps. At the same time the model results reveal important issues on the validity of SAR wind speed maps, e.g. that the near-coastal zone of around 800 m have a strong negative bias in the SAR wind speed maps. Another important feature of the SAR wind speed maps are that tidal currents near complex bottom topography is evident is some cases. An in-depth analysis of this phenomenon is beyond the scope of the validation study but observations on current, waves, tidal height and bathymetry are available.

The validation study has focused on wind speed in different regimes, seasonal patterns and atmospheric stability. The results show that for offshore flow in stable conditions a marine internal boundary layer has developed. Therefore the wind in at the surface is decoupled from the wind at higher levels, and the SAR wind speed maps underestimates the wind speed at 10 m (and above) strongly. Stable conditions prevailed in spring and summer whereas unstable conditions appeared all year round. High wind speeds were always associated with near-neutral conditions.

At the site Maddalena in Italy the atmospheric flow is more challenging to model due to complex topography of Corsica and Sardinia, the two large islands near La Maddalena and the rugged cliff coastlines. The local scale model WAsP is good for modelling the flow very close to the local area including coastal effects of distances less than 5 km. The WAsP model results compares well to the SAR wind speed maps in the near coastal regions. However further offshore the KAMM2 mesoscale model results seem superior. This is explained by the fact that the high orography of Corsica has a significant influence to the atmospheric flow far offshore. Satellite SAR wind speed maps from Maddalena include low, medium and high wind speeds, but it should be noted that such a definition should vary for each region dependent on the overall wind climate. The winds at Maddalena are lower than at Horns Rev.

For Gulf of Suez the winds, on the other hand, are very high. Only three cases of SAR wind speed maps have been compared to WAsP model results. The SAR wind speed maps show strong horizontal gradients in wind speeds. The gradients are known and they are exactly what makes the Gulf of Suez a very good site for wind farming. At the same time it is challenging to perform wind speed validation in the region.

The overall conclusion of the validation study at the three test sites located in very different regional climates, is that the SAR wind speed maps are biased negatively around 2 m s^{-1} and that the correlation R^2 is around 0.85 (0.88 for the combined data set). The main limitation of the validation analysis is that it was conducted on only 16 cases in Denmark, 5 cases in Italy and 3 cases in Egypt. The statistics of the linear correlation analysis could be improved by analysing a larger data set.

This leads to the issue "How many satellite SAR scenes are necessary for predicting wind resources?". The answer to this was found to be that around 60-70 randomly selected scenes are required to characterize the mean wind speed and Weibull c parameter, while of the order of 150 images are required to obtain a variance estimate, and nearly 2000 are needed to obtain a robust estimate of energy density (or Weibull k). This is under the assumption of no error in the SAR wind speed maps and for an uncertainty of ± 10% at a confidence level of 90% and assuming that no strong diurnal cycle exists in the wind speed signal.

The final conclusion of the validation study on the accuracy of SAR wind speed maps is that these have a random error of around 0.61 m s^{-1} and a bias of around 2 m s^{-1}. For offshore wind resource calculations it will be necessary to obtain around 60-70 scenes for a given site to calculate the mean wind speed and Weibull c parameter. This number of satellite scenes is available for a number of sites, yet for some sites far too few scenes are available. More new scenes will become available through time from ERS-2, RADARSAT-1 and –2 as well as ENVISAT.

17 Recommendations for applied use

The overall goal of the WEMSAR project is to develop a tool useful for offshore wind energy planning. The offshore wind resources are a major issue in the planning phase.

At the very early stage a feasibility study may be relevant and at this point in time a very sparse amount of wind speed information may be available for a given site, region or country. Therefore the existing observations from satellite SAR or satellite scatterometer observations of wind speed and wind directions offshore may offer a unique opportunity to learn about the offshore wind fields of the local area. The advantage of satellite SAR is the high spatial resolution (eg. 400 m) as compared to eg. NCAR/NCEP reanalysis data (eg. 200 km).

Based on a few selected satellite SAR wind speed maps some typical local scale wind patterns may be quantified. The spatial variations and features in the images may aid in the planning of siting meteorological masts such that these measure for a representative area or maybe aim for very special local wind fields. It should be noted that SAR wind speed maps in the nearest 800 m coastal zone are negatively biased very strongly and therefore cannot be used.

In case the offshore wind climate should be mapped from satellite SAR wind speed maps, at least 60-70 randomly selected scenes should be obtained for the analysis. The statistical analysis of the SAR wind speed maps should include a footprint area-averaging technique is possible (dependent upon the outlay of an expected wind farm) as well as a WAsP-like calculation to hub-height.

Possible errors in the SAR wind speed maps from eg. ocean currents, tidal effects, bathymetry, slicks and atmospheric features eg. offshore flow in stable conditions (marine internal boundary layer) should be investigated prior to performing the wind resource calculation.

A tool for using satellite SAR wind speed maps for offshore wind resources could include the following steps:

1. SAR PRI data reading and calibration
2. SAR image Fourier-transform for wind direction retrieval
3. CMOD-IFR2 with input of wind direction (from Fourier, NCAR/NCEP or other sources) for wind speed map retrieval
4. Sub setting of wind speed maps and stacking into footprint/microscale software
5. Presentation tool for viewing wind speed map, wind direction maps and wind resource maps
6. Statistical display of wind resource parameters

Several questions on the tool remains open e.g whether it will be a "service" from the current WEMSAR partners, a sellable software (including course/training), a web-based interactive tool, or something else. This will, in part, be decided from the preferences and needs of the potential costumers.

It is recommended that all wind speed maps are made available to the potential users as a binary AND an ASCII-formatted file of wind speed arranged in a longitude-latitude array. For wind direction a similarly defined file should be made available. Further, should pseudo-colored images in GIF, TIF or JPG format be displayed with a colour scale for wind speed and arrows for wind direction. This is for the visual interpretation (quicklook) of the SAR wind speed data.

Future developments should include satellite-derived wind speed products derived from other sensors than the ERS-1/2 SAR's e.g. from RADARSAT-1/2 and ASAR ENVISAT observations.

Larger scale wind resource maps should be based on scatterometer observations of wind speed and wind direction. For this purpose the scatterometer observations are ideal due to the more frequent observation rate from ERS scatterometer and Quikscat.

18 References

Adrian, G.: 1994, 'Zur Dynamik Des Windfeldes Über Orographisch Geglied-ertem Gelände', *Berichten Deutscher Wetterdienst* **188**, 1-142

Adrian, G.: 1998, 'Das Karlsruher Atmosphärische Mesoskalige Modell Prof. Dr. Franz Fiedler zum 60. Geburtstag, VBIMK, **21**, editor K. D. Beheng, IMK, 1998, Karlsruhe, Germany.

Adrian, G. and Fiedler, F.: 1991, 'Simulation of Unstationary Wind and Temperature Fields Over Complex Terrain and Comparison With Observations', *Beitrage Physical Atmosphere* **64** , 27-48

Astrup, P., Jensen, N. O., and Mikkelsen, T.: 1996, 'Surface Roughness Model for LINCOM'**Risø-R-900(EN)**,

Astrup, P., Larsen, S. E., Rathmann, O., Madsen, P. H., and Højstrup, J.: 1999, 'WAsP Engineering - Wind Flow Modelling Over Land and Sea'179-184

Astrup, P. and Larsen, S. E.: 1999, 'WAsP Engineering Flow Model for Wind Over Land and Sea'**Risø-R-1107(EN)**,

Atlas, R., Hoffman, R. N., Leidner, S. M., Sienkiewicz, J., Yu, T.-W., .Bloom, S. C., Brin, E., Ardizzone, J., Terry, J., Bungato, D., and Jusem, J. C.: 2001, 'The Effects of Marine Winds From Scatterometer Data on Weather Analysis and Forecasting', *Bulletin of the American Meteorological Society* **82**, 1965-1990

Attema, E., Desnos, Y.-L., and Duchossiois, G.: 2000, 'Synthetic Aperture Radar in Europe: ERS, Envisat, and Beyond', *John Hopkins APL Technical Digest* **21**, 155-169

Barthelmie, R.J., Courtney, M.S., Højstrup, J. and Sanderhoff, P., 1994. The Vindeby Project: a description. Risø-R-741(EN), Risø National Laboratory, Denmark.

Barthelmie, R.J., Grisogono, B. and Pryor, S.C., 1996b. Observations and simulations of diurnal cycles of near-surface wind speeds over land and sea. Journal of Geophysical Research (Atmospheres), 101(D16): 21,327-21,337.

Barthelmie, R.J., Courtney, M.S., Højstrup, J. and Larsen, S.E., 1996a. Meteorological aspects of offshore wind energy - observations from the Vindeby wind farm. Journal of Wind Engineering and Industrial Aerodynamics, 62(2-3): 191-211.

Barthelmie, R.J., Højstrup, J. and Courtney, M.S., 1995. Assessment of the wind power resource in the coastal zone using results from the Vindeby project. In: J.A. Halliday (Editor), *Proceedings of the 17th British Wind Energy Association Conference*. Mechanical Engineering Publications Limited, University of Warwick, UK, pp. 231-236.

Barthelmie, R.J., 1999. Monitoring offshore wind and turbulence characteristics in Denmark, Proceedings of the 21st British Wind Energy Association Conference. Professional Engineering Publishing, Cambridge, pp. 311-321

Bastiaanssen, W. G. M., Pelgrum, H., Wang, J., Ma, Y., Moreno, J. F., Roerink, G. J., and van der Wal, T.: 1998, 'A Remote Sensing Surface Energy Balance Algorithm for Land (SEBAL) - 2. Validation', *Journal of Hydrology* **213**, 213-229

Beal, R. C.: 2000, 'Toward an International Strom Watch Using Wide Swath SAR', *John Hopkins APL Technical Digest* **21**, 12-20

Beljaars, A.C.M., Holtslag, A.A.M. and van Westrhenen, R.M., 1989. Description of a software library for the calculation of surface fluxes. Technical report TR-112, KNMI, De Bilt, Netherlands.

Bergstrom, H., Johansson, P.-E. and Smedman, A.-S., 1988. A study of wind speed modification and internal boundary-layer heights in a coastal region. Boundary-Layer Meteorology, 42(4): 313-335.

Borreson, J.A., 1987. Wind Atlas for the North Sea and the Norwegian Sea. Norwegian University Press, Oslo, 346 pp.

Brown, R. A.: 2000a, 'On Satellite Scatterometer Model Functions', *Journal of Geophysical Research* **105**, 29195-29205

Brown, R. A.: 2000b, 'Serendipity in the Use of Satellite Scatterometer, SAR and Other Sensor Data', *John Hopkins APL Technical Digest* **21**, 21-26

Calkoen, C. J., Hesselmans, G. H. F. M., and Wensink, G. J.: 1998, 'The Use of Radar Imagery to Assess the Bottom Topography of Shallow Seas', *International Hydrographic Review* **75**, 43-50

Calkoen, C. J., Hesselmans, G. H. F. M., Wensink, G. J., and Vogelzang, J.: 2001, 'The Bathymetry Assessment System: Efficient Depth Mapping in Shallow Seas Using Radar Images', *International Journal of Remote Sensing* **22**, 2973-2998

Charnock, H.: 1955, 'Wind Stress on a Water Surface', *Quarterly Journal of the Royal Meteorological Society* **81**, 639-640

Clemente-Colón, P. Yan,X.-H..: 2000, 'Low-Backscatter Ocean Features in Synthertic Aperture Radar Imagery', *John Hopkins APL Technical Digest* **21**, 116-121

DHI/50395/2.ed.Nov-2001/PH/KAE. 2001. Bathymetry near Horns Rev, Denmark.

Dixon, J.C. and Swift, R.H., 1984. The dependence of wind speed and Weibull characteristics on height for offshore winds. Wind Engineering, 8(2): 87-98.

DWD Deutscher Wetterdienst Maps 1998-2000

EMD. 2001a. Orographic data for Denmark. Energi- og Miljødata, Aalborg, Denmark.

EMD. 2001b. Roughness data for Denmark. Energi- og Miljødata, Aalborg, Denmark.

ESA: 1993, 'Optical to ERS-1 SAR: A Cross-Over Course at ESRIN'

Frank, H. P. Larsen. S. E. Højstrup. J.: 1997, 'Simulated Wind Power Offshore Using Different Parametrizations for the Sea Surface Roughness', *Wind Energy* **3**, 67-79

Garratt, J. R.: 1992, 'The Atmospheric Boundary Layer'1-316

Gash, J. H. C.: 1986, 'A Note on Estimating the Effect of a Limited Fetch on Micrometeorological Evaporation Measurements', *Boundary-Layer Meteorology* **35**, 409-413

GLCC. 2001. Global Land Cover Characterization. US Geological survey (USGS) data from the web site of the Land processes Distributed Active Archive Center at http://edcdaac.usgs.gov/glcc/glcc.html

GTOPO30. 2001. Global 30 Arc-Second Elevation Data Set. From the web site of the Land processes Distributed Active Archive Center at http://edcdaac.usgs.gov/gtopo30/gtopo30.html

Gower, J. S. S.: 2000, 'Wind, Slick, and Fish Boat Observations With Radarsat ScanSAR', *John Hopkins APL Technical Digest* **21**, 68-74

Gryning, S. E., Holtslag, A. A. M., Irwin, J. S., and Sivertsen, B.: 1987, 'Applied Dispersion Modelling Based on Meteorological Scaling Parameters', *Atmospheric Environment* **21**, 79-89

Hasager, C. B., , Frank. H. P., and Furevik, B. R.: 2002, 'On Offshore Wind Energy Mapping Using Satellite SAR', *Canadian Journal of Remote Sensing* **28**, x-x(in press)

Hasager, C. B.: 2000a, 'Wind Energy Mapping Using Synthetic Aperture Radar'259-265

Hasager, C. B. Frank. H.: 2000b, 'Off-Shore Wind Energy Mapping Using Satellite SAR', *CERSAT News* **11**, 10-11

Horst, T. W. and Weil, J. C.: 1994, 'how Far Is Far Enough - The Fetch Requirements For Micrometeorological Measurement Of Surface Fluxes', *Journal of Atmospheric and Oceanic Technology* **11**, 1018-1025

Horstmann, J., Koch, W., Lehner, S., and Tonboe, R.: 2000a, 'Wind Retrieval Over the Ocean Using Synthetic Aperture Radar With C-Band HH Polarization', *IEEE Transactions on Geoscience and Remote Sensing* **38**, 2122-2131

Horstmann, J., Lehner, S., Koch, W., and Tonboe, R.: 2000b, 'Computation of Wind Vectors Over the Ocean Using Spaceborne Syntheric Aperture Radar', *John Hopkins APL Technical Digest* **21**, 100-107

Hsieh, C. H., Katul, C., and Chi, T. W.: 2000, 'An Approximate Analytical Model for Footprint Estimation of Scalar Fluxes in Thermally Statified Atmospheric Flows', *Advanced Water Research* **23**, 765-772

Hsu, S.A., 1988. Coastal Meteorology. Academic Press Inc., London, 260 pp.

Johannessen, O. M. E. H. F. B. S. S.: 2001, 'WEMSAR Data Access, SAR Wind Energy Retrieval Validation'**208**, 1-16

Johannessen, O. M. Sandven. S. Furevik. B. Kloster. K. Espedal. H.: 2000, 'WEMSAR Review of Wind Retrieval Algorithms'**194**, 1-23

Johnson, H. K. Højstrup. J. Vested. H. J. Larsen. S. E.: 1998, 'On the Dependence of Sea Surface Roughness on Wind Waves', *Journal of Physical Oceanography* **28**, 1702-1716

Knauss, J. A.: 1978, 'Introduction to Physical Oceanography'1-338

Kramer, H. J.: 1996, 'Observation of the Earth and Its Environment'**3rd**, 1-960

Lehner, S. Horstmann. J. Koch. W. Rosenthal. W.: 1998, 'Mesoscale Wind Measurements Using Recalibrated ERS SAR Images', *Journal of Geophysical Research* **103**, 7847-7856

Lehner, S., Schulz-Stellenfleth. J., Schättler, Breit. B. H. Horstmann, J.: 2000, 'Wind and Wave Measurements Using Complex ERS-2 SAR Wave Mode Data', *IEEE Transactions on Geoscience and Remote Sensing* **38**, 2246-2257

Lillesand, T. M. Kiefer. R. W.: 1987, 'Remote Sensing and Image Interpretation'**2**, 1-721

Mahrt, L. et al., 1998. Heat flux in the coastal zone. Boundary Layer Meteorology, 86: 421-446.

Mahrt, L. et al., 2001. Vertical structure of turbulence in offshore flow durign RASEX. Boundary Layer Meteorology, 100: 47-61.

Mahrt, L. et al., 1996. Sea surface drag coefficients in RASEX. Journal of Geophysical Research, 101: 14,327-14,335.

Mastenbroek, K.: 1998, 'High-Resolution Wind Fields From ERS SAR', *ESA-Earth Observation Quarterly* **59**, 20-22

Monaldo, F.: 2000, 'The Alaska SAR Demonstration and Near-Real-Time Synthetic Aperture Radar Winds', *John Hopkins APL Technical Digest* **21**, 75-79

Monaldo, F. M. Thompson. D. R. Beal. R. C. Pichel. W. G. Clemente.-Colon. P.: 2001, 'Comparison of SAR-Derived Wind Speed With Model Predictions and Ocean Byou Measurements', *IEEE Transactions on Geoscience and Remote Sensing*

Mortensen, N. G., Heathfield, D. N., Landberg, L., Rathmann, O., Troen, I., and Petersen, E. L.: 2000, 'Wind Atlas Analysis and Wind Atlas Analysis and Pllication Program:WAsP 7.0 Help Facility'**ISBN 87-550-2667-2**, 1-277

Mortensen, N. G., Landberg, L., Troen, I., and Petersen, E. L.: 1993, 'Wind Atlas Analysis and Application Program (WAsP). Vol. 2. Users's Guide'**Risø-I-666(EN)(v.2)**, 1-133

Mortensen, N. G. and Said, U. S.: 2002, 'Wind Atlas for the Gulf of Suez. Measurements and Modelling 1991-1995'**ISBN87-550-2143-3**, 1-110

Mourad, P. D.: 1999, 'Footprints of Atmospheric Phenomena in Synthetic Aperture Radar Images of the Ocean Surface: a Review'269-290

Mourad, P. D. Thompson. D. R. Vandemark.: 2000, 'Extracting Fine-Scale Wind Fields From Synthetic Aperture Radar Images of the Ocean Surface', *John Hopkins APL Technical Digest* **21**, 108-116

NCEP Reanalysis Data 2002

Neckelmann, S. Petersen. J.: 2000, 'Evaluation of the Stand-Alone Wind and Wave Measurement Systems for Horns Rev 150KW Offshore Wind Farm in Denmark' Proceedings of OWEMES offshore wind energy in Meidterranean and other European Seas, 13-15 April 2000, Sircusa, Sicily, Italy, ATENA/ENEA; Rome

Offiler, D.: 1994, 'The Calibration of ERS-1 Satellite Scatterometer Winds', *Journal of Atmospheric and Oceanic Technology* **11**, 1002-1017

Panofsky, M.A. and Dutton, J.A., 1984. Atmospheric turbulence. Wiley, New York.

Petersen, E.L., Troen, I., Frandsen, S. and Hedegaard, K., 1981. Windatlas for Denmark. RISØ-R-428, Risø National Laboratory, Roskilde, Denmark

Pryor, S.C. and Barthelmie, R.J., 1998. Analysis of the effect of the coastal discontinuity on near-surface flow. Annales Geophysicae, 16: 882-888.

Pryor, S.C. and Barthelmie, R.J., 2002. Statistical analysis of flow characteristics in the coastal zone. Journal of Wind Engineering and Industrial Aerodynamics, 90: 201-221.

Pryor, S.C. and Barthelmie, R.J., 2002. Comparison of potential power production at on- and off- shore sites. Wind Energy, In press

Quilfen, Y., Chapron, B., Elfouhaily, T., Katsaros, K., Tournadre, J., and Chapron, B.: 1998, 'Observation of Tropical Cyclones by High-Resolution Scatterometry', *Journal of Geophysical Research* **103**, 7767-7786

Rice, J.A., 1995. Mathematical statistics and data analysis. Duxbury Press, Belmont, California, 602 pp

Romeiser, R. and Alpers, W.: 1997, 'An Improved Composite Surface Model for the Radar Backscattering Cross Section of the Ocean Surface .2. Model Response to Surface Roughness Variations and the Radar Imaging of Underwater Bottom Topography', *Journal of Geophysical Research-Oceans* **102**, 25251-25267

Sikora, T. D., Young, G. S., Shirer, H. N., and Chapman, R. D.: 1997, 'Estimating Convective Atmospheric Boundary Layer Depth From Microwave Radar Imagery of the Sea Surface', *Journal of Applied Meteorology* **36**, 833-845

Sikora, T. D. and Thompson, D. R. B. J. C.: 2002, 'Testing the Diagnosis of Marine Atmospheric Boundary-Layer Structure From Synthetic Aperture Radar', *John Hopkins APL Technical Digest* **21**, 94-99

Smedman, A., Hogstrom, U., Bergstrom, H., Rutgersson, A., Kahma, K. K., and Pettersson, H.: 1999, 'A Case Study of Air-Sea Interaction During Swell Conditions', *Journal of Geophysical Research-Oceans* **104**, 25833-25851

Smedman, A.S., Hogstrom, U. and Bergstrom, H., 1996. Low level jets - a decisive factor for off-shore wind energy siting in the Baltic Sea. Wind Engineering, 20(3): 137-147.

Smedman, A.-S., Bergstrom, H. and Hogstrom, U., 1995. Spectra, variances and length scales in a marine stable boundary layer dominated by a low level jet. Boundary-Layer Meteorology, 76: 211-232.

Smith, D. K.: 2002, 'Detection and Characterization of Diurnal Winds Using QuikScat Data', *EOS, Transactions American Geophysical Union* **82**, OS31A-0380-

Stoffelen, A. Anderson. D. L. T.: 2002, 'Wind Retrieval and ERS-1 Scatterometer Radar Backscatter Measurements', *Advance Space Research* **13**, 53-60

Stull, R. B.: 1991, 'An Introduction to Boundary Layer Meteorology'1-666

Sutton, O. G.: 1953, 'Micrometeorology'1-333

Thompson, D. R. Beal. R. C.: 2000, 'Mapping High-Resolution Wind Fields Using Synthetic Aperture Radar', *John Hopkins APL Technical Digest* **21**, 58-67

Thompson, D. R. Monaldo. F. M. Beal. R. C. Winstead. N. S. Pichel. W. G. Clemente.-Colon. P.: 2001, 'Combined Estimates Improve High-Resolution Coastal Wind Mapping', *EOS, Transactions, American Geophysical Union* **82**, 1-3

Troen, I. and Petersen, E. L.: 1989, 'European Wind Atlas', Risø National Laboratory, Roskilde, Denmark

Vachon, P. W. Dobson. E. W.: 2000, 'Wind Retrieval From RADARSAT SAR Images: Selection of a Suitable C-Band HH Polarization Wind Retrieval Model', *Canadian Journal of Remote Sensing* **26**, 306-313

van Ulden, A. P.: 1978, 'Simple Estimates for Vertical Diffusion From Sources Near the Ground', *Atmospheric Environment* **12**, 2125-2129

Wu, J., 1995. Sea surface winds - a critical input to oceanic models but are they accurately measured? Bulletin of the American Meteorological Society, 76(1): 13-19

Young, G. S.: 2000, 'SAR Signatures of the Marine Atmospheric Boundary Layer: Implications for Numerical Forecasting', *John Hopkins APL Technical Digest* **21**, 27-32

Appendix I

List of publication from the WEMSAR project

Refereed journal

Hasager, C.B, H.P.Frank, B.R. Furevik 2002 On offshore wind energy mapping using satellite SAR. *Canadian Journal of Remote Sensing,* **28/1**, 80-89

Proceedings

Hasager, C.B., Jensen, N.O., Nielsen, M., Furevik, B. 2002 SAR satellite image derived wind speed maps validated with in-situ meteorological observations and footprint theory for offshore wind resource mapping. *Proceedings of Global Windpower Conference, Paris, 2-5 April, 2002.* See proceedings, poster and Award for best poster.

Jørgensen, B.H., Furevik, B., Hasager, C.B., Astrup, P., Rathmann, O., Barthelmie, R., Pryor, S. 2002 Developments in mesoscale modeling and satellite SAR imaging of offshore wind maps. *Proceedings of Global Windpower Conference, Paris, 2-5 April, 2002.* See proceedings

Pryor, S., Barthelmie, R., Hasager, C.B. 2002 Can satellite sampling of offshore wind represent wind speed distributions? *Proceedings of Global Windpower Conference, Paris, 2-5 April, 2002.* (in press). See poster

Jørgensen, B.H., Furevik, B., Hasager, C.B., Astrup, P., Rathmann, O., Bartehlmie, R., Pryor, S., 2001 Off-shore wind fields obtained from mesoscale modeling and satellite SAR images. *Offshore Wind Energy, EWEA Special Topic Conference, 10-12 December 2001, Brussels, Belgium.* (CD-ROM). See proceedings

Hasager, C.B., Furevik, B., Dellwik, E., Sandven, S. Frank, H.P., Jensen, N.O., Astrup, P., Joergensen, B.H., Rathmann, O., Barthelmie, R.; Johannessen, O., Gaudiosi, G.; Christensen, L.C., 2001 Satellite images used in offshore wind resource assessment. 2001 Eds. P.Helm and A.Zervos. *Proceedings of the European Wind Energy Conference and exhibition (EWEC), Copenhagen (DK), 2-6 July 2001, 673-677,* See proceedings

Pryor, S.C. and R.J. Barthelmie, Persistence of offshore winds: Implications for power quality. *Proceedings of the European Wind Energy Conference and exhibition (EWEC), Copenhagen, Denmark, 2-6 July 2001, Eds. P.Helm and A.Zervos, (DK), 2-6 July 2001,* 717-720. See poster

Hasager, C.B and H.P.Frank 2000. Off-shore wind energy mapping using satellite SAR. *CERSAT NEWS*, Special Issue No. 11, *Ocean Winds Proceedings of Workshop on present and emerging remote sensing methods*, 19-21 June 2000. IFREMER, p. 10

Hasager, C.B. 2000 Wind energy mapping using syntheric aperture radar, *Proceedings of Fifth International Winds Workshop*, 28 February - 3 March

2000, Lorne, Australia. EUMETSAT, Germany, EUM P28, ISSN 1023-0416, ISBN 92-9110-036-6, p 259-265

Published abstract

Hasager, C.B., Nielsen, M. and Furevik, B. 2002 Validation of wind speed maps from satellite SAR through footprint analysis of in-situ data from an off-shore meteorological mast in Denmark. *European Geophysical Society 2002, XXVII General Assembly, Nice, France, 21-26 April, Geophys. Research (CD-ROM).* See abstracts. Poster available

Furevik, B.R., Espedal, H.A., Hasager, C.B., Johannessen, O.M., Jørgensen, B.H., Rathmann, O. and Sandven. S. 2002 Wind estimates at the Norwegian west coast from modelling, in situ and satellite observations. *European Geophysical Society 2002, XXVII General Assembly, Nice, France, 21-26 April, Geophys.* Research (CD-ROM). See abstracts

Hasager, C.B. and H. Frank, 2000, Off-shore wind energy mapping using satellite SAR. *Abstracts of Ocean Winds Workshop on Present and Emerging Remote Sensing Methods.* IFREMER, Brest, France, 19-22 June 2000, p 41 See abstract and poster (pdf).

Hasager, C.B., Furevik, B., Dellwik, E., and O. Johannessen (2001) Comparison of satellite sar-derived wind speed maps and off-shore in-situ wind observations in the North Sea. European Geophysical Society 2001, XXVI General Assembly, Nice, France, 25-30 March, (CD-ROM). See abstract (pdf).

Hasager, C.B. and H. Frank, 2000, Off-shore wind energy mapping using satellite SAR. Ocean winds workshop on present and emerging remote sensing methods. IFREMER, Brest, France, 19-22 June 2000, p 41-42

Other

Hasager, C.B. 2001 Offshore vind fra satellitbilleder, Risøs Vinddag, Risø National Laboratory, 28 November 2001. See slides

Hasager, C.B., Furevik, B., Jørgensen, B.H., and Astrup, P. 2001 Offshore wind from SAR satellite images. *Danish Society of Atmospheric Research (DSAR*) annual meeting, Copenhagen 15 November 2001, see poster

Hasager, C.B. and H. Frank, 2000, Off-shore wind energy mapping using satellite SAR. Ocean winds workshop on present and emerging remote sensing methods. IFREMER, Brest, France, 19-22 June 2000. Poster available at http://www.risoe.dk/vea-atu/remote/IFREMERworkshop.pdf

Johannessen, O.M., S. Sandven, H.Espedal, B.Furevik, T.Hamre, J.Højstrup, C.Hasager, G.Jevne, G.Gaudiosi, 2000, Wind energy mapping using Synthetic Aperture Radar (WEMSAR), *European Seminar: Offshore Wind Energy in Mediterranean and other European Seas* (OWEMES) 2000, 13-15 April 2000, Sicily, Italy (poster)

Submitted

Hasager, C.B Furevik, B., Pryor, S.C. and Barthelmie, R.J. 2002 Offshore wind resources quantified from satellite SAR: methodology and technical aspects. *1st International Symposium on Recent Advances in Quantitative Remote Sensing, 16-20 September 2002, Valencia, Spain. Session "Active Microwaves".* (Abstract submitted)

Abstract (max. 2000 characters)

A validation study has been performed in order to investigate the precision and accuracy of the satellite-derived
ERS-2 SAR wind products in offshore regions. The overall project goal is to develop a method for utilizing the
satellite wind speed maps for offshore wind resources, e.g. in future planning of offshore wind farms. The report
describes the validation analysis for 16 cases in Denmark, 5 in Italy and 3 in Egypt. Wind speed maps and wind
direction maps from the ERS-2 SAR satellite are derived at the Nansen Environmental and Remote Sensing Cen-
ter. Wind speed and wind direction maps at 10 m above sea level have been compared to in-situ observations
from a met-mast at Horns Rev in the North Sea located 14 km offshore. The SAR wind speeds have been area-
averaged by simple and advanced footprint modelling. The comparison results are very promising with a stan-
dard error of ± 0.61 m s^{-1}, a bias ~ 2 m s^{-1} and R^2 ~ 0.88. Wind speeds predicted by the local scale model LINCOM
and the mesoscale model KAMM2 have been sucessfully compared to the spatial variations in the SAR wind
speed maps. Near the coast is an 800 m wide band in which the SAR wind speed observations have a strong
negative bias. Shallow water and tidal currents bias in the SAR wind speed maps in some cases. At the Italian
site the SAR wind speed maps compared very well to WAsP model results from the coast to 5 km offshore. Fur-
ther offshore the KAMM2 model results seemed more reliable. This is likely due to mesoscale effects of high
orography at Corsica. At least 60-70 randomly selected satellite images are required to characterize the mean
wind speed and Weibull c parameter, while of the order of 150 images are required to obtain a variance estimate,
and nearly 2000 are needed to obtain a robust estimate of energy density (or Weibull k). This is under the as-
sumption of no error in the SAR wind speed maps and for an uncertainty of $\pm$ 10% at a confidence level of 90%.
Around 100 satellite SAR scenes may be available for some sites on Earth but far few at other sites. The number
of available satellite SAR scenes is increasing rapidly with ERS-2, RADARSAT-1 and ENVISAT in orbit.
Hence the technique holds promise for future utilization in offshore wind resource assessment.

Descriptors INIS/EDB

BOUNDARY LAYERS; DATA; MATHEMATICAL MODELS;
OFFSHORE SITES; RADAR; SATELLITES; VELOCITY;
VERIFICATION; WIND